Numerical Simulation of Seismic Site Amplification Effects

by

Roshanak Varjavand

A Dissertation Presented to the

FACULTY OF THE USC GRADUATE SCHOOL

UNIVERSITY OF SOUTHERN CALIFORNIA

In Partial Fulfillment of the

Requirements for the Degree

DOCTOR OF PHILOSOPHY

(CIVIL ENGINEERING)

May 2013

Acknowledgements

I would like to express my gratitude toward my mentor and adviser, Professor Hung Leung Wong, for his guidance and support. I would like to thank Professor Anderson and Professor Wellford for guiding me through my qualifying exam with research ideas. I am also grateful to my dissertation committee, Professor Vincent Lee, Professor Lucio Soibelman, Professor Mihailo Trifunac, and Professor Chungmin Wang. And the last but not the least, I would like to thank my parents Moonta and Mehran for their unconditional love and support.

Table of Contents

Acknowledgements ii

List of Figures vi

Abstract x

Chapter 1 – Introduction 1
1.1 – Effects of site amplification on structural response during earthquakes . . . 2
1.2 – Empirical Modeling of Site Amplification 3
1.3 – Site amplification Factors in Seismic Building Codes 5
1.4 – Analytical Modeling of Site Amplification 8

Chapter 2 – Theoretical Development 14
2.1 – Level of Difficulty of Various Wave Propagation Models 16
2.2 – The Concept of Substructure Deletion 18
2.3 – Theoretical Development of the Proposed Method 21
2.4 – Accuracy of the Modified Substructure Deletion Method 28
2.5 – Response of a Canyon to Incident SH-Waves 33
2.6 Response of an arbitrary shape Canyon to Incident SH-Waves 37

Chapter 3 – Site Amplification for Anti-Plane Problems 45
3.1 – Boundary Conditions for Alluvial Valley Problem 46
3.2 – Comparison with Exact Solutions 48
3.3 – Solutions at High Frequencies 52
3.4 – Response of an Arbitrary Shaped Alluvial Valley 54
3.5 – Computation of Time Histories 60

Chapter 4 – Wave Scattering by a Canyon for In-Plane Waves 72
4.1 – Validation of Plane Strain Green's Functions 72
4.2 – Comparison with Available Results 81
4.3 – Response of an arbitrary shape Canyon to Incident P and SV-Waves 84

Chapter 5 – Site Amplification for Plane Strain Problems 93
5.1 – Validation of Results Using Model Refinement 93
5.2 – Response of an Elliptical Alluvial Valley to P and SV-waves 97
5.3 – Response of an Arbitrary Shape Alluvial Valley to P and SV-waves . . . 104
5.4 – Time History Calculation for Alluvial Valley Surface 107

Chapter 6 – Conclusions 120

References 124

Appendix A – The Boundary Integral Equation Method 129

Appendix B – Anti-Plane Green's Function Matrices 134
B.1 – Green's Functions for an Infinite Medium 134
B.2 – Green's Functions for a Semi-Infinite Medium 135
B.3 – Surface Green's Functions for a Semi-Infinite Medium 136

Appendix C – Plane Strain Green's Function Matrices 138
C.1 – Green's Functions for an Infinite Medium 138
C.1.1 – Displacements and Stresses Generated by a Vertical Line Load 138
C.1.1.1 – Displacements 140
C.1.1.2 – Stresses 141
C.1.2 – Displacements and Stresses Caused by a Horizontal Line Load 143
C.1.2.1 – Displacements 144
C.1.2.2 – Stresses 145
C.1.3 – Formation of [U] and [T] 145
C.2 – Surface Green's Functions for a Semi-Infinite Medium 146

Appendix D – Wave Motion in a Semi-Infinite Medium 150
D.1 – Two-Dimensional Plane-Strain Problem 150
D.2 – Incident P-Wave Solution 151
D.2.1 – Displacement Wavefields for Incident P-Waves 156
D.2.2 – Stress Wavefields for Incident P-Waves 157
D.3 – Incident SV-Wave Problem 158
D.3.1 – Displacement Wavefields for Incident SV-waves 162
D.3.2 – Stress Wavefields for Incident SV-waves 164
D.4 – Incident SH-Wave Solution 164
D.4.1 – Displacement Wavefields for Incident SH-Waves 166
D.4.2 – Stress Wavefields for Incident SH-Waves 166
D.5 – Rayleigh Wave Solution 166

Appendix E – Accurate Calculation of Bessel's Functions 171
E.1 – Functions with Small to Medium Arguments 171
E.2 – Functions with Large Arguments 172

Appendix F – Three-Dimensional Green's Function Matrices 179
F.1 – Green's Functions for an Infinite Medium 179
F.1.1 – Displacements and Stresses Generated by a Vertical Point Load 179
F.1.1.1 – Displacements 181
F.1.1.2 – Stresses 182
F.1.2 – Displacements and Stresses Generated by a Point Load in the X-Direction 185

F.1.2.1 – Displacements 186
F.1.2.2 – Stresses 187
F.1.3 – Displacements and Stresses Generated by a Point Load in the Y-Direction 187
F.1.3.1 – Displacements 188
F.1.3.2 – Stresses 189
F.1.4 – Formation of matrices $[U]$ and $[T]$ 189
F.2 – Surface Green's Functions for a Semi-Infinite Medium 190
F.2.1 – Surface Displacements Generated by Point Forces 190
F.2.2 – Formation of $[U]$ and $[T]$ 192

List of Figures

Figure 1.1. Geologic map of Kobe, Japan, and the site characterization locations. The near-surface S-wave slowness Ss(30) range is shown for each SASW site . 7

Figure 1.2. Location and Geology of Taiwan sites 9

Figure 2.1. A Basic Half Space Model 15

Figure 2.2. A Medium With Contrasting Stiffness 17

Figure 2.3. Two Media With The Same Material 19

Figure 2.4. An Embedded Elliptical Foundation in an Elastic Half Space 29

Figure 2.5. Comparison of Results for a Circular Foundation at $a_0 = 1$. 31

Figure 2.6. Comparison of Results for an Elliptical Foundation at $a_0 = 1$. 32

Figure 2.7. Comparison of Results for an Elliptical Foundation at $a_0 = 4$. 34

Figure 2.8. Average Error Comparisons as a function of Scattterer Depth. 35

Figure 2.9. An Elliptical Canyon Subjected to Incident SH-Waves 36

Figure 2.10. A Circular Canyon Subjected to Incident SH-Waves at $a_0 = 1$ 38

Figure 2.11. A Circular Canyon Subjected to Incident SH-Waves at Higher Values of a_0. 39

Figure 2.12. An Arbitrary Shaped Canyon. 40

Figure 2.13. Arbitrary Shape Canyon Response at $\eta = 2$. 41

Figure 2.14. Arbitrary Shape Canyon Response at $\eta = 4$. 42

Figure 2.15. Arbitrary Shape Canyon Response at $\eta = 8$. 44

Figure 3.1. Models with Available Solutions 49

Figure 3.2. Results for Circular Valley for $\eta = 0.5$ 50

Figure 3.3. Results for Circular Valley for $\eta = 1.0$ 51

Figure 3.4. Results for Elliptical Valley for $\eta = 1.5$ 53

Figure 3.5. High Frequency Calculation at $\eta_v = 8$ 55
Figure 3.6. An Arbitrary Shape Alluvial Valley 56
Figure 3.7. Low Frequency Response of Alluvial Valley 57
Figure 3.8. High Frequency Response of Alluvial Valley 58
Figure 3.9. Response of Alluvial at $\eta = 4$. Left Side Incident 59
Figure 3.10. Response of Alluvial at $\eta = 4$. Right Side Incident 61
Figure 3.11. Ricker Wavelets and their Fourier Transforms 63
Figure 3.12. Complex Transfer Functions and Their Amplitudes 65
Figure 3.13. Response to Ricker Wavelet with Vertically Incident SH-Wave 67
Figure 3.14. Response to Ricker Wavelet with Horizontally Incident SH-Wave . . . 68
Figure 3.15. Response at Station 4 to Ricker Wavelet with Various Incident Angles . 69
Figure 3.16. Response at Station 4 as a Function of Stiffness Ratios 71
Figure 4.1. A Rigid Strip Foundation 73
Figure 4.2. Comparison of Compliance Functions C_{vv} 74
Figure 4.3. Comparison of Compliance Functions C_{hh} 75
Figure 4.4. Compliance Functions C_{vv} with Various Levels of Approximation . . . 77
Figure 4.5. Compliance Functions C_{hh} with Various Levels of Approximation . . . 78
Figure 4.6. Amplitude Comparisons for P-Wave Incident, $\eta = 1$ 80
Figure 4.7. Amplitude Comparisons for SV-Wave Incident, $\eta = 1$ 82
Figure 4.8. Aspect Ratio Comparison. SV-wave Incidence, $\theta = 60°$, $\eta = 1$ 83
Figure 4.9. Aspect Ratio Comparison. SV-wave Incidence, $\theta = 90°$, $\eta = 1$ 85
Figure 4.10. P-wave Incidence, $\eta = 1$ 86
Figure 4.11. P-wave Incidence, $\eta = 2$ 87

Figure 4.12. P-wave Incidence, $\eta = 5$ 89

Figure 4.13. SV-wave Incidence, $\eta = 1$ 90

Figure 4.14. SV-wave Incidence, $\eta = 2$ 91

Figure 4.15. SV-wave Incidence, $\eta = 5$ 92

Figure 5.1. Aspect Ratio Comparison. P-wave Incidence, $\theta = 60^\circ$, $\eta = 1$ 95

Figure 5.2. Aspect Ratio Comparison. SV-wave Incidence, $\theta = 60^\circ$, $\eta = 1$ 96

Figure 5.3. Amplitude Variation of Alluvial Valley to Incident P-waves, $\eta = 1$ . . . 98

Figure 5.4. Amplitude Variation of Alluvial Valley to Incident P-waves, $\eta = 2$ . . . 99

Figure 5.5. Amplitude Variation of Alluvial Valley to Incident P-waves, $\eta = 5$ . . 100

Figure 5.6. Amplitude Variation of Alluvial Valley to Incident SV-waves, $\eta = 1$ . . 102

Figure 5.7. Amplitude Variation of Alluvial Valley to Incident SV-waves, $\eta = 2$ . . 103

Figure 5.8. Amplitude Variation of Alluvial Valley to Incident SV-waves, $\eta = 5$ . . 104

Figure 5.9. Low Frequency Response of Alluvial Valley to
P-wave Incidence, $\eta = 1$ 105

Figure 5.10. Medium Frequency Response of Alluvial Valley to
P-wave Incidence, $\eta = 2$ 107

Figure 5.11. Low Frequency Response of Alluvial Valley to
SV-wave Incidence, $\eta = 1$ 108

Figure 5.12. Medium Frequency Response of Alluvial Valley
to SV-wave Incidence, $\eta = 2$ 109

Figure 5.13. Transfer Functions for u_x and u_y at Station 4 110

Figure 5.14. Transfer Functions for u_x and u_y at Station 4 111

Figure 5.15. Vertical Response to P-wave Incidence, $\theta = 120^\circ$ 113

Figure 5.16. Horizontal Response to SV-wave Incidence, $\theta = 75^\circ$ 114

Figure 5.17. Vertical Response to SV-wave Incidence, $\theta = 75^\circ$ 115

Figure 5.18. Response to Rayleigh wave Incidence 117

Figure 5.19. Attenuation of Rayleigh Wave Over Distance 118

Figure A.1 – Schematic of the formulation of the Boundary Integral Equation. . . 129

Figure C.1 – Vertical Q_Y Line Force Configuration. 139

Figure C.2 – Horizontal Q_X Line Force Configuration. 143

Figure D.1 – Incident and reflected P-wave. 151

Figure D.2 – Incident and reflected SV-wave. 159

Figure D.3 – Incident and reflected SH-wave. 165

Figure F.1 – Vertical Q_Z Point Force Configuration. 180

Figure F.2 – Horizontal Q_X Point Force Configuration. 185

Figure F.3 – Horizontal Q_Y Point Force Configuration. 188

Figure F.4 – The Definition of the Cylindrical Coordinate System. 193

Abstract

The concept of substructure deletion proposed for the analysis of a rigid embedded foundation was adapted for the analysis of site amplification effects in alluvial valleys. A major modification was made for the present application such that the boundary integration equation method was used for both the finite size interior problem and semi-infinite exterior wave radiation problem. The modification was made to reduce the possible incompatibility between the finite element method, a volume formulation, and the boundary integral equation method, a surface formulation. The substructure deletion concept allows simple, century-old, basic Green's Functions to be used to produce excellent wave scattering results for topographical irregularities as well as arbitrarily shaped alluvial valleys overlying a stiffer bedrock. The concept is applicable to three-dimensional geometries as well as two-dimensional problems. Results are given for incident SH, P, SV and Rayleigh waves.

Chapter 1

Introduction

It is well-known to a geophysics researcher that a theoretically generated wave solution from a fault rupture model seems overly simplistic compared to a recorded seismogram. Although there are major approximations made in a well-defined dip-slip or strike-slip model, the inhomogeneous contents along the wave path, from the fault to the recording station, contribute in a major way to the complexity of the recorded wave form.

Since many civilizations were founded near a water source with an alluvial deposit to grow vegetation and sustain life; it is therefore highly likely that an urban earthquake would be amplified by soft alluvium deposit over a stiff bedrock. The duration of the seismic event could be longer due to wave energy trapped within the top layers of sediment. It is relatively easy for wave energy to enter the soft upper layers from the rock layers below because of the contrast of material strength. Once the wave energy entered the softer layers, it is trapped there as a large percentage of the outgoing waves are reflected from the stiffer lower layers. This phenomenon leads to prolonged seismic records as it requires time for the interior wave energy to dissipate into the lower layers and not return.

Effect of site conditions on earthquake intensity has always been an important part of earthquake engineering. It was noticed that during earthquakes degree of damage to similar structures located on different site conditions is not the same and this started the investigation and research on effect of soil conditions on earthquake strong motion. In the 1989 Loma Prieta earthquake, the greatest damage occurred in areas where site response increased the ground motion (Holzer et al.,1994). In the 1994 Northridge earthquake, distribution of damage was irregular throughout Los Angeles even within a distance of 1 Km. Seismic

recording have been found different at sites which are located only 200 meters from each other. This inconsistency in seismic risk indicates the effects of site conditions are major factors (Holzer, 1994, Hatzell, 1996 and Field, 2000).

There are at least two types of site-effects that can enhance earthquake damage: one is soil failure such as liquefaction and the other is geological compositions which amplify incoming waves. In the 1985 Mexico City earthquake the catastrophic damage to buildings and bridges was identified as a result of amplification of waves in soft clay on much stiffer soil or rock. During this particular earthquake long duration induced soil resonance without much soil nonlinearity (Anderson et al, 1986). In the 2000 Western Tottori earthquake in Japan, a detailed study of damage to wooden houses indicated a pattern that site condition has strong effects (Matsunami et al, 2002). In the 1989 Loma Prieta and the 1996 Kobe earthquakes, two well-documented events (Iwata et al, 1996, Aguirre and Irikura, 1998, Ishihara and Kijima, 2001), both site amplification and soil liquefaction was reported.

1.1. Effects of site amplification on structural response during earthquakes

It is of great interest to study the effects of site amplification because of the direct impact it has on the response of structures during earthquakes. In the 1985 Chile earthquake the one- and two-story buildings, which were built on volcanic or sedimentary rocks and alluvium, resulted in resonance; wave amplification caused higher spectral acceleration values. In the 1985 Mexico City earthquake large amplitudes were results of site amplification effects and it has certain dominant frequencies associated with the geological conditions of the area (Ordaz et al, 2000). It was reported (Anderson et al, 1986) that the medium-rise structures were damaged most seriously.

Matsunami et al (2002) conducted a research on damage to wooden houses in Shimoenoki, Tottori, Japan, by the 2000 Western Tottori earthquake. They concluded

that damage was the result of variation of site amplification factors at frequencies between 2 and 5 Hz and that frequency range is close to the first natural frequency of the wooden buildings. Zhang et al (2003) conducted research on the effects of site amplification on structural response of base-fixed 6-storey framed structure. They used the finite elements method with the aid of boundary elements to study structural response on a soft clay site. They concluded that soil nonlinearity has a significant influence on structural response if the site response has a period near the fundamental period of the structure. Wong et al (1977) measured the response near a canyon in Pasadena generated by a nine-storey building excited harmonically by a shaker at its roof. The observed results indicated that surficial irregularities can affect the incoming wave amplitudes.

Hao and Chouw (2008) studied the response of bridge structures to site amplified ground motions. They utilized the Australian design spectrum for bedrock movement simulation and described the subsoil properties using a combined finite element and boundary element method. Their results show the importance of site amplification. The authors indicated that site amplification can result in relative response between two adjacent bridge locations and it can cause pounding which damages bridge girders.

1.2 Empirical Modeling of Site Amplification

Many researchers have estimated site amplification from weak and strong motion records including S waves, coda waves, and ambient noise. Kagami et al (1982) found that spectral amplitude of long period microtremors increases as the thickness of soil deposit increases. Therefore, observation of long period microtremors at a number of stations can help estimate deep soil amplification.

Borcherdt (1994), used the Loma Prieta strong motion record and averaged site amplification factors over the short period (0.1-0.5 sec), intermediate period (0.5-1.5 sec),

mid period (0.4-2 sec), and long period (1.5-5 sec) bands. These coefficients were obtained from Fourier amplitude spectra for the radial and transverse components of ground motion. Site amplification in recent building codes are developed from the averages of amplification estimates in short and mid period.

Crouse and McGuire (1996) estimated site coefficients utilizing empirical attenuation curves developed from strong motion recording of 16 US earthquakes considering various spectral magnitude and acceleration levels.

Su et al (1996) concluded that site amplification determined from S waves and coda waves are consistent within epicentral distance greater than focal depth, the reason for the inconsistency within smaller distances is that S waves can be affected by the wave propagation path. Stations in this study were located on sites with various geological characteristics, including alluvial sites. The authors indicated that for deep alluvial sites, such as San Francisco, further study need to be conducted since the generation of resonant waves is possible.

Harmsen (1997) derived amplification factors relative to a single reference rock site (Caltech Seismic Lab) using the inversion approach of Andrews (1986). Strong motion data from main shock recordings in the San Fernando Valley and the Los Angeles basin from the 1971 San Fernando, the 1987 Whittier, the 1991 Sierra Madre and the 1994 Northridge earthquakes were used. Amplification factors were proposed through linear relationships for intermediate (0.5-1.5 Hz) and high (2.0-6.0 Hz) frequency bands.

Trifunac and Todorovska (2000) studied site amplification factors based on weak and strong motions. Their results show that small amplitude waves (aftershocks, coda waves and small earthquakes) cannot be used for the prediction of site amplification factors in the near field if the soil response is nonlinear.

Yamanaka et al (2008) observed the ground motions of the 2007 Noto Hanto earthquake aftershocks. Their results suggest that amplification mechanism in Terrace deposits is different from Quaternary sediments. They reported that amplitude of spectral ratios is twice those of microtremors; but there is a linear correlation between them. They indicated that microtremors can be used for estimating site effects in shallow soils.

Taylor et al (2009) developed a method for estimating site factors from ambient noise. Based on their results for hard rock sites, amplitudes are lower and resonance peaks are narrower as compared to softer sites. At higher amplitudes, the spectral peaks are more symmetric and have higher frequencies because sites with higher amplification have lower densities and smaller strain nonlinearity.

1.3 Site amplification Factors in Seismic Building Codes

Starting in the 1990s shear wave velocity in the upper $30\,\mathrm{m}$ of soil (Vs30) has been incorporated in building codes around the world. In the United States, Uniform Building Code (UBC) 1997, in Europe, Eurocode 8 (1998) and in Canada National Building Code of Canada (NBCC) 2005 are examples.

In the United Sates, site coefficient S which depends on local soil conditions was introduced in 1978 (ATC, 1987) for calculating seismic force of buildings. Values of S were small and independent of level of shaking and they only amplified the long period of the spectrum. Over the years, using analytical results, laboratory and instrumental results, recorded amplification of earthquake waves (in soft soil during the Loma Prieta earthquake in 1989), it has been shown that the S factor does not incorporate all the necessary site characteristics for seismic design.

After some new studies, new site characterization and site coefficients were introduced to 1994 edition of Seismic Provision of National Earthquake Hazard Reduction Program (NEHRP, 1994) and 1997 Uniform Building Code (UBC 1997). The new F_a and F_v defined site coefficients at the short and large periods, respectively. The factors depend on both site class and the intensity of rock motion, and they decrease as the level of rock seismic hazard increases. The reason for this reduction is based on soil non-linearity. Average shear wave velocity in the upper 30m of the site is used for site classification; 30 m is the typical depth of the soil boring tests which provide detailed site properties.

Code provisions are based on National Earthquake Hazard Reduction Program (NEHRP 1994) soil classification schemes (BSSC 2003). NEHRP provides amplification factors based on Vs30 (Finn and Wightman, 2003). F_a and F_v were developed from averages of amplification estimates in short and mid period from the research conducted by Borcherdt (1994). Loma Prieta strong motion records were applied to average site amplification factors over the short period (0.1-0.5 sec), intermediate period (0.5-1.5 sec), mid period (0.4-2 sec), and long period (1.5-5 sec) bands.

Dobry and Lai (2000) studied development of understanding site response and implementation of it in US seismic codes. They concluded that effects of soil and rock below upper 30 m, basin edge, other two-dimensional and three-dimensional effects, some combination of sites, earthquakes and period ranges are not considered in the code. Liquefaction and strong soil nonlinearity are also not sufficiently considered. They suggested that microzonation of cities and urban areas can be included to improve the simplifications used in codes. Fig. 1.1 and Fig. 1.2 show seismic zones of Kobe, Japan, and Taiwan, respectively.

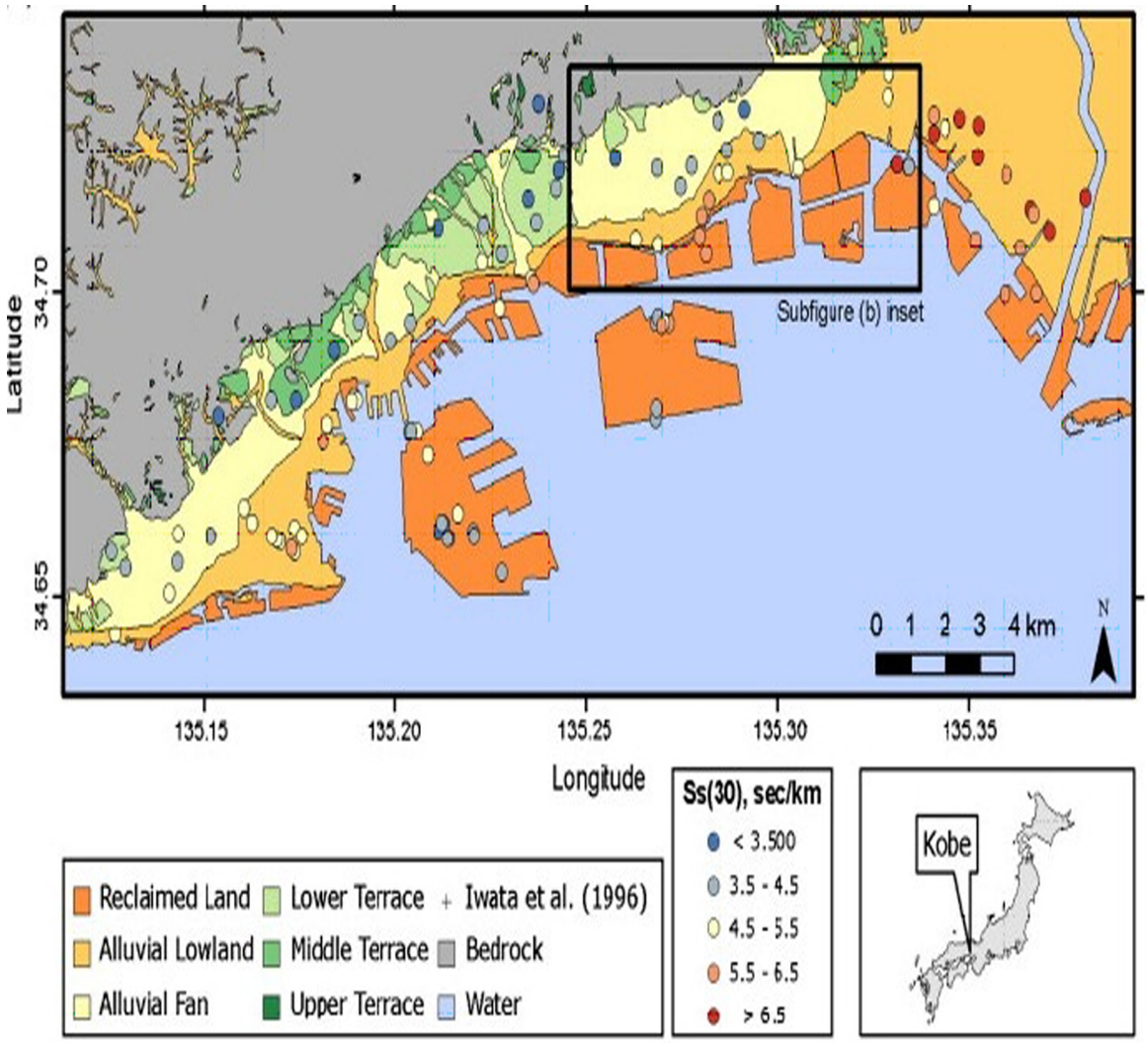

Figure 1.1. Geologic map of Kobe, Japan, and the site characterization locations. The near-surface S-wave slowness Ss(30) range is shown for each SASW site

Anderson et al (1996) studied seismograms for vertically incident S waves through flat, solid, elastic layers. The authors investigated the effect of both surficial and underling geology on peak amplitude and integrated the squared amplitude of the seismogram. Their results show that 30 m is too thin of a layer for a typical earthquake with focal depth of 10 to 15 km and that 30 m represents only 0.3% of the propagation path. Unless the shear wave

velocity is as low as 300 m/sec, the top layer is less than the wavelength, even at 10Hz. The conclusion is that the geological effects on ground motion cannot be determined based on near surface properties alone.

Based on research conducted by Lee et al (2010) average shear velocity in the upper 30 m of soil alone should not be used in site classification or scaling strong motion amplitudes. Their results suggest using a parameter which considers much deeper soil layer thickness and also near surface geology. Hassani et al (2011) suggest that shear wave velocity in the top 30 m is not sufficient for site classification and site effect calculation.

Huang et al (2010) developed Next Generation Attenuation (NGA) relationships using strong motion recordings of shallow earthquakes and compared their results with site coefficients in ASCE 7 and NEHRP provisions. Based on their results for VS30 smaller than 270 m/s, site factors significantly depend on period and are greater than the NEHRP provision site factors.

Le Pense et al (2011) investigated the influence of soil properties and site geometry of sediment filled valleys on earthquake response spectra. Based on their studies current building codes consider site effects only based on a one-dimensional analysis and avoided complex cases of irregular two-dimensional configurations. They indicated two-dimensional complex site effects have higher amplification of seismic waves than one-dimensional site effects, furthermore, it causes extension of signal length.

1.4 Analytical Modeling of Site Amplification

In addition to the observed site amplification effects during earthquakes, there is still a need to simulate these effects using analytical models. The wave propagation problem in solids involves a vector wave equation with at least two body wave speeds. Additionally,

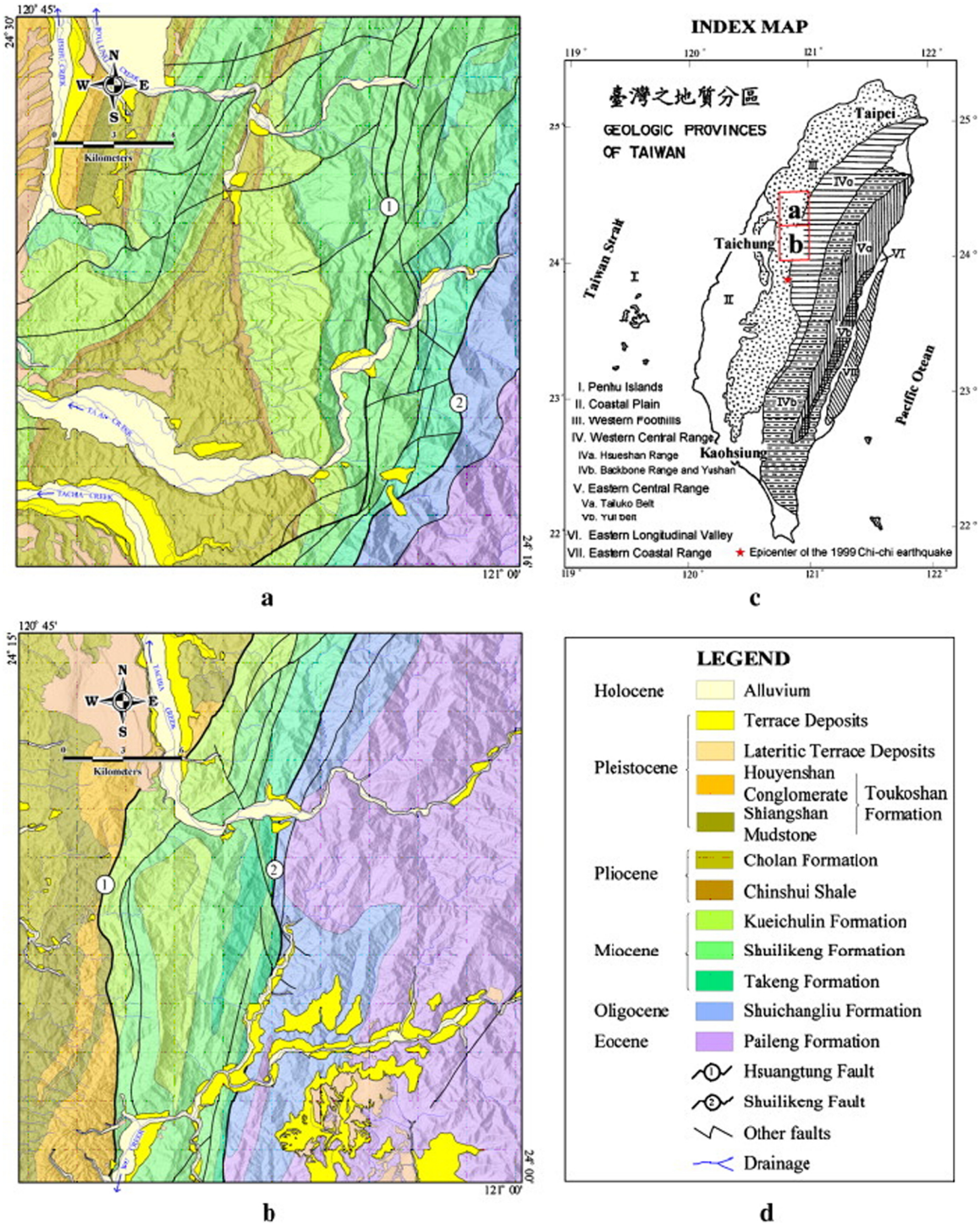

Figure 1.2. Location and Geology of Taiwan sites

surface Love waves (antiplane motion) travel with frequency dependent phase velocities and each mode of that has a different characteristic. There are Rayleigh waves (inplane motion) which have a retrograde type of motion and is to be blamed for many landslide episodes. Because of the complexity of the problem, there are still limited viable theoretical solutions to adequately simulate the site amplification problem in three-dimensions.

Modern numerical tools such as finite elements and finite differences can theoretically handle material and geometrical nonlinearities but the size of this geophysical problem is so large that artificial boundaries must be introduce to limit the problem size. There are still issues to be resolved for numerical instabilities of the artificial boundary algorithms. The number of unknown variables increase quickly in a three-dimensional analysis and the problem can easily become unmanageable.

The continuum mechanics solution cannot handle nonlinear material properties but it offers solutions which allows the far-field conditions to be modeled by a basic half space configuration. The Sommerfeld radiation boundary condition at infinity allowed solutions to be obtained so there is basically no concern for reflected waves from an artificial boundary. The far field can be modeled approximately by a homogenous half space or a layered half space with horizontal layers. Within the linear model framework, the continuum mechanics models can help explain the physics of wave scattering, reflection and diffraction involved in the site amplification problem.

Using SH-wave models, Trifunac (1971) explained the amplitude of waves on the surface of an alluvial valley could be an order of magnitude larger than the amplitude of the bedrock beneath. The amplification factor is dependent of the contrast of material properties as well as the geometrical configurations of the layers. Other researchers such as Wong and Trifunac (1974) and Lee (1985) also contributed similar conclusions for different layer geometries.

Wong (1982) studied the effects of P, SV and Rayleigh waves on an arbitrary shaped canyon and concluded that topographical irregularities can affect wave amplitudes. Kawase H. (1988), Sanchez-Sesma and Campillo (1991), Dravinski and Mossessian (1987) provided more excellent results in that same area. Gatmiri et al (2007, 2009) performed in the time domain a hybrid method which includes a finite element model for sedimentary layer and a boundary element method for the bedrock. The authors also suggested shape factors for possible use in building codes, an attempt to improve the existing one-dimensional wave propagation model currently employed. Dravinski and Wilson (2001) extended the study of wave scattering to include anistropic effects. Dravinski and Mossessian (1990) also did analysis for a three-dimensional alluvial valley by providing interesting transient response at various locations. Most of the above analyses were performed using an indirect boundary integral method where the wave solutions are generated by sources not directly on the boundary of the wave scatterer.

Le Pense et al (2011) investigated the influence of soil properties and site geometry of sediment filled valleys on earthquake response spectra. The authors indicated that two-dimensional and complex site effects could yield higher amplification of seismic waves than one-dimensional site effects. Their research conducted resulted in a two-dimensional method for calculating site amplification of trapezoidal valleys with various geometrical characteristics and soil properties.

The boundary integral equation method, based on the representation theorem introduced by DeHoop (1958) and subsequent work by Haskell (1966, 1969), has the ability to handle irregular geometries and it seems to be an excellent tool for wave scattering problem with some simplification of the actual geological conditions. But the basic component, the Green's Functions, are difficult to calculate. In the particular case of a layered medium with buried sources and buried observers, the program code could require several thousand lines

(Apsel, 1979). Furthermore, there are singularities to be dealt with. The above reasons lead to the fact that it is not yet a popular approach among earth scientists.

In this dissertation, the concept of substructure Deletion as proposed by Dasgupta (1980) to solve rigid embedded foundation problems will be adapted to analyze site amplification problems. This method can replace the depth dependence of the buried Green's Functions by representing those characteristics by a finite layer of the same material. As proposed, if a fill-in layer of the same material is placed on top of the irregular interface, the combination will merge to become a basic half space. With a basic half space, the traction Green's Function matrix at the surface of the half space is zero because the half plane surface is stress free. Therefore, only the displacement Green's Function matrix needs to be calculated. And since there is no depth dependence for the Green's Functions, the problem is significantly simpler, perhaps by an order of magnitude in effort. Betti (1994) applied the same method to a three-dimensional embedded foundation using the boundary integral equation method for both media I and II while Dasgupta originated the method by using the finite element method for the fill-in layer.

The present application applies the same concept to analyze surface or subsurface irregularities and their effects on wave amplification. The two applications are different and the substructure deletion concept should be more efficient for the present site amplification problem because the lateral dimensions of a typical alluvial valley is much larger than its depth, therefore, the fill-in layer is thin in aspect ratio compared to those employed for embedded foundations. From a physics point of view, the traction-displacement relationships for the half space and that for the irregular interface should not be appreciably different.

The main challenge of the present application would be that the motion at every point of the model is of interest. Unlike the foundation analysis, where the traction at the surface of the rigid foundation is only an intermediate result, they are later integrated to yield one complex number per frequency, i.e., the impedance function of the foundation. The inaccuracies of the traction solution would be diminished by the surface integration. The shorter wavelengths are also filtered out by the rigidity of the foundation, a phenomenon known as kinematic interaction. For site amplification studies, however, the point-by-point solution is needed because the overall response at the surface of the entire canyon or alluvial valley is of interest. The development in the later chapters will demonstrate the value of the substructure deletion concept as a potential tool to analyze complex three-dimensional wave scattering problems.

Chapter 2

Theoretical Development

There are two of the major analysis methods available for dynamics problems: the finite element method and the continuum mechanics method. The finite element method is excellent for three-dimensional geometrical and material modeling of finite size models, but the vast scale of geophysical problems make computation not feasible because of issues associated with an artificial boundary introduced to limit the model size. The continuum methods are limited by the number of coordinate systems which are amenable to solutions for the vector elastic wave equation.

Most geophysics related wave propagation problems are simplified to that with a half-space configuration in which the out-going waves are assumed to radiate away and not return. The far-field approximation is crude, simply a half-space or a layered half-space with horizontal layers. The near-field locations demand more detailed modeling and the boundary integral equation method seems to be the most promising analysis tool to meet the challenge.

The form of the representation theorem (Haskell 1969) for waves generated by sources from a surface S is

$$\vec{u}(\vec{r}_p) = \int_S \left[\, U(\vec{r}_p|\vec{r}) \,\right] \vec{t}(\vec{r})\, dS - \int_S \left[\, T(\vec{r}_p|\vec{r}) \,\right] \vec{u}(\vec{r})\, dS \qquad . \tag{2.1}$$

Using the above integral representation, the displacement vector $\vec{u}(\vec{r}_p)$ at any location $\vec{r}_p$ within the homogeneous soil medium can be calculated in terms of the boundary displacement $\vec{u}(\vec{r})$ and the boundary traction $\vec{t}(\vec{r})$. The derivation of Eq. (2.1) is based on the reciprocal theorem and it is explained in Appendix A. The surface S represents the

scattering surface of the problem and must be defined so it is consistent with the Green's Function matrices $[U]$ and $[T]$. If a semi-infinite medium is considered, S can have an infinite dimension to cover the entire half space surface if full-space Green's Functions were used. However, if local conditions of a particular site is of greater interest, the far-field can be assumed to be a half-space surface and it is expedient to use Green's Function matrices, $[U]$ and $[T]$ such that the stress free boundary condition at the half-space surface is accounted for automatically. With this condition, the surface S would be reduced to that of a localized, finite size wave scatterer, S, between points A and B as shown in Fig. 2.1. The boundary condition of the free surface from A to $x \to -\infty$ and from B to $x \to \infty$ are accounted for by using the Green's Function derived specifically for a half-space configuration.

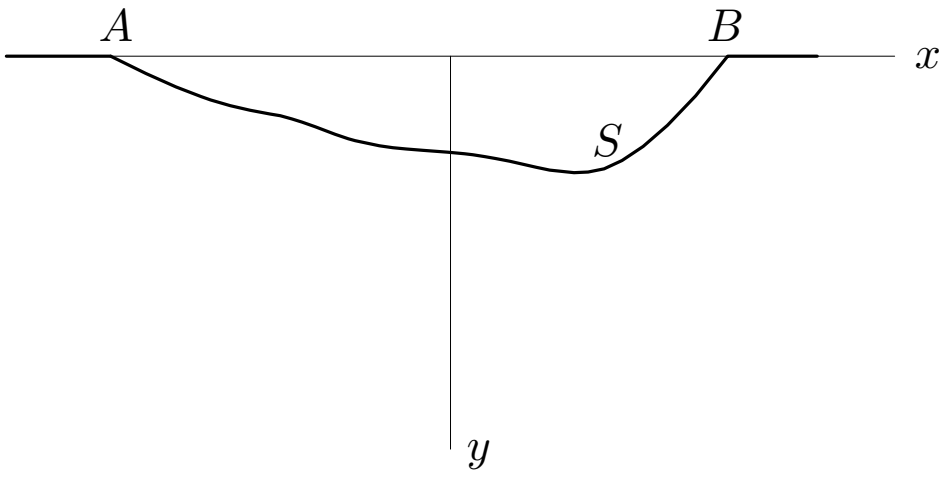

Figure 2.1. A Basic Half Space Model

2.1 Level of Difficulty of Various Wave Propagation Models

The boundary integral equation, as shown in Eq. (2.1), is applicable to a large number of wave propagation problems. It is particular important for modeling wave problems where the outgoing waves are not expected to return. For this reason, the analysis is normally concentrated near the scattering surface S and the details of the far field is less important. This method has an advantage over methods such as the finite element or the finite difference method because the information far removed from the points of interest is critical to the stability of the numerical algorithm.

One of the difficulties of using Eq. (2.1) is that the Green's Functions have singularities. For two-dimensional problems, the displacement matrix $[U]$ has the integrable singularity of $\log r$ as $r \to 0$ and the traction matrix $[T]$ has a $1/r$ singularity. For three-dimensional models, the displacement matrix $[U]$ has the integrable singularity of $1/r$ as $r \to 0$ and the traction matrix $[T]$ has a $1/r^2$ singularity. In both cases, the Principle Value integral must be taken for the integration of the $[T]$ matrix in the second term on the right side of Eq. (2.1) when the observation point $\vec{r}_p$ is placed on the surface to form an integral equation.

In addition to the challenges met while dealing with the singularities, the Green's Functions are difficult to evaluate for some cases and nearly impossible for others. The purpose of this section is to explore the relative difficulties of the problems and then propose a way to simplify the formulation to achieve the solution with less complicated Green's Functions. It is important to note that the principle of superposition which led to the development of Eq. (2.1) is applicable only to linear problems.

Shown in Fig. 2.2a is a simplified model of an alluvial layer overlying the bedrock. This schematic represents both two-dimensional and three-dimensional models. Region I represents the alluvial valley and it has a finite dimension as shown in Fig. 2.2b. Region II

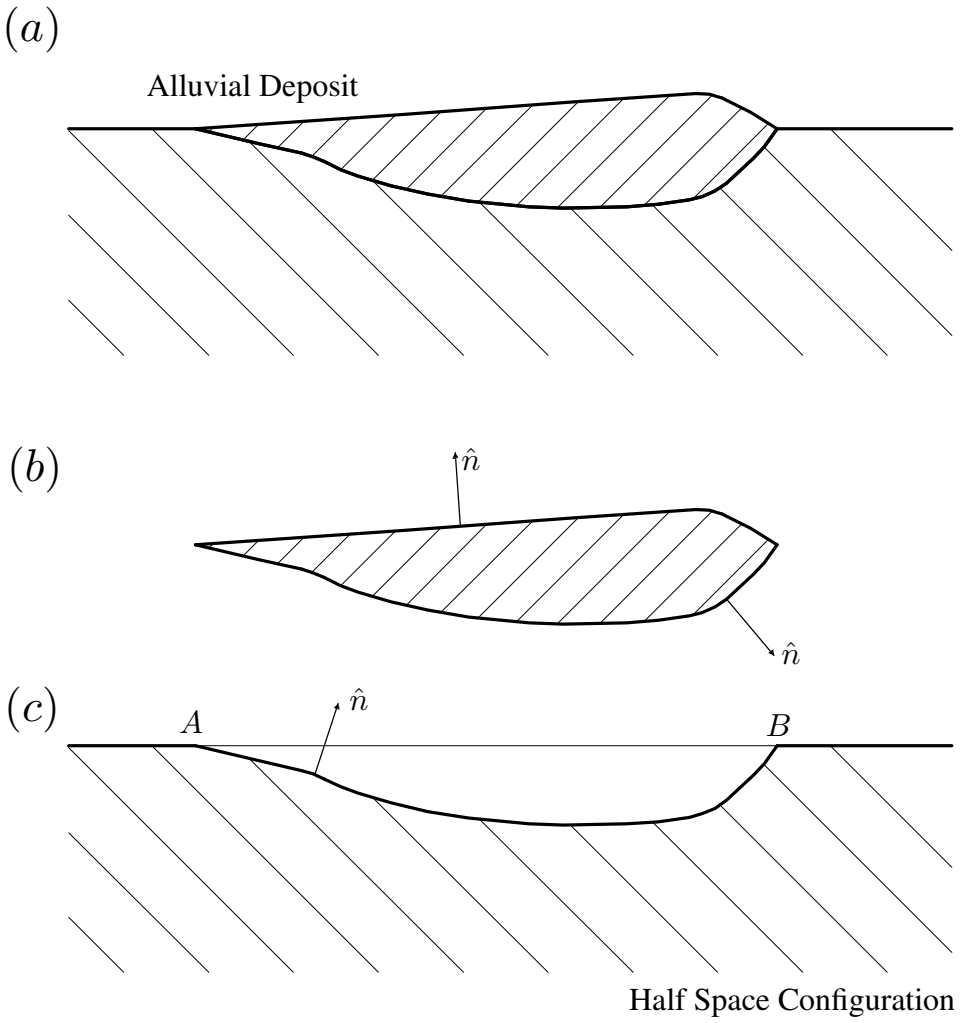

Figure 2.2. A Medium With Contrasting Stiffness

has an irregular interface carved out of a basic half-space configuration and it is assumed to have infinite dimensions in the lower portion of the model.

To use Eq. (2.1) to model the alluvial layer as shown in Fig. 2.2b, the Green's Functions for an infinite medium are used. The scatterer's surface S would be the two faces which enclose the body. The traction matrix $[T]$ would be calculated using the normal vector $\hat{n}$ directed outward from the medium. This is known as an interior problem and the model possesses resonance behavior typical of a finite model. The Green's Functions for an infinite

space are formed by basic algebraic and trigonometric functions as shown in Appendix B, Section B.1 for two-dimensional anti-plane wave problems, Appendix C, Section C.1 for two-dimensional plane strain wave problems and Appendix F, Section F.1 for three-dimensional problems. Although many of the expressions seem lengthy and tedious, they can be calculated easily with a computer program. The geometry of the alluvial layer can be approximated by a parametric surface or a Triangulated Irregular Network (TIN) surface, the latter for three-dimensional models.

To use Eq. (2.1) to model a half space with an irregular surface as shown in Fig. 2.2c, the main challenge is the numerical evaluation of the Green's Functions with buried sources and observation points both placed beneath the surface. Even for the case of a homogeneous half space, the Green's Functions have the form of an infinite integral over wave number to represent a superposition of body waves of all incident angles. The two-dimensional anti-plane SH-wave problem is the only exception, its Greens Function can be written in terms of Bessel's Function using a mirror image to form the stress-free boundary (Section B.2). For all the other cases, however, the complete expression for the Green's Functions is worthy of an entire dissertation such as that provided by Apsel (1979) for a layered viscoelastic half space. The expressions for plane strain or three-dimensional Green's Functions provided in Appendices C and F are those with sources and observations on the half space surface only. With the proposed method in the next two sections, the use of the more complicated Green's Functions can be avoided.

2.2 The Concept of Substructure Deletion

The substructure Deletion concept as proposed by Dasgupta (1980) can replace the depth dependence of the buried Green's Functions by representing those characteristics by a finite volume of the same material. As proposed, if a fill-in layer of the same material is placed

on top of the irregular surface, the combination becomes a basic half space as shown in Fig. 2.3a. With a basic half space, the traction Green's Function matrix $[T]$ at the surface of the half space in Eq. (2.1) is zero because the half plane surface is stress free. Therefore, only the displacement Green's Function matrix $[U]$ needs to be calculated. And since there is no depth dependence for the Green's Functions, the problem is simpler by an order of magnitude in effort. The Green's Functions on the surface of a half space are given in Sections B.3, C.2 and F.2 for the two-dimensional anti-plane, two-dimensional plane strain and three-dimensional problems, respectively.

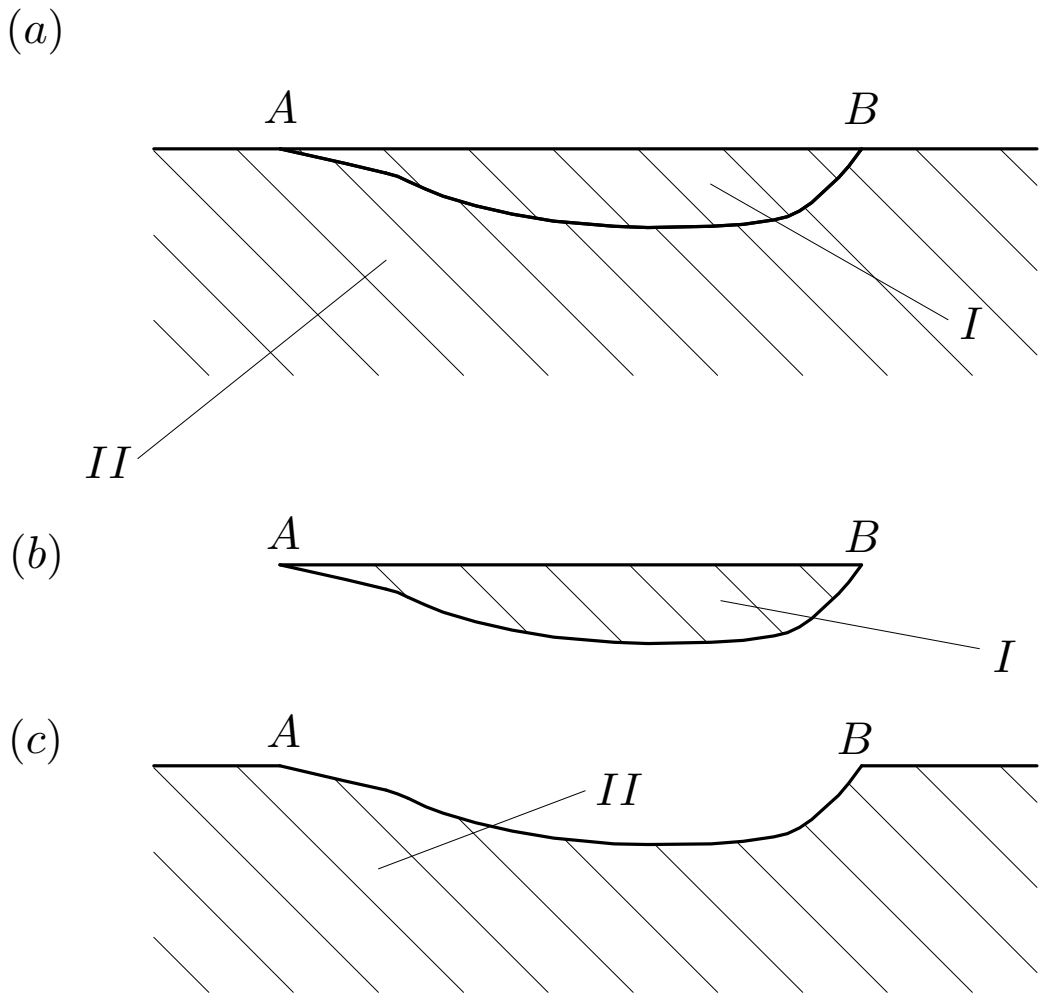

Figure 2.3. Two Media With The Same Material

To clarify the procedures of this concept, it is proposed to first develop the traction-displacement relationship of a flat half space surface between points A and B as shown in Fig. 2.3a. That can be done by setting $[T]$ to zero in Eq. (2.1). The next step is to recognize the combination of medium I and medium II in Fig. 2.3b is the same as a flat half space surface. The traction-displacement relationship of the fill-in layer can be obtained using full-space Green's Functions while the traction-displacement relationship of the underlying medium with an irregular surface, Fig. 2.3c, is much more complicated to obtain. It is proposed to subtract, using matrix manipulation, the traction-displacement relationship for the fill-in layer from that of the half space, and the difference would yield the traction-displacement relationship of the irregular subsurface beneath the surface. This concept is expected to be applicable to both two-dimensional and three-dimensional problems.

Since its original proposal over 30 years ago, the substructure deletion method has not been developed further to reach its great potential. Dasgupta (1980) applied the method to a deeply embedded two-dimensional foundations using a finite element model to represent the fill-in portion and the boundary integral equation method for the plane half space model. Betti (1991) applied the same method to a three-dimensional embedded foundation using the boundary integral equation method for both media I and II. The present application applies the same concept to analyze surface or subsurface irregularities and their effects on wave amplification. The two applications are different and the substructure deletion concept should be more efficient for the site amplification problem because the lateral dimensions of a typical alluvial valley is much larger than its depth, therefore, the fill-in layer is thin in aspect ratio compared to those of embedded foundations. From a physics point of view, the traction-displacement relationships for the half space and that for the irregular surface should not be appreciably different.

The main challenge of the present application would be that the motion at every point of the model is of interest. In the foundation analysis, the traction at the surface of the rigid foundation is only an intermediate result, they are integrated to yield one complex number per frequency, and that would be the impedance function of the foundation. The inaccuracies of the traction solution would decrease by the surface integration. The shorter wavelengths are to be filtered out by the rigidity of the foundation. For site amplification studies, however, the point-by-point solution is needed because the overall response at the surface of the entire canyon or alluvial valley is of interest. For that reason, obtaining high frequency results could pose a more severe challenge.

The remaining chapters of this dissertation would address the feasibility of this method to be applied to practical site amplification problems.

2.3 Theoretical Development of the Proposed Method

From Eq. (2.1), the boundary integral equation on the stress-free surface of a homogeneous half space can be simplified to

$$\vec{u}(\vec{r}_p) = \int_S \left[\, U(\vec{r}_p|\vec{r}) \,\right] \vec{t}(\vec{r})\, dS \qquad , \tag{2.2}$$

because the traction matrix $[T]$ is zero on a stress-free half space surface. In the above equation, the displacement vector at any point on the surface, $\vec{r}_p$, can be calculated as a surface integral of the tractions at the same surface multiplied by the displacement Green's Functions $[U]$. Eq. (2.2) is a vector formulation of a boundary value problem which yields a unique solution to the vector wave equation. After the boundary values are determined, Eq. (2.2) can be used to calculate the wave solution at other locations away from S.

A numerical solution of Eq. (2.2) can be accomplished by first subdividing S into N subregions, $S_i, i = 1, 2, \ldots, N$, then, it can be expressed as

$$\vec{u}(\vec{r}_p) = \sum_{j=1}^{N} \int_{S_j} \left[\, U(\vec{r}_p|\vec{r}) \,\right] \vec{t}(\vec{r})\, dS \qquad , \tag{2.3}$$

with $\vec{r}_p$ placed within the confine of S. The next step is to approximate $\vec{t}(\vec{r})$ as a constant vector, $\vec{t}_j$, within subregion S_i as a zero order approximation. It has been shown in previous formulations of this type (Wong 1975), that higher order approximations often do not improve the accuracy because the traction distribution has unusually high values at the edges. Therefore, a constant value which represents the average traction distribution in the subregions provides a good approximation. With the above assumptions, Eq. (2.3) can be simplified to

$$\vec{u}(\vec{r}_p) = \sum_{j=1}^{N} \left(\int_{S_j} [U(\vec{r}_p|\vec{r})]\, dS \right) \vec{t}_j \qquad . \tag{2.4}$$

Assign the source point of the Green's Function, $\vec{r}_p$, to be equal to $\vec{r}_i$, the centroid of the subregions, S_i, then Eq. (2.4) can be expressed as a 3×3 matrix equation

$$\vec{u}_i = \sum_{j=1}^{N} [U_{ij}]\, \vec{t}_j \qquad , \qquad i = 1, 2, \ldots, N, \tag{2.5}$$

in which $\vec{u}_i$ is the displacement vector at the centroid of S_i and

$$[U_{ij}] = \int_{S_j} [U(\vec{r}_i|\vec{r})]\, dS \qquad , \tag{2.6}$$

is the influence matrices. Replace the summation in Eq. (2.5) by a matrix equation of order $3N \times 3N$ and it can be expressed as

$$\vec{u} = \big[U\big]\vec{t} \qquad . \tag{2.7}$$

The concept for two-dimension problems is the same, except the order of the matrix equation is $2N \times 2N$ for a two-dimension P-SV wave problem and $N \times N$ for a two-dimensional SH-wave problem.

For later application, the above equation will be denoted as

$$\vec{u}_1 = \left[U_{11}^H\right]\vec{t}_1 \qquad , \tag{2.8}$$

in which the subscribe 1 refers to surface 1 (Fig. 2.3a) and the superscript of the influence matrix, H, marks it as the formulation for a half space surface.

Consider now the application of Eq. (2.1) to the fill-in layer model as shown in Fig. 2.3b. The representation theorem, Eq. (2.1), can be changed into a boundary integral equation by limiting the source point $\vec{r}_p$ onto surface S to leave an integral equation of the form

$$\tfrac{1}{2}\vec{u}(\vec{r}_p) = \int_S \left[\, U(\vec{r}_p|\vec{r}) \,\right] \vec{t}(\vec{r})\, dS - \int_S \left[\, T(\vec{r}_p|\vec{r}) \,\right] \vec{u}(\vec{r})\, dS \quad , \quad \vec{r}_p \text{ on } S \quad . \tag{2.9}$$

In the above equation, the displacement vector at any point on the surface, $\vec{r}_p$, can be calculated as a surface integral of the displacements and tractions on the same surface multiplied by the traction and displacement Green's Functions, respectively. The factor, $\frac{1}{2}$, is the result of the principle value integral of the $[T]$ matrix when the source point is located on the surface S.

A numerical solution of Eq. (2.9) can be accomplished by first subdividing S into N subregions, $S_i, i = 1, 2, \ldots, N$. Then, Eq. (2.9) can be expressed as

$$\tfrac{1}{2}\vec{u}(\vec{r}_p) = \sum_{j=1}^{N} \int_{S_j} \left[\, U(\vec{r}_p|\vec{r}) \,\right] \vec{t}(\vec{r})\, dS - \sum_{j=1}^{N} \int_{S_j} \left[\, T(\vec{r}_p|\vec{r}) \,\right] \vec{u}(\vec{r})\, dS \qquad , \tag{2.10}$$

with $\vec{r}_p$ placed on S. The next step is to approximate $\vec{t}(\vec{r})$ as a constant vector, $\vec{t}_j$ and $\vec{u}(\vec{r})$ as a constant vector, $\vec{u}_j$, on S_j, as a zeroth order approximation. With the above assumptions, Eq. (2.10) can be simplified to

$$\sum_{j=1}^{N} \left(\int_{S_j} [U(\vec{r}_p|\vec{r})]\, dS \right) \vec{t}_j = \tfrac{1}{2}\vec{u}(\vec{r}_p) + \sum_{j=1}^{N} \left(\int_{S_j} [T(\vec{r}_p|\vec{r})]\, dS \right) \vec{u}_j \quad . \tag{2.11}$$

Assign the source point of the Green's Function, $\vec{r}_p$, to be equal to $\vec{r}_i$, the centroid of the subregions, S_i, Eq. (2.11) can be expressed as a 3×3 matrix equation

$$\sum_{j=1}^{N} [U_{ij}]\, \vec{t}_j = \tfrac{1}{2}\vec{u}_i + \sum_{j=1}^{N} [T_{ij}]\vec{u}_j \quad , i = 1, 2, \ldots, N, \tag{2.12}$$

in which

$$[U_{ij}] = \int_{S_j} [U(\vec{r}_i|\vec{r})]\, dS \qquad , \tag{2.13}$$

and

$$[T_{ij}] = \int_{S_j} [T(\vec{r}_i|\vec{r})]\, dS \qquad , \tag{2.14}$$

will be referred to as the influence matrices. Replace the summation in Eq. (2.12) by a matrix equation of order $3N \times 3N$ and it can be expressed as

$$\big[U\big]\vec{t} = \left(\tfrac{1}{2}\big[I\big] + \big[T\big]\right) \vec{u} \qquad , \tag{2.15}$$

in which $\vec{u}$ contains the displacement vectors at the centroids of the N subregions.

Since the fill-in layer has both surfaces 1 and 2, Eq. (2.15) needs to be reorganized for application by using partitioned matrices as

$$\begin{bmatrix} [U_{11}] & [U_{12}] \\ [U_{21}] & [U_{22}] \end{bmatrix} \begin{Bmatrix} \vec{t}_1 \\ \vec{t}_2 \end{Bmatrix} = \begin{bmatrix} \frac{1}{2}[I] + [T_{11}] & [T_{12}] \\ [T_{21}] & \frac{1}{2}[I] + [T_{22}] \end{bmatrix} \begin{Bmatrix} \vec{u}_1 \\ \vec{u}_2 \end{Bmatrix} \qquad , \tag{2.16}$$

in which the subscribes, 1 and 2, represent the surfaces, 1 and 2, respectively. To simplify algebraic derivation, there is no superscribe assigned to this model.

The last remaining model is the boundary integral equation formulation of the embedded surface as shown in Fig. 2.3c. To be consistent with the half space model notation used in Eq. (2.8), the matrix representation for the embedded surface model can be written as

$$\left[U_{22}^{E}\right]\vec{t}_{2}^{E} = \left(\tfrac{1}{2}[I] + \left[T_{22}^{E}\right]\right)\vec{u}_{2}^{E} \qquad , \tag{2.17}$$

in which the subscribes 2 represents surface 2 as shown in Fig. 2.3c and the superscribe E denotes the embedded subsurface. Unlike the formulations in Eq. (2.8) and Eq. (2.15), the numerical integration of Eq. (2.17) will not be performed. Rather, the matrices $\left[U_{22}^{E}\right]$ and $\frac{1}{2}[I] + \left[T_{22}^{E}\right]$ will be obtained through matrix manipulation of the components of the half space model and the fill-in layer model. The radiation of waves will be provided by $\left[U_{11}^{H}\right]$ and the irregular surface depth dependence will be accounted for by the submatrices in Eq. (2.16).

The first step is to invert the $\left(\frac{1}{2}[I] + [T]\right)$ matrix of the fill-in layer in Eq. (2.16) to yield a compliance matrix $[G]$ defined as

$$\left\{ \begin{array}{c} \vec{u}_1 \\ \vec{u}_2 \end{array} \right\} = \left[\begin{array}{cc} [G_{11}] & [G_{12}] \\ [G_{21}] & [G_{22}] \end{array} \right] \left\{ \begin{array}{c} \vec{t}_1 \\ \vec{t}_2 \end{array} \right\} \qquad . \tag{2.18}$$

The next step is to rewrite Eq. (2.17) in a similar manner to

$$\vec{u}_{2}^{E} = \left[G_{22}^{E}\right]\vec{t}_{2}^{E} \qquad . \tag{2.19}$$

The operation to obtain Eq. (2.18) requires perhaps the largest effort as the large matrix involves both surfaces 1 and 2. The form in Eq. (2.19) is actually not calculated, it is a symbolic form to be achieved by the substructure deletion concept, i.e., the matrix $\left[G_{22}^{E}\right]$ is

to be obtained using the submatrices of Eq. (2.18) and Eq. (2.8). There is no extra operation to obtain a compliance matrix for surface 1 of the half space model as it is already in that form due to the stress free conditions of the half space surface. To achieve a consistent notation, rewrite Eq. (2.8) in the form

$$\vec{u}_1^H = \left[G_{11}^H\right]\vec{t}_1^H \qquad , \tag{2.20}$$

in which $\left[G_{11}^H\right]$ is the same as $\left[U_{11}^H\right]$ in Eq. (2.8).

To assemble the matrices, apply the boundary conditions shown below:

$$\vec{u}_1 = \vec{u}_1^H \qquad , \tag{2.21a}$$

$$\vec{t}_1 = \vec{t}_1^H \qquad , \tag{2.21b}$$

$$\vec{u}_2 = \vec{u}_2^E \qquad , \tag{2.21c}$$

$$\vec{t}_2 = -\vec{t}_2^E \qquad . \tag{2.21d}$$

The sign of Eq. (2.21d) is opposite because the outer normal of the two formulations are in opposite directions. The fill-in layer is an interior problem while the irregular half space surface is an exterior problem.

The expansion of the first row of the matrix equation in Eq. (2.18) yields

$$\vec{u}_1 = [G_{11}]\vec{t}_1 + [G_{12}]\vec{t}_2 \qquad . \tag{2.22}$$

Applying the boundary conditions Eq. (2.21a) and Eq. (2.21b) to Eq. (2.20) to yield

$$\vec{u}_1 = \vec{u}_1^H = [G_{11}^H]\vec{t}_1^H = [G_{11}^H]\vec{t}_1 \qquad . \tag{2.23}$$

The substitution of Eq. (2.23) into Eq. (2.22) generates

$$[G_{11}^H]\vec{t}_1 = [G_{11}]\vec{t}_1 + [G_{12}]\vec{t}_2 \qquad . \tag{2.24}$$

The above equation is now in a form to relate the tractions of the two surfaces as

$$\vec{t_1} = \left([G_{11}^H] - [G_{11}]\right)^{-1} [G_{12}]\vec{t_2} \qquad . \tag{2.25}$$

Expand now the second row of the matrix equation in Eq. (2.18) in the form

$$\vec{u}_2 = [G_{21}]\vec{t_1} + [G_{22}]\vec{t_2} \qquad , \tag{2.26}$$

and the substitution of Eq. (2.25) into Eq. (2.26) generates the equation

$$\vec{u}_2 = \left([G_{22}] + [G_{21}]\left([G_{11}^H] - [G_{11}]\right)^{-1}[G_{12}]\right)\vec{t}_2 \qquad . \tag{2.27}$$

Apply now boundary conditions in Eq. (2.21c) and Eq. (2.21d), the above equation can be written as

$$\vec{u}\,_2^E = -\left([G_{22}] + [G_{21}]\left([G_{11}^H] - [G_{11}]\right)^{-1}[G_{12}]\right)\vec{t}\,_2^E \qquad . \tag{2.28}$$

With the comparison between the above equation and Eq. (2.19), it is clear that

$$[G_{22}^E] = -\left([G_{22}] + [G_{21}]\left([G_{11}^H] - [G_{11}]\right)^{-1}[G_{12}]\right) \qquad . \tag{2.29}$$

Therefore, the compliance matrix of the irregular surface 2 is obtained using the half space compliance matrix $[G_{11}^H]$ and the four submatrices of the fill-in layer's compliance matrix without the Green's Functions of a buried load with subsurface displacements and tractions. Dasgupta (1970) has the same equation in his application, the major difference is that his compliance matrix for the fill-in layer was formed using the finite element method whereas the corresponding matrix for this application will be obtained using full-space Green's Functions. It is anticipated that the present formulation would have less issues with compatibility. Another advantage of using the boundary integral equation method over the finite element method is the reduction of one spatial dimension. For two-dimensional problems, finite element uses an area formulation whereas boundary integral equation uses

line segments. Similarly in three-dimensional problems, the reduction is from a volume formulation to a surface formulation. One more factor is that the degrees of freedom inside the bounding surfaces are of no practical value in site amplification studies, only the response at the free surface is of interest.

The present application is formulated to obtain results for wave amplification effects of alluvial layers; Dasgupta introduced his method with the intention of obtaining impedance functions for embedded foundations. For soil-structure interaction problems, some foundations are deeply embedded and there is a limitation of how deep this formulation can be extended. For most alluvial valleys of interest, the depths are much smaller than the layers' lateral dimensions. For example, in geophysics, a typical sedimentary valley has a depth of the order of 2 to 3 km, but the lateral dimension is of the order of 20 km, or more. Therefore, the aspect ratio of the layer is not deeply embedded and the substructure deletion concept should be effective. The irregularity of the layer could aid the understanding of the local effects of wave focusing as the incident, refracted and reflected waves interfere constructively or destructively.

2.4 Accuracy of the Modified Substructure Deletion Method

The simplest cases to test the effectiveness of the Substructure Deletion Method are those of two-dimensional SH wave problems. Consider first the case of an elliptical cylindrical foundation embedded in an elastic half space as shown in Fig. 2.4. A more special case of a circular foundation has a simple exact solution (Luco 1968) and in this particular case, the ratio h/a is 1. The exact solution for the traction is

$$\vec{t_0} = \mu k \Delta H_1^{(2)}(ka)/H_0^{(2)}(ka) \qquad , \tag{2.30}$$

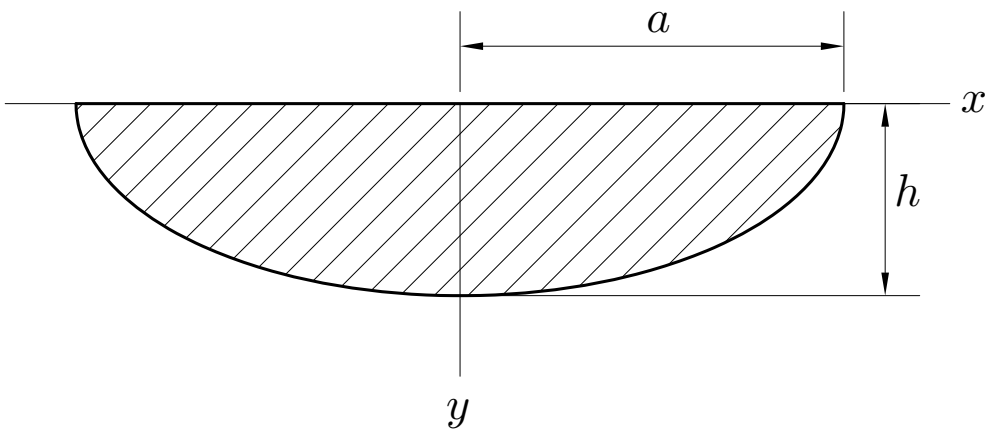

Figure 2.4. An Embedded Elliptical Foundation in an Elastic Half Space

in which μ is the shear modulus of the soil medium, $k = \omega/\beta$ is the wave number, Δ is the displacement of the embedded foundation, a is the radius of the circular cylinder, $H_0^{(2)}$ and $H_1^{(2)}$ are the Hankel Functions of the Second Kind of zeroth order and first order, respectively. The traction is constant throughout the symmetrical cylindrical surface.

To obtain the approximate solution using the substructure deletion method, calculate the traction $\vec{t}$ by inverting Eq. (2.19) as

$$\vec{t} = [G_{22}^E]^{-1}\Delta \qquad , \tag{2.31}$$

in which $[G_{22}^E]^{-1}$ is to be calculated by the formula in Eq. (2.29). The results for $a_0 = \omega a/\beta = 1$ is shown in Fig. 2.5. In the top figure, the number of segments used to approximate the cylindrical surface, N, is 20. The results are oscillatory and are not accurate. The real part of the traction represents the stiffness of the foundation and the imaginary part is related to the radiation damping of the foundation. In both cases, the results in the top figure is not

acceptable. On the other hand, the impedance function, being the integral of the oscillatory traction, has an error of 10% or less. Better results can be obtained using a more refined grid of 40 segments and the results are shown in the center figure of Fig. 2.5. Finally, 320 segments are used to obtain the results in the lower figure of Fig. 2.5 and the results are excellent, especially near the center portion of the foundation surface. There are still some small oscillation near the steeper portion of the foundation surface.

It is anticipated that an even more refine model may not completely eliminate the small errors at the edge, it is perhaps the limitation of this method when the aspect ratio of the scatterer's geometry is deeply embedded. A shallower geometry is attempted next as the aspect ratio is decreased to $h/a = 0.5$. Shown in Fig. 2.6 are the results for the elliptical foundation. The exact solution can no longer be obtained using Eq. (2.30), the exact solution for an elliptical foundation requires the use of Matthieu Functions (Wong, 1974). In this particular test, the comparative "exact" solution is calculated using the boundary integral equation method using the embedded Green's Function. The proven results will be labeled as "benchmark" in the figures. For the anti-plane case, the embedded Green's Function is not difficult to obtain (Appendix B, Section B.2).

As shown in the figure, the traction is no longer constant throughout the elliptical surface. The results by the substructure deletion method are remarkably accurate, indicating that for shallower geometries, it is effective. The value of $a_0 = \omega a/\beta$ is 1 for Fig.2.6, therefore, the wavelength is long and it is not numerically challenging.

Shown in Fig. 2.7 are the results for an elliptical foundation with the dimensionless frequency a_0 equals to 4. The wavelength is now shorter than the lateral dimension of the elliptical foundation. In the top figure, it shows that the number of segments equals to 20 is not sufficient to obtain a good solution. But the more refined cases of $N = 40$ and $N = 320$

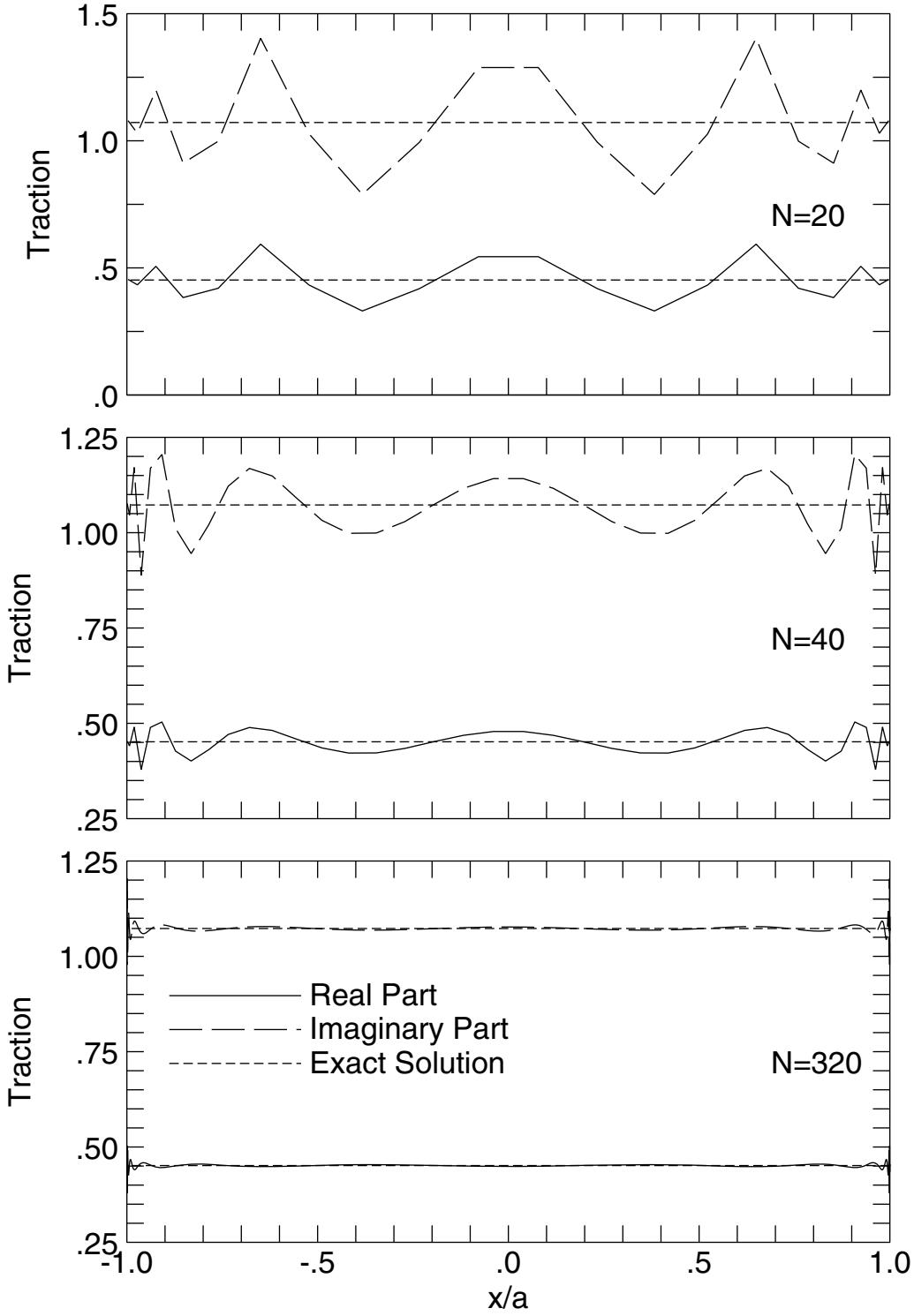

Figure 2.5. Comparison of Results for a Circular Foundation at $a_0 = 1$.

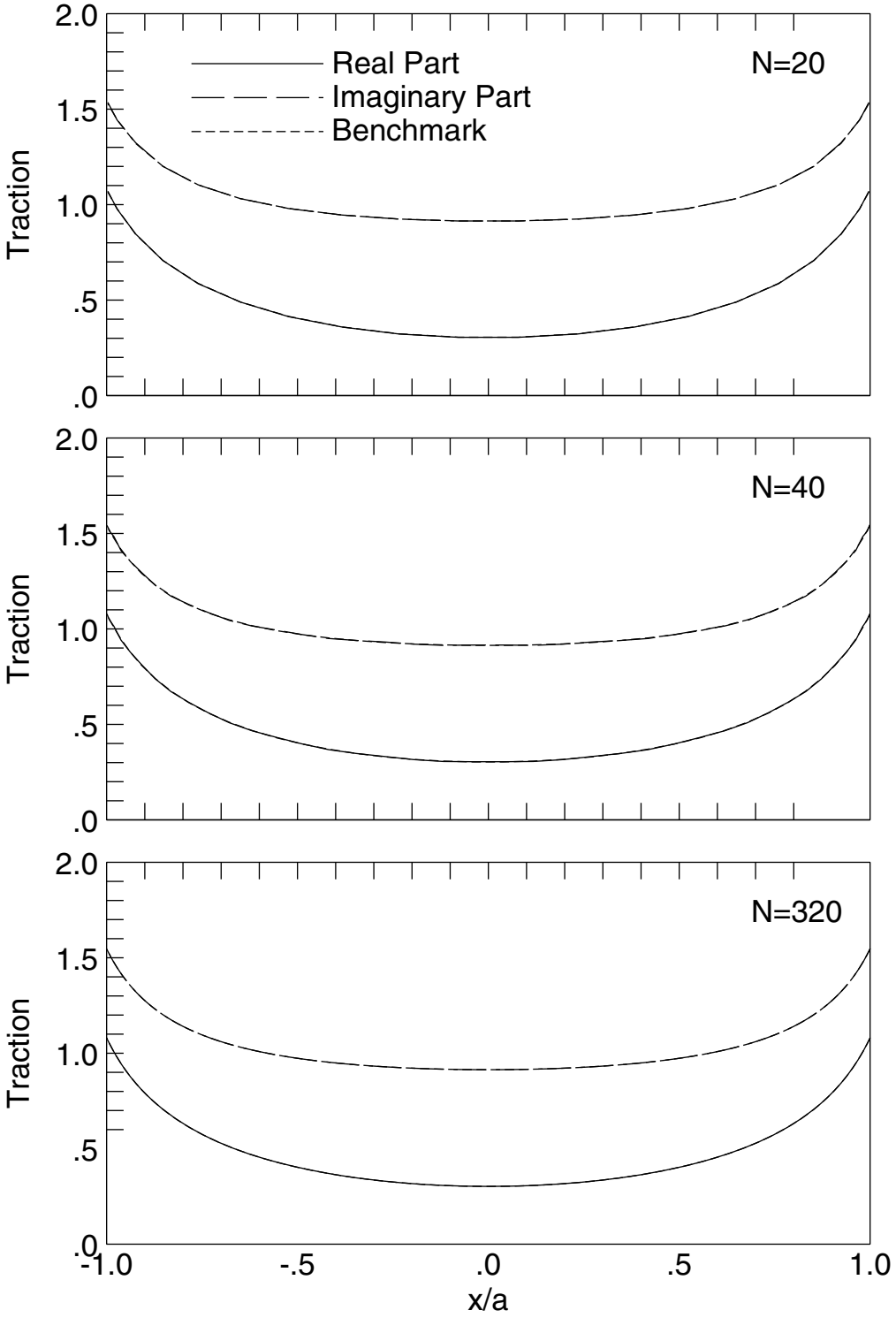

Figure 2.6. Comparison of Results for an Elliptical Foundation at $a_0 = 1$.

offered excellent results. It is clear that the potential of the substructure deletion method is excellent, especially for shallower geometries.

Shown in Fig. 2.8 is the average error resulted from the substructure deletion method. Three different depth ratios were chosen to illustrate the effectiveness of the method for shallow (b/a=0.25), medium (b/a=1) and deep (b/a=2) embedment. The errors were accumulated as the magnitude of the difference between the substructure deletion results and those of the benchmark solutions. The average decreases as N, the number of line segments used, increases. There are four dimensionless frequencies chosen in each figure, from a lower wave number to a high wave number. It is expected that the method would perform better at lower frequencies. Fig. 2.8 shows clearly that the substructure deletion method would perform most efficiently when the aspect ratio of the scatterer is shallow and it performs well for higher frequencies as well. It is perhaps too demanding for substructure deletion to work when the frequency is high and the fill-in medium is required to extend far beneath the surface. The results for $N < 100$ are not shown in the lower figure because the cumulative errors are too large.

2.5 Response of a Canyon to Incident SH-Waves

Another relatively simple case to test the validity of the substructure deletion method is the response of an elliptical canyon to incident SH-waves. Show in Fig. 2.9 is the schematic of the canyon with aspect ratio h/a and an incident wave making an angle of θ with the $x-$axis. Since the surface of the canyon is traction free, the boundary conditions can be stated as

$$\vec{t}_S = -\vec{t}_{ff} \qquad , \tag{2.32}$$

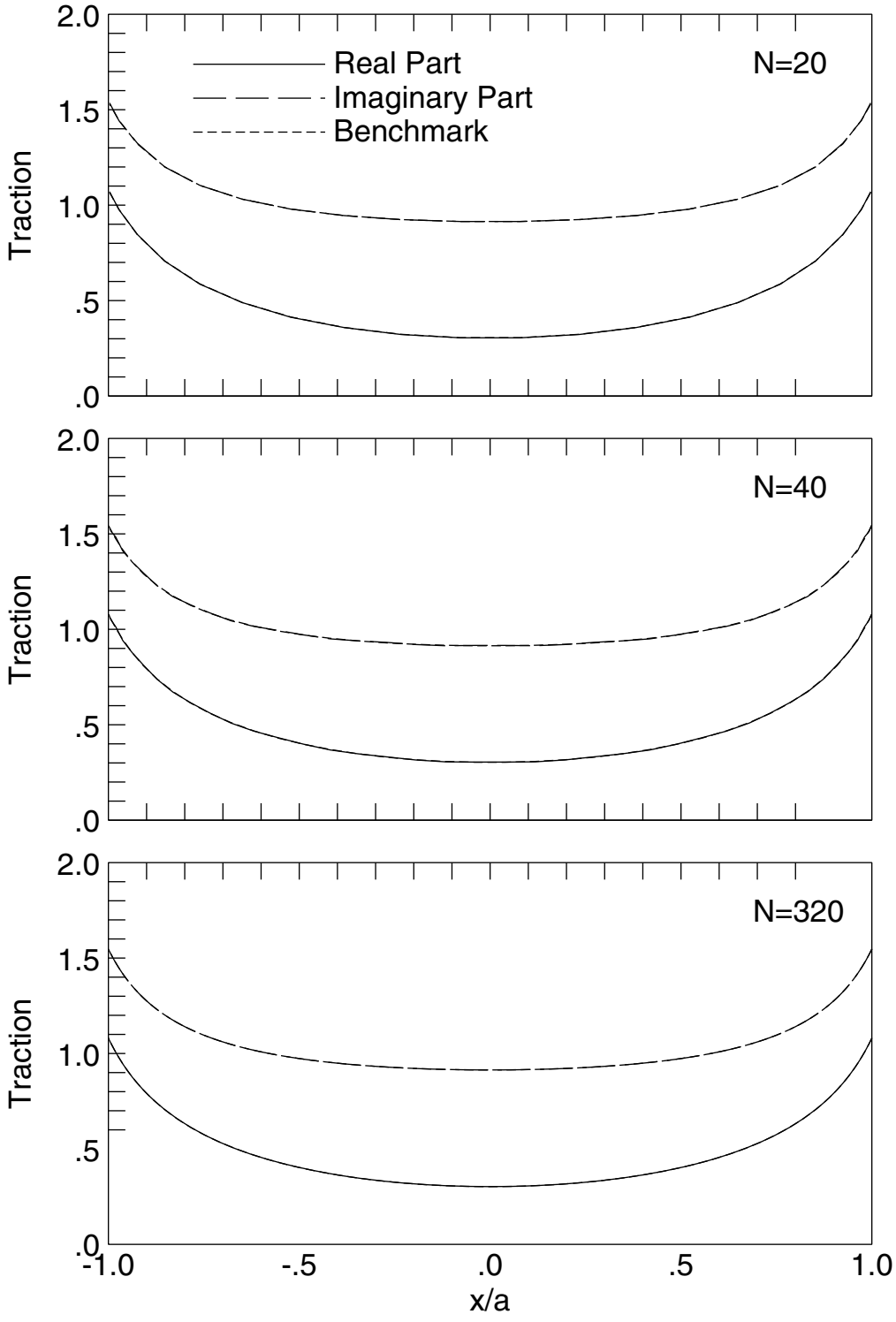

Figure 2.7. Comparison of Results for an Elliptical Foundation at $a_0 = 4$.

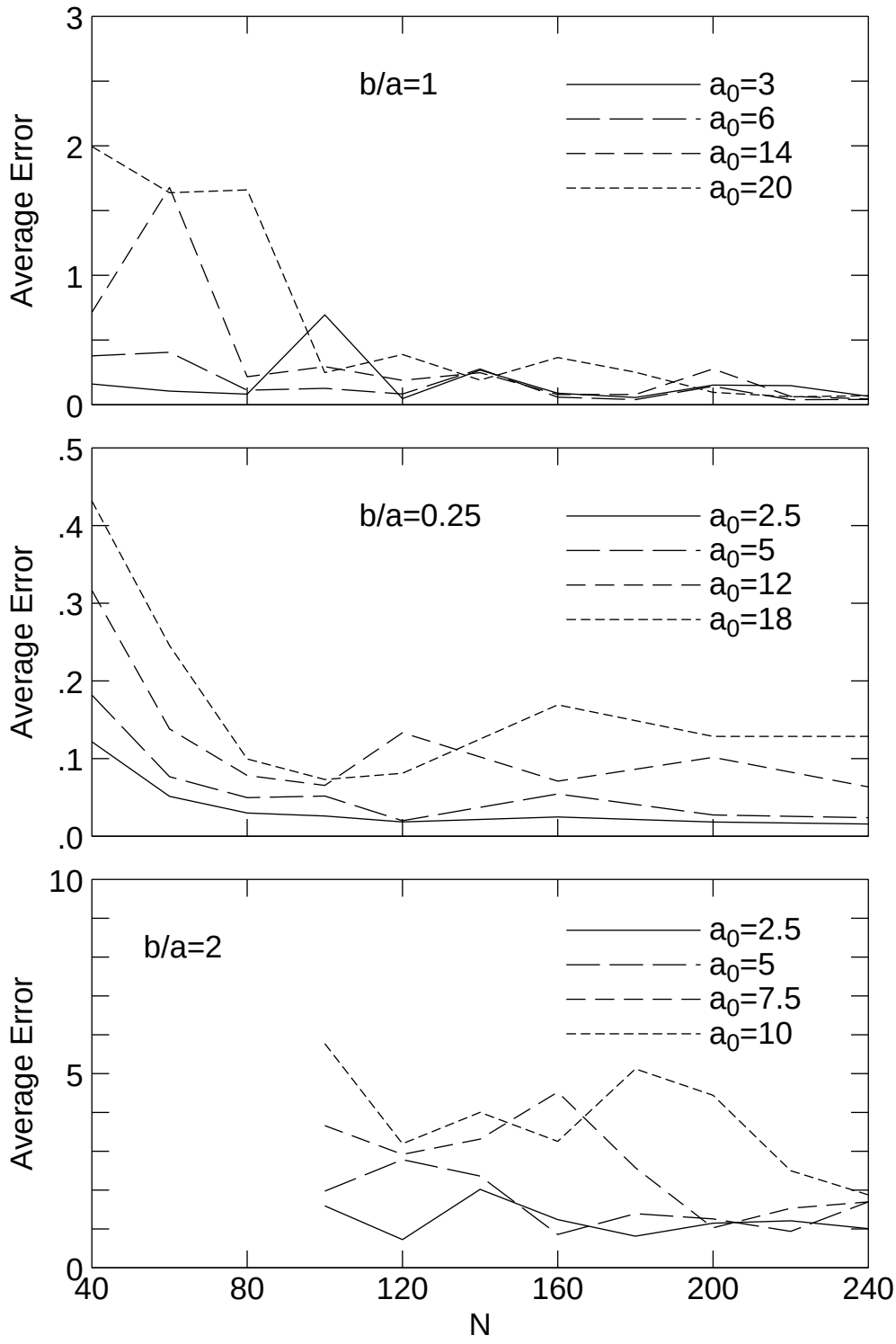

Figure 2.8. Average Error Comparisons as a function of Scattterer Depth.

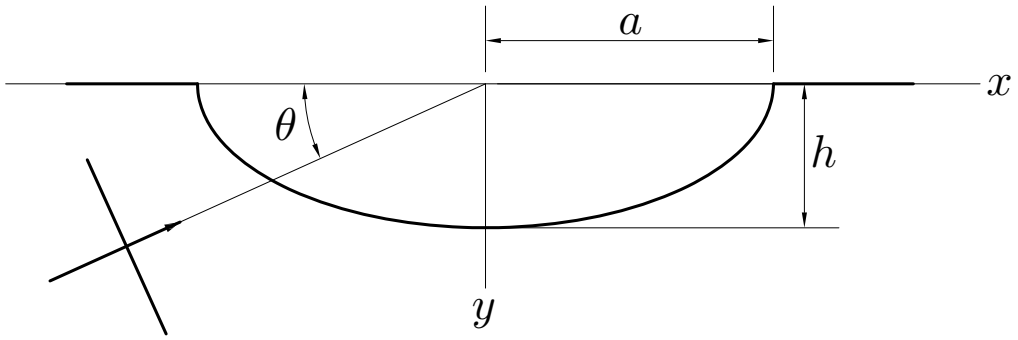

Figure 2.9. An Elliptical Canyon Subjected to Incident SH-Waves

in which $\vec{t}_S$ is the scattered wave from the canyon and $\vec{t}_{ff}$ is the traction of the free-field motion. The traction free half space surface is already dealt with by the definition of the Green's Functions.

The total displacement field, $\vec{u}_t$ in the half space medium can be expressed as the superposition of the scattered wave and the free-field motion as

$$\vec{u}_t = \vec{u}_S + \vec{u}_{ff} \qquad . \tag{2.33}$$

Applying the relationship given in Eq. (2.19), the scattered wave displacement can be written as

$$\vec{u_s} = \left[G_{22}^E\right]\vec{t}_s = -\left[G_{22}^E\right]\vec{t}_{ff} \qquad , \tag{2.34}$$

and the total displacement field can be determined as

$$\vec{u}_t = \vec{u}_{ff} - [G_{22}^E]\vec{t}_{ff} \qquad . \tag{2.35}$$

The free-field displacement, $\vec{u}_{ff}$, in Eq. (2.35) can be obtained using Eq. (D.75) in Appendix D. The free-field traction, $\vec{t}_{ff}$, can be computed using the expressions for τ_{xz} and τ_{yz} in Appendix D, Eqs. (D.77) and (D.78), respectively. Use an equation similar to Eq. (B9), i.e.,

$$\vec{t}_{ff} = \tau_{xz} n_x + \tau_{yz} n_y \tag{2.36}$$

to obtain $\vec{t}_{ff}$; n_x and n_y are the x and y components, respectively, of the outer normal $\hat{n}$.

The results for SH-wave incidence were obtained for incidence angles of $\theta = 30^\circ$ and $\theta = 90^\circ$. Both curves are plotted on the figures for various values of N. The case of $\theta = 90^\circ$ has a symmetrical response on both sides of the canyon but the inclined incident case of $\theta = 30^\circ$ the response is higher on the side of the wave approach. It is the shielding property of the canyon which causes the response to be lower on the rear. The results shown in Fig. 2.10 are excellent at $a_0 = 1$, the low frequency case. Higher values of a_0 are used in Fig. 2.11, $a_0 = 2$ for the case of $N = 20$, $a_0 = 3$ for the case of $N = 40$ and $a_0 = 6$ for $N = 320$. All figures show the capability of the proposed method for wave scattering. Perhaps this method is limited for highly embedded foundation in the field of soil-structure interaction. But it appears to be excellent for wave amplification studies. High frequency results, for an equivalent a_0 as high as 100 will be presented in Chapter Three.

2.6 Response of an arbitrary shape Canyon to Incident SH-Waves

This section continues with the demonstration of the effectiveness of the substructure deletion concept by applying the numerical procedure to an arbitrary shaped. Shown in Fig. 2.12 is such a canyon. The geometry can be best described as an arc with a small amplitude sine function superimpose on it. Even though the model geometry is a smooth one, the method should be able to handle all geometries. This one was chosen for the convenience of grid generation.

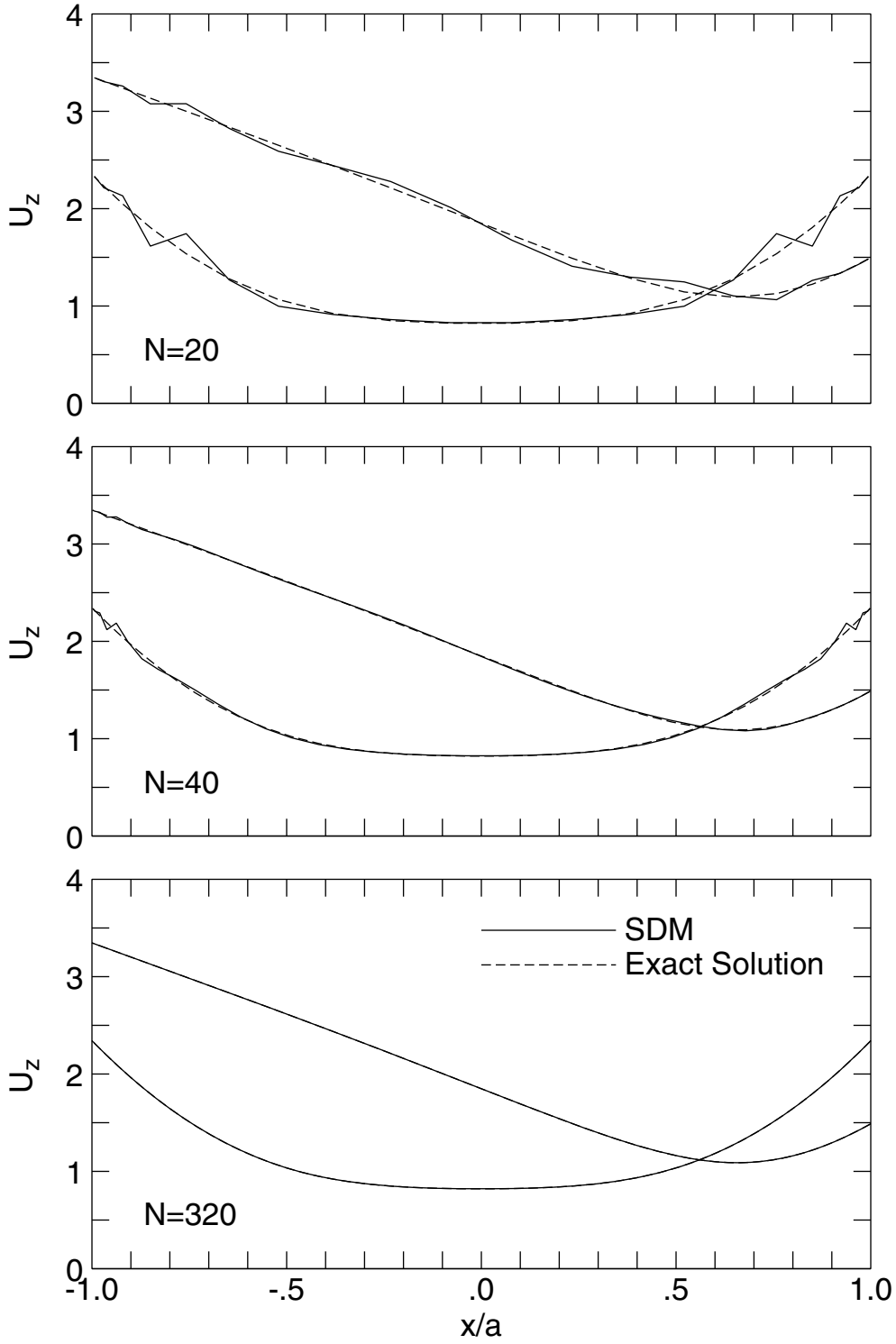

Figure 2.10. A Circular Canyon Subjected to Incident SH-Waves at $a_0 = 1$

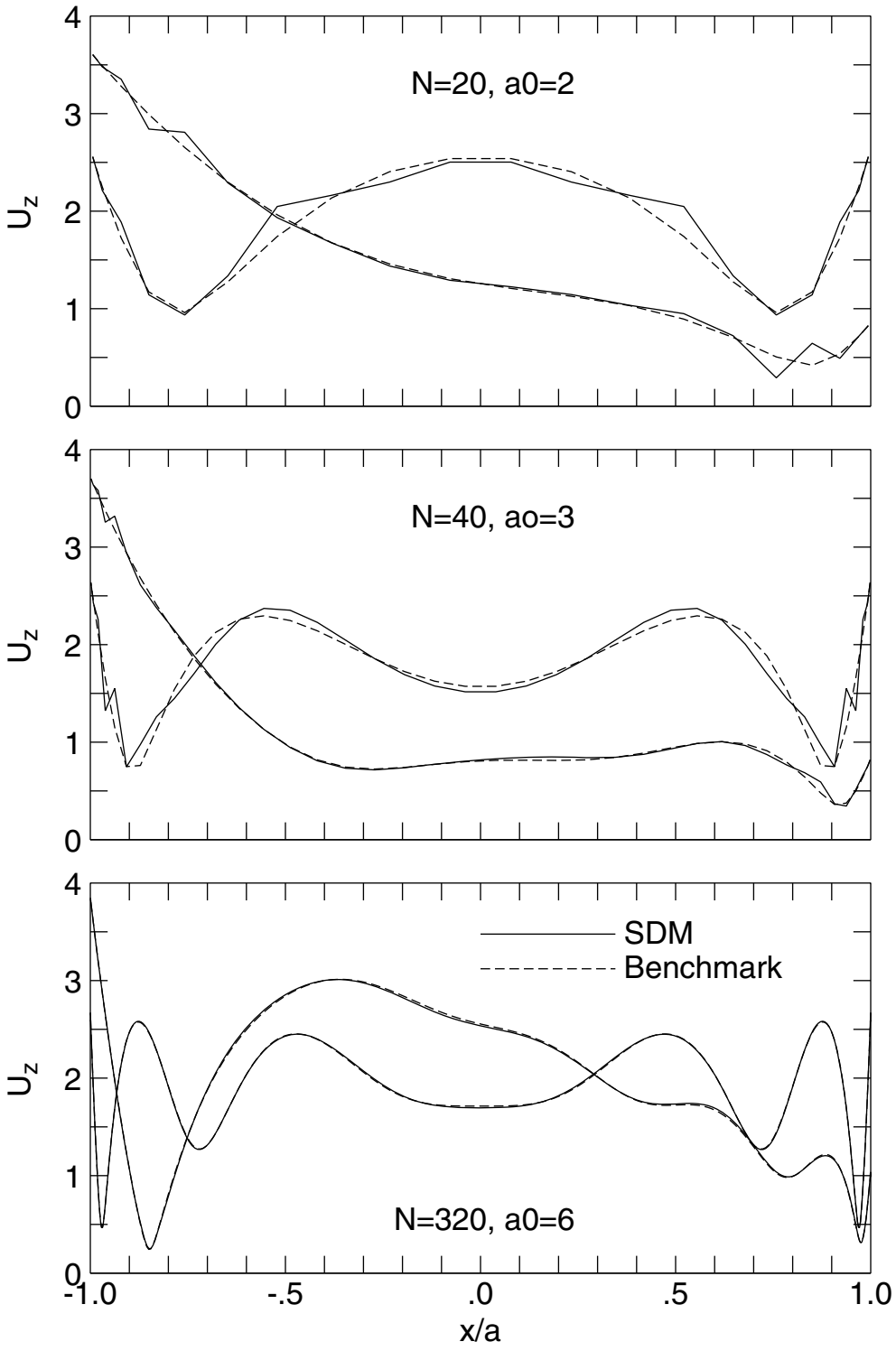

Figure 2.11. A Circular Canyon Subjected to Incident SH-Waves at Higher Values of a_0.

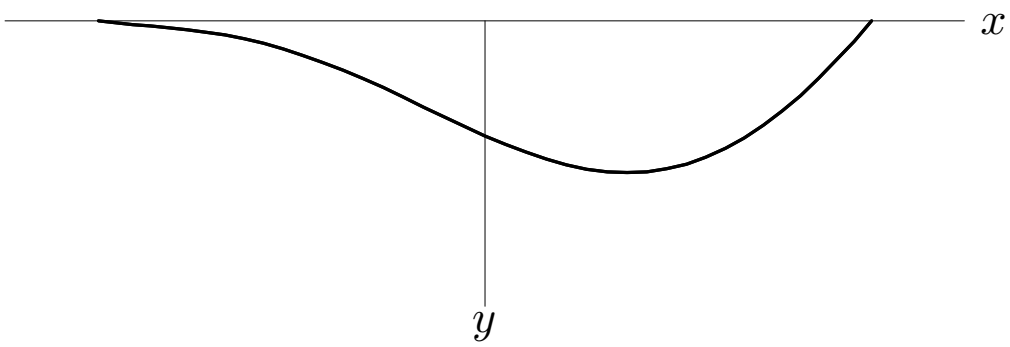

Figure 2.12. An Arbitrary Shaped Canyon

With this new model, there is a way to compare it to a solution obtained by another method, for example, the Boundary Integral Method because it is an antiplane problem. But with an anticipation to later chapters where there is no comparative solution available, the comparisons in this section will be done by comparing results of the same method for different level of model refinement.

Shown in Fig. 2.13, Fig. 2.14 and Fig. 2.15 are results of the present method for dimensionless frequency, η, of 2, 4 and 8, respectively. In each figure, there are results for three angles of incident, 30°, 60° and 90°. Three solutions with the number of line segments, N, equals to 40, 80 and 160 are presented. It is not difficult to calculate results for $N = 320$, but the solution for the case of N equal to 160 has already converged. In Chapter Three, when the transfer functions are calculated for one thousand dimensionless frequencies, $N = 320$ is the model refinement used.

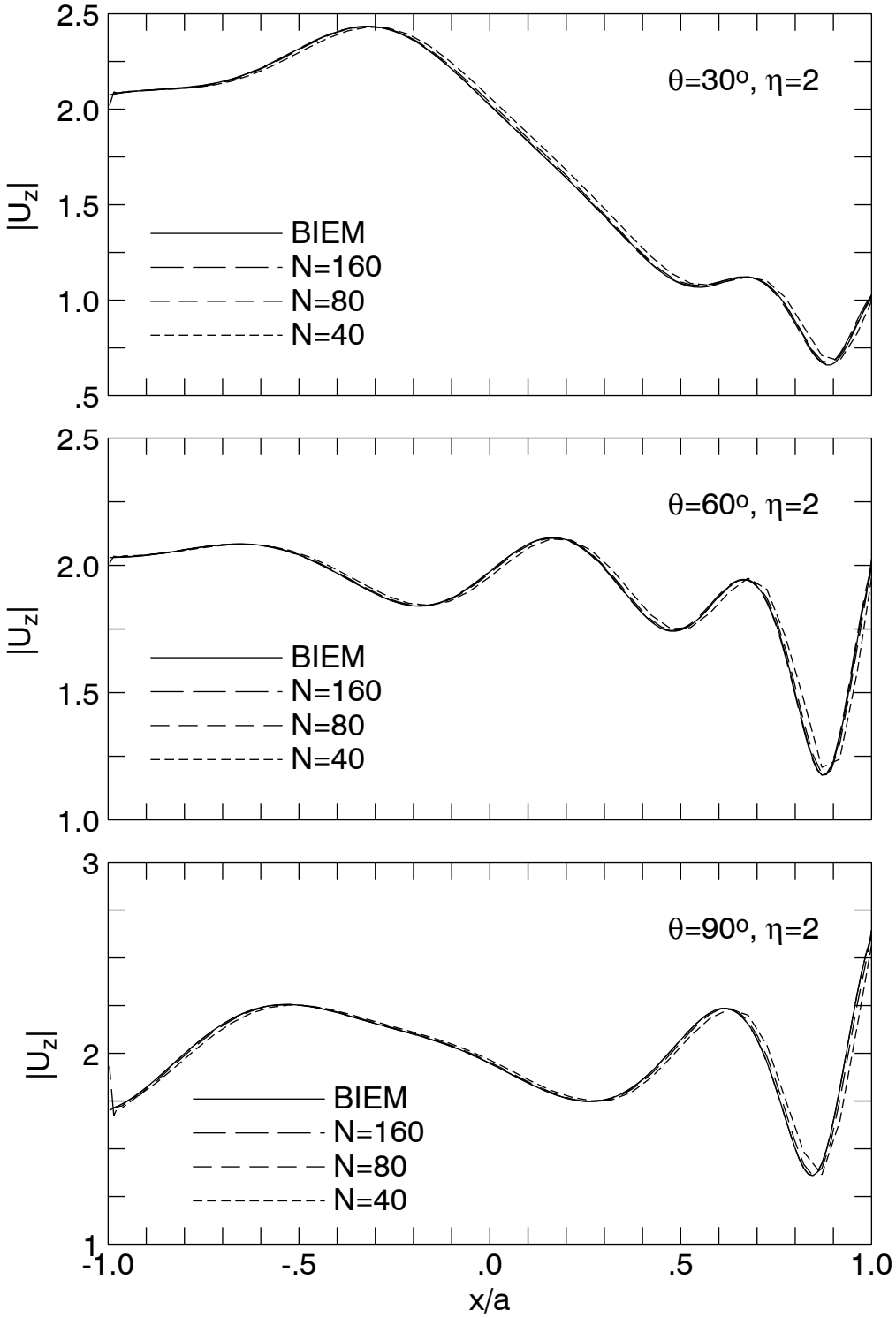

Figure 2.13. Arbitrary Shape Canyon Response at $\eta = 2$

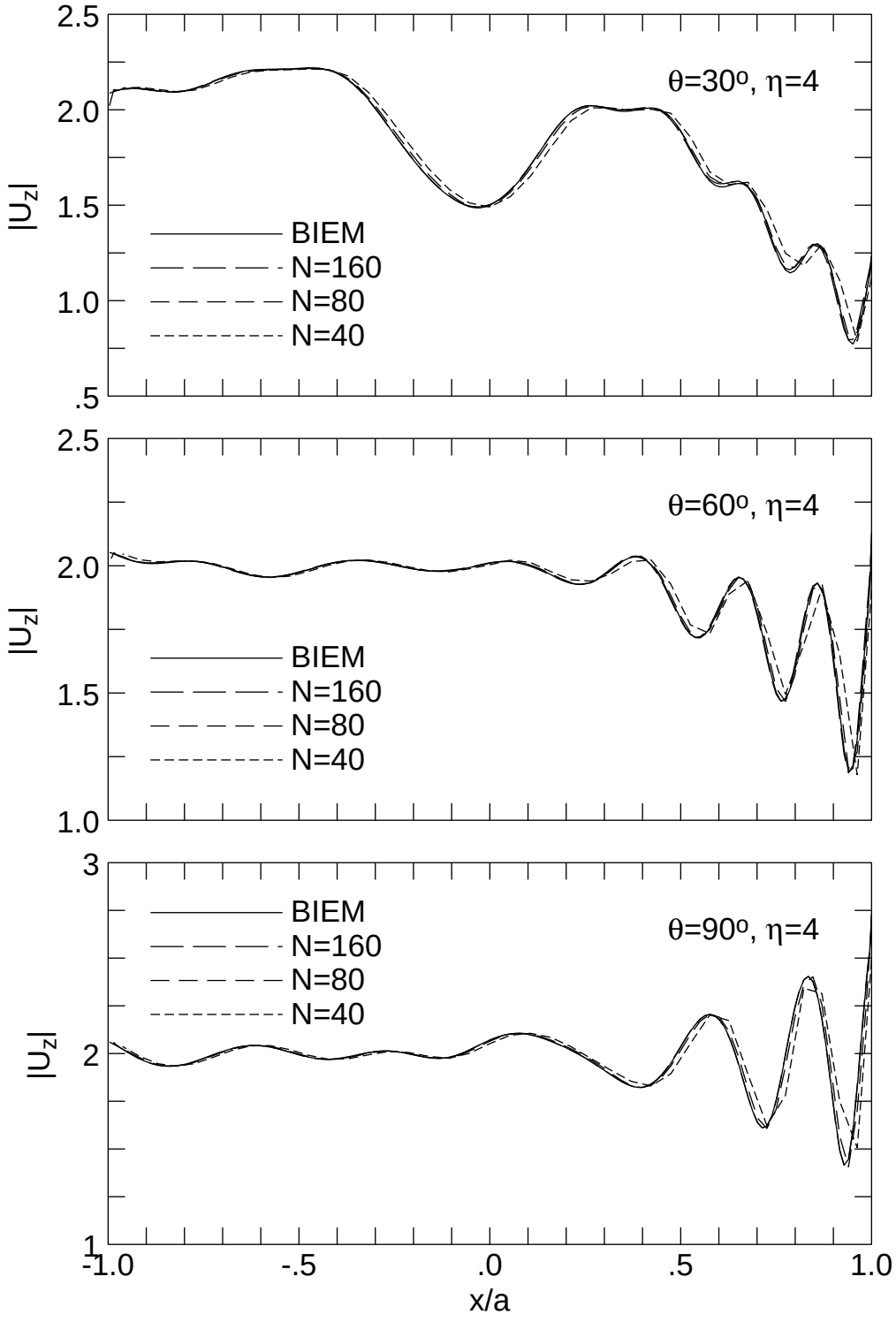

Figure 2.14. Arbitrary Shape Canyon Response at $\eta = 4$

The results presented demonstrate the method is convergent. Even for the case when $N = 40$, the results are excellent at the locations where a solution is available, the limited number of segments used cannot provide a value at locations that the more refined model could offer. Based on the results in this chapter, it can be concluded that the substructure deletion is excellent for site amplification studies.

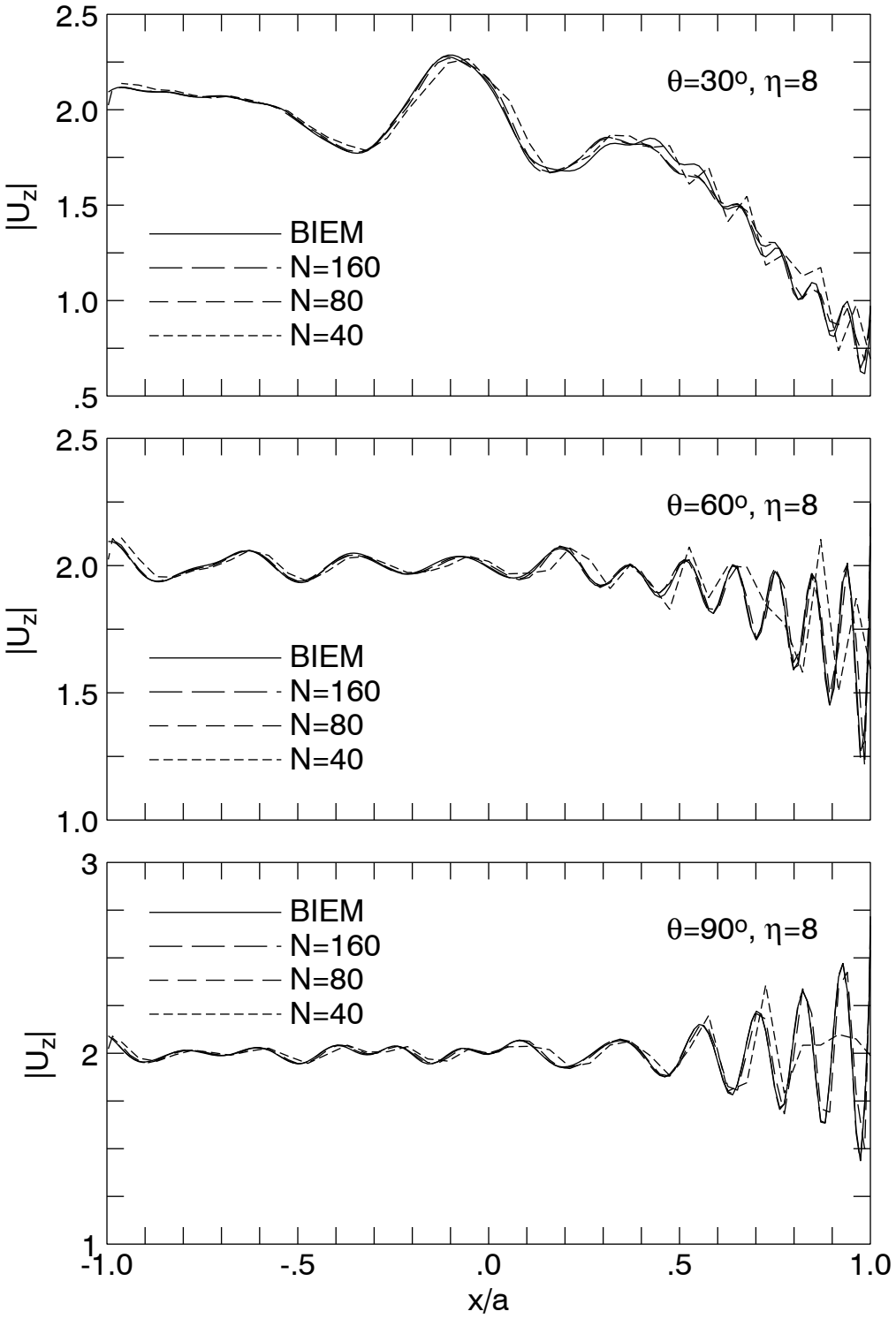

Figure 2.15. Arbitrary Shape Canyon Response at $\eta = 8$

Chapter 3

Site Amplification for Anti-Plane Problems

In Chapter Two, the substructure deletion method was shown to be effective for forming a compliance matrix for an embedded geometry in a half space. The verification were performed using (1) a rigid embedded foundation with a prescribed displacement boundary condition and (2) a surfacial irregularity of a canyon with a prescribed traction-free boundary condition under the influence of incident waves.

In this chapter, the application will add an extra alluvial layer of different material on top of the carved out half space configuration. This problem is more interesting from the site amplification point of view because the softer layer on top of a bedrock can create amplification of an order of magnitude higher than the free field motion (Trifunac, 1971). The top layer has very little resistance for the incident wave to enter from the bedrock, but it would be difficult for the wave energy to leave the soft layer because of the stiffness contrast. This phenomenon explains the trapped energy within a layer and the duration of motion could increase substantially. Some of these effects could be partially explained using a horizontal stack of layers with stiffness contrast and vertically incident waves. But the present proposed method could add to the understanding of focusing effects by an arbitrary shaped soft layer and perhaps more energy being trapped within the layer with no horizontal outlet to the far field. The effect of incident waves of various angles could also be studied using the present method; it has been shown for many years that an alluvial valley at a large distance from the epicenter would receive most of its seismic energy from waves traveling horizontally.

3.1 Boundary Conditions for Alluvial Valley Problem

Consider an alluvial layer to be added to the carved out half space configuration as shown in Fig. 2.2. The half space bedrock and the alluvial layer model have different material properties, the most prominent of which, for boundary condition applications, is the shear modulus, μ. Let μ represents the shear modulus of the bedrock (irregular half space model) and μ_v represents the shear modulus of the alluvial valley. Other material properties involved in the problem includes ρ, the mass density and β, the shear wave velocity. For elastic material, the properties are related as $\mu = \rho\beta^2$ and $\mu_v = \rho_v\beta_v^2$.

The dynamic characteristics of the half space with an irregular embedded surface can be summarized in a matrix equation, Eq (2.19), written as

$$\vec{u}_2^E = \left[G_{22}^E\right]\vec{t}_2^E \qquad . \tag{3.1}$$

The actual calculation of $[G_{22}^E]$ is to be done using Eq. (2.29). For the alluvial layer, the dynamic characteristics can be summarized by a matrix equation such as that in Eq. (2.18), i.e.,

$$\left\{ \begin{array}{c} \vec{u}_1 \\ \vec{u}_2 \end{array} \right\} = \left[\begin{array}{cc} [G_{11}] & [G_{12}] \\ [G_{21}] & [G_{22}] \end{array} \right] \left\{ \begin{array}{c} \vec{t}_1 \\ \vec{t}_2 \end{array} \right\} \qquad . \tag{3.2}$$

In Eq. (2.18), the layer model has the same properties as those of the half space model and it was used as a part of the substructure deletion process. Eq. (3.2) was written the same way with two notable differences: (1) The material properties of the alluvial layer is vastly different from those of the underlying half space and (2) the top surface, labeled with the index "1", does not have to be a flat surface. A different grid generation algorithm is to be used for the surface "1" while surface "2" should have the same configuration as the irregular embedded surface of the half space. For the problems to be studied in this chapter, the motion at the top surface is of the greatest interest because that is the location of civilization.

To apply the boundary conditions, let the subscripts a, r and ff represent the alluvial layer, the rock half space and the free field motion (incident wave motion), respectively. In the half space, the total wave field is the sum of the free field motion and the scattered wave from the interface; in the alluvial layer, the wave motion is that of the scattered waves from the interface. To ensure a compatibility of displacement at the layer interface, apply the condition

$$\vec{u}_{sr} + \vec{u}_{ff} = \vec{u}_{sa} \qquad , \tag{3.3}$$

and the continuous stress condition can be applied using tractions as

$$\vec{t}_{sr} + \vec{t}_{ff} = -\vec{t}_{sa} \qquad . \tag{3.4}$$

The negative sign in Eq. (3.4) is a result of the fact that the outward normal vectors of the rock layer and the alluvial layer are in opposite directions as shown in Fig. 2.2.

Assigning values to displacements and tractions in Eq. (3.2), the matrix equation for the alluvial layer is

$$\begin{bmatrix} [G^a_{11}] & [G^a_{12}] \\ [G^a_{21}] & [G^a_{22}] \end{bmatrix} \begin{Bmatrix} \vec{0} \\ \vec{t}_{sa} \end{Bmatrix} = \begin{Bmatrix} \vec{u}_{top} \\ \vec{u}_{sa} \end{Bmatrix} \qquad . \tag{3.5}$$

In the above equation, the traction at the free surface of the alluvial layer was set to zero, whereas the vector $\vec{t}_{sa}$ is to be determined. Rewrite the upper submatrix equation as

$$\vec{u}_{top} = [G^a_{12}]\vec{t}_{sa} \qquad , \tag{3.5}$$

and that is the vehicle to obtain the motion at the free alluvial layer surface after the vector $\vec{t}_{sa}$ is determined. The lower submatrix equation can be written as

$$\vec{u}_{sa} = [G^a_{22}]\vec{t}_{sa} \qquad . \tag{3.6}$$

The substitution of Eq. (3.6) into Eq. (3.3) yields

$$[G^a_{22}]\vec{t}_{sa} = \vec{u}_{sr} + \vec{u}_{ff} \qquad . \tag{3.7}$$

Using the bedrock equation, Eq. (3.1), and assigning the boundary values yields

$$\vec{u}_{sr} = \left[G_{22}^{E}\right]\vec{t}_{sr} \qquad . \tag{3.8}$$

Replace $\vec{u}_{sr}$ in Eq. (3.7) by Eq. (3.8), the boundary condition displacement compatibility becomes

$$[G_{22}^{a}]\vec{t}_{sa} = \left[G_{22}^{E}\right]\vec{t}_{sr} + \vec{u}_{ff} \qquad . \tag{3.9}$$

Replace $\vec{t}_{sr}$ in Eq. (3.9) by the traction boundary condition in Eq. (3.4), Eq. (3.9) can be written as

$$[G_{22}^{a}]\vec{t}_{sa} = \left[G_{22}^{E}\right]\left(-\vec{t}_{sa} - \vec{t}_{ff}\right) + \vec{u}_{ff} \qquad . \tag{3.10}$$

Reorder Eq. (3.10) in the form,

$$\left([G_{22}^{a}] + [G_{22}^{E}]\right)\vec{t}_{sa} = \vec{u}_{ff} - [G_{22}^{E}]\vec{t}_{ff} \qquad , \tag{3.11}$$

and the boundary traction can be obtained using a matrix inversion as

$$\vec{t}_{sa} = \left([G_{22}^{a}] + [G_{22}^{E}]\right)^{-1}\left(\vec{u}_{ff} - [G_{22}^{E}]\vec{t}_{ff}\right) \qquad . \tag{3.12}$$

After $\vec{t}_{sa}$ is determined, the response at the top surface of the alluvial layer can be obtained using Eq. (3.5).

3.2 Comparison with Exact Solutions

There are several exact series solutions for two-dimensional SH-wave problems that could be used as a benchmark. Trifunac (1971) presented results for a circular cylindrical alluvial valley overlying a half space. The results were obtained using a separation of variable technique for partial differential equation and the solution was written as an infinite series in Hankel Functions and harmonic functions. Later, Wong and Trifunac (1974) presented results for an elliptical cylindrical alluvial valley overlying a half space; the results

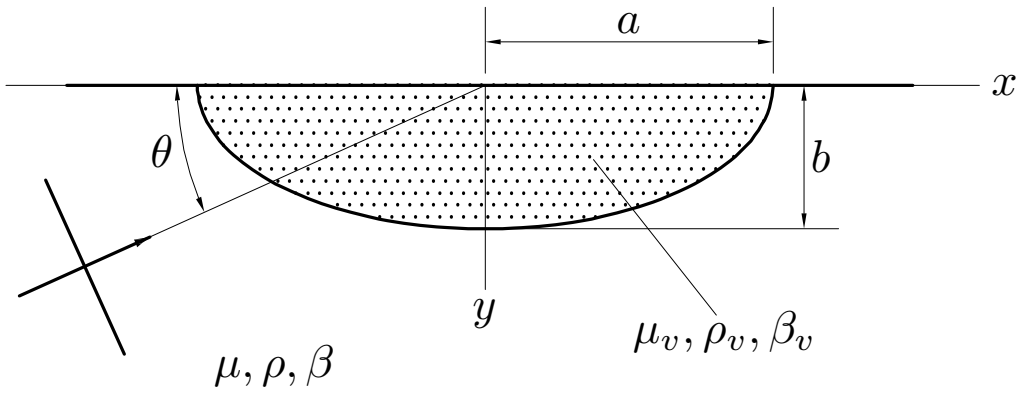

Figure 3.1. Models with Available Solutions

were obtained using a similar method for partial differential equation and the solution was written as an infinite series in Mathieu Functions. These results could be identified as "exact solutions" in the traditional sense. The numerical results of the substructure deletion method will be compared against those results for accuracy.

In both of the exact solution in which the proposed method is to be compared against, the basic model can be illustrated by Fig. 3.1. The material property of the bedrock was represented by μ, the shear modulus, ρ, the mass density, and β, the shear wave velocity of the medium. For the alluvial valley, the respective material properties were represented by μ_v, ρ_v and β_v. In the case of the comparisons, the ratios of $\mu/\mu_v = 6$ and $\rho/\rho_v = 1.5$ were used. Since an elastic material requires only two constants to define, the shear wave velocity β can be calculated as $\beta = \sqrt{\mu/\rho}$ and that gives rise to a ratio of $\beta/\beta_v = 0.5$. One interesting parameter on the results is that the wave number $k = \omega/\beta$ would be different for the bedrock and the valley; the wave number k_v would be twice that of k. Therefore, the wavelength within the alluvial valley would be shorter and more amplitude variation over distance is expected.

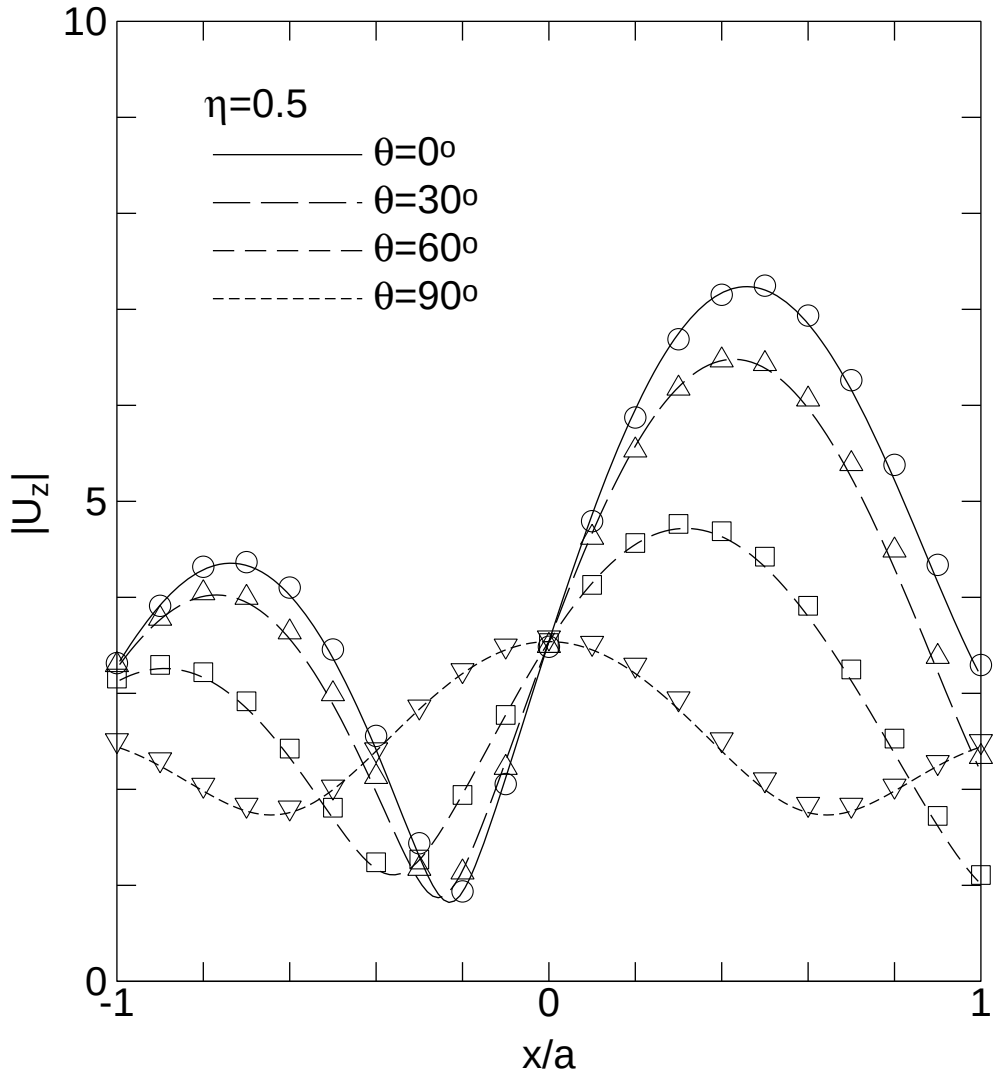

Figure 3.2. Results for Circular Valley for $\eta = 0.5$

The angle of incidence, θ, will be a prominent parameter in the comparison because the effect on ground motion is highly dependent on the direction of the incident wave energy. Since the geometry of the wave scatterer is symmetric, of angles of 0°, 30°, 60° and 90° are selected to be used. For the circular cylindrical valley comparison, the aspect ratio of $b/a = 1$ will be used. The elliptical valley has more flexibility in the geometry and several

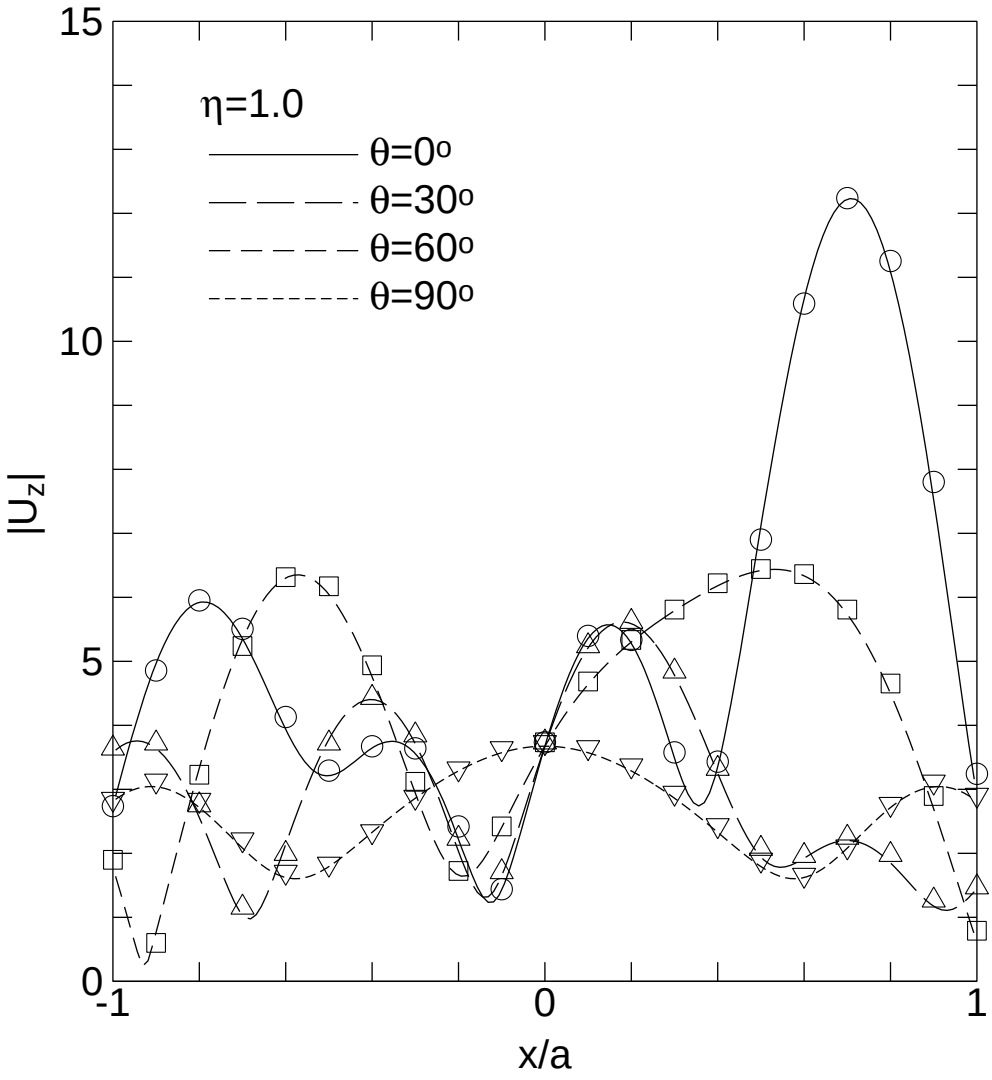

Figure 3.3. Results for Circular Valley for $\eta = 1.0$

values were presented. But the case of a shallower geometry, $b/a = 0.3$, will be used for comparison.

Shown in Fig. 3.2 is the comparison of the substructure deletion results with the exact solution. The curves of the present numerical solution are identified by solid line for a horizontally incident wave ($\theta = 0$) and various length segments of dashed lines for three

other angles. The digitized results from Trifunac (1971) are plotted with symbols, open-circles for $\theta = 0$, triangles for $\theta = 30^\circ$, squares for $\theta = 60^\circ$ and inverted triangles for $\theta = 90^\circ$. The comparison of the four curves and the symbols are remarkable in their consistency since two different methods were used. No legends for the symbols were given in the figures as the results for the different incident angles were easily distinguishable.

In Fig. 3.3 the comparison is for a higher dimensionless frequency, $\eta = 1$. The value of η is that of the bedrock, the value for the valley, η_v is actually two times higher for the present case study, i.e., $\eta_v = 2$. The agreement between these two methods is again excellent, demonstrating that the substructure deletion method is performing properly.

The comparison now turns to another infinite series solution, that of an elliptical valley with an aspect ratio of $b/a = 0.3$. The comparative results are shown in Fig. 3.4. The dimensionless frequency of this case would be slightly higher, $\eta = 1.5$ and $\eta_v = 3$, to see if the performance of the proposed method is valid for a higher frequency. Given the resolution of the published figures available for digitization, the results match well and the comparison further elevates the confidence of the newer method.

3.3 Solutions at High Frequencies

From the previously published results, even the infinite series solutions, it is difficult to produce results at higher frequencies, e.g., $\eta > 3$. Since there are no published results to compare against, a form of self comparison will be performed by using the present method for different values of N, the number of subregions (line segments) used for the solution.

In Fig. 3.5, three different values of N, 80, 160 and 320, were used. The value of N is the number of line segments used for the generation of the half space matrix, $[G_{11}^H]$, the number of line segments for the grid to generate the full-space matrix would be $2N$. The

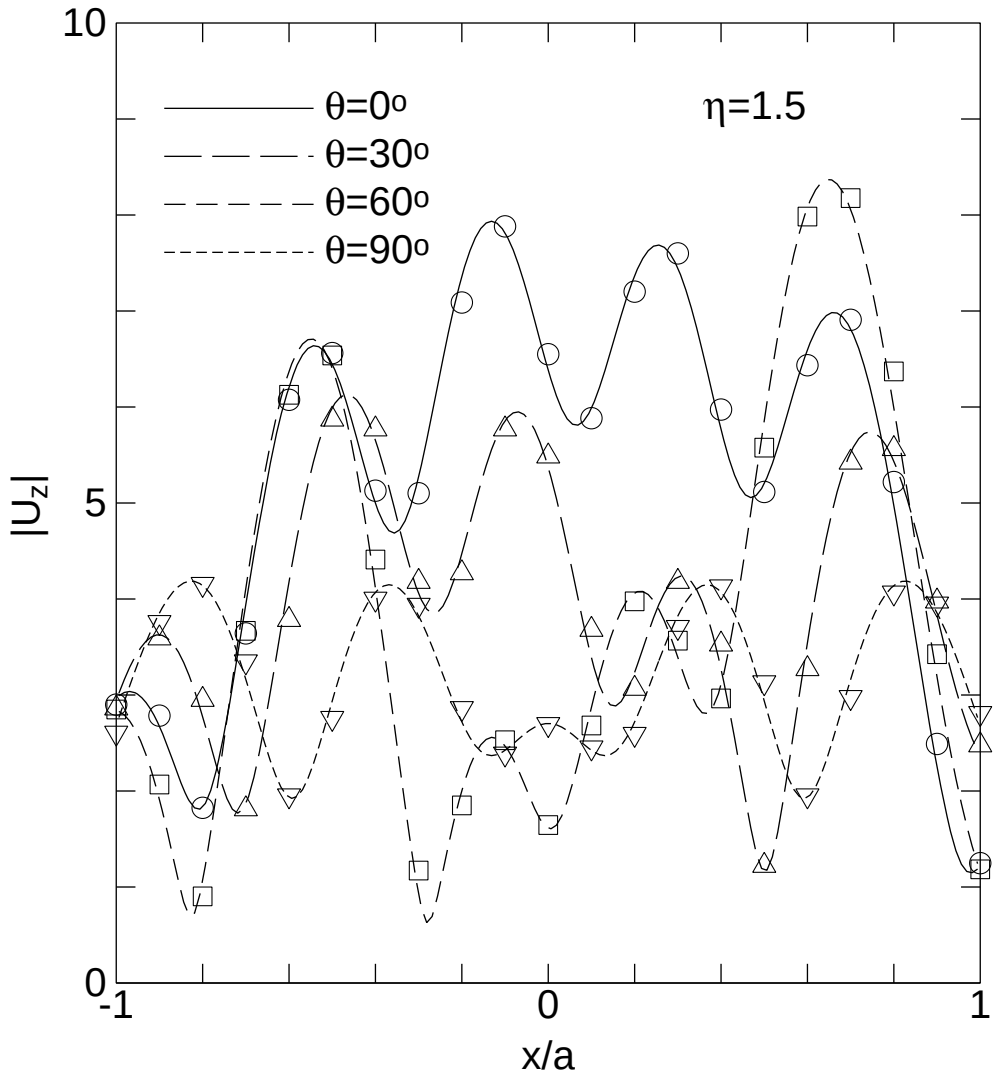

Figure 3.4. Results for Elliptical Valley for $\eta = 1.5$

dimensionless frequencies used for the calculation in Fig. 3.5 is $\eta_v = 8$ and three angles of incidence were considered: $\theta = 30°$, $60°$ and $90°$. As shown in the figure, there is no appreciable difference between the results of the models, showing a convergent trend that is accurate even at high frequencies. There are some spots where the $N = 80$ solution appears

to be deficient, but those are locations where the less refined model did not offer a sample point.

3.4 Response of an Arbitrary Shaped Alluvial Valley

Consider now the response of an arbitrary shaped alluvial valley overlying bedrock. The interface of the two materials, the bedrock and the alluvium, has a shape similar to the arbitrary shaped canyon in Chapter Two, but shallower. The top surface of the alluvium is represented by a small amplitude sine function. Again, any shape could be used with this numerical method, only the grid generation program needs to be changed.

With this layer model, many different parameters can be utilized to gain as much physical understanding of the problem as possible. In later sections, time histories will be used to gain a different perspective. In the present section, use the same contrast ratios for the two materials as described in section 3.2, i.e., $\mu/\mu_v = 6$, $\rho/\rho_v = 1.5$ and $\beta/\beta_v = 0.5$.

Shown in Fig. 3.7 is the variation of ground motion on the surface of the alluvial valley for the lower dimensionless frequencies of η equal to 0.5, 1.0 and 1.5. These are the typical values used for the exact series solution by previous authors. The values of η is that of the bedrock, meaning it is the ratio of the incident wavelength to the width of the alluvial valley. But the wavelength in the valley is two times shorter because of the ratio, $\beta/\beta_v = 0.5$. Therefore, there are significant variation over the surface of the alluvial valley even at these lower dimensionless frequencies. Within each of three sub-figures, results for four angles of incident, $\theta = 0^\circ$, 30°, 60° and 90°, are plotted. The results demonstrate that the direction of wave arrival is a significant factor which contributes to site amplification. In future development of seismic ground excitation levels for building codes, some form of risk analysis is recommended when amplification factors are determined.

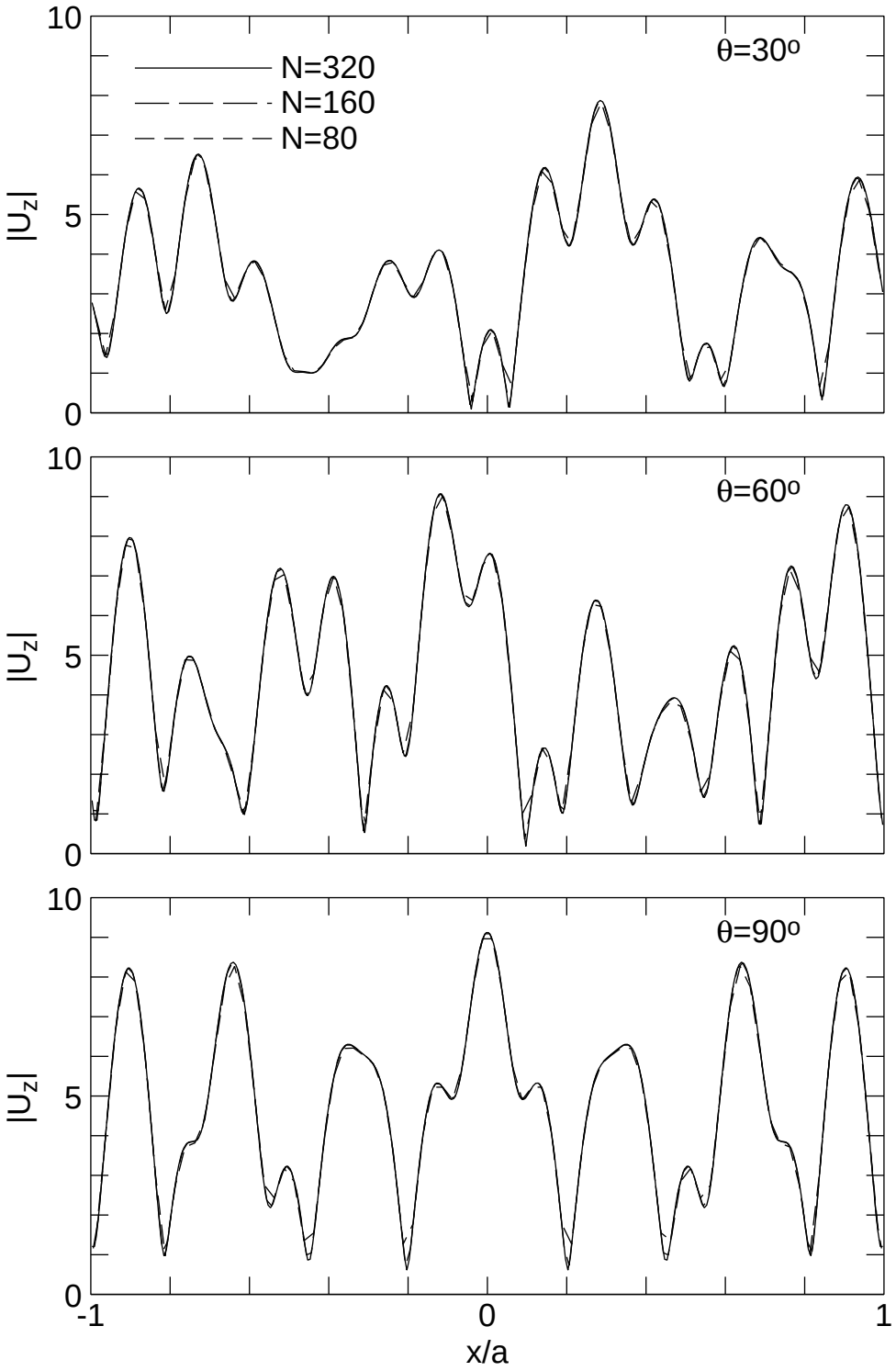

Figure 3.5. High Frequency Calculation at $\eta_v = 8$

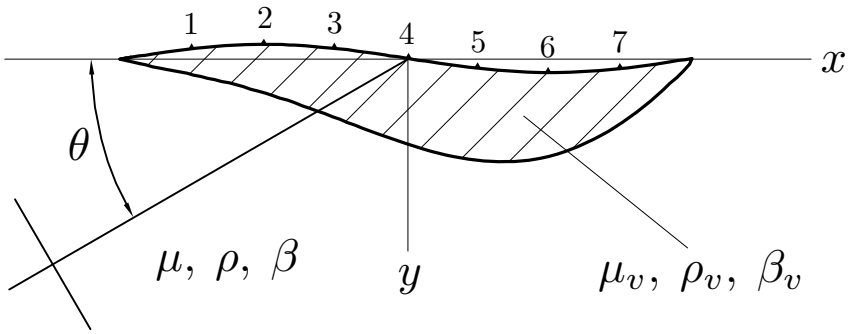

Figure 3.6. An Arbitrary Shape Alluvial Valley

Fig. 3.8 shows the response of the alluvial valley when subjected to the higher dimensionless frequencies of η equal to 2, 3 and 4. The graphs are also plotted for 4 incident angles as those in Fig. 3.7. The variation of surface response paints a very busy picture and it is difficult to physically understand the significance of such a graph. Although many high values, some as high as an order of magnitude larger than the unit amplitude of the incident wave, are observed on the surface of the alluvial valley, there are also quiet spots where the amplitude may be lower than 1. The same location, where there is a quiet zone in one particular frequency, may have a high amplitude in another frequency. It is clear that a constant-frequency amplitude plot is not the best way to assess seismic site amplification effects. Another avenue for assessing the risk of site amplification is to use time histories. In the next section, the response at various locations of the alluvial valley to incident wave impluse time functions will be presented. The time history results will provide another method to analyze the amplification factor of a soft alluvial layer.

One interesting observation to bring out from the results is that the low amplitude spots are actually locations where a large torsional response might exist (Trifunac, 1971). The

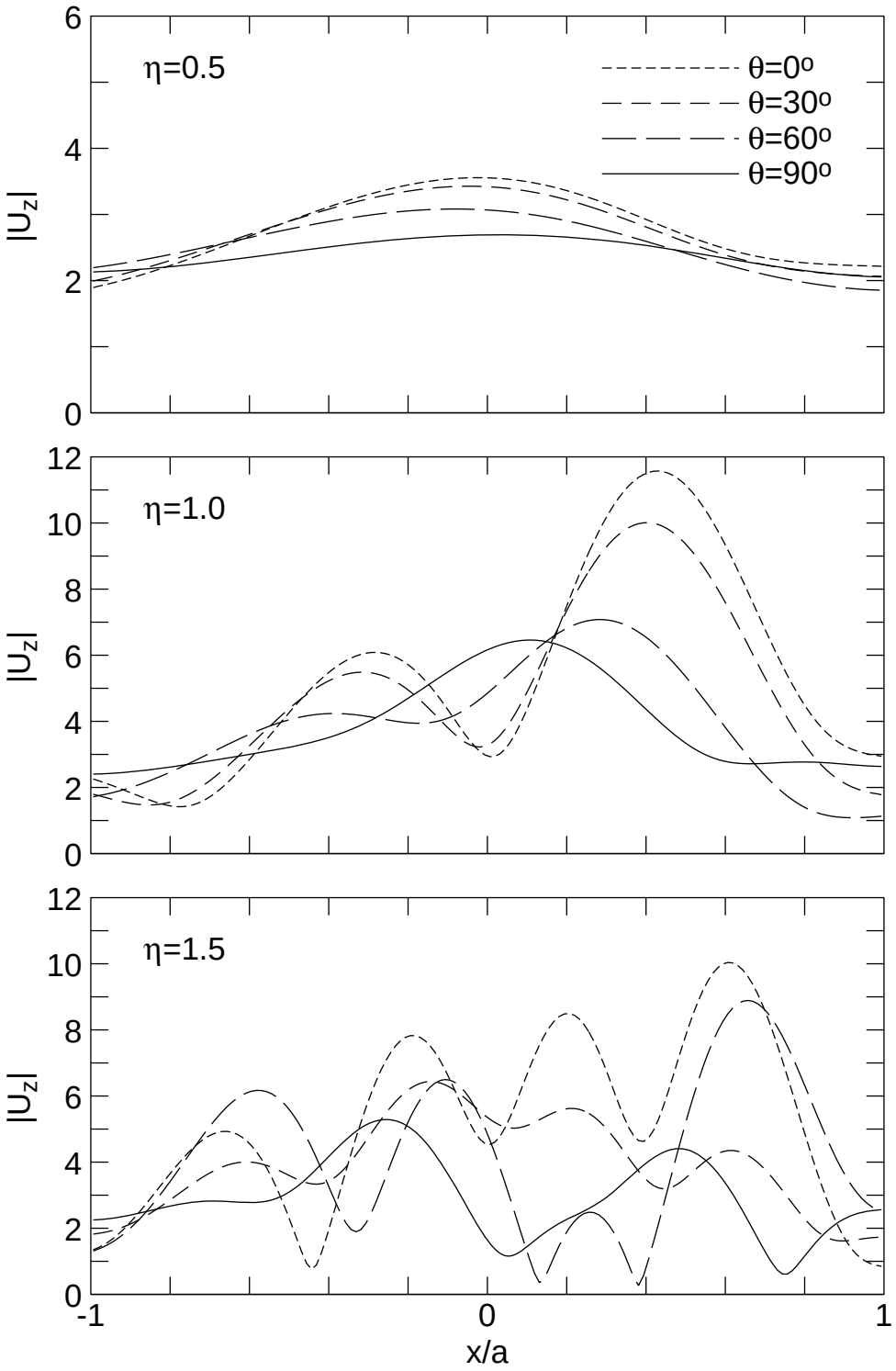

Figure 3.7. Low Frequency Response of Alluvial Valley

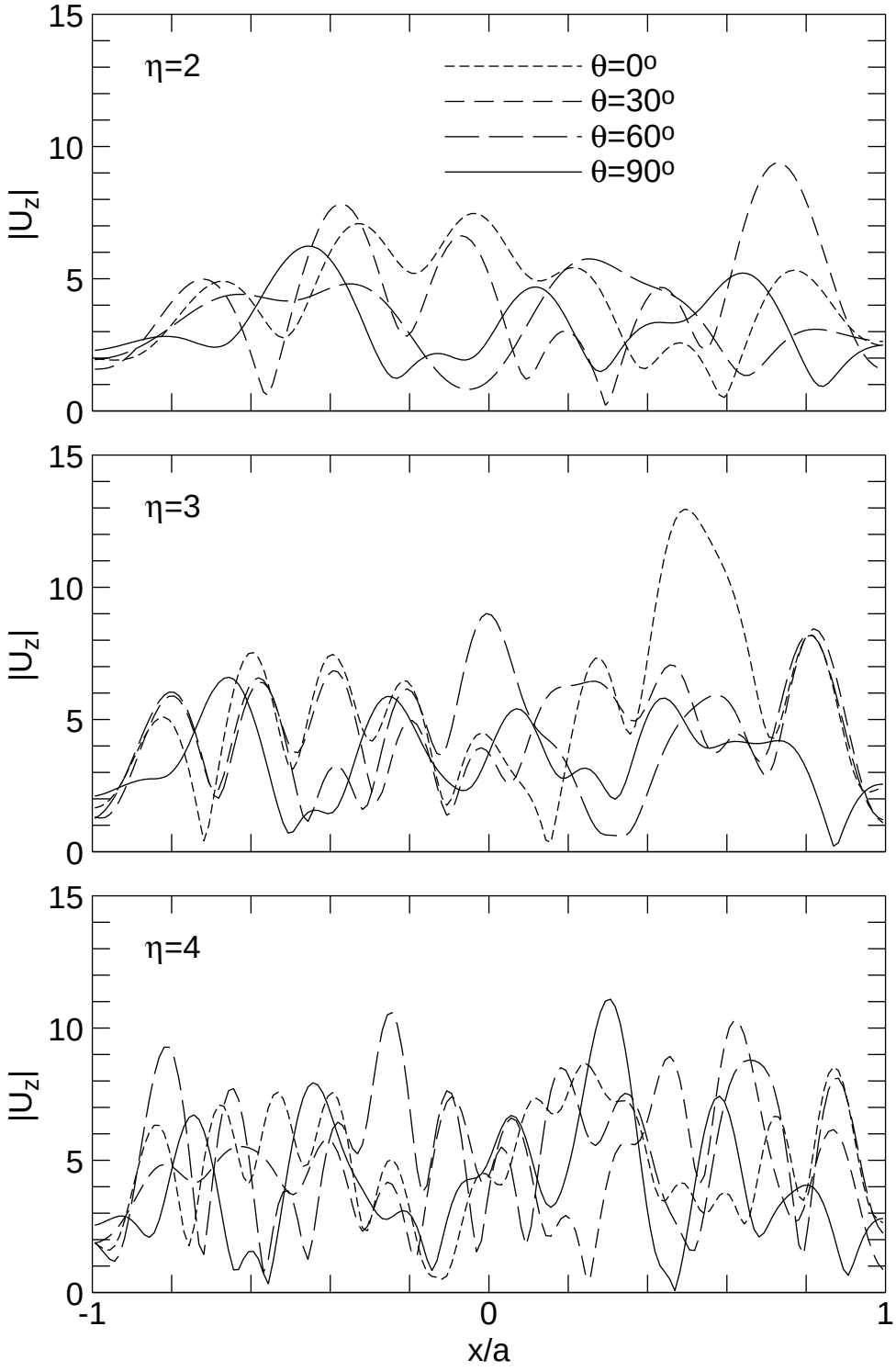

Figure 3.8. High Frequency Response of Alluvial Valley

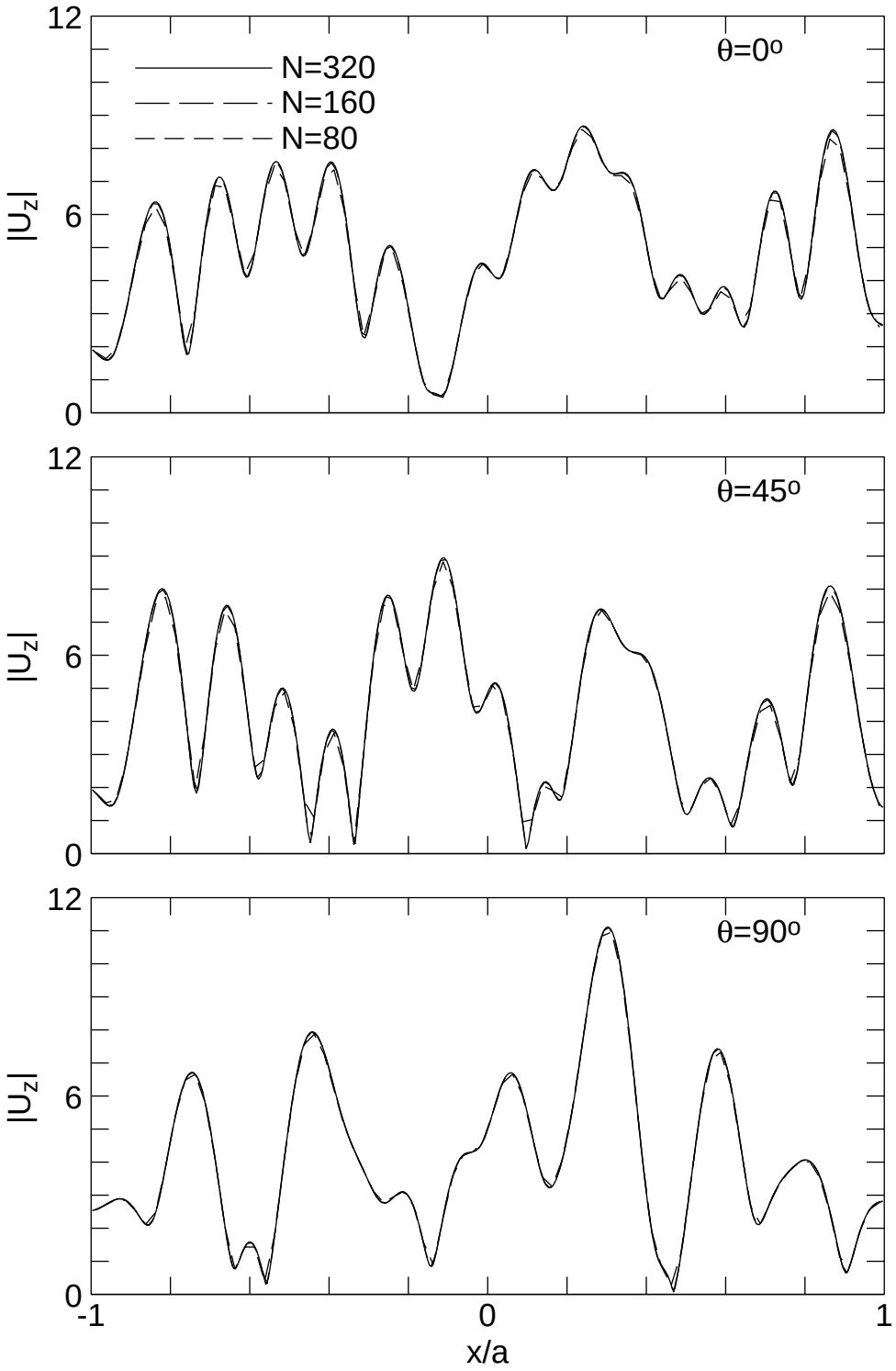

Figure 3.9. Response of Alluvial at $\eta = 4$. Left Side Incident

amplitude plots show only the absolute value of the displacement, therefore, two large amplitudes on either side of a low amplitude generally point to a sign change and the large displacements are actually out of phase by 180°. This situation in a SH-wave problem describes a torsional response.

In the work of the exact series solutions for the circular valley (Trifunac, 1971) and the elliptical valley (Wong and Trifunac, 1974), there are four example angles are used for the analysis. But since the current arbitrary shaped alluvial valley, shown in Fig. 3.6, is not symmetric about the y-axis, the wave arrival from an opposite direction would also cause a different variation of ground motion. Fig. 3.9 and Fig. 3.10 serve two purposes, one is to show the response of the alluvial valley at a high dimensionless frequency of $\eta = 4$ and six different incident angles, 0°, 45°, 90°, 120°, 150° and 180°. The other purpose to show the convergence of the solution by using a less refined model of $N = 80$, and compare its accuracy to models with $N = 160$ and $N = 320$. The comparisons are excellent and they are also excellent for larger values of η, but the graphical representations of those cases are difficult.

With the confidence gained from all forms of testing, the results in Section 3.5 will take the results to a high limit when the transfer functions at selected locations are computed. The high values of dimensionless frequency will reach $ka = 100$, or $\eta = 100/\pi$; meaning there will be over 60 wavelengths within the alluvial valley. The transfer functions will be plotted to show the outstanding stability of this numerical formulation.

3.5 Computation of Time Histories

Since the numerical solution using the substructure deletion concept is performed in the frequency domain, time histories could be obtained using Fourier Synthesis. The Fourier

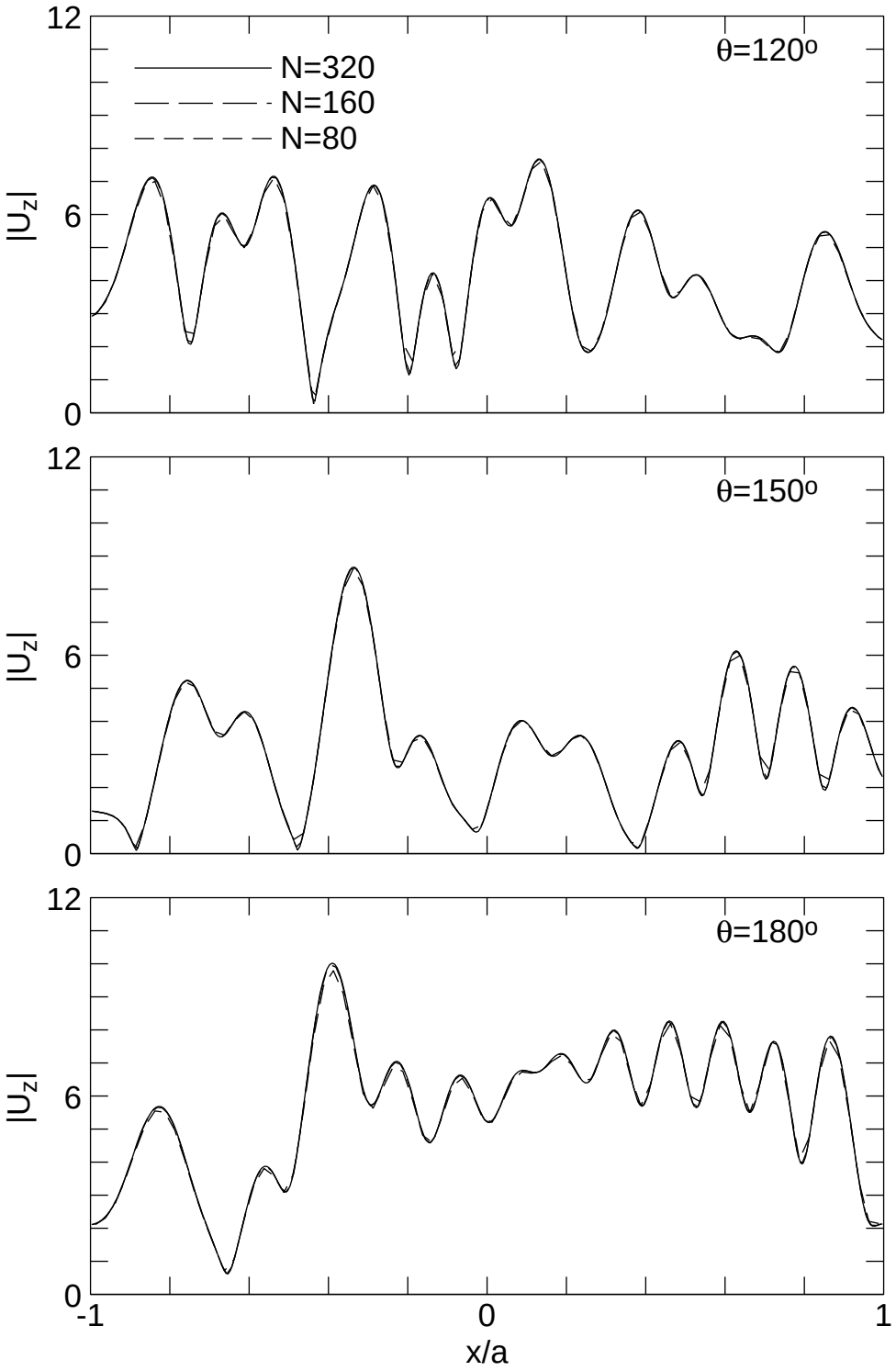

Figure 3.10. Response of Alluvial at $\eta = 4$. Right Side Incident

Transform pair can be expressed as

$$F(\omega) = \int_{-\infty}^{\infty} f(t)\, e^{-i\omega t}\, dt \qquad , \tag{3.13}$$

as the forward transformation and

$$f(t) = \frac{1}{2\pi} \int_{-\infty}^{\infty} F(\omega)\, e^{i\omega t}\, d\omega \qquad , \tag{3.14}$$

as the inverse transformation. The factor, $1/2\pi$, is sometimes distributed evenly to both parts of the pair as $1/\sqrt{2\pi}$

Consider the input motion to be in a form of a Ricker Wavelet as shown in Fig. 3.11. It has a mathematical form of

$$A(t) = \left(1 - 2\pi^2 f^2 t^2\right)\, e^{-\pi^2 f^2 t} \qquad , \tag{3.15}$$

in which $f = 1/t_p$ is the wavelet's peak frequency. There are three wavelets illustrated in Fig. 3.11, the high frequency wavelet has a period of $t_p = 0.75$ and a peak frequency of $f = 4/3$. The medium frequency wavelet has a period of $t_p = 1.5$ and a peak frequency of $f = 2/3$. The long period wavelet has a period of $t_p = 3$ and a peak frequency of $f = 1/3$. This wavelet is frequently used in seismic simulation as it has a very definite frequency band and it is a good input function.

If the complex frequency content of the incident wave time history can be obtained as

$$A(\omega) = \int_{-\infty}^{\infty} A(t)\, e^{-i\omega t}\, dt \qquad , \tag{3.16}$$

the response at the surface of the alluvial valley can be computed as

$$u(t) = \frac{1}{2\pi} \int_{-\infty}^{\infty} T(\omega) A(\omega)\, e^{i\omega t}\, d\omega \qquad , \tag{3.17}$$

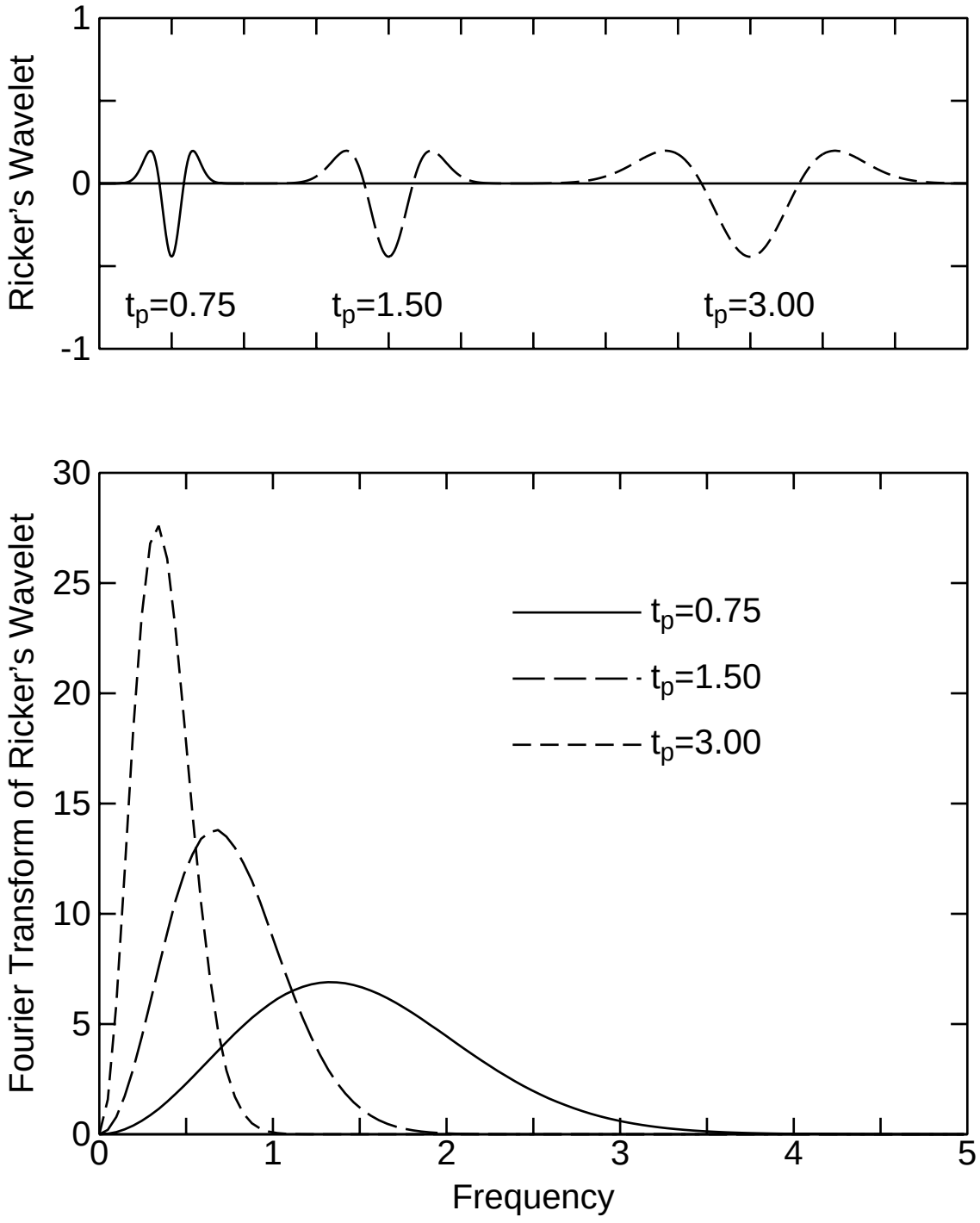

Figure 3.11. Ricker Wavelets and their Fourier Transforms

where $T(\omega)$ is the complex transfer function determined at a certain location based on a unit input of the incident wave. To obtain the transfer function, pick a location from the graphs shown in Section 3.4 and calculated the response (amplitude and phase) over the entire frequency spectrum.

Calculations were made to find the transfer functions at seven selected locations as shown in Fig. 3.6 for various stiffness ratios, $\mu/\mu_v = 3$, 6 and 9, angles of incidence from both sides of the alluvial valley. There are many parameters to be dealt with, but many interesting physical phenomena can be observed by this numerical simulation.

Shown in Fig. 3.12 are two transfer functions plotted versus dimensionless parameter ka from 0 to 100. a is the width of the alluvial valley and k is the wave number defined as $k = \omega/\beta$. ka is related to η used in the previous sections as $\eta = ka/\pi$. Therefore, the value of $ka = 100$ is equivalent to $\eta > 32$, a high dimensionless frequency rarely performed in previous research reports. In the top figure of Fig. 3.12 is the transfer function of Station 1 ($a/8$ from the left edge) for vertical incident SH-wave and a stiffness ratio of $\mu/\mu_v = 3$, The solid line represents the real part of the complex transfer function and the short dash line represents the imaginary part. For Fourier synthesis, the transfer function must be complex so that the correct phases are accounted for. The second figure of Fig. 3.12 is the amplitude of the complex transfer function, it was plotted to show that the results are stable over a large frequency band. The 3rd and the 4th figures of Fig. 3.12 shown the complex transfer function and its amplitude for a stiffness contrast ratio of $\mu/\mu_v = 6$. It is clear that transfer function values are much larger because the wave energy would be trapped in the softer layer.

It is important to point out that the media parameters used do not include viscous damping. This decision was made to avoid introducing one extra parameter into the

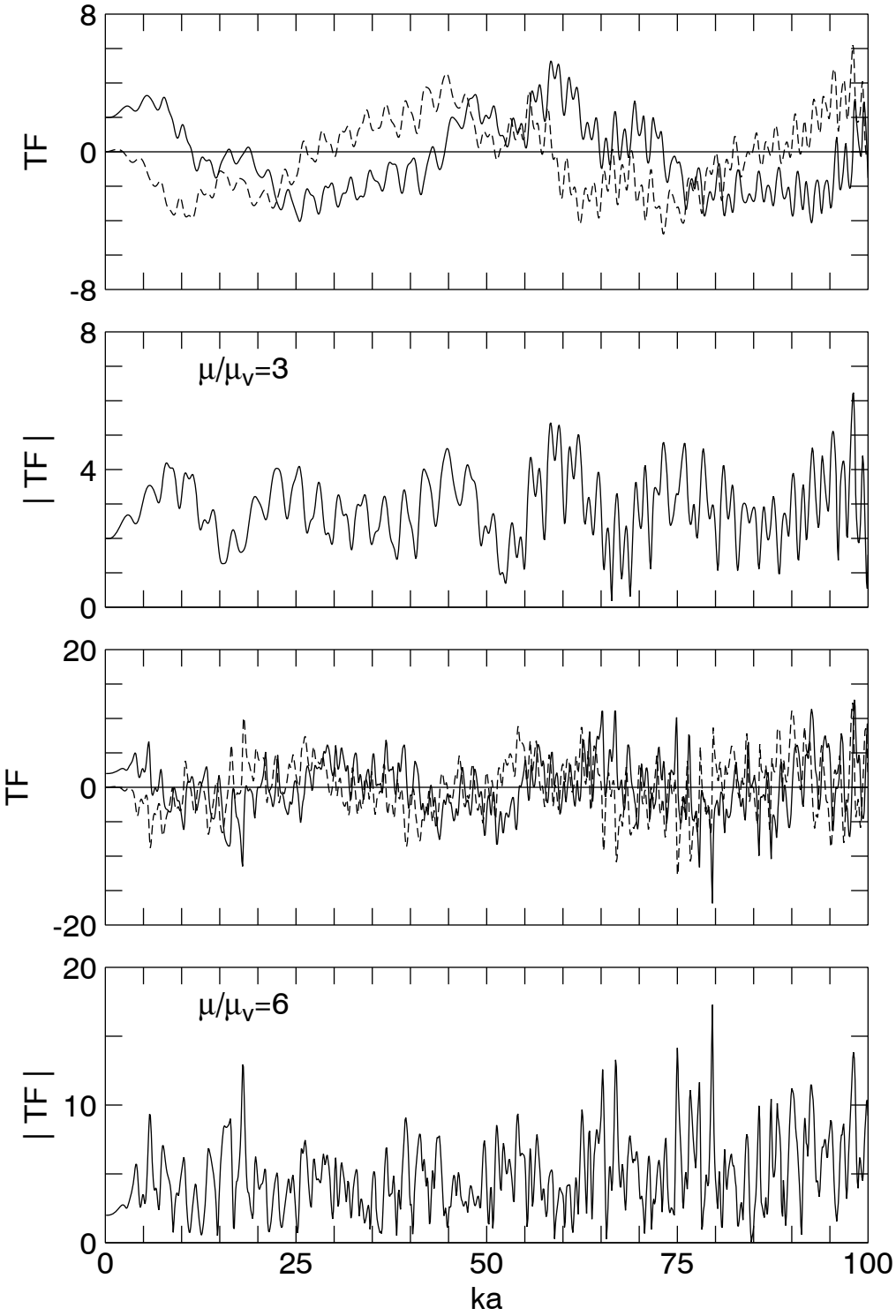

Figure 3.12. Complex Transfer Functions and Their Amplitudes

analysis. The fact that the transfer functions appear to be damped, i.e., no infinite values at resonance frequencies of the alluvial valley, is that radiation damping exists in the model. The Sommerfeld boundary condition at infinity was satisfied automatically by the choice of Green's Functions for the exterior medium.

Working in the frequency domain, it is impossible to extract the valuable quantity of duration. Putting physical dimensions into the analysis, let $\beta = 1250$ m/sec as the shear wave velocity of the bedrock and the width of the alluvial valley is 10.3 km. Seven recording stations are selected equally spaced over the alluvial valley's surface as shown in Fig. 3.6 with the distance between the station approximately equal to 1.3 km. Shown in Fig. 3.13 is the case where the incident wave has an angle of 90° and the stiffness ratio of $\mu/\mu_v = 6$. The vertical scale of the responses is normalized to the incident pulse as 1, therefore, the peak values represent the actual site amplification factors. The duration of the input pulse is approximately 2.5 seconds, but the response, due to site amplification, could go on for about 80 seconds. At station 5, the amplification reached as high as 6, based mainly on the secondary refracted waves. As shown, the response on the alluvial valley is quite different from the simple incident pulse. If an incident wave with a longer duration is used as the input, the amplitude of the response could be much higher.

Shown in Fig. 3.14 is the response with the same parameters as Fig. 3.13 except the angle of incident is $\theta = 0$. Since it is a horizontal incident wave, the response starts earlier on Station 1 and much later on Station 7. It is interesting to note that the reflection from the back of the alluvial valley interface arrives at Station 7 a long time before it reached Station 1. For this incident angle, the largest amplitude is less, about 4.5 times the strength of the incident pulse.

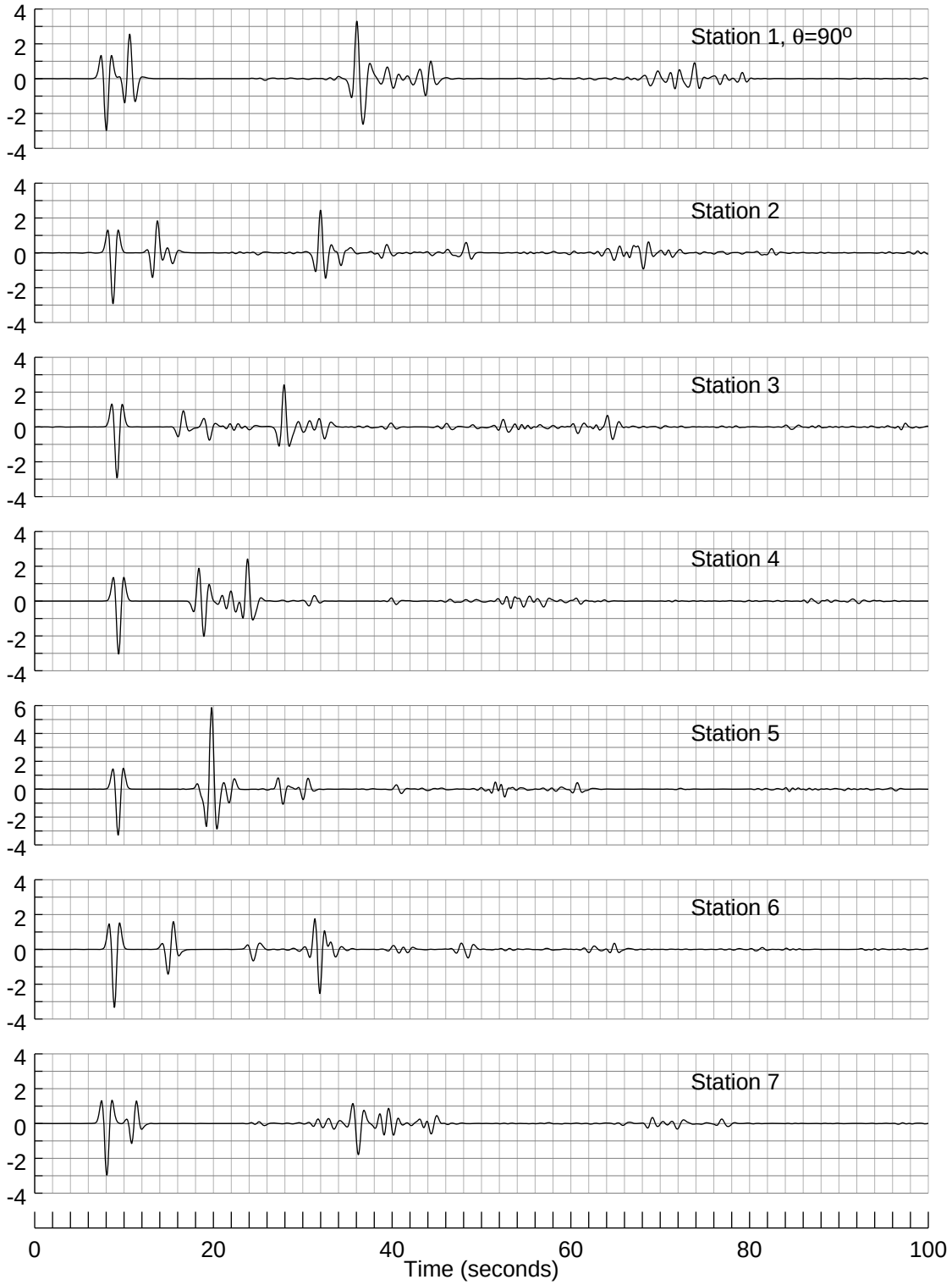

Figure 3.13. Response to Ricker Wavelet with Vertically Incident SH-Wave

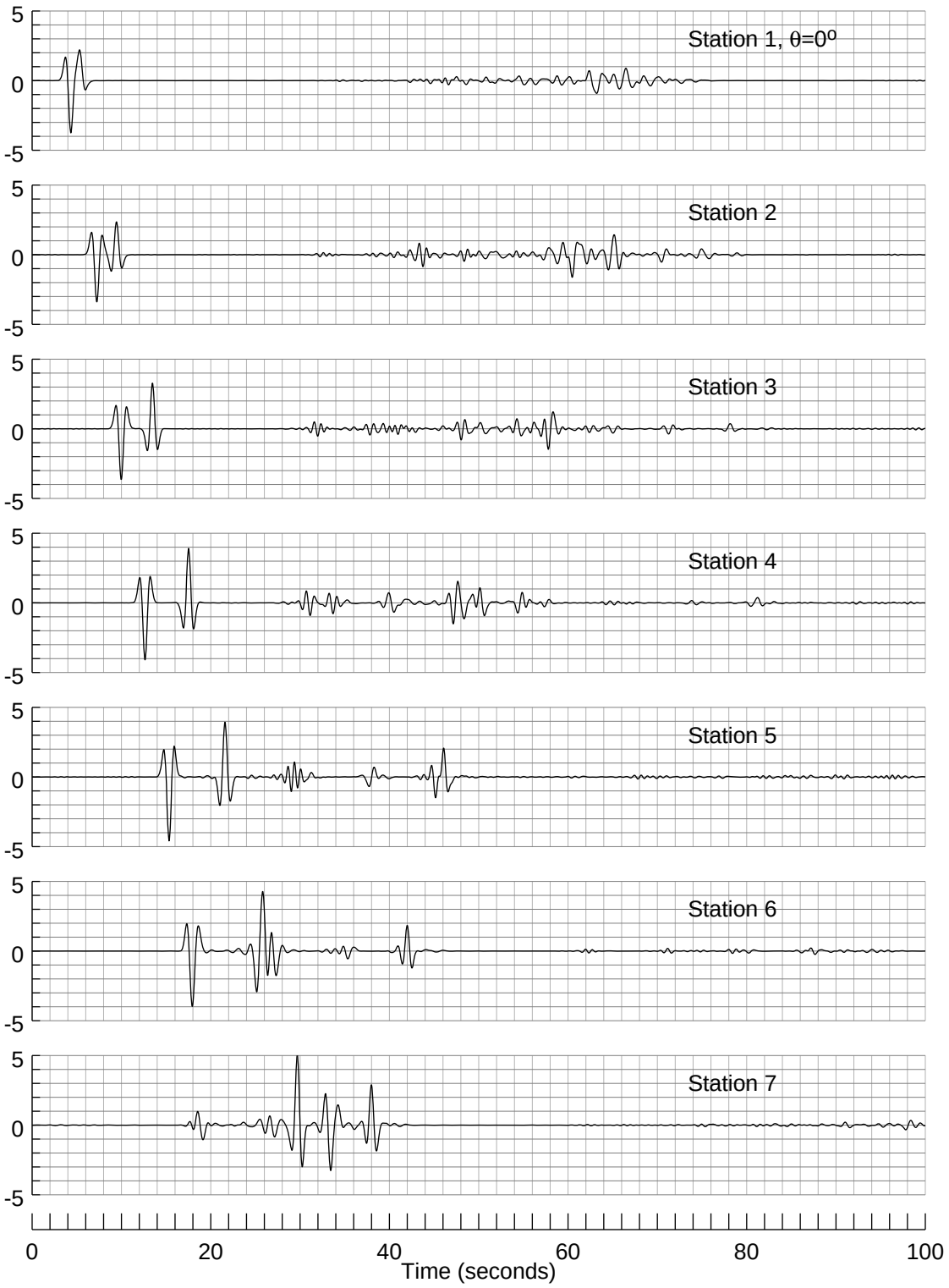

Figure 3.14. Response to Ricker Wavelet with Horizontally Incident SH-Wave

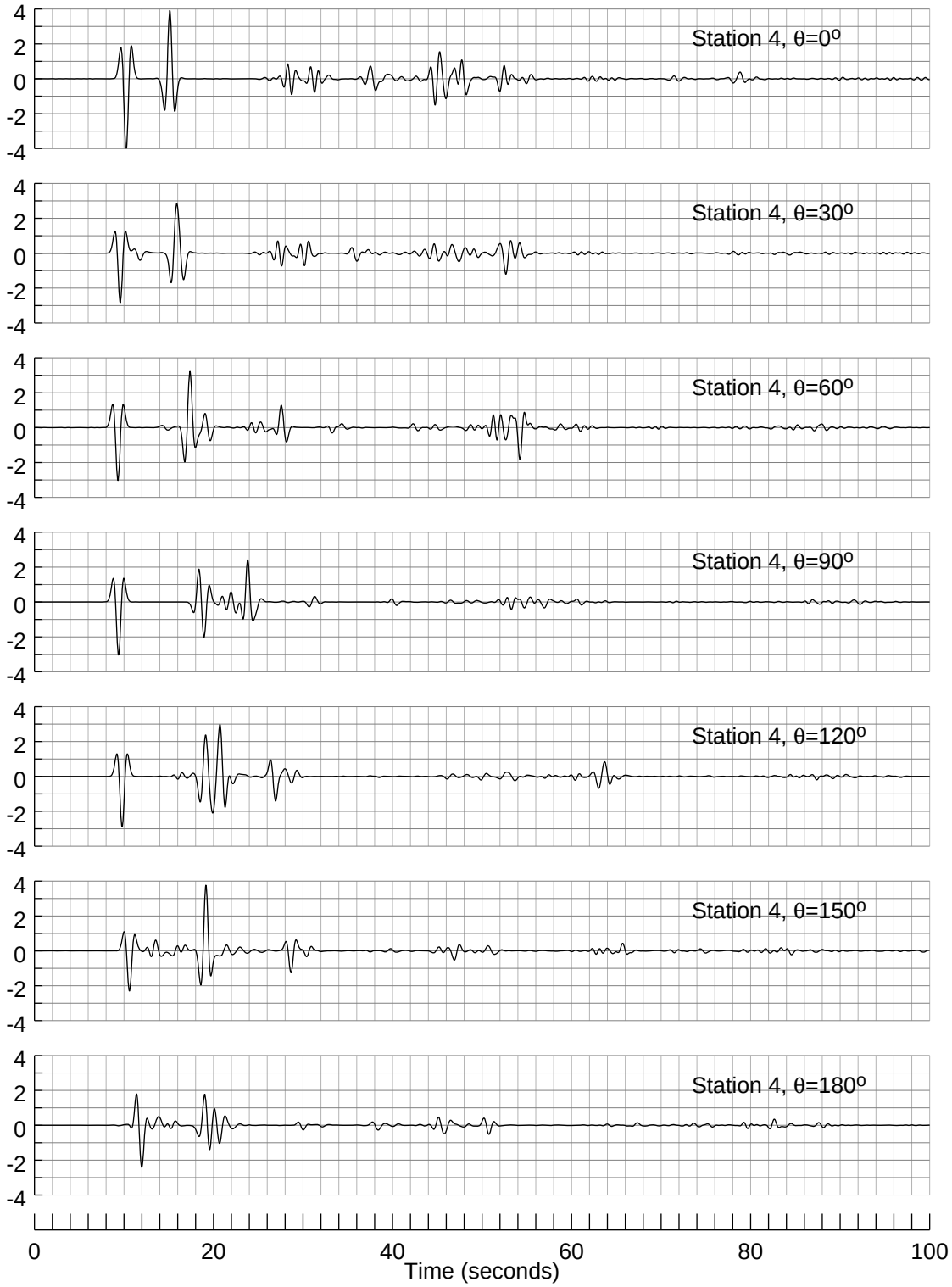

Figure 3.15. Response at Station 4 to Ricker Wavelet with Various Incident Angles

In Fig. 3.15, the response at Station 4, near the midpoint of the alluvial valley, is shown for seven incident angles, $\theta = 0^\circ$, 30°, 60°, 90°, 120°, 150° and 180°. The angle $\theta = 0^\circ$ represents the incident waves coming from the left side of the valley and $\theta = 180^\circ$ represents that from the right side. The stiffness ratio remains $\mu/\mu_v = 6$. This figure demonstrates that the response at a recording station is a function of the location of the seismic source.

In Fig. 3.16, the effect of stiffness ratio is examined. Three Different values, $\mu/\mu_v = 3$, 6 and 9 are used. The responses at Station 4 for all three stiffness contrasts were recorded for incident angles of $\theta = 30^\circ$ and $\theta = 90^\circ$. As expected, the amplification is larger for a softer alluvial valley, but the most important difference is the duration. Seismic energy would be trapped inside a softer layer longer as it is difficult to transmit and radiate the wave back into the bedrock. A more complex input time function than a Ricker Wavelet could cause much larger amplification as waves constructively interfere with each other.

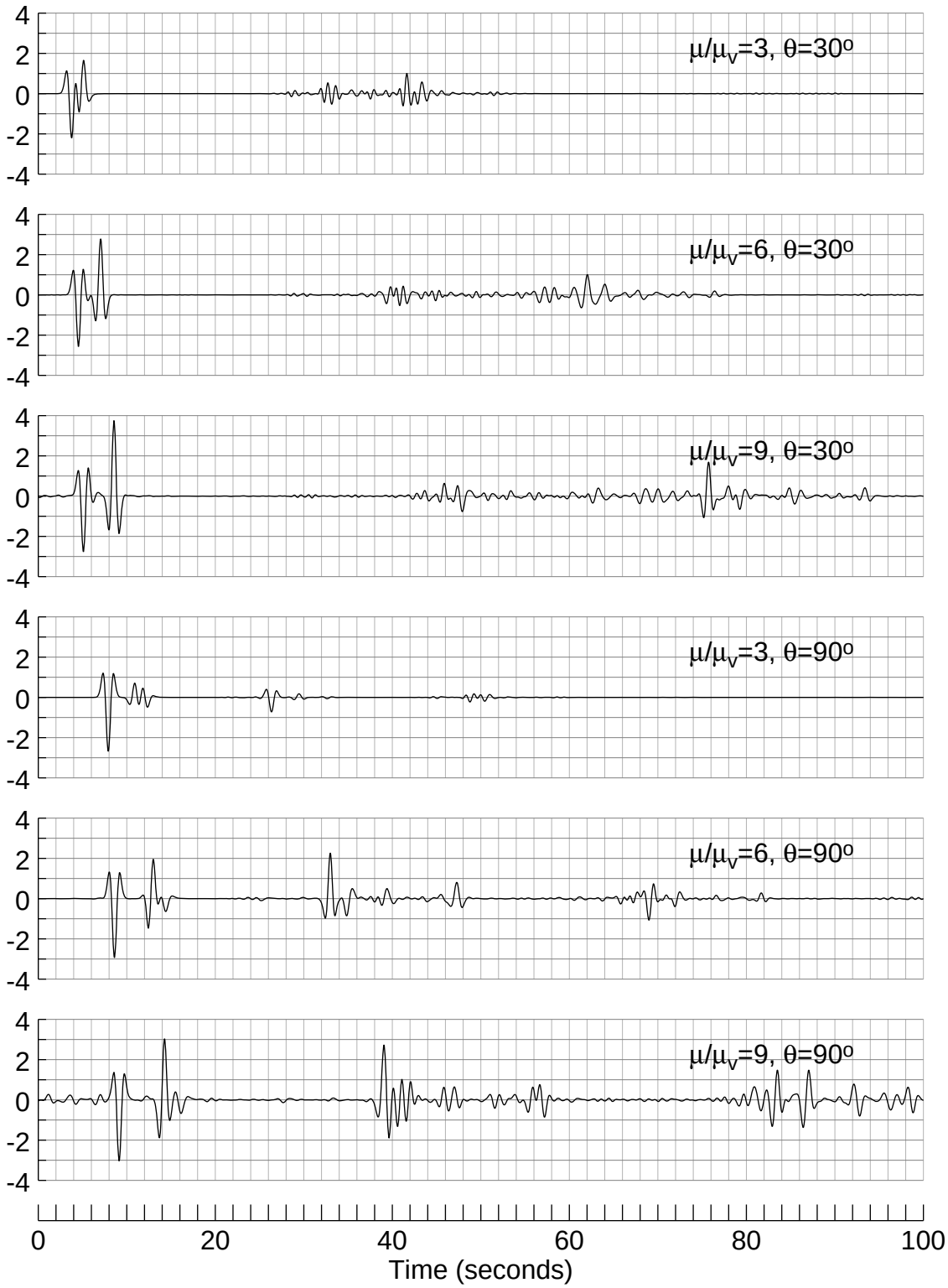

Figure 3.16. Response at Station 4 as a Function of Stiffness Ratios

Chapter 4

Wave Scattering by a Canyon for In-Plane Waves

In chapter Two, the substructure deletion method was shown to be effective for scattering of SH-waves by two-dimensional canyons. This chapter the method will be explored for in-plane motion. The number of degrees of freedom will increase by a factor of two as the inplane motion includes a vertical and a horizontal component of displacement. As described by wave propagation books, such as Ewing et al (1957), whenever an inplane wave strikes a boundary, mode conversion would occur. An incident compressional wave striking a boundary at an inclined angle would result in a reflection of a compressional wave and a shear wave. The same scenario would apply for a shear wave (SV) incident for a limited range of angles. This phenomenon is caused by the fact that the compressional wave and the shear wave have different velocities. The physics involved in this inplane problem is more advanced than those covered for the SH-wave diffraction problems.

The Green's Functions to be used for the formulation in this chapter will come from Appendix C. The Green's Function for the interior problem are those covered in Section C.1 and they are in the form of Hankel Functions. The Green's Functions for the exterior problem are the infinite integrals shown in Section C.2, better known as the solution to the Lamb's problem (Lamb, 1903).

4.1 Validation of Plane Strain Green's Functions

One benchmark to test the validity of this calculation is to match the results given by Luco and Westman (1971) for the compliance functions of a rigid strip foundation on a half space as shown in Fig. 4.1. The width of the foundation is $2b$ and the results for the compliances are given as a function of a dimensionless frequency defined as $a_0 = \omega b/\beta$, in which β

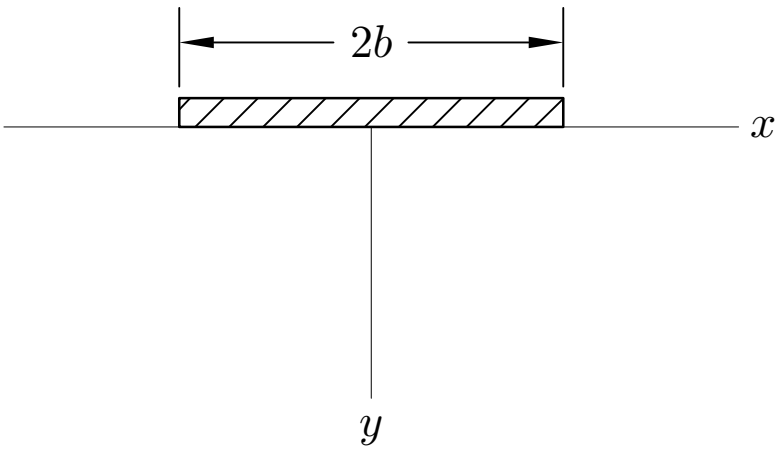

Figure 4.1. A Rigid Strip Foundation

is the shear wave velocity of the soil medium. The dimensionless compliance functions were normalized as $C_{vv} = \pi\mu\Delta_y/P_y$ for the vertical component and $C_{hh} = \pi\mu\Delta_x/P_x$ for the horizontal component. $Delta_x$ and $Delta_y$ are the harmonic displacements of the foundation in the x and the y directions, respectively. The parameter μ is the shear modulus of the soil medium and the harmonic forces, P_x and P_y, are the driving forces in the x and the y directions, respectively.

To calculate the compliance functions, the plane strain Green's Functions on the surface of a homogeneous half space must be computed. Therefore, if the comparison is successful, it would validate that particular subprogram. Shown in Fig. 4.2 are the vertical compliance functions, C_{vv}, for three different Poisson's ratios, $\nu = 0$, 0.25 and 0.33. The solid lines in each subfigures are the computed real parts and the dashed line are the computed imaginary parts. The open circles represent the real part of the results provided by Luco and Westman (1972) and the open triangle symbols represent the imaginary part. The results match remarkable well, considering they were computed using completely different

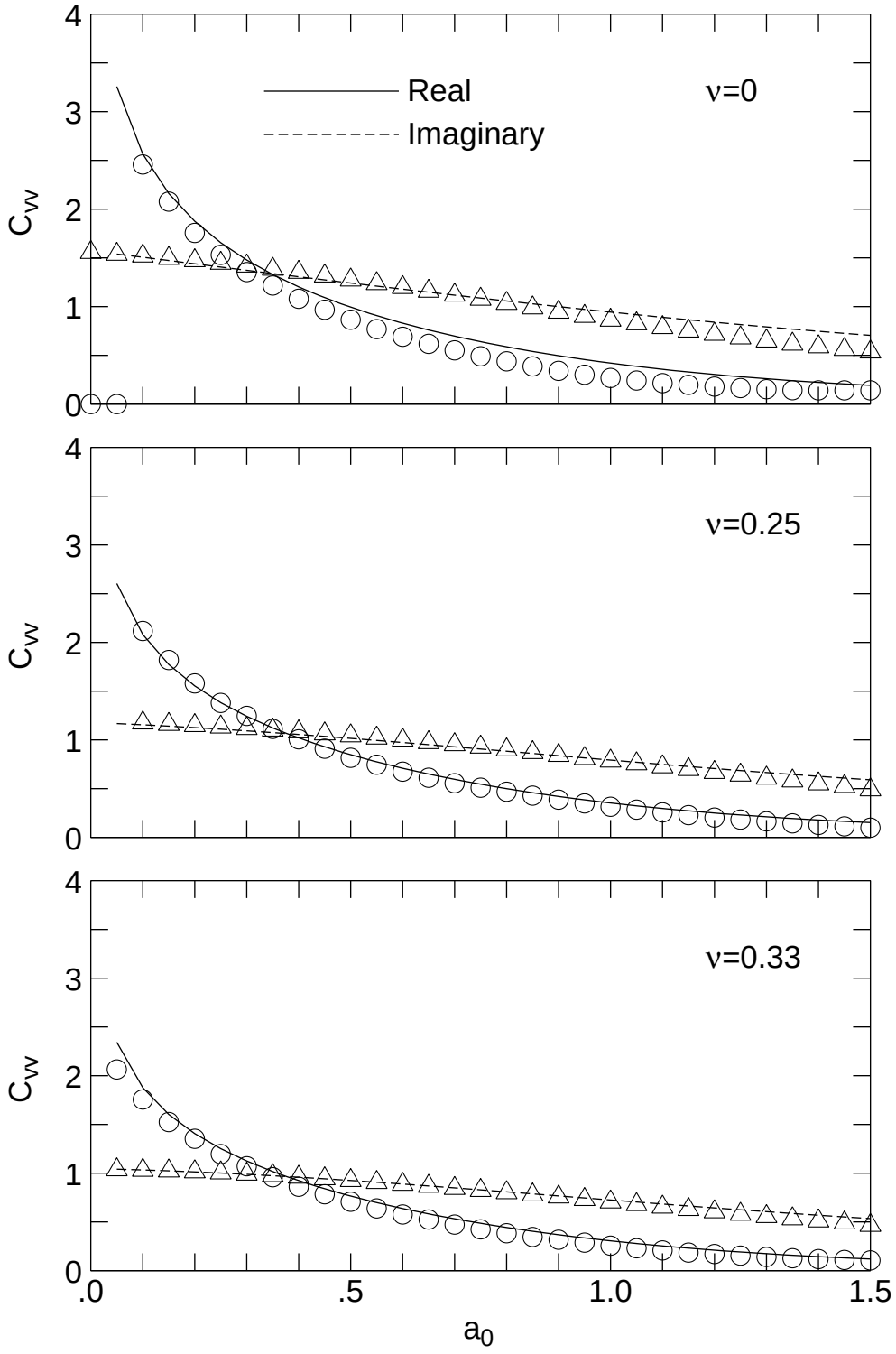

Figure 4.2. Comparison of Compliance Functions C_{vv}

methods. The Poisson's Ratio affects the ratio of the body wave speed; the ratio of shear wave velocity over compressional wave velocity, $\gamma = \beta/\alpha$, is related to the Poisson's Ratio as $\sqrt{(1-2\nu)/(2(1-\nu))}$.

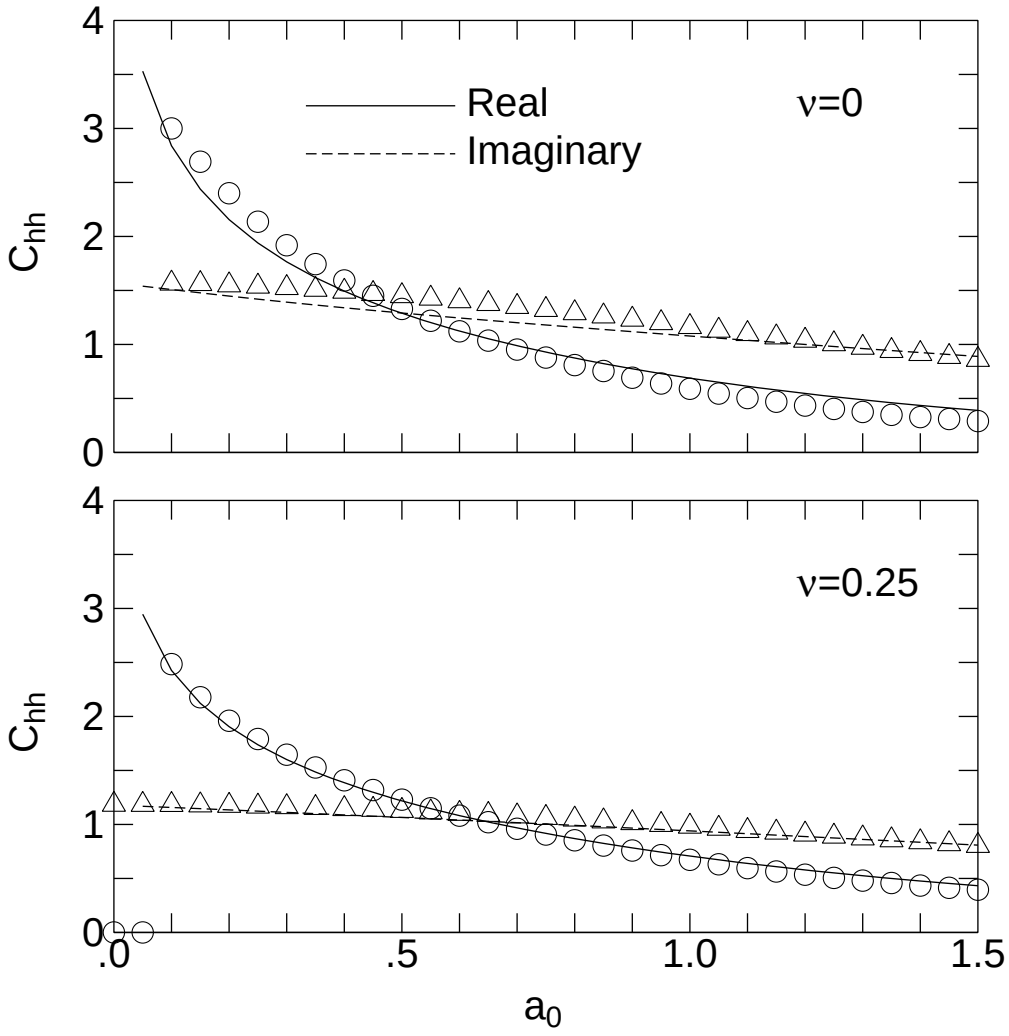

Figure 4.3. Comparison of Compliance Functions C_{hh}

Shown in Fig. 4.3 are the compliances for the horizontal component, C_{hh}. The comparison is again right on. The $\nu = 0.33$ case was not given by the authors for this component. With these two tests, the Green's Functions appear to be correct. A welded boundary condition was used for the computation at the foundation's interface with the soil medium.

For this particular application, the results converged quickly with very few subregions used for the approximation of the foundation surface. Shown in Fig. 4.4 is a comparison between results calculated using $N = 20$, 40, 80 and 160 subregions; the numerical results are within one or two percent of each other and the differences are not noticeable in the figure.

The reason this exercise was performed is to test the convergence and stability of the method. Initially, the results for the highly refined model were actually worse and that prompted an exercise to make sure the Green's Functions were calculated correctly. The Lamb's solutions shown in Eq. (C24) through (C27) are complex infinite integral and they contain a singularity known as the Raleigh Pole. To simplify the calculation, especially for an undamped medium, contour integration was employed and the results offered simpler and more manageable integrals and expressions in Eq. (C28) to (C31).

Two particular integrals, involve an infinite limit in the forms of

$$\int_0^\infty \frac{\sqrt{1+k^2}}{(2k^2+1)^2 - 4k^2\sqrt{k^2+\gamma^2}\sqrt{k^2+1}} e^{-a_0 kx} dk \quad , \tag{4.1}$$

and

$$\int_0^\infty \frac{\sqrt{k^2+\gamma^2}}{(2k^2+1)^2 - 4k^2\sqrt{k^2+\gamma^2}\sqrt{k^2+1}} e^{-a_0 kx} dk \quad , \tag{4.2}$$

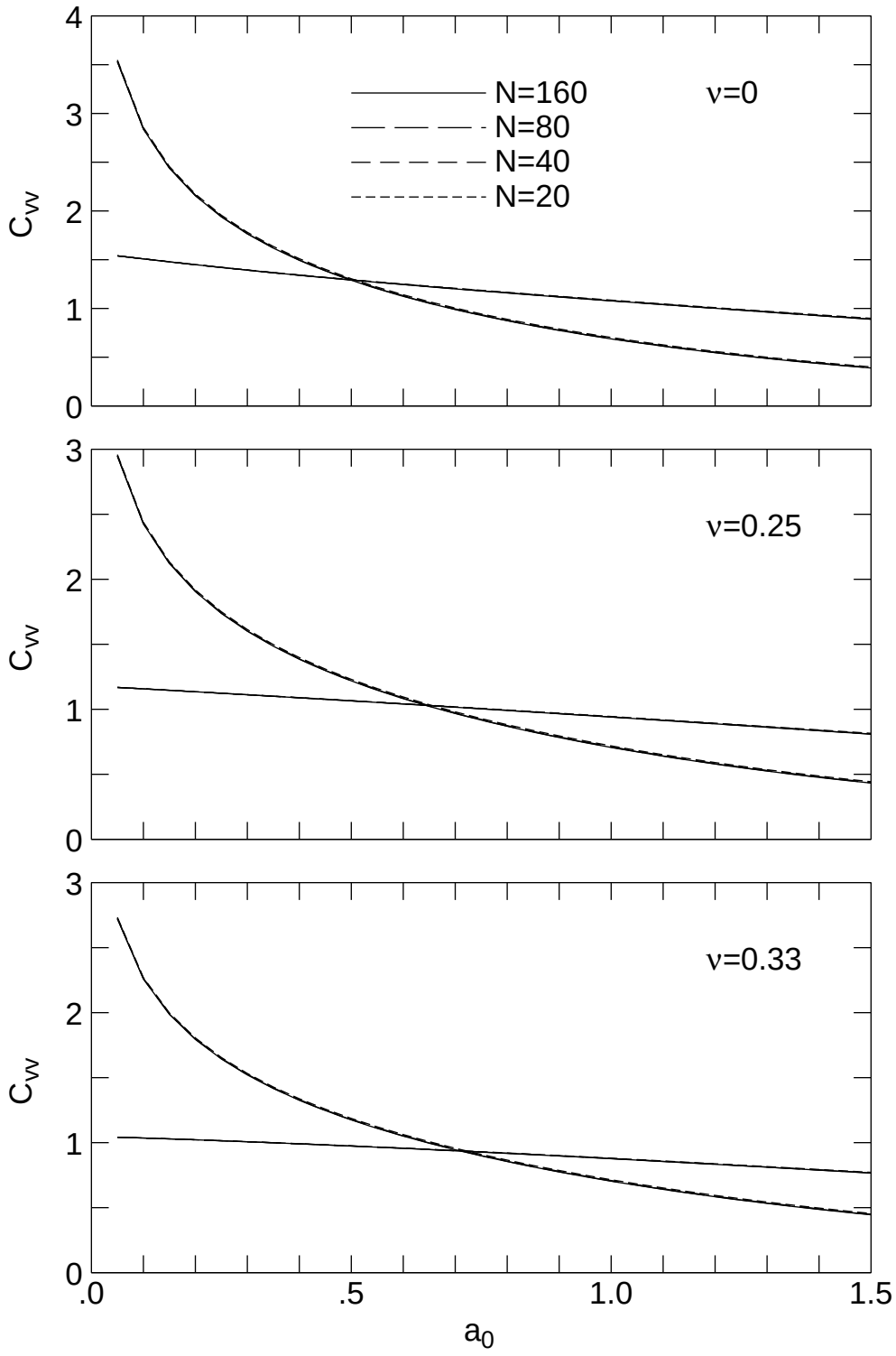

Figure 4.4. Compliance Functions C_{vv} with Various Levels of Approximation

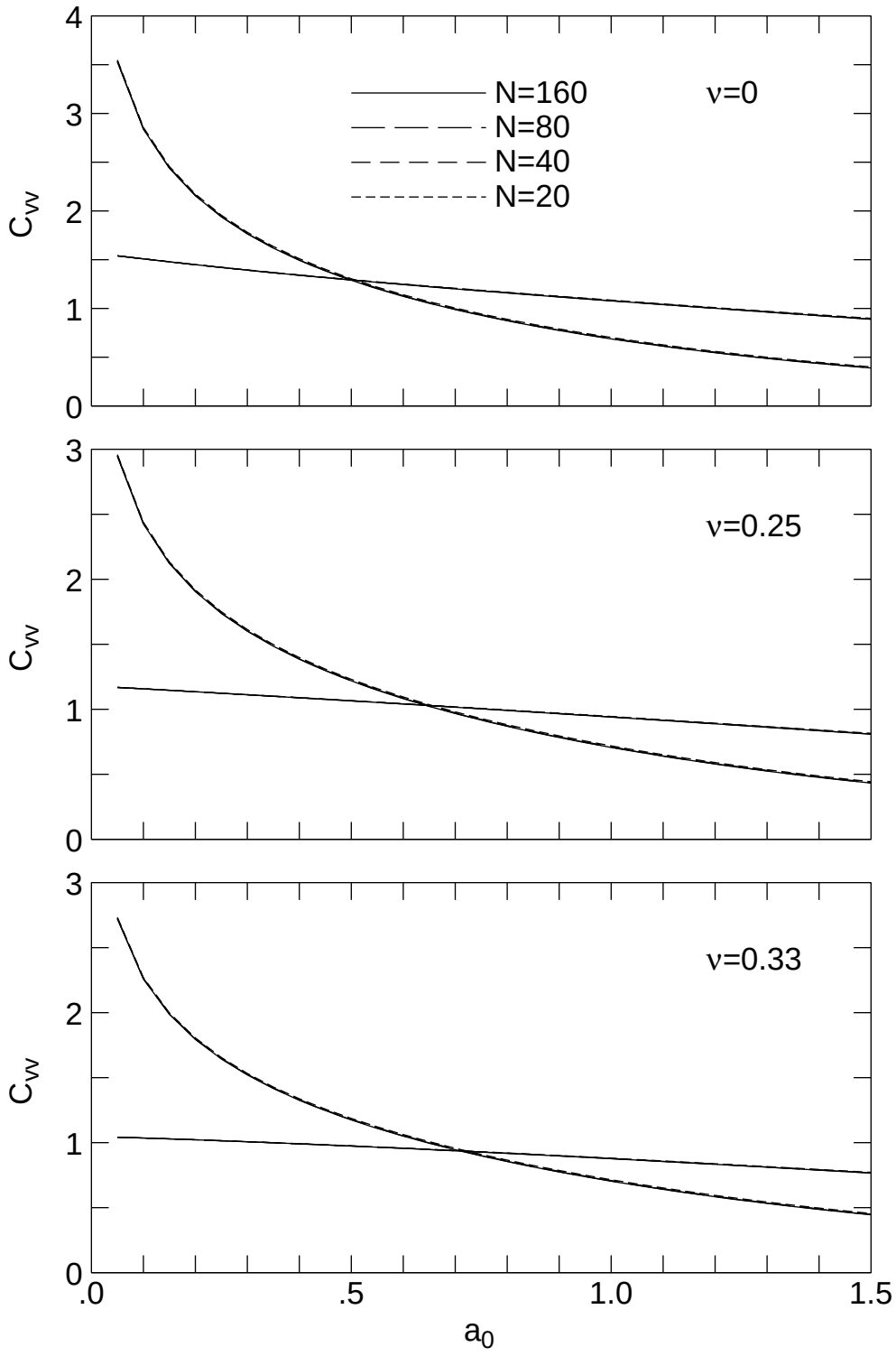

Figure 4.5. Compliance Functions C_{hh} with Various Levels of Approximation

are the troublesome ones if the argument $a_0 x$ is very small. In the case of the highly refined models, the subregions, or the line segments, are very short and that leads to a small value of $a_0 x$, especially at a low dimensionless frequency of a_0.

For normal values of $a_0 x$, the exponential function decays rapidly in both Eq. (4.1) and (4.2) and the numerical evaluation is simple. For extremely small values of $a_0 x$, the exponential function approaches 1 and the remaining integrand has the following limit:

$$\frac{\sqrt{1+k^2}}{(2k^2+1)^2 - 4k^2\sqrt{k^2+\gamma^2}\sqrt{k^2+1}} \approx \frac{1}{2(1-\gamma^2)k} \qquad , \tag{4.3}$$

as k approaches infinity. The integral of $1/k$ would result in a logarithmic singularity.

The modified method used to evaluate Eq. (4.1) is to split it into 3 integrals as follows:

$$\begin{aligned}
&\int_0^\infty \frac{\sqrt{1+k^2}}{(2k^2+1)^2 - 4k^2\sqrt{k^2+\gamma^2}\sqrt{k^2+1}} e^{-a_0 k x} dk \\
&\quad = \int_0^1 \frac{\sqrt{1+k^2}}{(2k^2+1)^2 - 4k^2\sqrt{k^2+\gamma^2}\sqrt{k^2+1}} e^{-a_0 k x} dk \\
&\quad + \int_1^R \left[\frac{\sqrt{1+k^2}}{(2k^2+1)^2 - 4k^2\sqrt{k^2+\gamma^2}\sqrt{k^2+1}} - \frac{1}{2(1-\gamma^2)k} \right] e^{-a_0 k x} dk \\
&\quad + \frac{1}{2(1-\gamma^2)} \int_1^\infty \frac{1}{k} e^{-a_0 k x} dk \qquad .
\end{aligned} \tag{4.4}$$

The first integral on the right hand side is simple to evaluate numerically, it is a finite integral. The second is integrated from 0 to R, an arbitrary value. If R is chosen to be 1000, the difference in the bracket at the upper limit is near zero, accurate to the order of 6 significant digits. The third integral is known as the Exponential Integral and it can be evaluated as $E_1(a_0)$. The Exponential Integral can be evaluate as a series (Abramowitz and Stegun, 1970) as

$$E_1(z) = -\gamma - \log z - \sum_{n=1}^{\infty} \frac{(-1)^n z^n}{n\, n!} \tag{4.5}$$

where $\gamma = 0.5772156649$ is the Euler Number. With the expressions in Eq. (4.4), the $\log(a_0 x)$ singularity has been isolated and it can be integrated analytically over x to for the diagonal elements of the singular matrices. A similar method could be used for Eq. (4.2). After this improvement is made, the matrix $[G_{11}^H]$ as shown in Eq. (2.8) can be evaluated consistently, no matter how refined the model maybe.

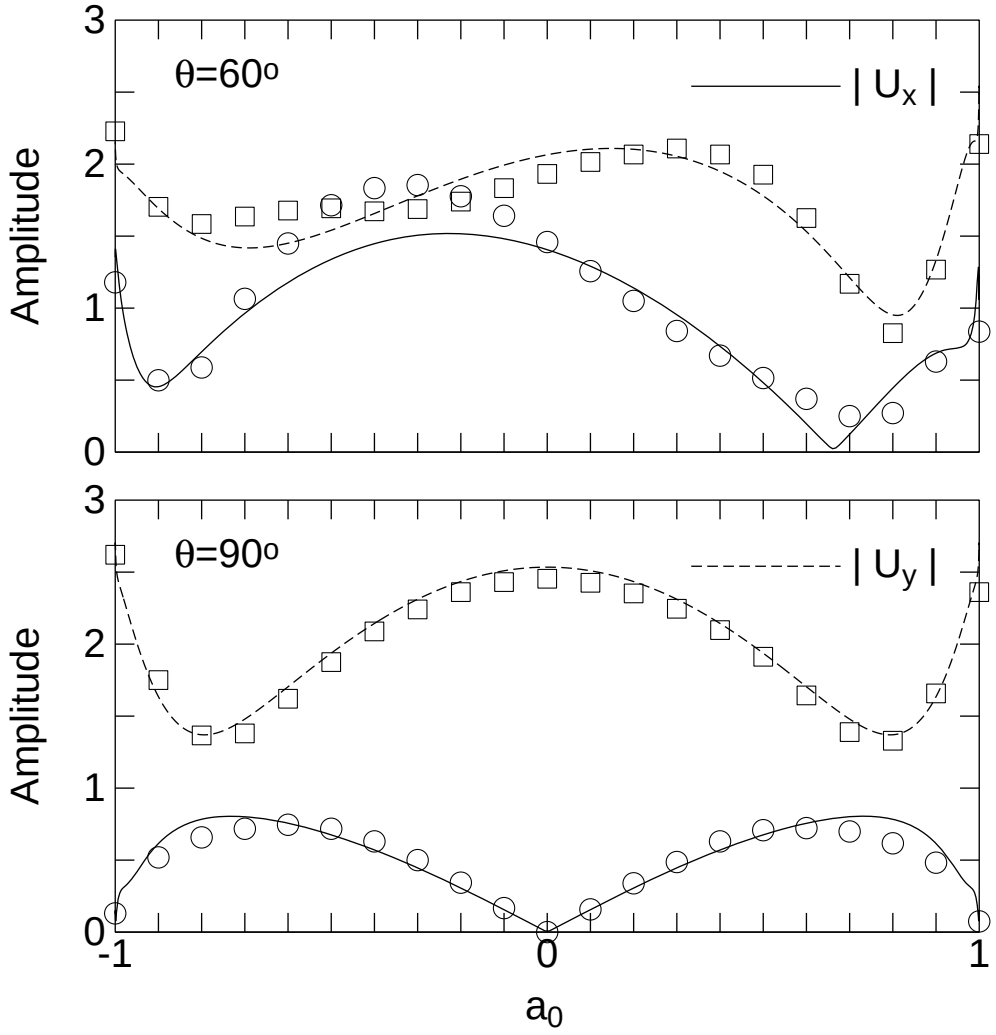

Figure 4.6. Amplitude Comparisons for P-Wave Incident, $\eta = 1$

4.2 Comparison with Available Results

There are a number of results available for wave scattering of P or SV-waves by arbitrary shaped canyons. Unlike the SH-wave problem where the half space boundary condition could be satisfied by symmetry, The boundary conditions for plane strain problems are much more difficult. Wong (1979) obtained his results using a least square approximation for the boundary conditions by placing sources within the boundary to provide the wave form for the scattered waves. From that paper, some results were provided for an elliptical canyon.

Shown in Fig. 4.6 are the results for P-wave incidence. The aspect ratio of the canyon is $b/a = 1$, a circular cylindrical canyon. Two angles of incident were considered, $\theta = 60^\circ$ and 90°. For both cases there is a horizontal component $|U_x|$ and a vertical component $|U_y|$, represented by a solid line and a dashed line, respectively. The results from Wong (1979) are plotted as open circles for $|U_x|$ and as open squares for $|U_y|$. The dimensionless frequency is $\eta = 1$. The results matched with about 20% difference. The overall shape of the response variation is correct even though there are some differences. One possible reason for the discrepancy is limitation of computer resources back in the late 1970s, there was no way to justify the cost of a model which has 320 subregions. The substructure deletion results are from a refined model. Later results will confirm that accurate results in the inplane model require a more refined model than the antiplane model.

Shown in Fig. 4.7 are the results for SV-wave incidence. The same two angles were used as in the P-wave case. The aspect ratio of the canyon is $b/a = 1$, a circular cylindrical canyon, as previously. But it needs to be pointed out that the SV-wave angle cannot be smaller than 60° for a Poisson Ratio of $1/3$. Therefore, 60° is a critical angle with a large amplitude free field motion. The amplitudes for the free field motion as a function of angles

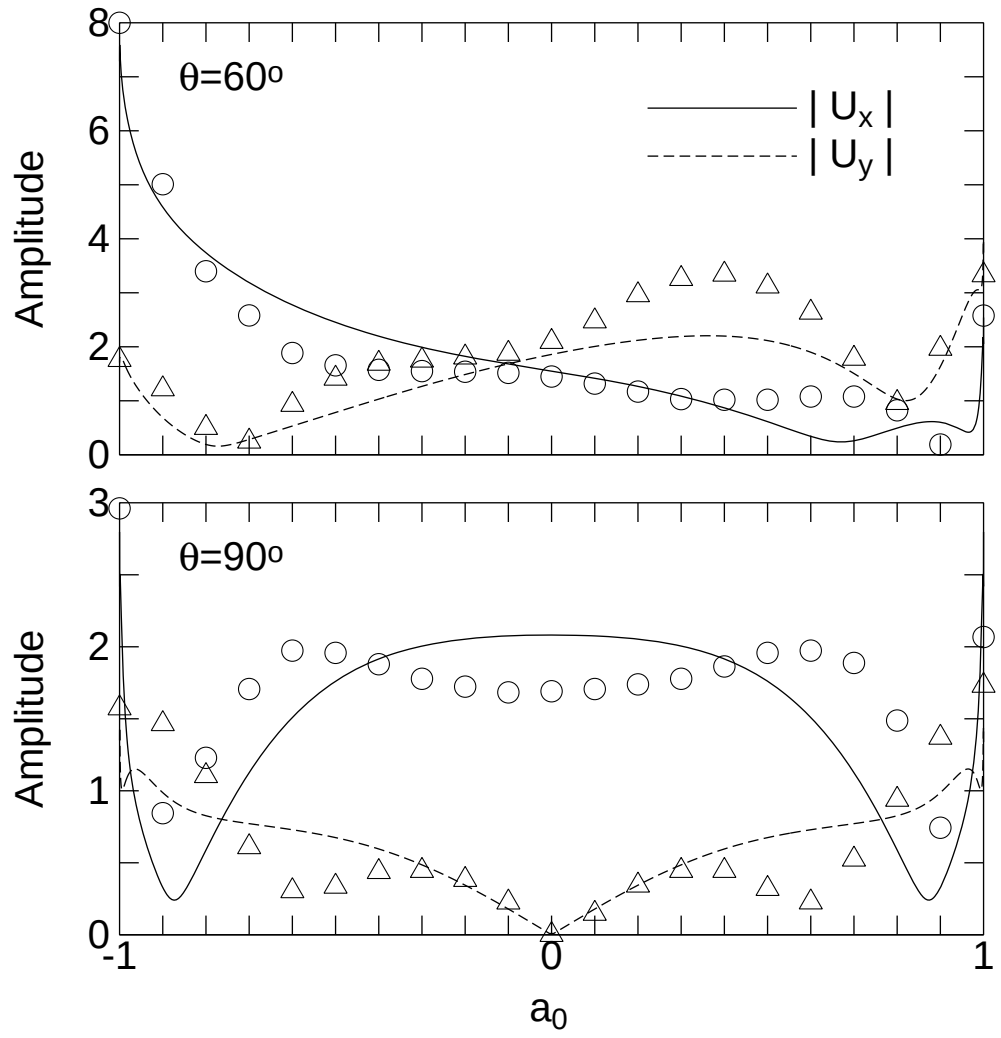

Figure 4.7. Amplitude Comparisons for SV-Wave Incident, $\eta = 1$

are shown in Appendix D. Judging from the fact that the two methods are significantly different, the agreement of the results is acceptable.

Another explanation for the discrepancy is that a circular canyon, having an aspect ratio of $b/a = 1$ is considered to be a deep canyon. It is expected that a shallower canyon would be better modeled by the substructure deletion method. Shown in Fig. 4.8 are the results from three different depths of canyon, $b/a = 0.25$, 0.50 and 1.00. For the two shallower cases,

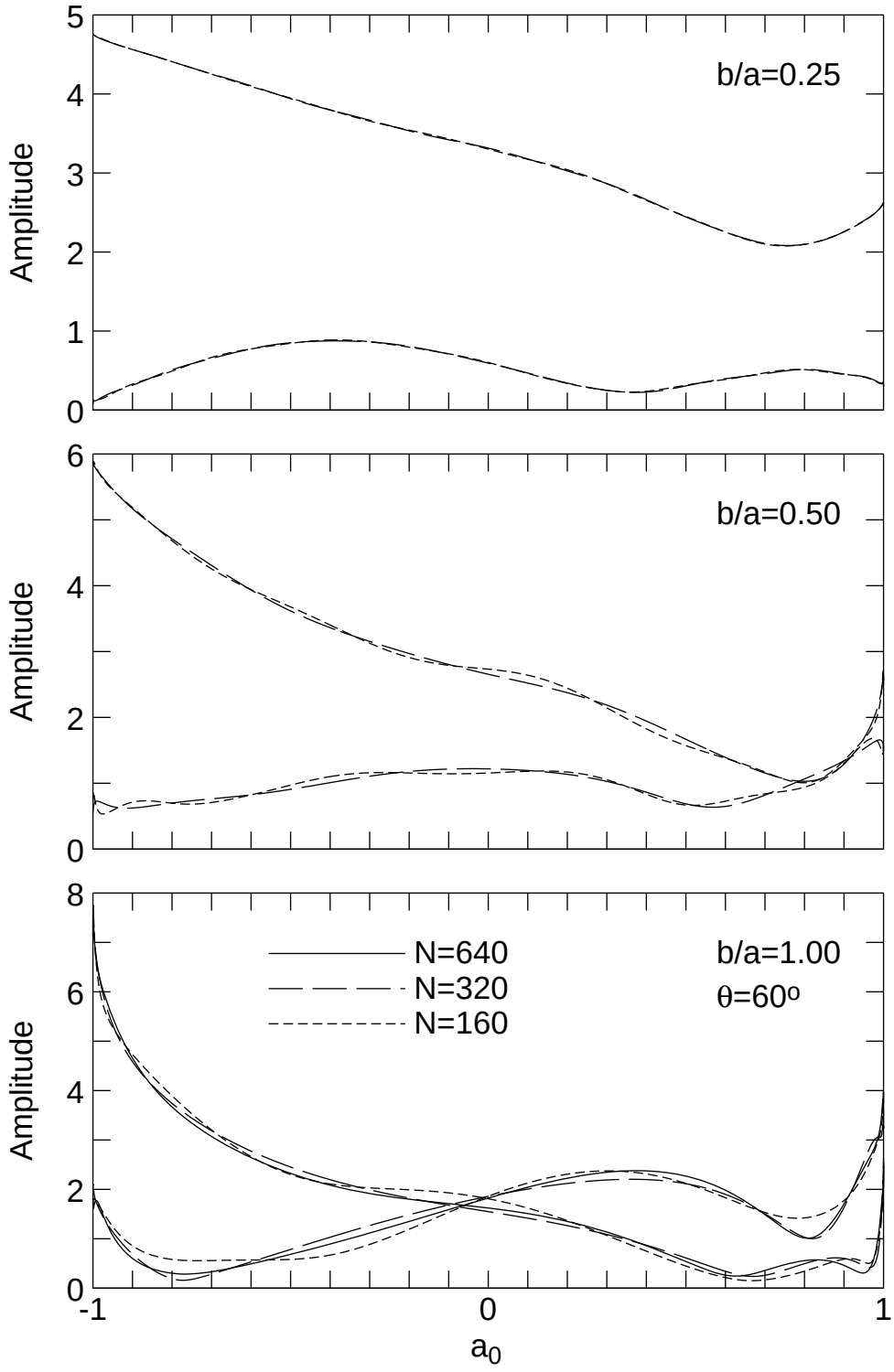

Figure 4.8. Aspect Ratio Comparison. SV-wave Incidence, $\theta = 60°$, $\eta = 1$

two different models were made, one with $N = 160$ (represented by short dashed lines) and another with double the refinement at $N = 320$ (represented by long dashed lines). For an angle of $60°$, it is clear that the shallower geometry model requires fewer line segments to create an accurate solution. The two models with different refinement matched perfectly for $b/a = 0.25$ and only minor differences existed for $b/a = 0.50$. The lower figure shows that as the canyon depth becomes deeper, when $b/a = 1.0$, the results differed noticeably. A third highly refined model with $N = 640$ was added to this case (represented by a solid line) and it shows a consistency of convergence. This exercise explains the differences shown in Fig. 4.6 and Fig. 4.7 as the older research lacks the computing resource for further refinement.

A similar conclusion can be drawn using Fig. 4.9 for an incident angle of $90°$. The results match with excellent accuracy if the canyon is shallow, this explains why the substructure deletion method would work well for site amplification studies, but not as well for deeply embedded foundations.

4.3 Response of an arbitrary shape Canyon to Incident P and SV-Waves

The response of an arbitrary shape canyon subjected to incident P and SV waves will be presented in this section. The same canyon as depicted in Fig. 2.12 will be used. One particular feature of this canyon is that left side of the model is a concave curve and it has no noticaeable effect of the diffraction of SH-waves. But this minor feature has important influence on the diffraction of inplane waves because there are now two wave speeds involved.

It is well known that an incident P-wave could generate a reflected SV-wave in addition to a reflected P-wave (Ewing et al 1957). Also, for a limited range of angles, an incident SV-wave could generate a reflected P-wave in addition to a reflected SV-wave. The detail

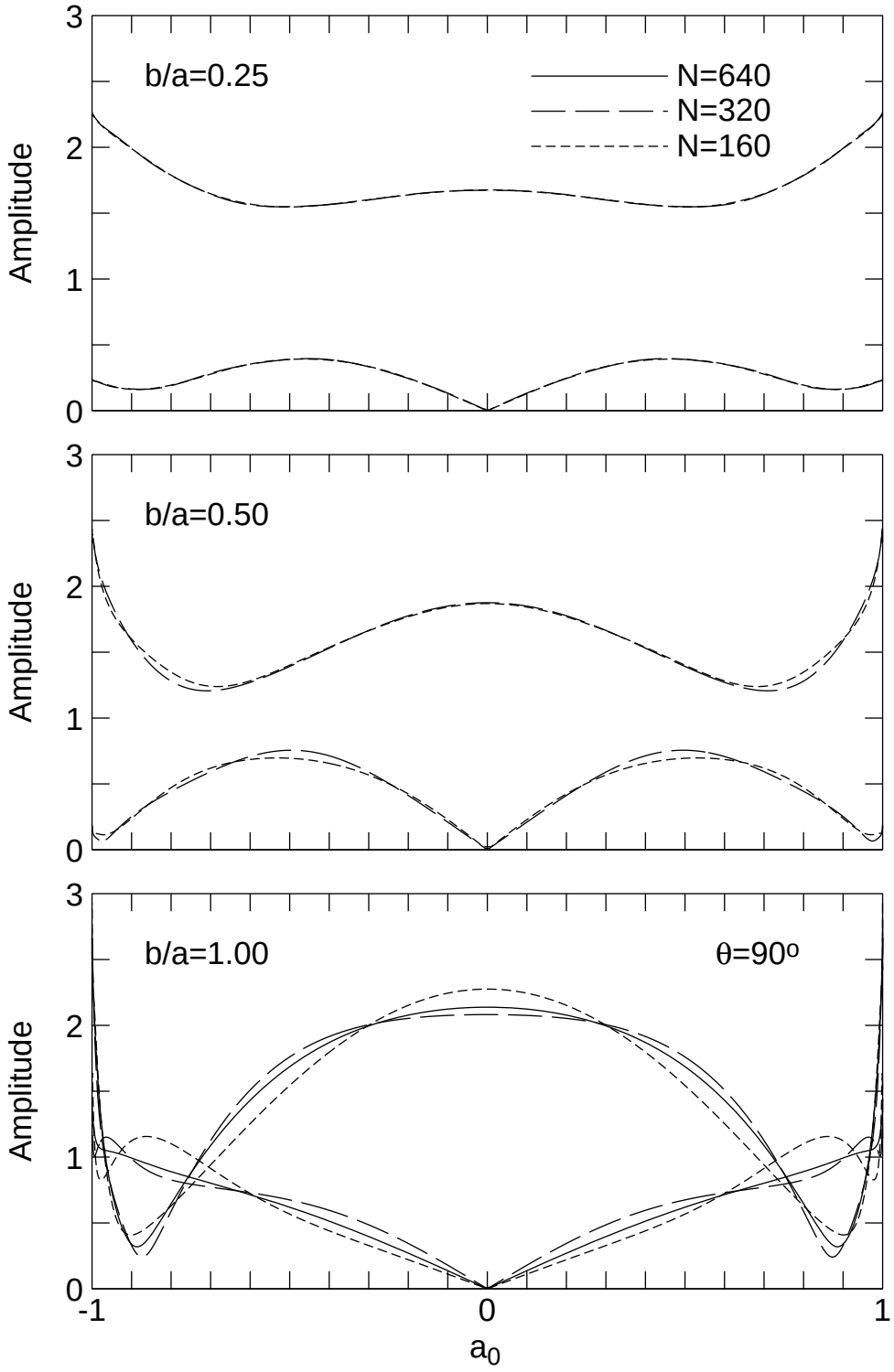

Figure 4.9. Aspect Ratio Comparison. SV-wave Incidence, $\theta = 90°$, $\eta = 1$

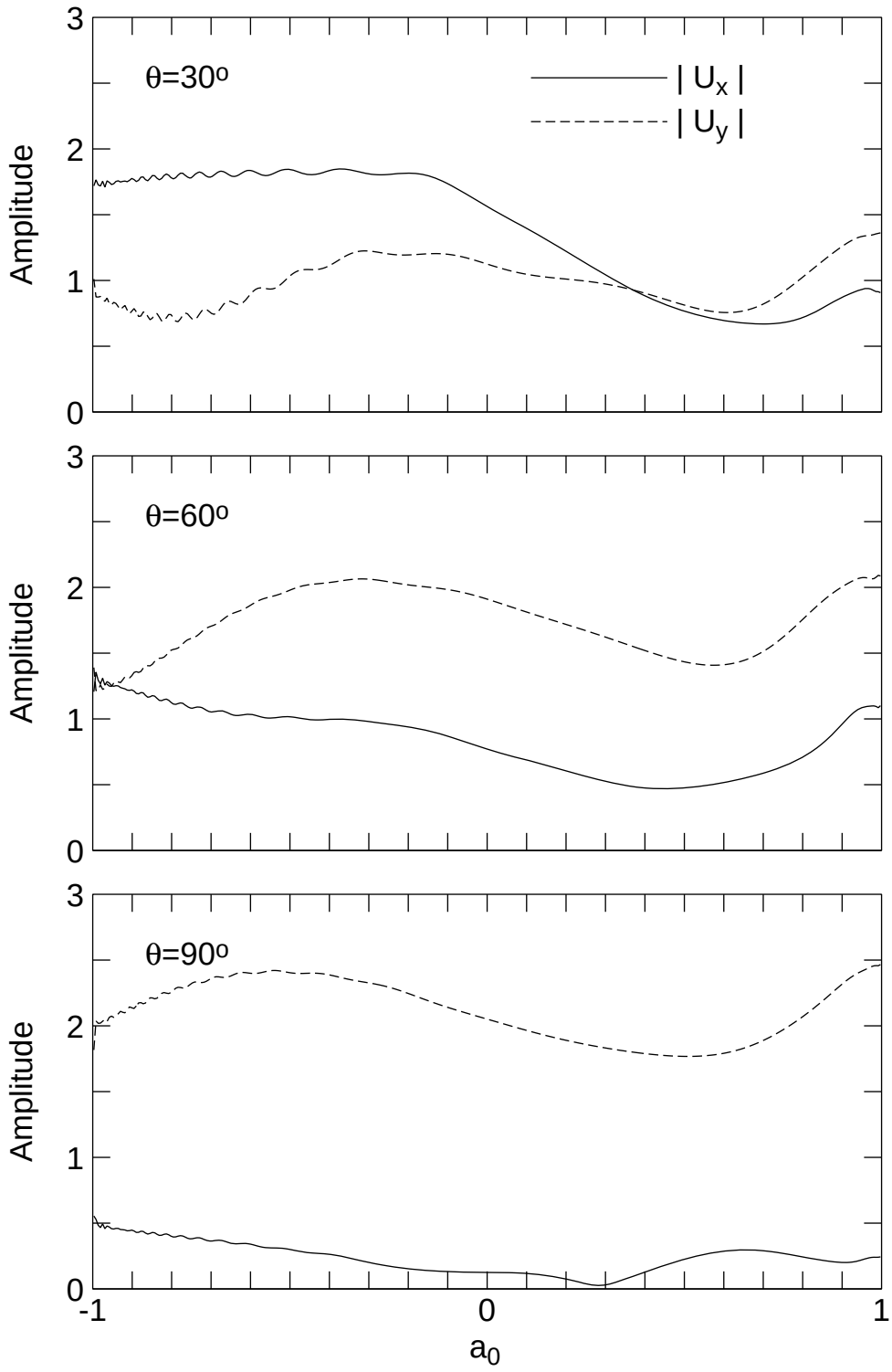

Figure 4.10. P-wave Incidence, $\eta = 1$

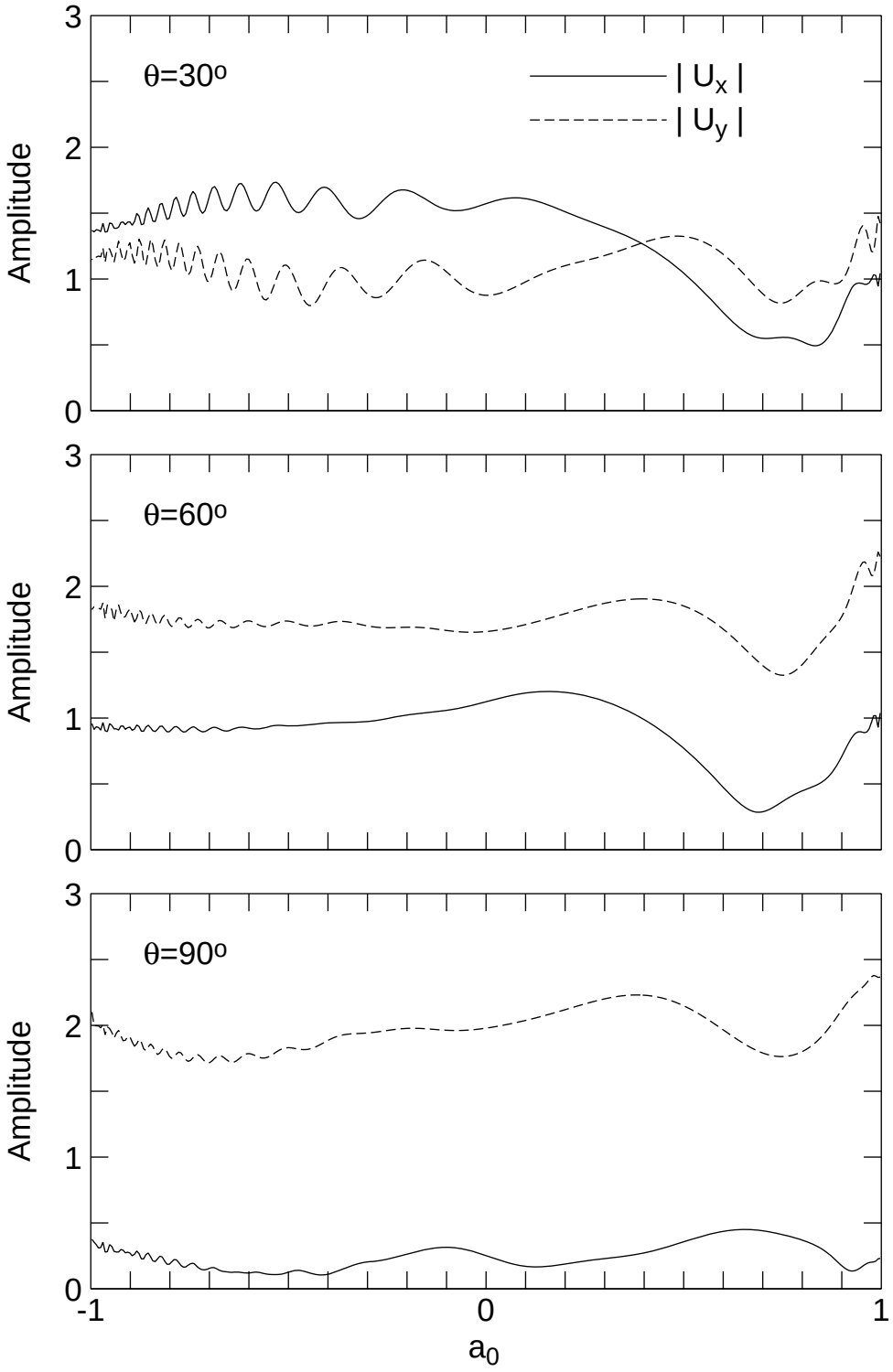

Figure 4.11. P-wave Incidence, $\eta = 2$

derivation of this simplest of boundary value problem, that with a flat surface, is given in Appendix D. As for a concave surface of the arbitrary shaped canyon, the incident body waves, at a certain angle, could impinge upon the curved surface and that the gradual change of slope will cause the reflected waves to interfere with each other. The result is an oscillatory response on the left side of the canyon as the wave type convert from compressional wave to shear wave, or vice versa.

The amplitude of the variation increases as the dimension frequency η is increased from 1 to 2 to 5; the slope of the concave surface is more prominent for waves with shorter wavelengths. The six figures from Fig. 4.10 to Fig. 4.15 include P-wave incidence for three dimensionless frequencies and SV-wave incidence for the same dimensionless frequencies. The number of subregions used for the computation was $N = 320$.

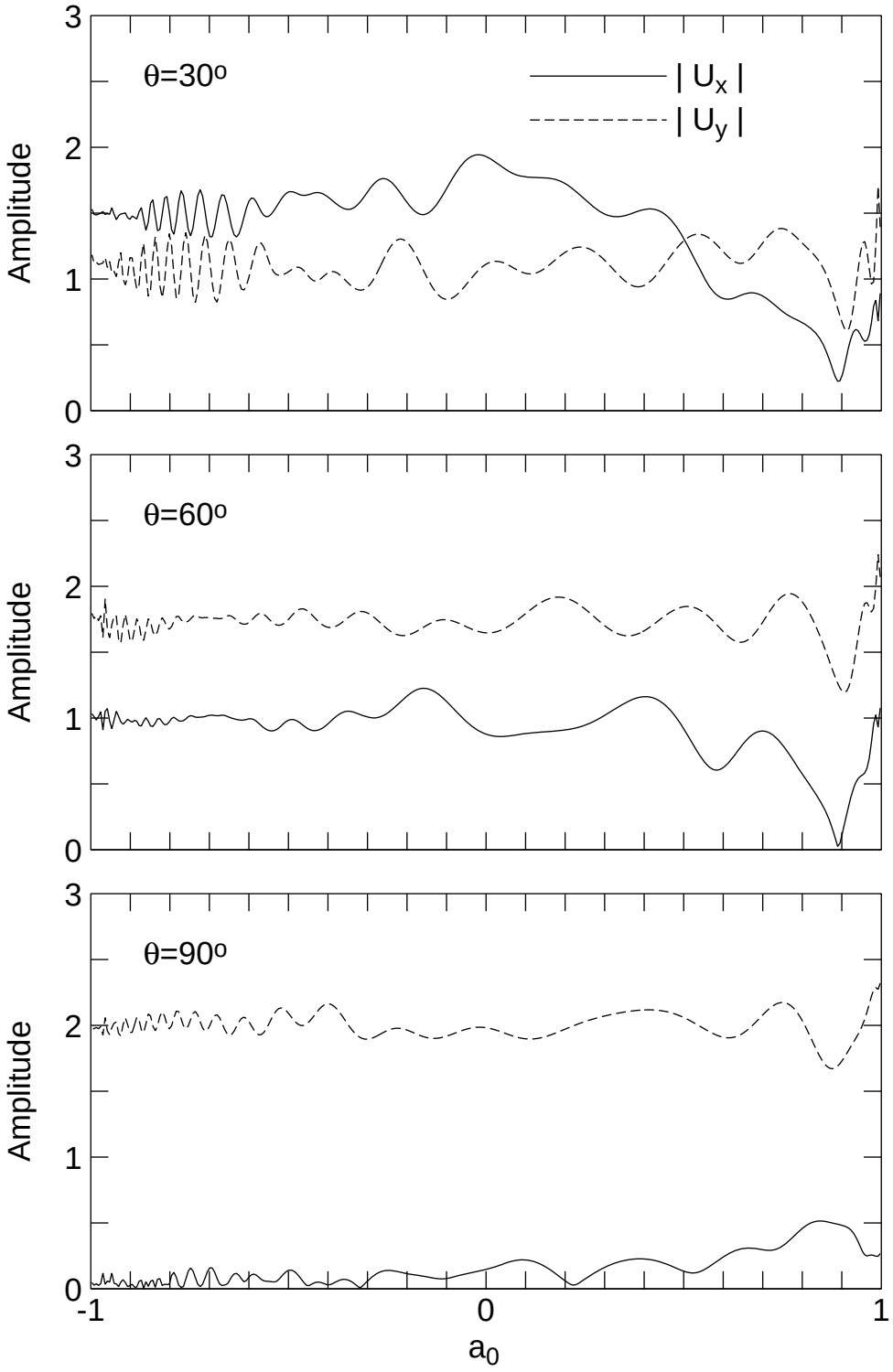

Figure 4.12. P-wave Incidence, $\eta = 5$

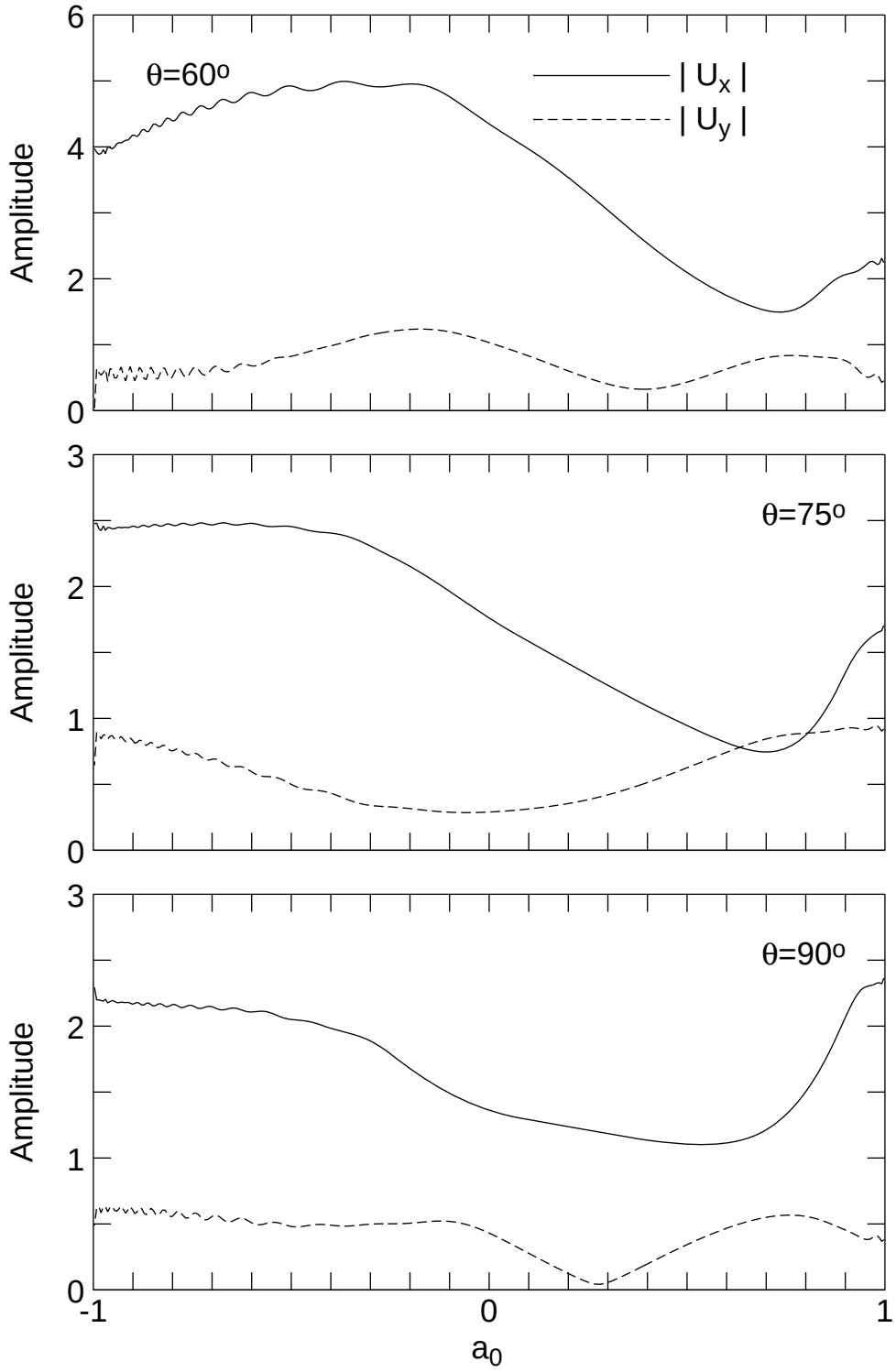

Figure 4.13. SV-wave Incidence, $\eta = 1$

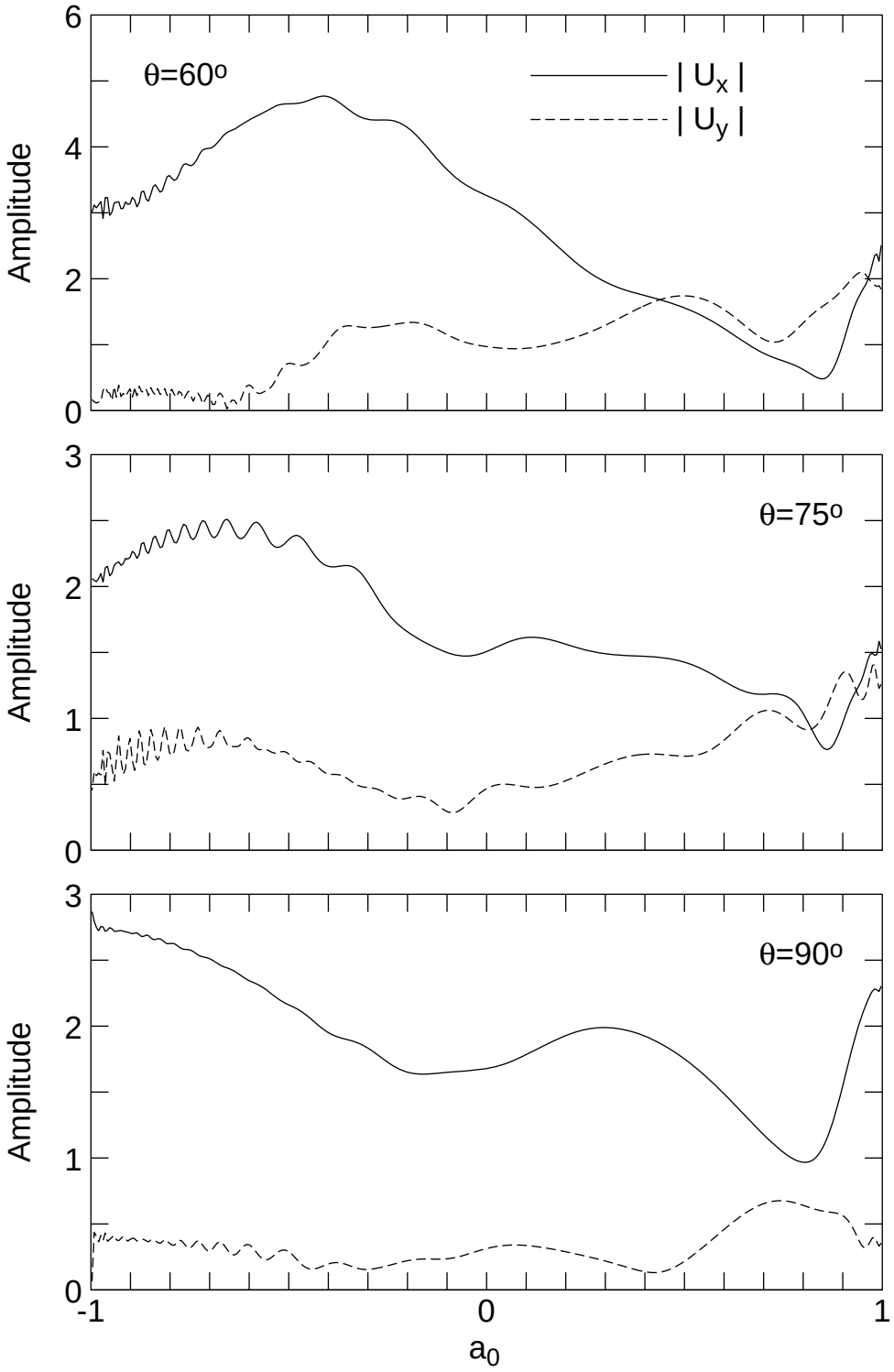

Figure 4.14. SV-wave Incidence, $\eta = 2$

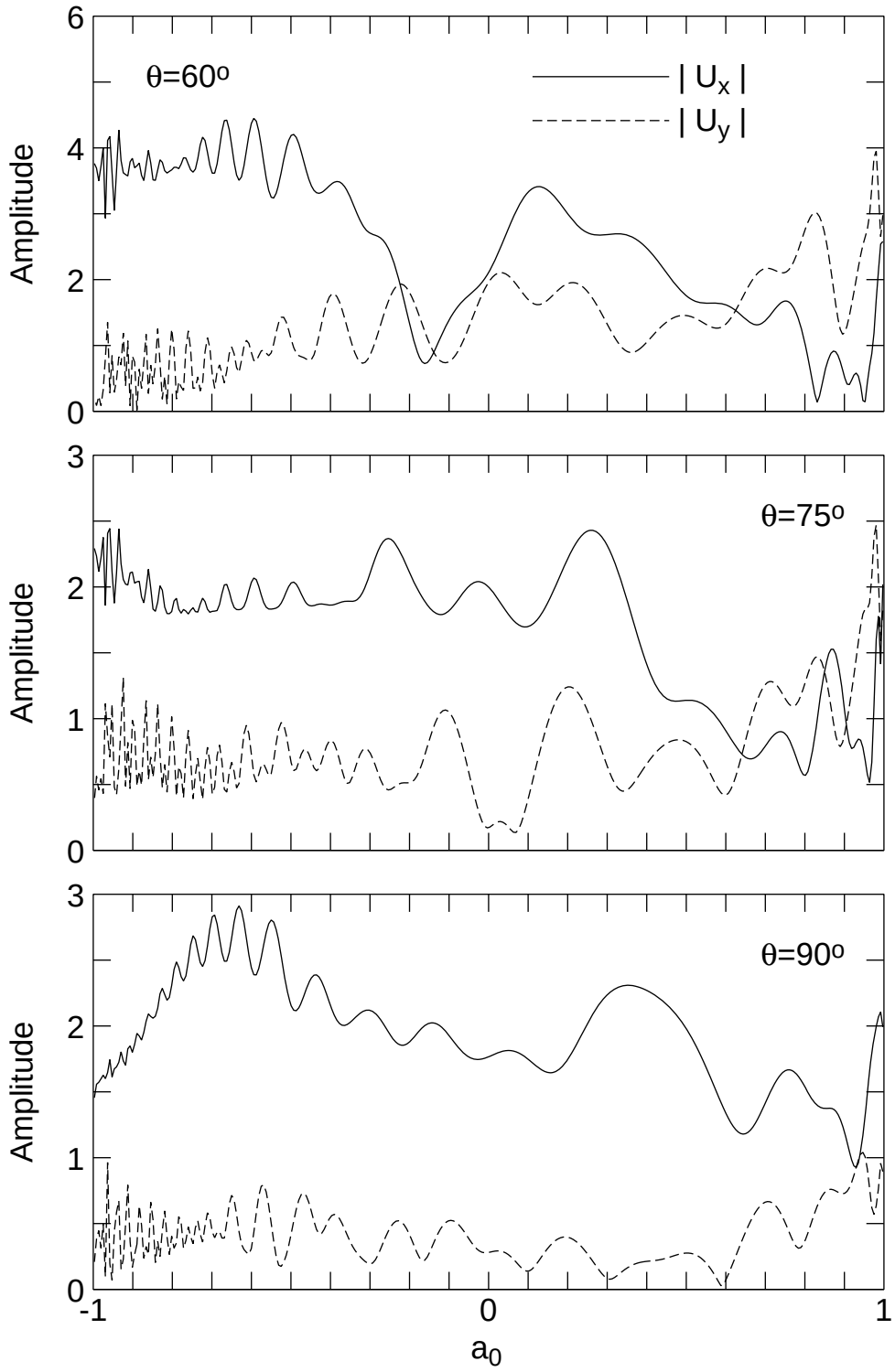

Figure 4.15. SV-wave Incidence, $\eta = 5$

Chapter 5

Site Amplification for Plane Strain Problems

From the development of previous chapters, it is now feasible to analyze an alluvial valley overlying a stiffer bedrock and subjected to inplane body waves. This problem is difficult in nature because of mode conversion between compressional and shear waves. A portion of the reflected waves is also converted into Raleigh surface waves. As much as it is still a two-dimensional problem; there is a lot of physical phenomena that must be understood before a full three-dimensional analysis can be made with strong fundamental knowledge of the elastic wave propagation problem.

There are some results available for comparison, such as Gatmiri et al (2007, 2009), who presented time dependent results for a trapezoidal alluvial valley overlying a stiff bedrock for vertically propagating SV-waves. The results were obtained using finite element for the alluvial layer and a boundary element solution for the bedrock. Since the authors' objective was to recommend changes to the existing code, it would be difficult to compare the results obtained using the substructure deletion method to those presented in the time domain and in the form of response spectra.

5.1 Validation of Results Using Model Refinement

As performed several times previously in this dissertation, one criterion used was to compare the results of models using different levels of refinement by controlling the parameter N, the number of subregions used to represent the soil interface. To do this comparative study, consider an alluvial layer to be added to the carved out half space configuration as shown in Fig. 3.1. the half space model and the alluvial layer model, in this case an ellipse with an aspect ratio of b/a. The two media have different material properties,

the most prominent of which, for boundary condition applications, is the shear modulus, μ. Let μ represents the shear modulus of the bedrock (irregular half space model) and μ_v represents the shear modulus of the alluvial layer. Other material properties involved in the problem includes rho, the mass density and β, the shear wave velocity. For elastic material, the properties are related as $\mu = \rho\beta^2$ and $\mu_v = \rho_v\beta_v^2$. For inplane waves, there is one more parameter of interest, the Poisson's Ratio, ν. This ratio influences the ratio of the shear wave velocity to the compressional wave velocity. For the present study, ν was chosen to be 1/3 for both the bedrock and the alluvium. With $\nu = 1/3$, $\gamma = \beta/\alpha = 1/2$ for both media.

The same approach as that used in the latter part of Section 4.2 will be employed to determine if the results for the response of an alluvial layer is convergent. In Fig. 4.8 and Fig. 4.9, it was shown that the accuracy for the substructure deletion method is best when the aspect ratio is relatively small. Shown in Fig. 5.1 are results obtained using the ratios $\beta/\beta_v = 2$ and $\mu/\mu_v = 6$. The angle, $\theta = 60^\circ$, was arbitrarily chosen. The top figure of Fig. 5.1 shows that the results for the aspect ratio $b/a = 0.25$ using $N = 160$ and $N = 320$ are basically the same and their plots match exactly in the figure. It is difficult to discern which component is vertical or horizontal because of the plot style chosen, but the aim of this figure to show whether the results are convergent, not to analyze the physics of the problem. It is safe to say that less refined models could be used for shallower geometries for the dimensionless frequency $\eta = 1$.

In the center figure, the aspect ratio of $b/a = 0.5$ is presented. The results are also practically the same. The lower plot has the aspect ratio of $b/a = 1$, that of a circular cylindrical shape, the results of the two models have larger deviations. It is supposed that an even finer model could be used, as was done in Fig. 4.8 and Fig. 4.9, but it is clear that the substructure deletion method performs best when the geometry of the scatterer is not deeply embedded.

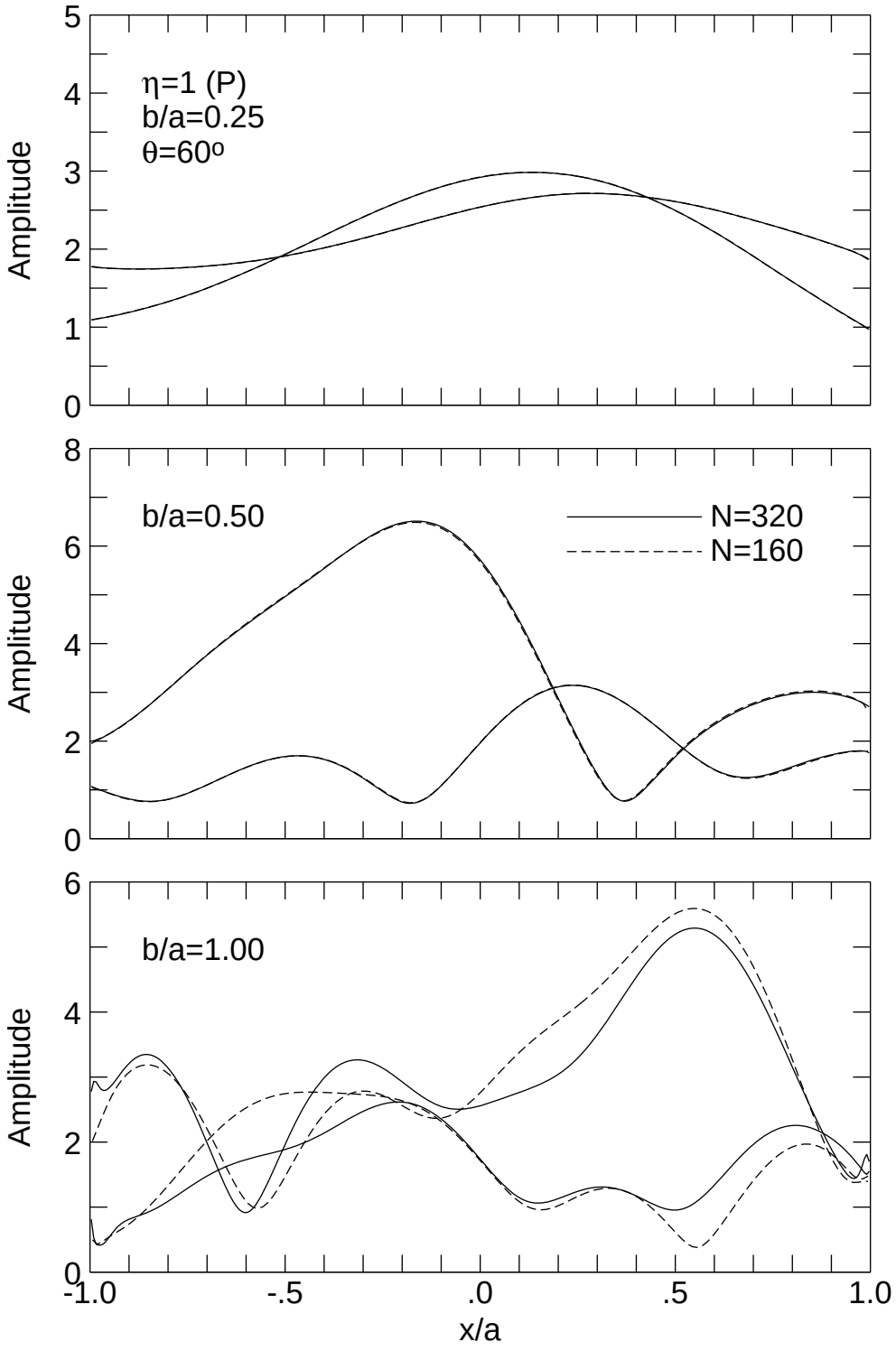

Figure 5.1. Aspect Ratio Comparison. P-wave Incidence, $\theta = 60°$, $\eta = 1$

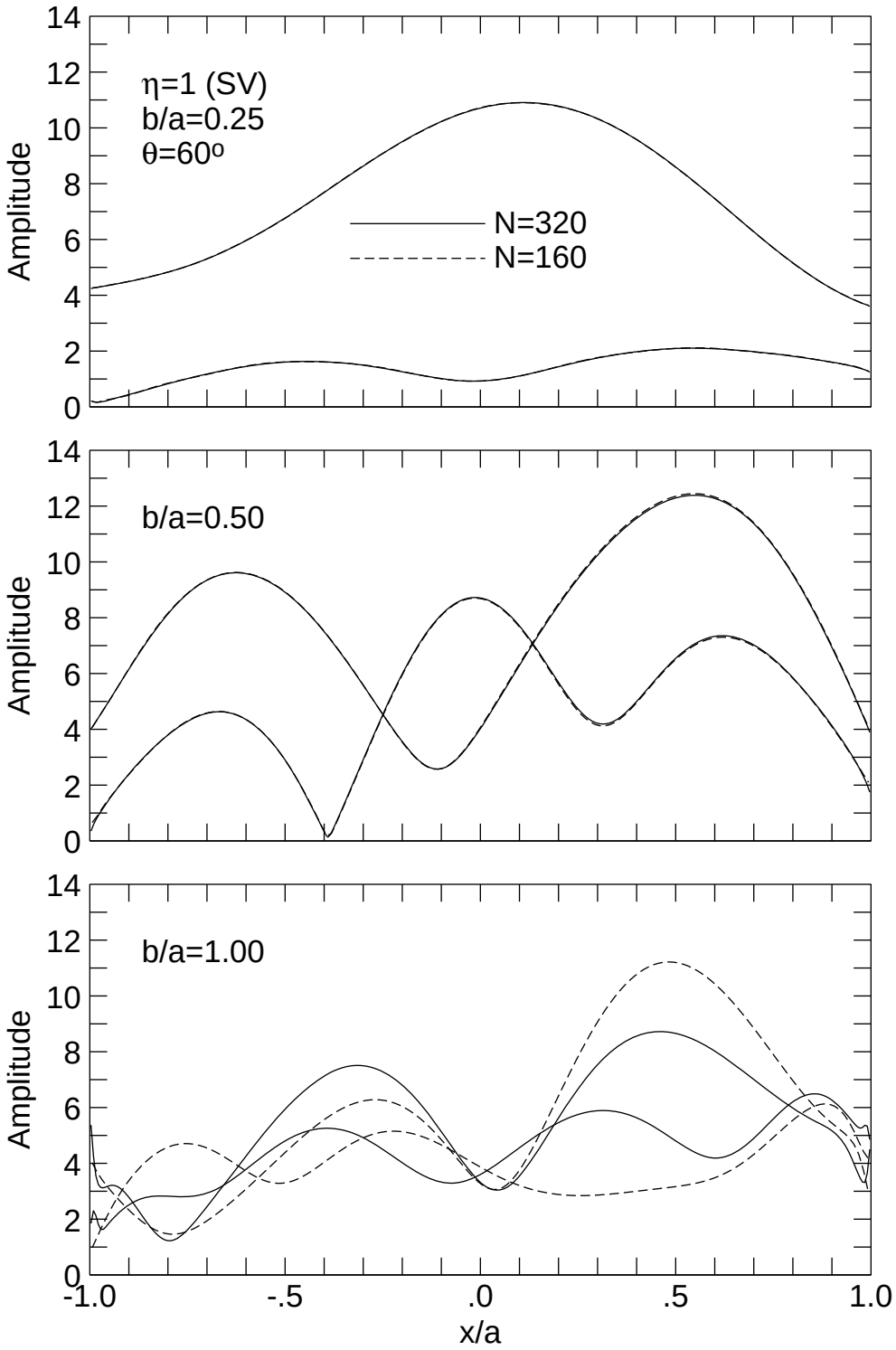

Figure 5.2. Aspect Ratio Comparison. SV-wave Incidence, $\theta = 60°$, $\eta = 1$

Shown in Fig. 5.2 is a similar type of comparison except the incident wave is an SV-wave. The same angle, $\theta = 60^\circ$, was chosen but this angle is a critical angle for the Poisson's Ratio of $1/3$. As shown in a table in Appendix D, the angle θ cannot be less than 60° and still remain a plane wave. The free field amplitude for an SV-wave at 60° is $u_x = 3.4179$ and $u_y = 0$. Therefore the large amplitudes shown in Fig. 5.2 are partly due to the large free-field amplitudes. The same conclusion can be made as that for Fig. 5.1. For the remaining part of Chapter 5, all the models have aspect ratios of the order of 1:4, layer depth versus layer width.

5.2 Response of an Elliptical Alluvial Valley to P and SV-waves

In several models for SH-wave analysis presented by Trifunac (1972), Wong and Trifunac (1974) and Wong (1979), the elliptical canyon or elliptical alluvial valley were used. The main reason for the first two references was that an exact infinite series solution could be obtained using Bessel's Functions and Matthieu Functions. But the third reference, able to handle an arbitrary shape canyon, use the elliptical shape nonetheless because the aspect ratio parameter, b/a, is convenient.

This section will includes some results to complete the series of solutions provided for an elliptical alluvial valley. Shown in Fig. 5.3, 5.4 and 5.5 are the variation of ground amplitudes on top of the elliptical alluvial valley for incident P-waves. The various lines represent the amplitudes for different incident angles of $\theta = 30^\circ$, 60° and 90°. The upper figures show the horizontal displacement amplitudes and the lower figures show the vertical displacement amplitudes. The phases are not shown to simplify the figures, they will be included in the time history calculations in Section 5.4.

Unlike the SH-wave problem, where the free field amplitude is always 2 times the incident amplitude because of the constructive interference between the incident wave and

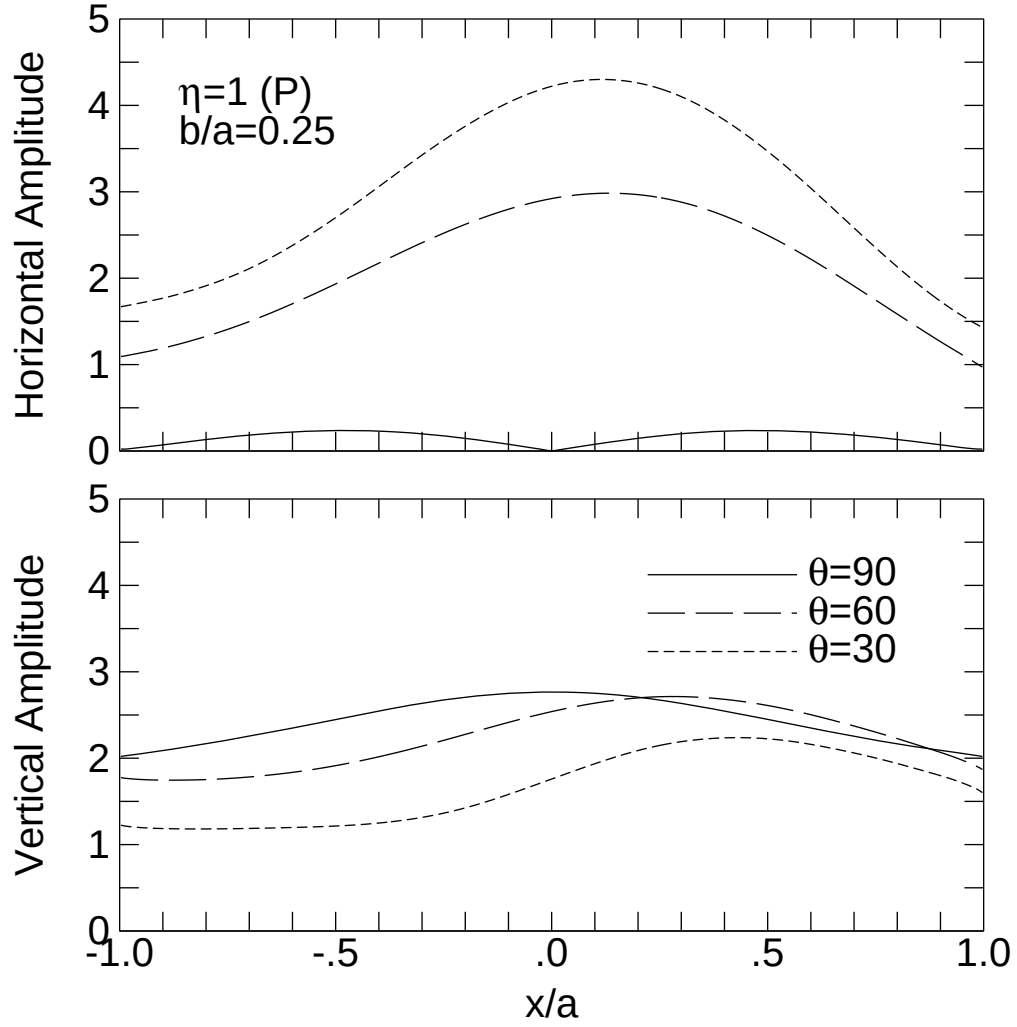

Figure 5.3. Amplitude Variation of Alluvial Valley to Incident P-waves, $\eta = 1$

its reflected wave from a plane boundary. The P-wave incident has a P-wave reflection and a SV-wave reflection (except for $\theta = 90^\circ$) because of mode energy conversion due to the wave speed difference between the two waves. From the table in Appendix D, Section D.2.1, the free field amplitudes for $\theta = 30^\circ$ are $|u_x| = 1.3949$ and $|u_y| = 1.1168$. When $\theta = 60^\circ$, the amplitudes are $|u_x| = 0.9633$ and $|u_y| = 1.7411$. These values are to be used to judge the site amplification factors, the amplification over the free field values. For

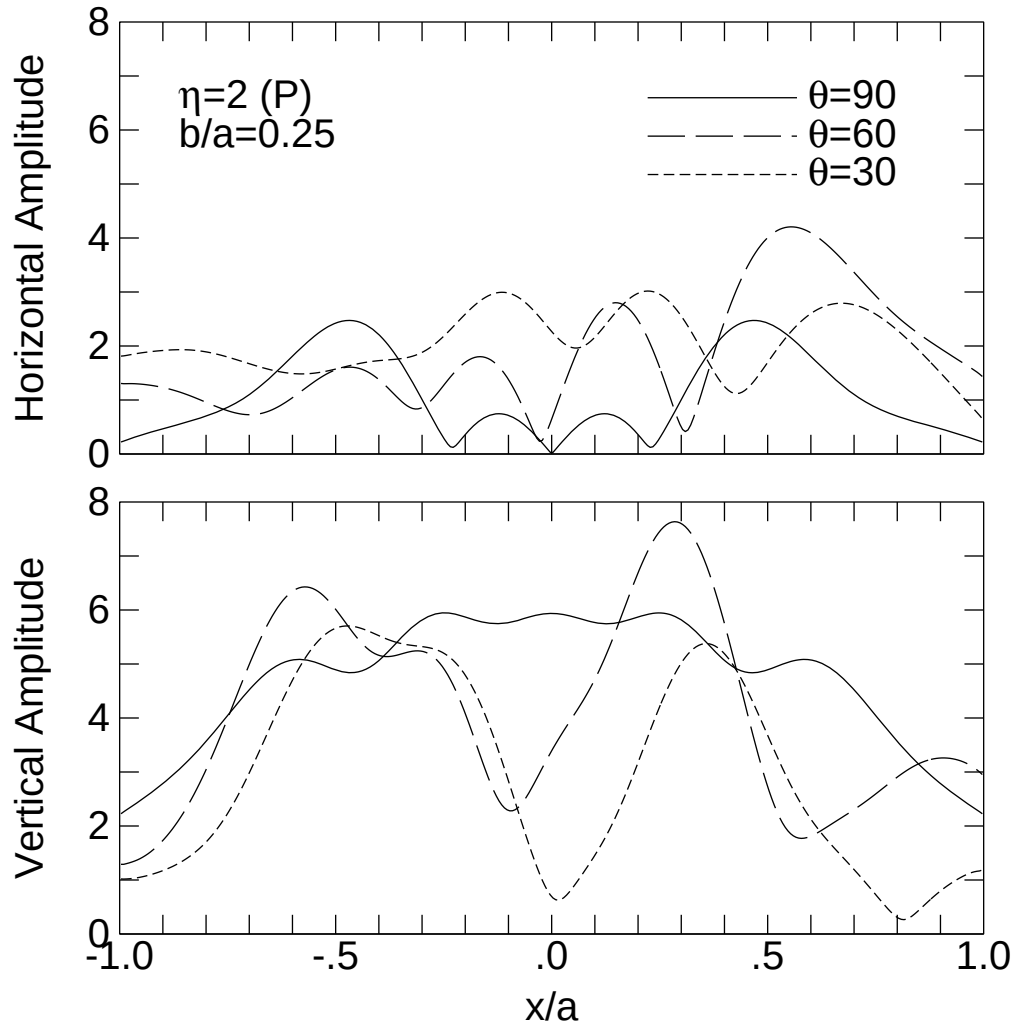

Figure 5.4. Amplitude Variation of Alluvial Valley to Incident P-waves, $\eta = 2$

vertically incident P-wave, the amplitudes are $|u_x| = 0$ and $|u_y| = 2$ because there is no mode conversion for wave incidence normal to the plane half space boundary.

The results for dimensionless frequencies of $\eta = 1$ (Fig. 5.3) and $\eta = 2$ (Fig. 5.4), the variation of amplitudes is quite regular in nature, having smooth response curves. In particular, the case $\theta = 90^\circ$ has symmetrical results for both vertical and horizontal components. There are higher amplitudes along the surface of the alluvial valley depending

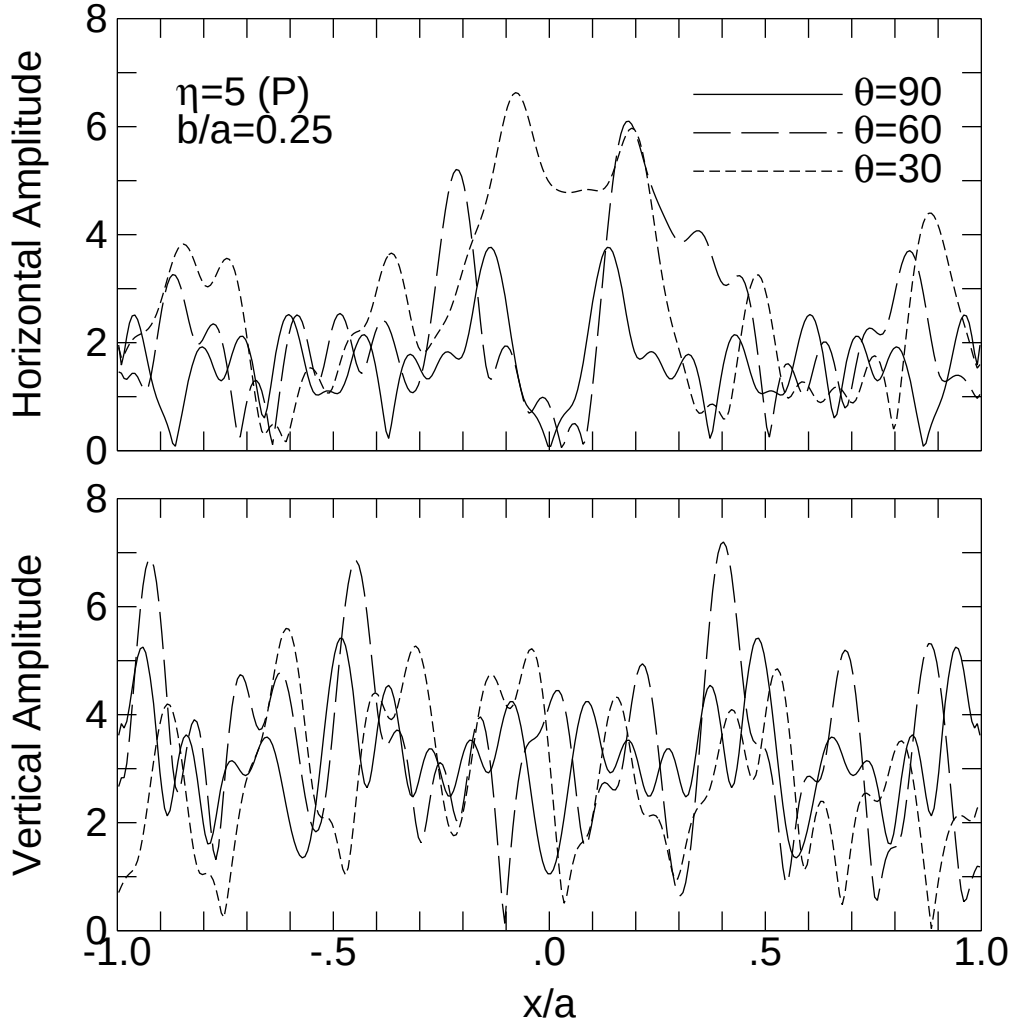

Figure 5.5. Amplitude Variation of Alluvial Valley to Incident P-waves, $\eta = 5$

on the angle of wave incident. They are caused by constructive and destructive interference of diffracted waves. The results for the case where the dimensionless frequency is $\eta = 5$, the variation patterns are too busy to be explained using physical interpretation. In this particular case, there are five wavelengths inside the alluvial valley and many modes inside the alluvial valley are excited. The fact the amplitudes are not even higher during resonance

for an undamped model is that radiation damping exists by wave energy escaping from the valley to the far field.

Beside the complicated variation patterns, there is one interesting fact to observe: there are location on the surface where the amplitudes are near zero. They appear to be quiet zones but the motion is deceptive because they are the locations where the rotational components are the largest. For the case of SH-waves as shown in Chapter Three, the large rotational components signify torsional responses. In the present case, the large rotational components are those of rocking for the vertical component. The low amplitude zone for the horizontal displacement is that of a standing wave oscillating between compression and tension.

The response to incident P-wave was also repeated for SV-waves in Fig. 5.6, Fig. 5.7 and Fig. 5.8 for $\eta = 1$, 2 and 5, respectively. Again, the free field motion amplitude is not a simple 2 as in the SH-wave case, mode conversion causes different amplitudes and angles for the reflected waves. As explained in Ewing et al (1957), the boundary conditions at the plane boundary requires that the apparent velocity at the free surface for both the compressional wave and the shear wave to be the same. That requirement coerce the waves to travel at different angles. For the case of SV-wave incident, the P-wave travels in the horizontal direction when SV-wave is at the critical angle. The critical angle is a function of Poisson's Ratio and in the particular case of $nu = 1/3$, the critical angle is 60°. When the angle is smaller than the critical angle, it would be impossible for the reflected P-wave to have a slow enough phase velocity to match the boundary condition.

From the table in Appendix D, Section D.3.1, the free field amplitudes for $\theta = 60^\circ$ are $|u_x| = 3.4179$ and $|u_y| = 0$. For $\theta = 75^\circ$, the amplitudes are $|u_x| = 1.9438$ and $|u_y| = 0.4970$. These values are to be used to judge the site amplification factors, the amplification over the free field values. For vertically incident SV-wave, the amplitudes are

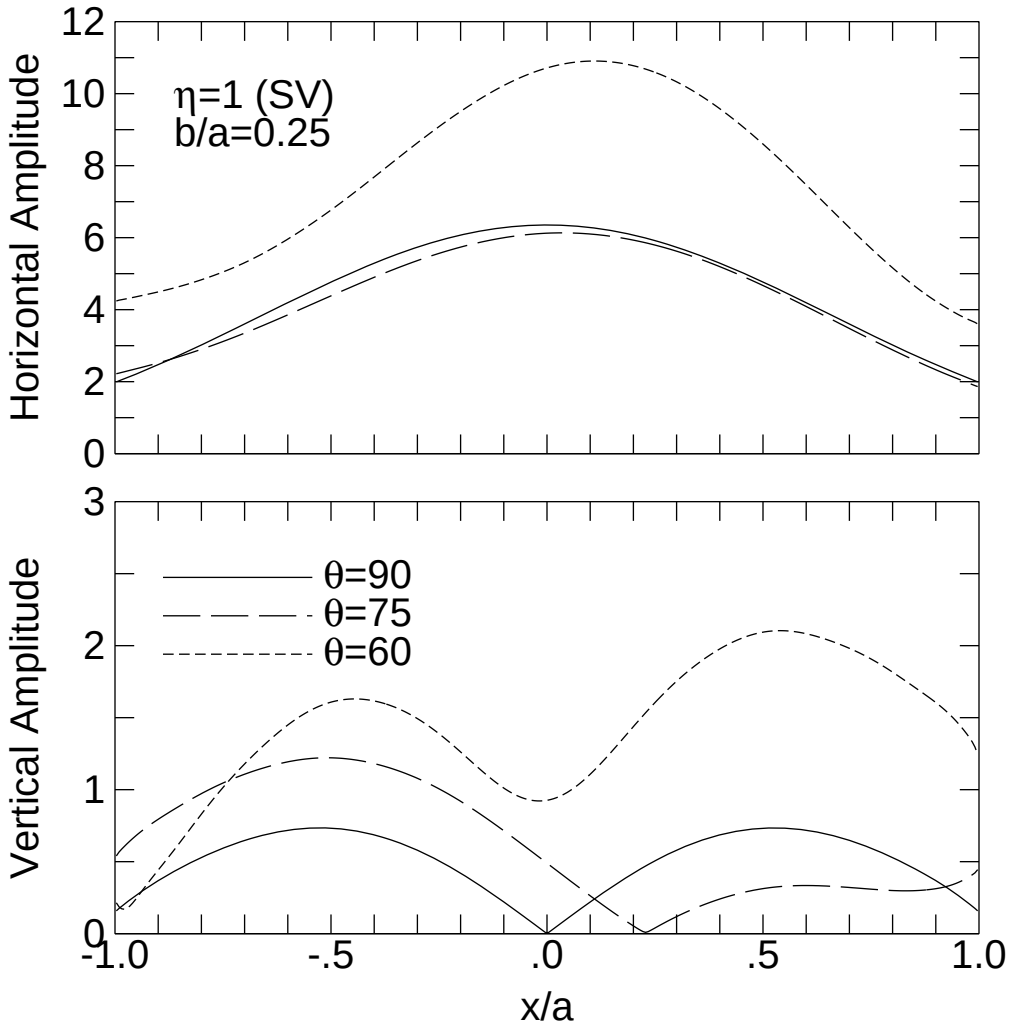

Figure 5.6. Amplitude Variation of Alluvial Valley to Incident SV-waves, $\eta = 1$

$|u_x| = 2$ and $|u_y| = 0$ because there is no mode conversion for wave incidence normal to the plane half space boundary.

As seen from the response curve on the top of the alluvial valley surface, the amplitudes for SV-wave incidence are significantly larger than those from P-wave incidence. Partly the large amplitudes are due to the large free field motion amplitudes, but since the horizontal motion is so large, there is sloshing type of behavior for the soft soil inside the valley,

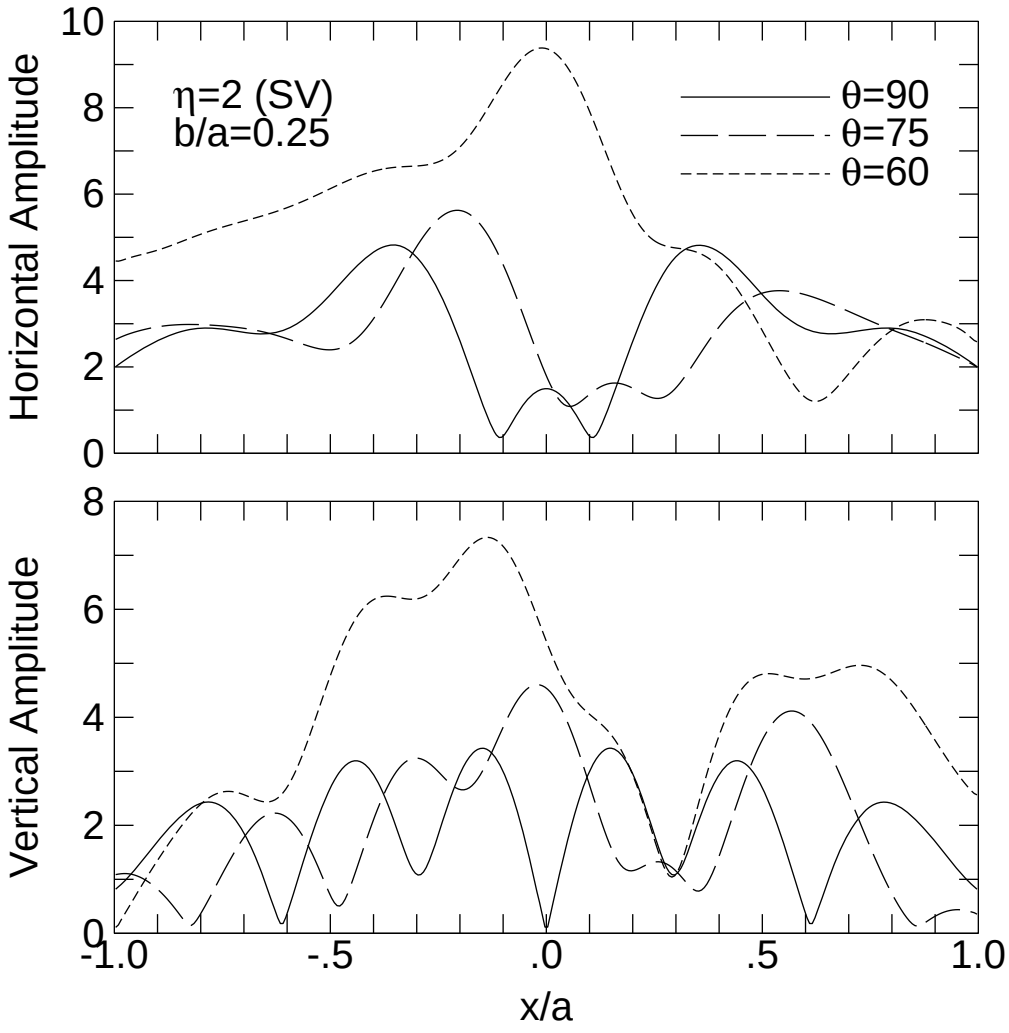

Figure 5.7. Amplitude Variation of Alluvial Valley to Incident SV-waves, $\eta = 2$

reminiscing of the terrible shaking of the Mexico City earthquake. The amplification is not as pronounced for vertical motion caused by a P-wave incidence because the thin layer has a larger stiffness in the vertical direction. One other factor is that the P-wave has a longer wavelength because of a faster wave velocity and the alluvial valley appears to be smaller as compared to the wavelength. For a Poisson's ratio of 1/3, the compressional wave travels at twice the speed of a shear wave.

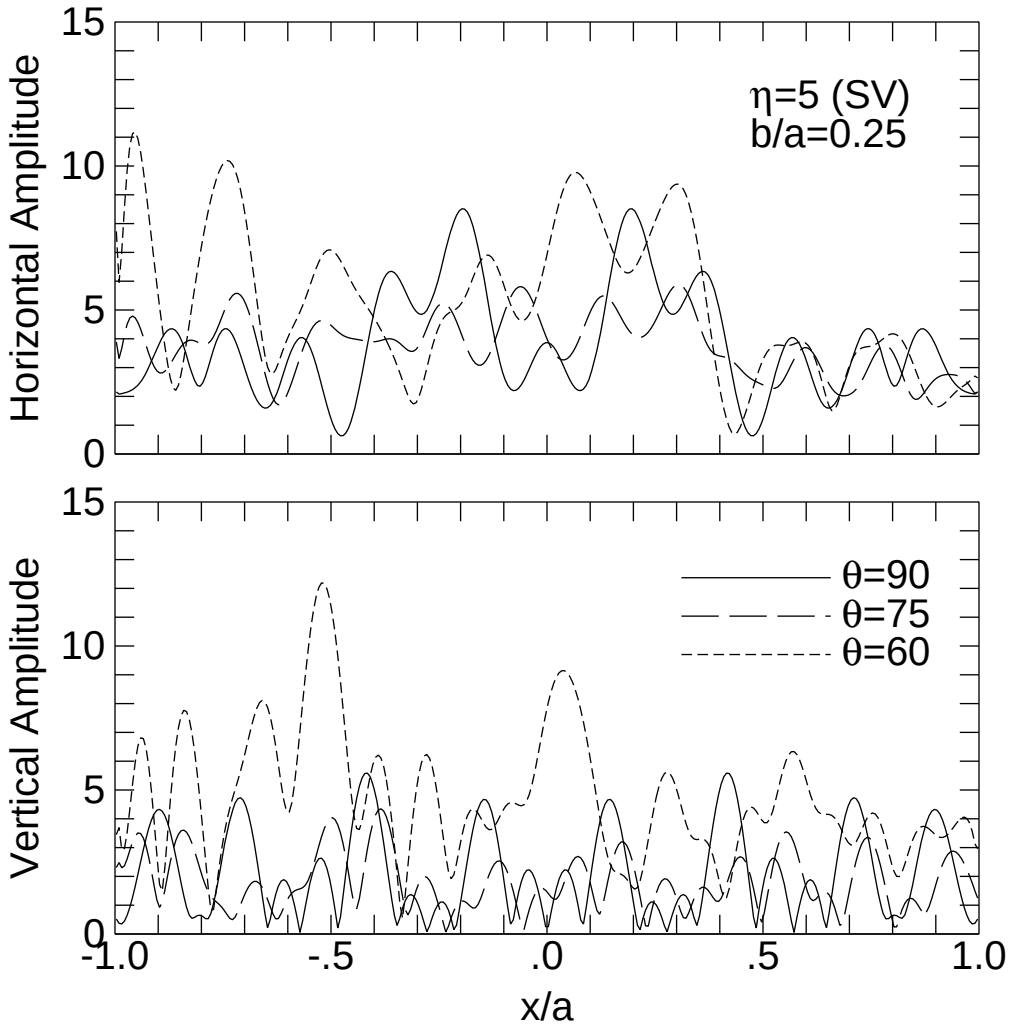

Figure 5.8. Amplitude Variation of Alluvial Valley to Incident SV-waves, $\eta = 5$

5.3 Response of an Arbitrary Shape Alluvial Valley to P and SV-waves

Consider now the response of an arbitrary shaped alluvial valley overlying bedrock. The same model used in Chapter 3 (Fig. 3.6) will be used in this section as well. The interface of the two materials, the bedrock and the alluvium, has a shape similar to the arbitrary shaped canyon in Chapter Two, but shallower. The basic shape of the interface is a superposition of an arc and a small amplitude sine function. The top surface of the alluvium is represented by

another small amplitude sine function. Again, any shape could be used with this numerical method, the x and y coordinates for any two-dimensional geometry could be obtained by a grid generation program.

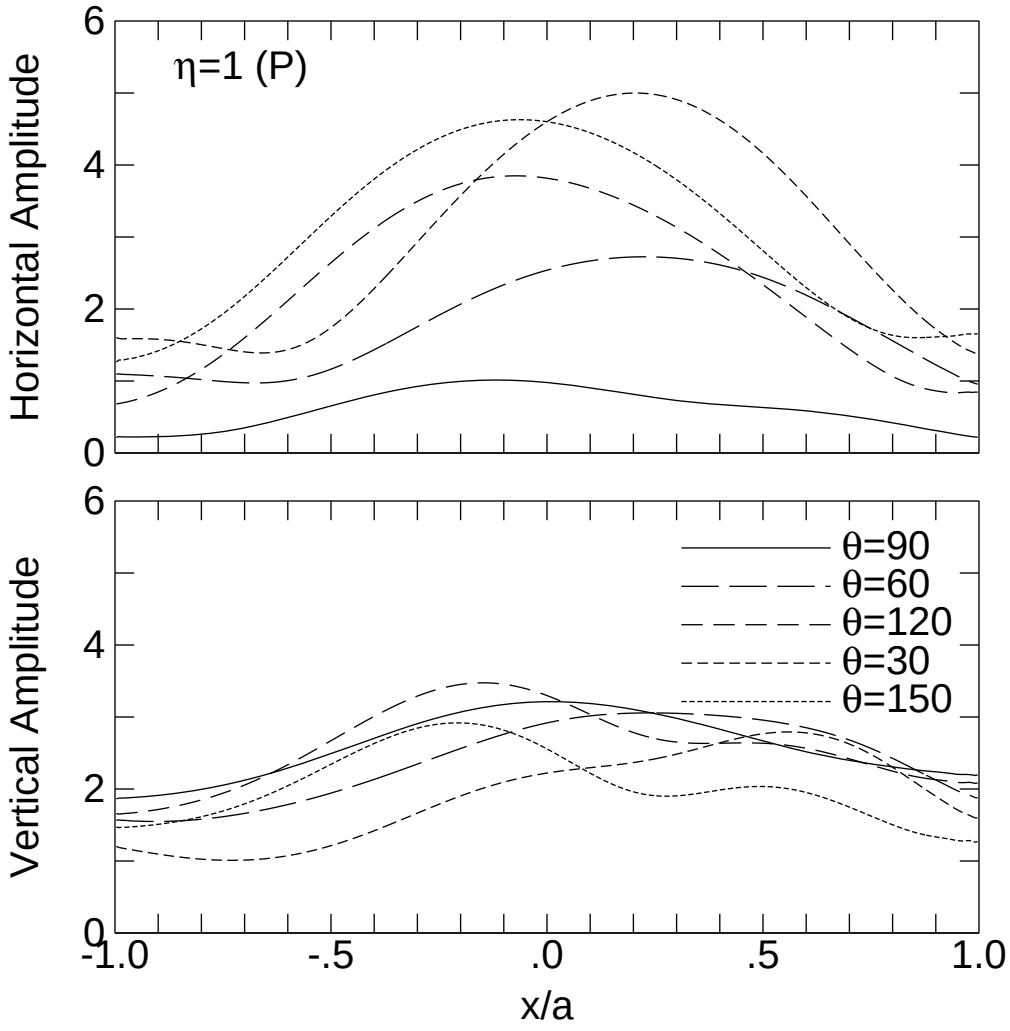

Figure 5.9. Low Frequency Response of Alluvial Valley to P-wave Incidence, $\eta = 1$

Since there are many parameters that could vary, the material properties to be used in the remaining sections of this chapter would be $\mu/\mu_v = 6$, $\rho/\rho_v = 1.5$, $\beta/\beta_v = 0.5$, $\beta/\alpha = 0.5$ and $\beta_v/\alpha_v = 0.5$. With the alluvial valley and also the alluvium-bedrock interface being not symmetric about the y-axis, wave incidence from the left side or the right side of the valley would generate a different response. For that reason, 5 angles are considered for P-wave incidence, $\theta = 30^\circ$, 60°, 90°, 120° and 150°. In Fig. 5.9 and Fig. 5.10. The solid line will identify the response to vertically incident P-wave and different length of dash lines represent the others.

One interesting result to indicate is that the response to a vertically incident P-wave is no longer symmetrical about the y-axis because the alluvial valley itself has a nonsymmetrical shape. That was one of the limitations of the elliptical alluvial valley model, that it is symmetric about the y-axis. The response to a medium dimensionless frequency of $\eta = 2$ is significantly higher than that of the lower dimensionless frequency $\eta = 1$. It will be noted in the next section, and was also noted back in Chapter Three, that there is a certain limit to the site amplification factor, it would not become unrealistically high because of radiation damping in the semi-infinite medium.

Shown in Fig. 5.11 and Fig. 5.12 are the response curves at the alluvial valley's surface subjected to SV-wave incidence. Five angles are considered for SV-wave incidence, $\theta = 60^\circ$, 75°, 90°, 105° and 120°. In these figures, the solid line will identify the response to vertically incident SV-wave and different length of dash lines represent the others. As explained in the previous section, SV-wave incidence has a larger amplitude from the free field motion itself, therefore, the response is in general higher.

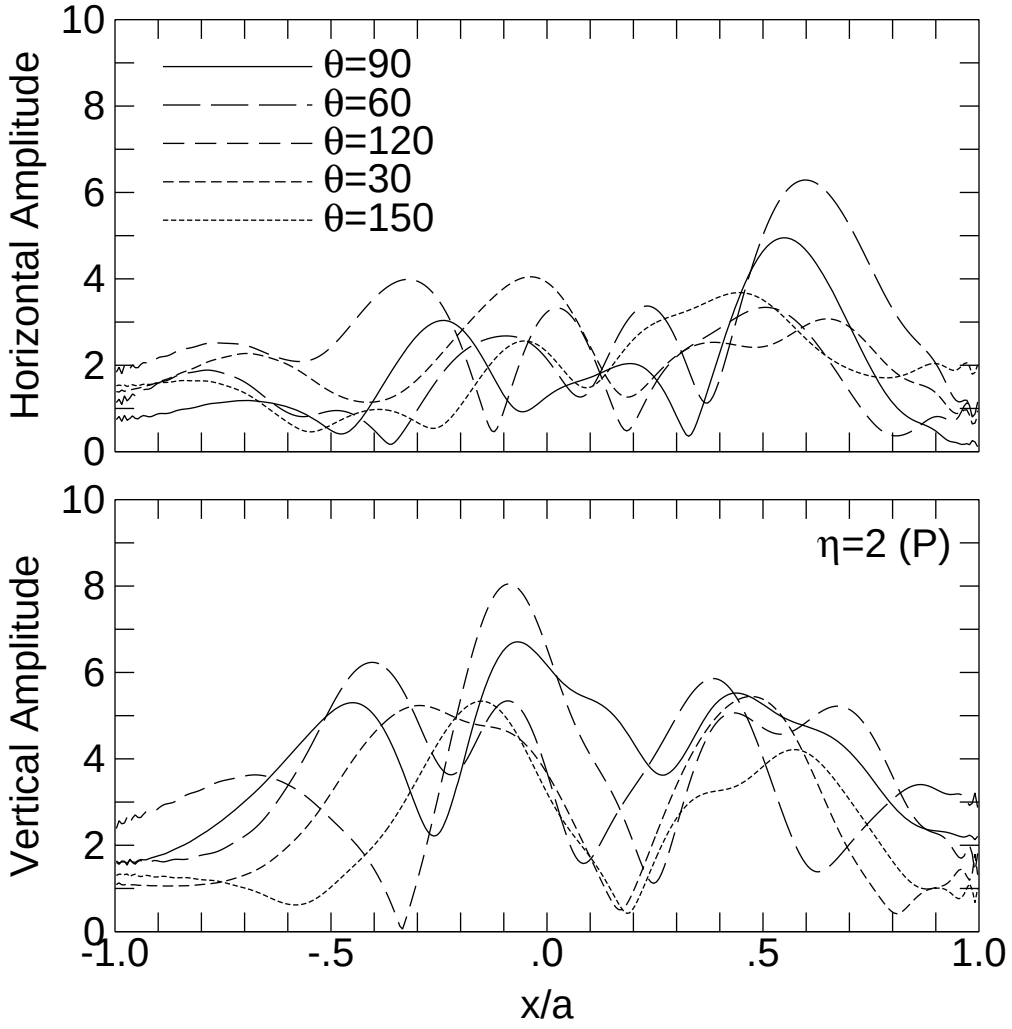

Figure 5.10. Medium Frequency Response of Alluvial Valley to P-wave Incidence, $\eta = 2$

5.4 Time History Calculation for Alluvial Valley Surface

The concept of Fourier Transform was explained in Section 3.5 and the method applies in this section as well. The input Ricker Wavelet is the same but it represents the strength of the unit pulse, P or SV, arriving at the site. The maximum value of the response at the site is then the site amplification factor for that particular location. Transfer Functions are

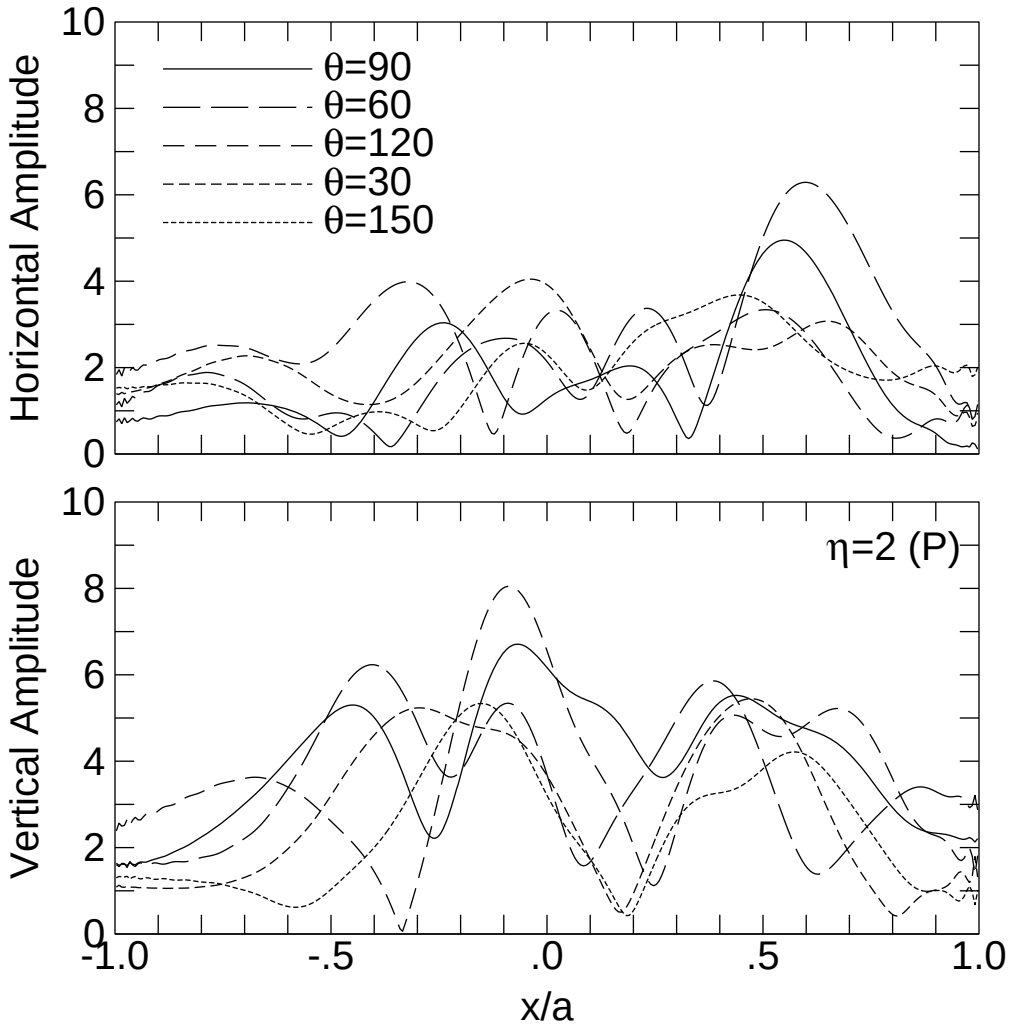

Figure 5.11. Low Frequency Response of Alluvial Valley to SV-wave Incidence, $\eta = 1$

calculated for many parameters and stored in files ready to be used. There are simply too many interesting cases to show, therefore, only a few selected cases will be presented.

Shown in Fig. 5.13 are the transfer functions for Station 4 (fig. 3.6). The top figure includes the real and the imaginary parts of the u_x component of motion. Both the real and the imaginary parts are needed for the Fourier Transformation because the phases are important for superposition purposes. The second part of the figure is the amplitude of the

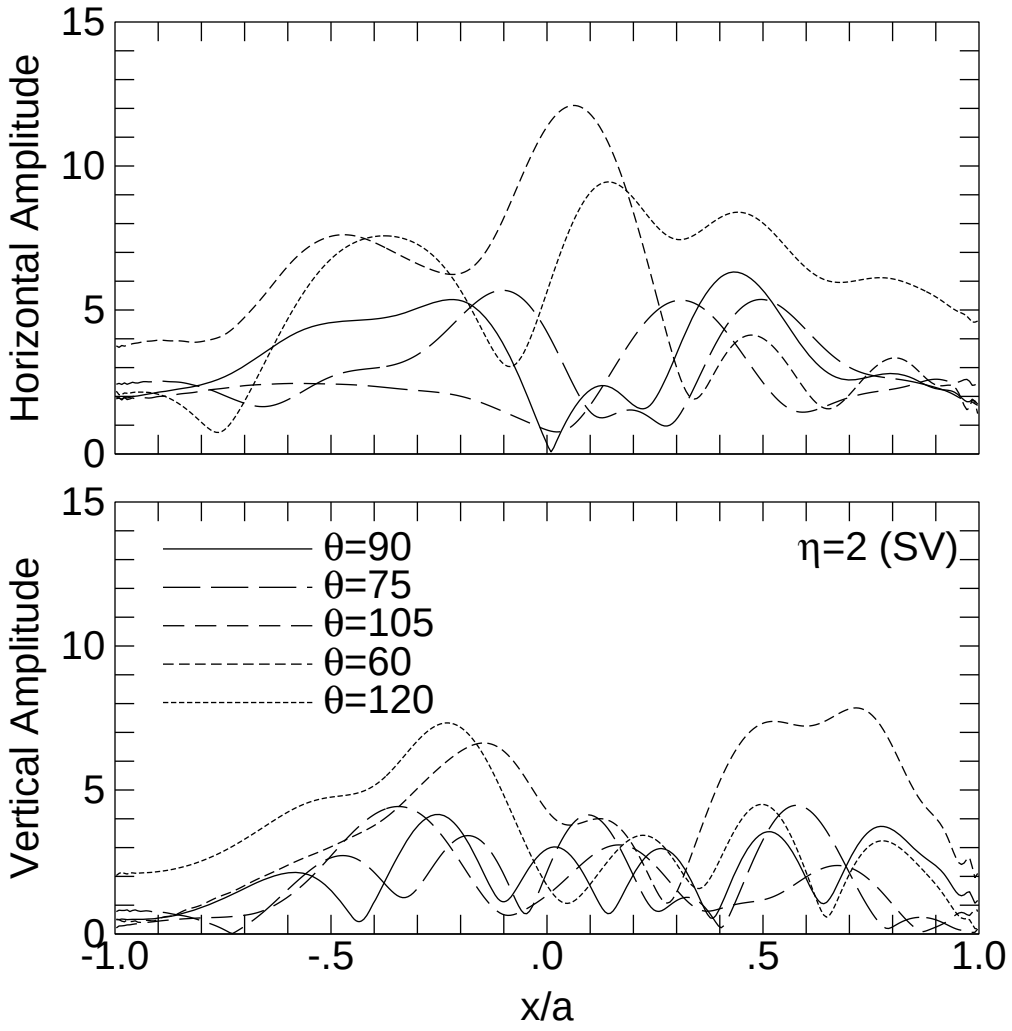

Figure 5.12. Medium Frequency Response of Alluvial Valley to SV-wave Incidence, $\eta = 2$

complex u_x function. The maximum value of the transfer function amplitude is about 12 but that does not mean the time history will have a maximum of 12 because the phases could invoke subtraction as well. This is interesting that the amplitude of the transfer function has a limit, depending on the material contrast of the two soil media. Although the theory for an undamped medium, the radiation damping resulted from outgoing waves prevents the amplitude to be out of control.

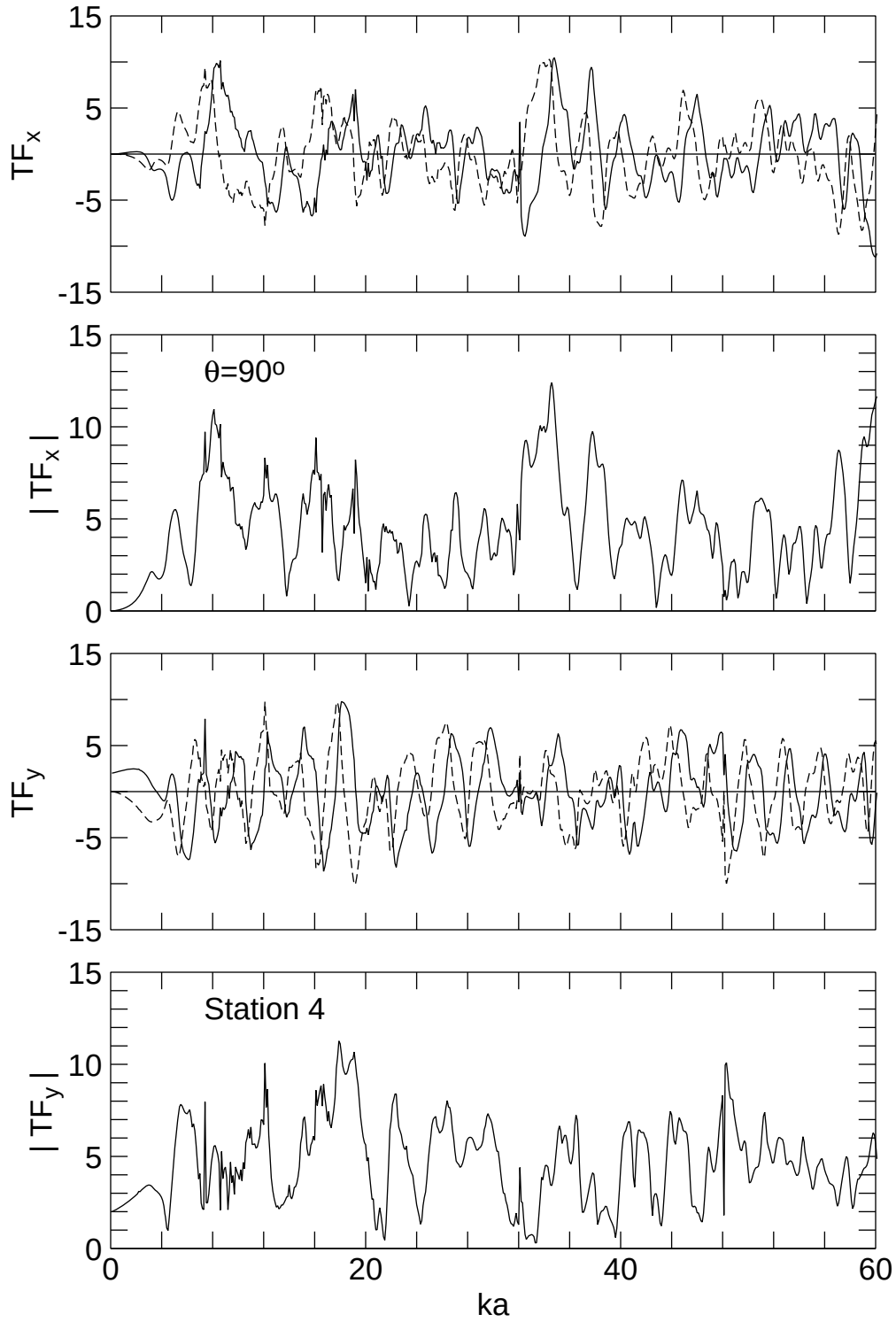

Figure 5.13. Transfer Functions for u_x and u_y at Station 4

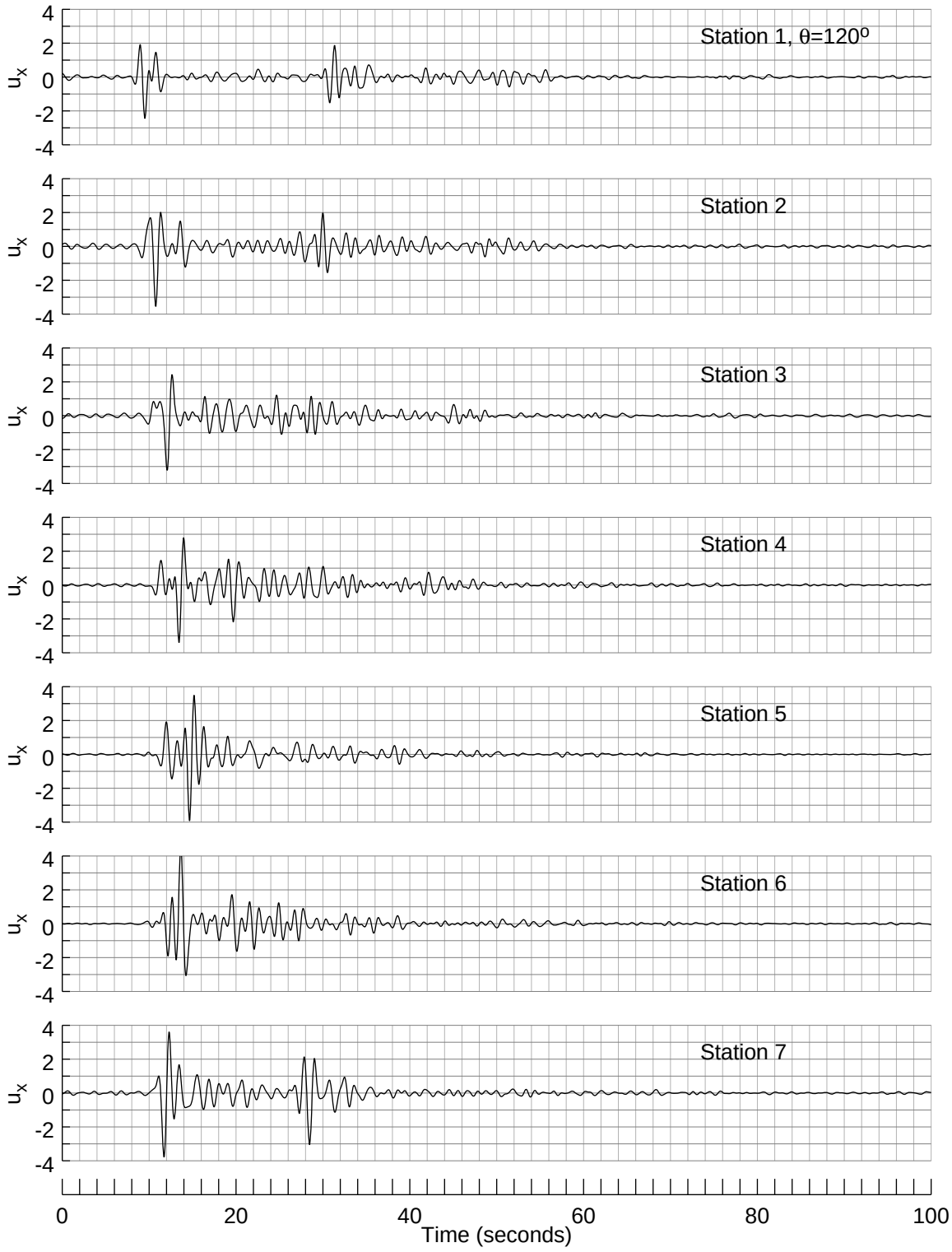

Figure 5.14. Transfer Functions for u_x and u_y at Station 4

In the third subfigure of Fig. 5.13 is the transfer function for the vertical component u_y. For a wave propagation problem with an irregular shaped alluvial valley, it is expected all components will be excited. The ratio of the amplitudes can be different for various incidence angles. Since over 90% of the computation effort comes from the formation of the embedded matrix $[G_{22}^E]$, computation for a large array of incident waves is a relatively small effort. It is recommended that a probabilistic model could be used to estimate the site amplification factors, including all effects such as variation of material properties, characteristics of wave types and directions of wave arrival.

Shown in Fig. 5.14 and Fig. 5.15 are the time histories for the horizontal u_x component and the vertical u_y component, respectively. The response functions were calculated for a P-wave incidence with angle $\theta = 120^\circ$, i.e., the wave arriving from the right side of the alluvial valley. Because of the mode conversion effects, the wave forms appear to be more complicated than those observed for SH-waves in Chapter 3. It is anticipated that a three-dimensional model would generate even more complicated time histories as reflected waves would arrive from all directions. The time history response functions were generated by one simple pulse, that of the Ricker Wavelet, but it managed to create a response with significant duration. Clearly, site amplification effect would cause the duration of the seismic event to be significantly longer.

The time history responses to a SV-wave incident at the angle of $\theta = 75^\circ$ are shown in Fig 5.16 for the horizontal component u_x and in Fig. 5.17 for the vertical component u_y. The nature of the incident wave has an influence on the generated waveform and it is anticipated that for a typical seismic event, many different types of waves would arrive at the site of interest, including many surface waves. This dissertation fails to analyze the effects of Love Waves because the bedrock was modeled as a homogeneous half space. Future work could extend to include layers and the modeling would be more sophisticated. But the

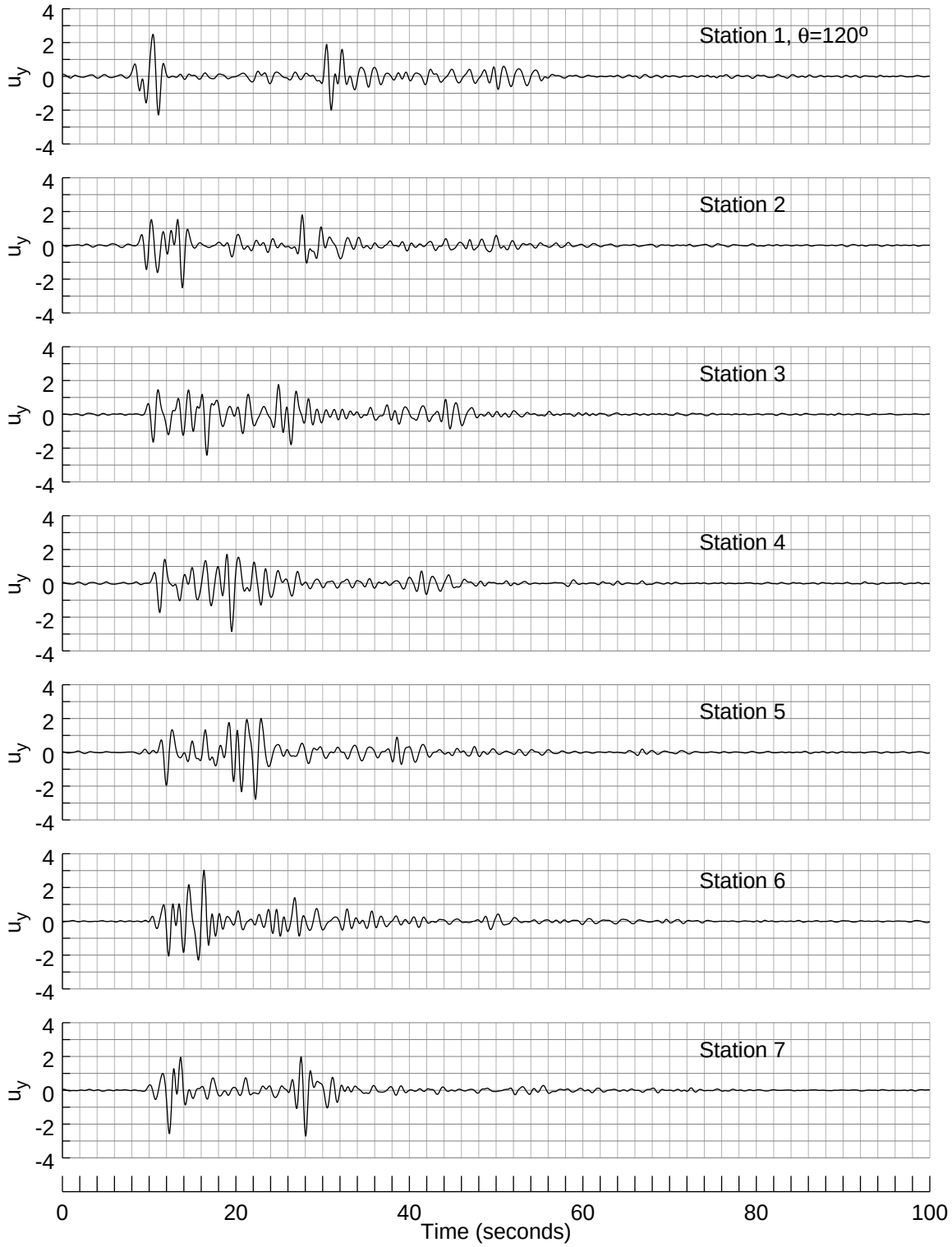

Figure 5.15. Vertical Response to P-wave Incidence, $\theta = 120°$

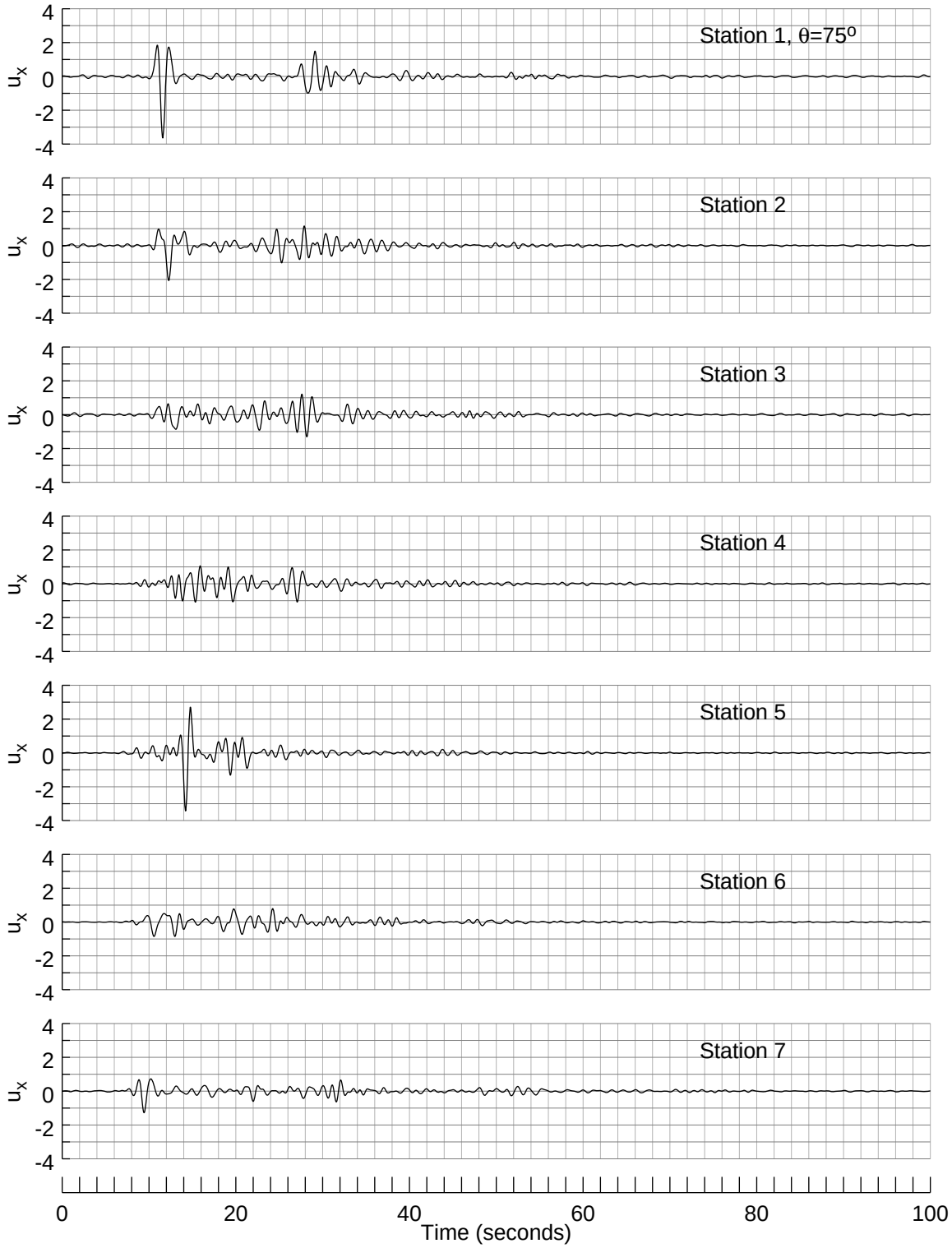

Figure 5.16. Horizontal Response to SV-wave Incidence, $\theta = 75°$

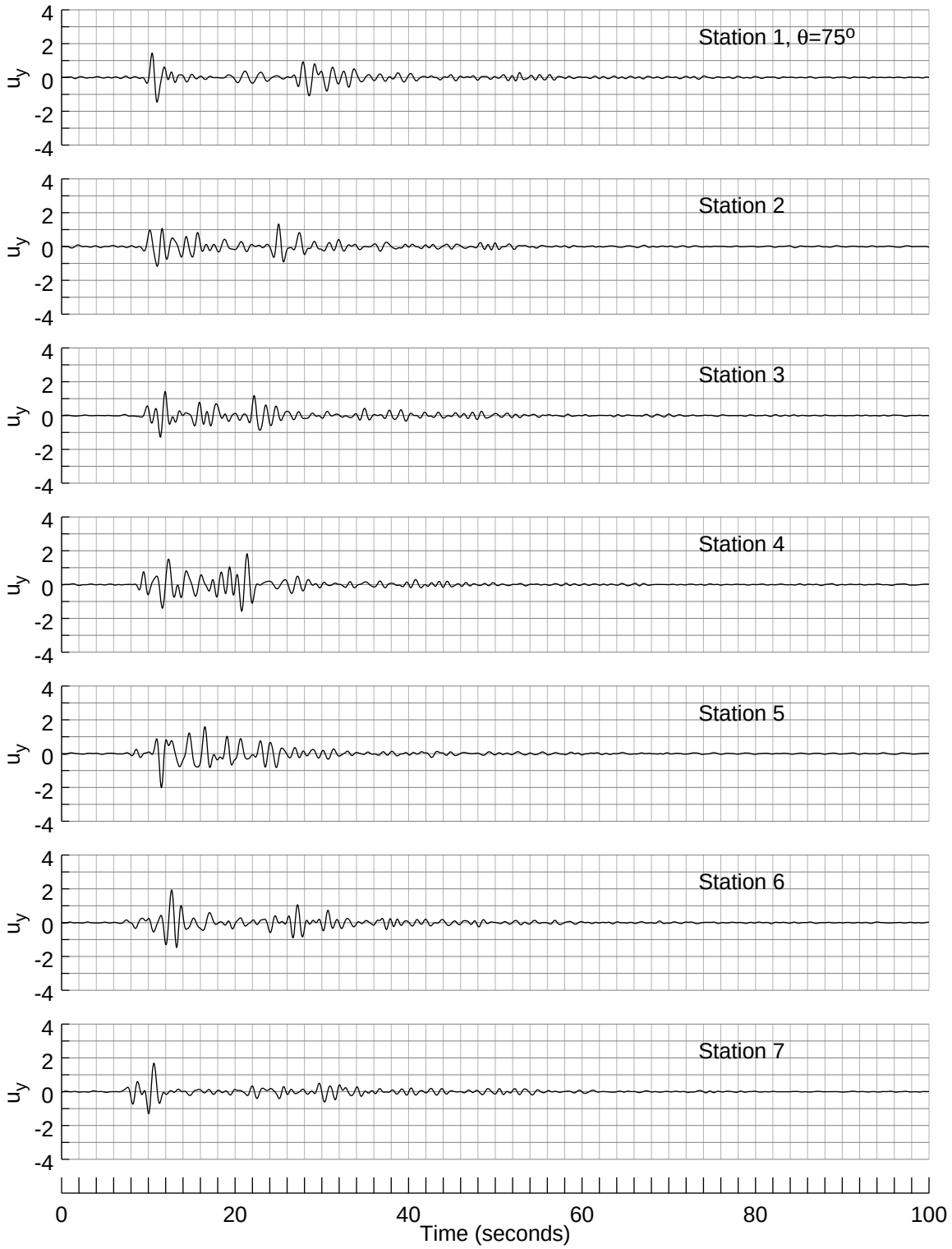

Figure 5.17. Vertical Response to SV-wave Incidence, $\theta = 75^{\circ}$

substructure deletion method opens up a new avenue for the development of tools to handle the three-dimensional problem, especially those with shallow aspect ratios.

There is one other interesting wave to examine for inplane problems, that of the Rayleigh Wave at the surface of a half space. Truly no such wave exists in nature because there is no homogeneous half space on this planet. But academically there is such a wave and it propagates at a speed slower than the shear wave speed. In Lamb's solution, i.e., the half space Green's Function used in the present application, there is a Rayleigh Pole in each function. That indicates that the Rayleigh Wave would be excited by wave scattering around the canyons and alluvial valleys studied.

In Appendix D, Section D.5, a table is shown for the Rayleigh Wave speed as a function of Poisson's Ratio, $\bar{\nu}$. When the Poisson's Ratio is 1/3, the Rayleigh Wave speed is 0.932526β. There is also a ratio of vertical amplitude to horizontal amplitude of 1.565199. The two components of displacement are out of phase by 90°, creating a retrograde or rolling type of motion.

Shown in Fig. 5.18 are some time histories related to Rayleigh Wave incidence. The top two figures are the horizontal and vertical displacements of the incident pulse. The vertical component is a factor of 1.565199 higher; it is also out of phase with the horizontal component. When one component reaches zero, the other reaches the maximum, and vice versa. The third and the fourth figures in Fig. 5.18 show the horizontal and vertical response at station 1, near the edge of the alluvial valley. It appears even at station 1 the characteristics of the Rayleigh Wave were lost. The horizontal component is now larger than the vertical component and the phase difference of 90° is no longer discernable.

As shown in Eq. (D.92) and Eq. (D.93), the free field displacements of a Rayleigh Wave attenuate exponentially with respect to depth. The rate of attenuation is especially high for

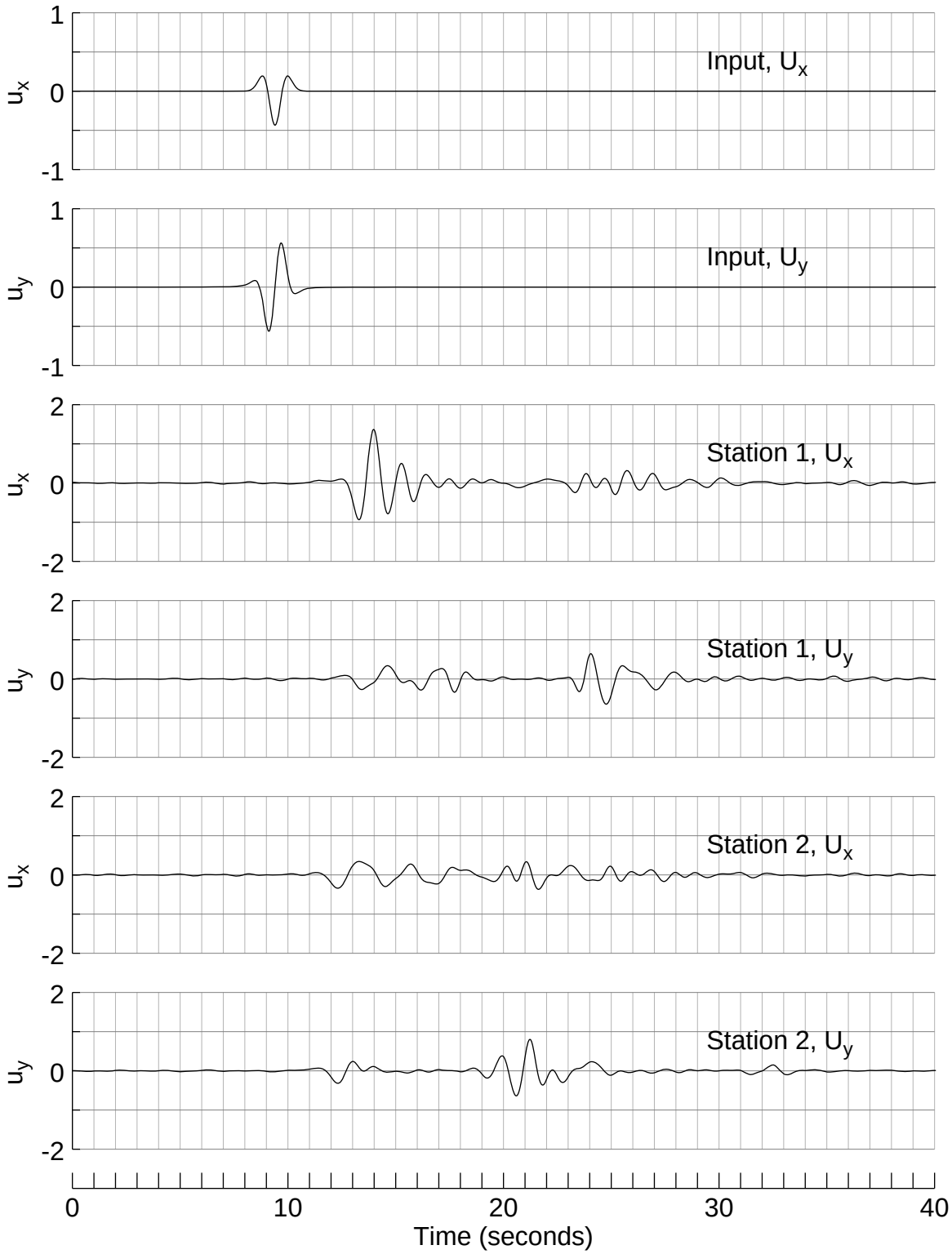

Figure 5.18. Response to Rayleigh wave Incidence

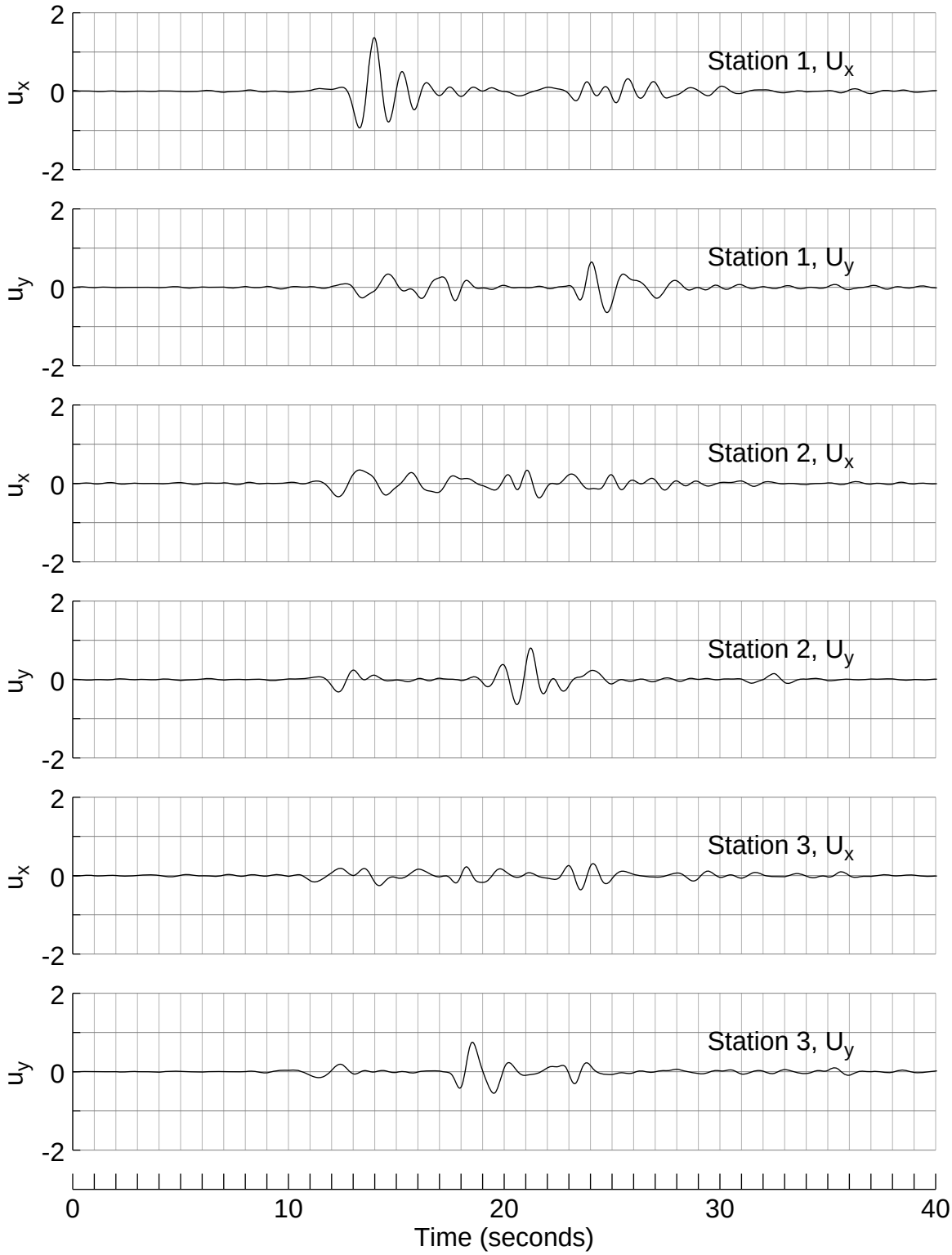

Figure 5.19. Attenuation of Rayleigh Wave Over Distance

high wave numbers k. For this reason, the incident Rayleigh Wave cannot reach the base of the alluvial valley at higher frequencies. The wave must therefore enter the alluvial valley only at its edge and most of the incident energy would be reflected. Shown in Fig. 5.19 are the responses to a Rayleigh Wave incidence at Stations 1, 2 and 3. There is a quick decay of amplitudes further back into the alluvial valley at stations 4 through 7 and they were not presented in the figure.

It is anticipated that many modes of Rayleigh Waves would have a larger influence on the response of an alluvial valley. However, a layered medium must be used to model the bedrock to be able to analyze these most interesting cases and they are beyond the scope of this dissertation.

Chapter 6

Conclusions

The concept of Substructure Deletion, pioneered by Professor Dasgupta for the calculation of embedded rigid foundations, was adapted to analyze site amplification problems in this dissertation. The concept simplified the calculation of the so-called boundary element solution which allows the outgoing waves to escape into the far-field to be represented by a simple half space or a horizontally layered half space.

The substructure deletion concept uses only the Green's Functions on the surface of the basic half space model, the effects of buried sources are accounted for by adding to the irregular embedded interface a replacement soil of the same material to form a whole half space. The replacement soil model, being finite in size, could be modeled with size-limited methods such as finite element or finite difference. The displacement-traction relationship for the embedded interface could then be obtained by a matrix manipulation and subsequent subtraction of the finite model matrix (of the same material) from the surface formulation of the half space. There are major advantages of this method because the compliance matrix for a flat surface has no traction because of the free surface boundary condition, thus eliminating the need to generate stress Green's Functions. The flat surface also allows geometrical modeling advantages, if the elements have equal size, the compliance matrix (displacement-traction relationship) could be formed using symmetry arguments and similarity arguments so that only one row of the matrix needs to be constructed. The computation time can be reduced by an order of magnitude using these advantages.

Since its introduction in 1979, there has been limited application of this method in the soil-structure interaction field. Perhaps modeling deeply embedded foundations is a difficult

challenge for this concept, having the buried interface too far away from the flat half space surface. There might have been other issues with the compatibility of the finite element formulation and the continuum mechanics formulation. The present application uses the boundary integral equation formulation for both the interior (finite model) and the exterior models, thus eliminating the alleged compatibility issues. Another possible advantage of the present application is that site amplification problems have models which are not deeply embedded beneath the free surface. The typical aspect ratio of an alluvial valley is of the order of 1:10, depth versus lateral dimensions. This fact plays into the favor of the substructure deletion concept.

A careful formulation, by computing all values using extra precision, showed that this method can be formulated to provide a stable solution, even for high frequencies. One major difference between the rigid embedded foundation problem and the site amplification problem is that the former targets only the integral of the surface results to obtain the impedance function, thus smoothing over some inaccuracies of the results. For the site amplification problem, results at every node on the free surface are of interest, therefore, accurate computation is important. By making larger and larger models, the elements become smaller and smaller, the task of handling Green's Function singularities becomes an issue and attention to detail was required to make the formulation perform properly.

The substructure deletion concept was tested against exact infinite series solution in the SH-wave case, against simple rigid foundation calculation and against results in the plane strain (P, SV, Rayleigh waves) case and the accuracy was founded to be excellent. For cases where there are no comparative solutions, the numerical solution was tested using different levels of refinement to ensure that the results converge. All these tests were conclusive that the method performs well for site amplification problems.

The computer programs developed for this dissertation were deployed to analyze several samples of arbitrary shaped canyons and alluvial valleys. The calculation of transfer functions to a dimensionless frequency of over 30 and the formulation was able to perform in a stable fashion. This method can handle actual dimensions of the physical problems, tens of kilometers in size with wavelengths less than one tenth of a kilometer. Using a boundary integral formulation, it has one reduction in dimension compared to the volume formulation such as finite element and finite difference. For three-dimensional wave scattering problems, this substructure deletion concept should be able to make the problem manageable. Of course, there is a limitation that the problem must be linear and that the material inside the scatter's surface must be homogeneous. But the number of problems that this method can address makes it a good tool for numerical simulation; it can help create a better understanding of the site amplification problem.

The contribution of this dissertation is the provision of a tool to analyze site amplification problems for a better understanding of the physics of the problem. Since the current seismic related building codes relied on one-dimensional vertically propagated wave solutions. Subsequent research in this area have added the effects of two-dimensional geometry and the concept of wave focusing to the possible explanation of why observed site amplification factors are highly localized. The present method provides a way to obtain the response of an alluvial valley to incident body waves from any direction and is able to handle surface waves as well. The major computational cost of this method is during the process of matrix formation, the computation of the alluvial valley response to various incident wave motion is less than 5% of the effort if the matrix is stored in today's terabyte storage units. This offers a benefit that probabilistic methods could be employed by generating random response to many different types of free field motion. The present method opens up possibilities for a realistic analysis of the site amplificaton effects.

The next step for the development of this method is to extend the solution to include horizontal layers for the half space Green's Functions. The finite replacement model to fill that buried interface must also be layered. After the compliance matrix is developed for the buried interface of the bedrock, fully three-dimensional arbitrary shaped and non-horizontal layered alluvial valley could be placed on top and a linear solution of this major problem is within reach.

References

Abramowitz, M.A., and I.A. Stegun (1970).“Handbook of Mathematical Functions,” Dover 0-486-61272-4, New York.

Aguirre, J., Irikura, K. (1998). “High frequency inversion of the seismic source during the 1995 Hyogo-ken nanbu earthquake using GA and EGF,” Proc. 2nd International Symposium on The Effects of Surface Geology on Seismic Motion, A.A. BALKEMA, 2, 1109-1114.

Anderson, J.G., Bodin, P., Brune, J.N., Prince, J., Singh, S.K., Quaas, R. and Onate, M. (1986). “Strong Ground Motion from the Michoacan, Mexico, Earthquake,” Science, New Series, Vol. 233, No. 4768 pp. 1043-1049.

Anderson, J.G., Lee, Y., Zeng, Y. and Day, S. (1996). “Control of Strong Motion by the Upper 30 Meters,” Bulletin of the Seismological Society of America, Vol. 86, No. 6, pp. 1749-1759.

Andrews, D.J. (1986). “Objective determination of source parameters and similarity of earthquakes of different size,” Earthquake Source Mechanics, American Geophysical Union, Monograph 37, pp. 259-268.

Apsel, R.J. (1979). “Dynamic Green’s Functions for Layered Media and Applications to Boundary-Value Problems,” Ph.D. Dissertation, University of California, San Diego, La Jolla, California.

Betti, R. (1994). “An Alternative Formulation of the Substructure Deletion Method for the Seismic Analysis of Embedded Foundations,” Journal of Mechanics of Materials and Structures, Vol. 35, pp. 359-378.

Borcherdt, R.D. (1994). Estimates of site-dependent response spectra for design (methodology and justification). Earthquake Spectra, Vol. 10, No. 4, pp. 617-653.

Chien, A.Y. (2007). “A Complete Time-Harmonic Radiation Boundary for Discrete Elastodynamic Models,” Ph.D. Dissertation, University of Southern California, Los Angeles, California.

Chouw, N. and Hao, H. (2008). “Response Of Bridge Structures To Spatially Varying And Site-Amplified Ground Motions,” The 14 th World Conference on Earthquake Engineering, October 12-17, Beijing, China.

Crouse, C. B., McGuire, J. W. (1996). “Site response studies for purpose of revising NEHRP seismic provisions,” Earthquake Spectra, Vol. 12, pp. 407-439.

Dasgupta, G. (1980). “Foundation impedance matrices by substructure deltion,” Journal of the Engineering Mechanics Division, ASCE, No. EM3, pp. 517-523.

De Hoop, A. T. (1958). “Representation theorems for the displacement in an elastic solid and their application to elastodynamic diffraction theory,” Thesis, Technische Hogeschool, Delft.

Dobry, R. and Lai, S. (2000). “Recent developments in the understanding of earthquake site response and associated seismic code implementation,” GeoEng2000, An International Conference on Geotechnical and Geological Engineering, Melbourne, Australia, pp. 186-229.

Dravinski, M. and Mossessian, T.K. (1987). “Scattering of Plane Harmonic P, SV,and Rayleigh Waves by Dipping Layers of Arbitrary Shape,” Bulletin of the Seismological Society of America, Vol. 77, No. 1, pp. 212-235.

Dravinski, M. and Mossessian, T.K. (1990). “Amplification of Elastic Waves by a Three-Dimensional Valley. Part 2: Transient Response,” Earthquake Engineering and Structural Dynamics, Vol. 19, pp. 681-691. Dravinski, M. and Wilson, M.S. (2001). “Scattering of elastic waves by a general anisotropic basin. Part 1: a 2D model,” Earthquake Engineering and Structural Dynamics, Vol. 30, pp. 675-689.

Elgamal, A.W., Zeghal, M., Parra, E.,Gunturi, R. , Tang, H.T. and J. C. Stepp (1996). “Identification and modeling of earthquake ground response I. Site amplification,” Soil Dynamics and Earthquake Engineering, Vol. 15, pp. 499-522.

Ewing, W.M., W.S. Jardetsky, and F. Press (1957).“Elastic Waves in Layered Media,” McGraw-Hill Book Company, Inc., New York.

Field, E. H. (2000). “A modified ground motion attenuation relationship for southern California that accounts for detailed site classification and a basin depth effect,” Bulletin of the Seismological Society of America, Vol. 90, pp. 209-221.

Finn W.D.L., Wightman A. (2003). Ground motion amplification factors for the proposed 2005 edition of the National Building Code of Canada. Canadian Journal of Civil Engineering, Vol. 30, pp. 272-278.

Gatmiri, B., Nguyen. K.V., Dehghan, K. (2007). “Seismic response of slopes subjected to incident SV wave by an improved boundary element approach,” International Journal of Numerical and Analytical Methods in Geomechanics, Vol. 31, No. 10, pp. 1183-1195.

Gatmiria, B., Maghoul,. Arson, C. (2009). “Site-specific spectral response of seismic movement due to geometrical and geotechnical characteristics of sites,” Soil Dynamics and Earthquake Engineering, Vol. 29, pp. 51-70

Harmsen, S.C. (1997). "Determination of site amplification in the Los Angeles urban area from inversion of strong motion records," Bulletin of the Seismological Society of America, Vol. 87, pp. 866-887.

Hartzell, S., A. Leeds, A. Frankel, and J. Michael (1996). "Site response for urban Los Angeles using aftershocks of the Northridge earthquake," Bulletin of Seismological Society of America, Vol. 86, No. 18, pp. 168–192.

Haskell, N.A. (1969). "Elastic Displacements in the Near-Field of a Propagating Fault," Bulletin of the Seismological Society of America, Vol. 59, No. 2, pp. 865-908.

Haskell, N.A. (1966). "Total Energy and Energy Spectral Density of Elastic Wave Radiation From Propagating Faults. Part II. A Statistical Source Model," Bulletin of the Seismological Society of America, Vol. 56, No. 1, pp. 125-140.

Holzer, T.L. (1994). "Loma Prieta damage largely attributed to enhanced ground shaking," Transactions, American Geophysical Union, Eos, Vol. 75, Np. 26, pp. 299-301.

Holzer, T.L., Padovani, A.C., Bennett, M.J.,Noce, T.E. and Tinsley, J.C. (2009). "Mapping NEHRP VS30 Site Classes" Earthquake Spectra, Earthquake Engineering Research Institute, Vol. 21, No. 2, pp. 1–18.

Hoshiba, M., Iwakiri, K. (2011). "Initial 30 seconds of the 2011 off the Pacific coast of Tohoku Earthquake (M_w 9.0) - amplitude and τ_c for magnitude estimation for Earthquake Early Warning," Meteorological Research Institute, Nagamine 1-1, Tsukuba 305-0031, Japan.

Huang, Y.N., Whittaker, A.S. and Luco, N. (2010). "NEHRP Site Amplification Factors and the NGA Relationships," Earthquake Spectra, Earthquake Engineering Research Institute, Vol. 26, No. 2, pp. 583–593.

Ishihara, K. and Kijima, T. (2001). "Effects of Liquefaction on Seismic Response of A Storage Tank On Pile Foundations," Proceeding of Fourth International Conference on Recent Advances in Geotechnical Earthquake Engineering and Symposium in Honor of Professor W. D. Liam Finn, San Diego, California.

Iwata,T., Hatayama, K. and Pitarka,A.(1996). "Site Amplification of Ground Motion During The 1995 Hyogo-Ken Nabu Earthquake ,Japan, In Severely Damaged Zone," Proceedings of the Eleventh World Conference on Earthquake Engineering, Acapulco, México.

Kawase H. (1988). "Time-domain response of a semi-circular canyon for incident SV, P and Rayleigh waves calculated by the discrete wavenumber boundary element method," Bulletin of the Seismological Society of America, Vol. 78, pp. 1415-1437.

Lamb, H. (1903). "On the Propagation of Tremors Over the Surface of an Elastic Solid," Phil. Transaction of Royal Phil. Soc. Of London, 1-4-2.

Le Pense S., Gatmiri B., Maghoul P. (2011). "Influence of soil properties and geometrical characteristics of sediment-filled valleys on earthquake response spectra," Proceedings of the 8th International Conference on Structural Dynamics, EURODYN 2011 Leuven, Belgium, 4-6 July 2011, De Roeck, G., Degrande, G., Lombaert, G., M¨uller, G. (eds.).

Lee, V.W., Trifunac,M.D. (2010), "Should average shear-wave velocity in the top 30m of soil be used to describe seismic amplification?" Soil Dynamics and Earthquake Engineering, Vol. 30, No. 11, pp. 1250-1258

Love, A.E.H. (1926). "A Treatise on the Mathematical Theory of Elasticity," ISBN 0-486-60174-9, Dover Publications, New York.

Luco, J.E. and R.J. Apsel (1983). "On the Green's Functions for a Layered Half-Space, Part I," Bulletin of Seismological Society of America, Vol. 73, No. 4, pp. 907-929.

Luco, J.E. and R.J. Apsel (1983). "On the Green's Functions for a Layered Half-Space, Part II," Bulletin of Seismological Society of America, Vol. 73, No. 4, pp. 931-951.

Luco, J.E., Wong. H.L., Barros, F.C.P. (1990). "3D Response of a cylindrical canyon in a layered half-space," Earthquake Engineering and Structural Dynamics, Vol. 19, pp. 799–817.

Luco, J.E., Barros, F.C.P. (1995). "3D response of a layered cylindrical valley embedded in a layered half-space," Earthquake Engineering and Structural Dynamics, Vol. 24, pp. 109-125.

Matsunami, K., Morii, T., Okamoto, Y. and Fujiwara, T. (2002). "Local site amplification and damage to wooden houses in Shimoenoki, Tottori, Japan, by the 2000Western Tottori Earthquake," Earth Planets Space, Vol. 54, pp. 861–870.

Sadigh, K., Chang, C.Y., Egan, J.A., Makdisi, F., Youngs, R.R. (1997). "Attenuation relationships for shallow crustal earthquakes based on California strong motion data," Seismological Research Letters, Vol. 68, No. 1, pp. 180-189.

Sanchez-Sesma, F.J., Campillo, M. (1991). "Diffraction of P, SV and Rayleigh waves by topographic features: aboundary integral formulation," Bulletin of the Seismological Society of America, Vol. 81, No. 6, pp. 2234-2253.

Sanchez-Sesma,F.J., Faccioli, E., Fregonese,R. (1986). "An index for measuring the effects of topographyon seismic ground motion intensity," Earthquake Engineering and Structural Dynamics, Vol. 14, pp. 719-731.

Su, F., Anderson, J.G., Brune, J.N., and Zeng,Y. (1996). "Comparison of Direct S-Wave and Coda-Wave Site Amplification Determined from Aftershocks of the Little Skull Mountain Earthquake," Bulletin of the Seismological Society of America, Vol. 86, No. 4, pp. 1006-1018.

Taylor, S.R., Gerstoft, P. and Fehler, M.C. (2009). "Estimating site amplification factors from ambient noise," Geophysical Research Letters, Vol. 36, No. 10, pp. 1029.

Trifunac, M.D. (1971). "Surface motion of a semi-cylindrical alluvial valley for incident plane SH waves," Bulletin of the Seismological Society of America, Vol. 61, No. 6, pp. 1755–1770.

Trifunac, M.D. (1990). "How To Model Amplification Of Strong Earthquake Motions By Local Soil And Geologic Site Conditions," Earthquake Engineering And Structural Dynamics, Vol. 19, pp. 833-846.

Trifunac, M.D. and Todorovska, M.I. (2000). "Can aftershock studies predict site amplification factors? Northridge, CA, earthquake of 17 January 1994," Soil Dynamics and Earthquake Engineering, Vol. 19, pp. 233–251.

Wong, H.L., Trifunac, M.D. (1974). "Surface Motion of a Semi-Elliptical Alluvial Valley for Incident Plane SH Waves," Bulletin of Seismological Society of America, Vol. 64, pp. 1389-1408.

Wong, H.L., Jennings, P. (1975). "Effect of canyon topographies on strong ground motion," Bulletin of the Seismological Society of America, Vol. 65, No. 12, pp. 39-57.

Wong, H.L., Trifunac, M.D. and Westermo, B. (1977). "Effects of Surface and Subsurface Irregularities on the Amplitudes of Monochromatic Waves," Bulletin of the Seismological Society of America, Vol. 67, No. 2, pp. 353-368.

Wong, H.L. (1982). "Effects of Surface Topography on the Diffraction of P, SV and Rayleigh Waves," Bulletin of Seismological Society of America, Vol. 72, No. 4, 1167-1183.

Yamanaka, H., Motoki, K., Yamada, N., Sugawara, T., Mabuchi, Y. and Seo, K. (2008). "Observation of ground motions of aftershocks of the 2007 Noto Hanto earthquake in Monzenmachi, the Wajima city, for estimation of site amplification," Earth Planets Space, Vol. 60, pp. 1063–1067.

Zhang, J.J., Moss, P.J. and Carr, A.J. (2003). "Non-linear Local Site Amplification and Its Effect on Structural Response," Pacific Conference on Earthquake Engineering.

Appendix A

The Boundary Integral Equation Method

Applying the representation theorem of elastodynamics first introduce by DeHoop (1958) and later applied by Haskell (1966, 1969), the waves in a medium can be represented by sources placed at the surface of a scatterer. In particular, the wave motion in an exterior medium, in which the outgoing waves are assumed to propagate into the far-field, can be expressed in terms of the boundary values at the scatterer's surface and the Green's functions of the propagating medium. The Green's functions account for all soil properties such as the configuration of layers, shear and compressional wave velocities, mass densities, damping characteristics, etc. This integral representation theorem can be derived by using Betti-Rayleigh relationship (Fung, 1965) to a body Ω as shown in Fig. A.1.

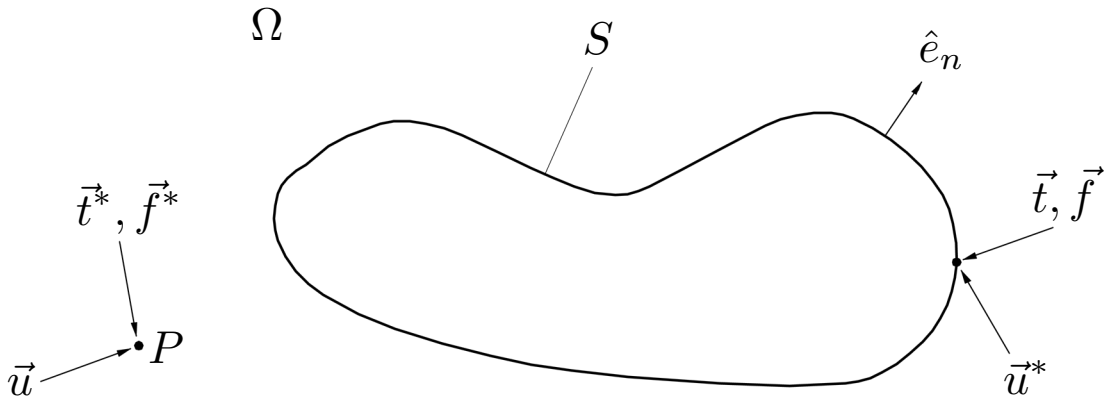

Figure A.1 – Schematic of the formulation of the Boundary Integral Equation.

The body Ω, bounded by a surface S, is subjected to loading conditions with $\vec{t}$ being the traction vector applied at the surface and $\vec{f}$ being the body force per unit volume within the body. The displacement vector resulting from this loading condition is $\vec{u}$. Consider now the action of a separate loading condition with $\vec{t^*}$ and $\vec{f^*}$, they will create a new displacement vector $\vec{u^*}$. The reciprocal relationship, based on the principles of physics, can be written as

$$\int_S \vec{u^*}^T \vec{t}\, dS + \int_\Omega \vec{u^*}^T \vec{f}\, d\Omega = \int_S \vec{u}^T \vec{t^*}\, dS + \int_\Omega \vec{u}^T \vec{f^*}\, d\Omega \qquad , \qquad (A1)$$

indicating that in a linear elastic solid, the work done by a set of forces acting through the corresponding displacement produced by a second set of forces is equal to the work done by the second set of forces acting through the corresponding displacements produced by the first set of forces. The inner products of all four terms in Eq. (A1) are scalars.

To simplify Eq. (A1) for applications in this dissertation, the body force $\vec{f}$ is assumed to be zero. Re-ordering the inner-products of the right-hand-side of Eq. (A1), the equation can be written as

$$\int_S \vec{u^*}^T \vec{t}\, dS = \int_S \vec{t^*}^T \vec{u}\, dS + \int_\Omega \vec{f^*}^T \vec{u}\, d\Omega \qquad . \qquad (A2)$$

To make Eq. (A2) useful for general applications, let the loading conditions annotated by "*" be those generated by unit point loads in orthogonal directions. More specifically, consider 3 different cases where the body force $\vec{f^*}$ is a point force applied at location $\vec{r}_p = [x_p, y_p, z_p]^T$:

CASE 1: Body force in the x-direction at point $\vec{r}_p$:

$$\vec{f}^*_x = \Big[\ \delta(\vec{r} - \vec{r}_p) \quad , \quad 0 \quad , \quad 0 \ \Big]^T \qquad (A3a)$$

CASE 2: Body force in the y-direction at point $\vec{r}_p$:

$$\vec{f}_y^* = \Big[\ 0 \quad , \quad \delta(\vec{r} - \vec{r}_p) \quad , \quad 0\ \Big]^T \tag{A3b}$$

CASE 3: Body force in the z-direction at point $\vec{r}_p$:

$$\vec{f}_z^* = \Big[\ 0 \quad , \quad 0 \quad , \quad \delta(\vec{r} - \vec{r}_p)\ \Big]^T \tag{A3c}$$

The resulting displacement vector $\vec{u^*}$ at $\vec{r} = [x, y, z]^T$ for the above loading conditions are

CASE 1:

$$\vec{u}_x^* = \Big[\ U_{xx}(\vec{r}_p|\vec{r}) \quad , \quad U_{xy}(\vec{r}_p|\vec{r}) \quad , \quad U_{xz}(\vec{r}_p|\vec{r})\ \Big]^T \tag{A4a}$$

CASE 2:

$$\vec{u}_y^* = \Big[\ U_{yx}(\vec{r}_p|\vec{r}) \quad , \quad U_{yy}(\vec{r}_p|\vec{r}) \quad , \quad U_{yz}(\vec{r}_p|\vec{r})\ \Big]^T \tag{A4b}$$

CASE 3:

$$\vec{u}_z^* = \Big[\ U_{zx}(\vec{r}_p|\vec{r}) \quad , \quad U_{zy}(\vec{r}_p|\vec{r}) \quad , \quad U_{zz}(\vec{r}_p|\vec{r})\ \Big]^T \tag{A4c}$$

in which U_{ij} is the displacement in the $\hat{e}_j$-direction caused by a point load in the $\hat{e}_i$-direction. The column vectors in Eq. (A4) represent the displacement Green's functions. The index notation for $\hat{e}_i$ is defined as $\hat{e}_1 = \hat{\imath}$, $\hat{e}_2 = \hat{\jmath}$ and $\hat{e}_3 = \hat{k}$.

Following similar steps, the traction vector $\vec{t^*}$ at $\vec{r}$ resulting from the given loading conditions are

CASE 1:

$$\vec{t}_x^* = \Big[\ T_{xx}(\vec{r}_p|\vec{r}) \quad , \quad T_{xy}(\vec{r}_p|\vec{r}) \quad , \quad T_{xz}(\vec{r}_p|\vec{r})\ \Big]^T \tag{A5a}$$

CASE 2:

$$\vec{t}_y^* = \Big[\ T_{yx}(\vec{r}_p|\vec{r}) \quad , \quad T_{yy}(\vec{r}_p|\vec{r}) \quad , \quad T_{yz}(\vec{r}_p|\vec{r})\ \Big]^T \tag{A5b}$$

CASE 3:

$$\vec{t}_z^{\,*} = \left[\; T_{zx}(\vec{r}_p|\vec{r}) \quad , \quad T_{zy}(\vec{r}_p|\vec{r}) \quad , \quad T_{zz}(\vec{r}_p|\vec{r}) \; \right]^T \qquad (A5c)$$

in which T_{ij} is the traction developed at $\vec{r}$ in the $\hat{e}_j$-direction by a point load at $\vec{r}_p$ in the $\hat{e}_i$-direction. The traction vectors in Eq. (A5) can be calculated by performing the matrix product of the Green's function stress tensor and the direction cosines of the outward normal vector $\hat{e}_n$ on surface S as

$$\begin{bmatrix} T_x \\ T_y \\ T_z \end{bmatrix} = \begin{bmatrix} \sigma_{xx} & \sigma_{xy} & \sigma_{xz} \\ \sigma_{yx} & \sigma_{yy} & \sigma_{yz} \\ \sigma_{zx} & \sigma_{zy} & \sigma_{zz} \end{bmatrix} \begin{bmatrix} n_x \\ n_y \\ n_z \end{bmatrix} \qquad , \qquad (A6)$$

in which n_x, n_y and n_z are the direction cosines of $\hat{e}_n$.

By substituting the three sets of loading conditions as defined in Eq (A3), Eq. (A2) can be written with the Green's Functions as a matrix equation in the following form,

$$\int_S \left[\; U(\vec{r}_p|\vec{r}) \; \right] \vec{t}(\vec{r}) \, dS = \int_S \left[\; T(\vec{r}_p|\vec{r}) \; \right] \vec{u}(\vec{r}) \, dS + \vec{u}(\vec{r}_p) \qquad , \qquad (A7)$$

in which

$$\left[\; U(\vec{r}_p|\vec{r}) \; \right] = \begin{bmatrix} U_{xx}(\vec{r}_p|\vec{r}) & U_{xy}(\vec{r}_p|\vec{r}) & U_{xz}(\vec{r}_p|\vec{r}) \\ U_{yx}(\vec{r}_p|\vec{r}) & U_{yy}(\vec{r}_p|\vec{r}) & U_{yz}(\vec{r}_p|\vec{r}) \\ U_{zx}(\vec{r}_p|\vec{r}) & U_{zy}(\vec{r}_p|\vec{r}) & U_{zz}(\vec{r}_p|\vec{r}) \end{bmatrix} \qquad , \qquad (A8)$$

$$\left[\; T(\vec{r}_p|\vec{r}) \; \right] = \begin{bmatrix} T_{xx}(\vec{r}_p|\vec{r}) & T_{xy}(\vec{r}_p|\vec{r}) & T_{xz}(\vec{r}_p|\vec{r}) \\ T_{yx}(\vec{r}_p|\vec{r}) & T_{yy}(\vec{r}_p|\vec{r}) & T_{yz}(\vec{r}_p|\vec{r}) \\ T_{zx}(\vec{r}_p|\vec{r}) & T_{zy}(\vec{r}_p|\vec{r}) & T_{zz}(\vec{r}_p|\vec{r}) \end{bmatrix} \qquad , \qquad (A9)$$

and the vector $\vec{u}(\vec{r}_p)$ is the result of the integral

$$\int_\Omega \begin{bmatrix} \delta(\vec{r}-\vec{r}_p) & 0 & 0 \\ 0 & \delta(\vec{r}-\vec{r}_p) & 0 \\ 0 & 0 & \delta(\vec{r}-\vec{r}_p) \end{bmatrix} \begin{bmatrix} u_1(\vec{r}) \\ u_2(\vec{r}) \\ u_3(\vec{r}) \end{bmatrix} d\Omega \qquad . \qquad (A10)$$

Using the integral representation of Eq. (A7), the displacement vector $\vec{u}(\vec{r}_p)$ at any location $\vec{r}_p$ within the soil medium can be calculated in terms of the boundary displacement $\vec{u}(\vec{r})$ and boundary traction $\vec{t}(\vec{r})$ as

$$\vec{u}(\vec{r}_p) = \int_S \left[\, U(\vec{r}_p|\vec{r}) \,\right] \vec{t}(\vec{r})\, dS - \int_S \left[\, T(\vec{r}_p|\vec{r}) \,\right] \vec{u}(\vec{r})\, dS \qquad . \qquad (A11)$$

The integrals are evaluated over the surface S only.

Appendix B

Anti-Plane Green's Function Matrices

To calculate the response, $\vec{u}$, at observation point $\vec{r}_p$, a representation theorem based on the reciprocity relationship and the known displacements, $\vec{u}$, and known tractions, $\vec{t}$, at the surface, S, can be written as

$$\int_S \Big[U(\vec{r}_p, \vec{r})\Big]\vec{t}(\vec{r})\, dS - \int_S \Big[T(\vec{r}_p, \vec{r})\Big]\vec{u}(\vec{r})\, dS = \vec{u}(\vec{r}_p) \quad , \tag{B1}$$

in which $[U]$ is the Green's Function matrix for displacements, $[T]$ is the Green's Function matrix for tractions, and $\vec{r}$ is the position vector on the surface S.

B.1 Green's Functions for an Infinite Medium

For two-dimensional SH-wave problems, the component of interest is in the z-direction, the representation theorem is simplified to

$$\int_S U_{zz}(\vec{r}_p, \vec{r})\, t_z(\vec{r})\, dS - \int_S T_{zz}(\vec{r}_p, \vec{r})\, u_z(\vec{r})\, dS = u_z(\vec{r}_p) \quad , \tag{B2}$$

in which U_{zz} is the only applicable element of the matrix $[U]$ and it is defined as

$$U_{zz} = -\frac{i}{4\mu} H_0^{(2)}(kR) \qquad , \tag{B3}$$

where k is the wave number ω/β, β is the shear wave velocity, $H_0^{(2)}$ is the Hankel Function of the Second Kind and zeroth order, and

$$R = \sqrt{(x - x_p)^2 + (y - y_p)^2} \qquad .$$

The traction matrix $[T]$ is calculated using the stress matrix and the outward normal, $\vec{n}$, of the surface S, defined as $\vec{n} = [n_x, n_y, n_z]^T$. One column of the traction matrix, $[T]$, can be determine by the matrix product,

$$\begin{bmatrix} T_{xi} \\ T_{yi} \\ T_{zi} \end{bmatrix} = \begin{bmatrix} \sigma_{xx} & \sigma_{xy} & \sigma_{xz} \\ \sigma_{yx} & \sigma_{yy} & \sigma_{yz} \\ \sigma_{zx} & \sigma_{zy} & \sigma_{zz} \end{bmatrix}_i \begin{bmatrix} n_x \\ n_y \\ n_z \end{bmatrix} \tag{B4}$$

in which i is the direction of a point load at $\vec{r}_p$ and the stress matrix contains the stresses generated by that point load.

The antiplane motion of SH-waves requires only one component of $[T]$ and it is defined as

$$T_{zz} = [\, \sigma_{zx} \quad \sigma_{zy} \quad 0 \,] \begin{bmatrix} n_x \\ n_y \\ 0 \end{bmatrix} = \sigma_{zx} n_x + \sigma_{zy} n_y \qquad . \tag{B5}$$

Using the shear modulus, μ, the stresses generated by an antiplane line load are

$$\sigma_{zx} = \mu \frac{\partial U_{zz}}{\partial x} = -\frac{ik}{4} H_1^{(2)}(kR) \frac{\partial R}{\partial x} \qquad , \tag{B6a}$$

$$\sigma_{zy} = \mu \frac{\partial U_{zz}}{\partial y} = -\frac{ik}{4} H_1^{(2)}(kR) \frac{\partial R}{\partial y} \qquad , \tag{B6b}$$

in which $H_1^{(2)}$ is the Hankel Function of the Second Kind and first order,

$$\frac{\partial R}{\partial x} = \frac{x - x_p}{R} \qquad \text{and} \qquad \frac{\partial R}{\partial y} = \frac{y - y_p}{R} \quad . \tag{B7}$$

B.2 Green's Functions for a Semi-Infinite Medium

For two-dimensional SH-wave problems in a semi-infinite medium, the component of interest is in the z-direction, the representation theorem is simplified to that shown in Eq. (B2). But U_{zz}, the only applicable element of the matrix $[U]$, is obtained using a mirror image with respect to the $x-$axis so that its symmetry generates a condition so that the shear

stress σ_{Zy} is 0 on the half-space boundary. The displacement Green's Function, U_{zz}, can therefore be written as

$$U_{zz} = -\frac{i}{4\mu}\left[H_0^{(2)}(kR_1) + H_0^{(2)}(kR_2)\right] \qquad , \tag{B8}$$

in which

$$R_1 = \sqrt{(x-x_p)^2 + (y-y_p)^2} \qquad ,$$
$$R_2 = \sqrt{(x-x_p)^2 + (y+y_p)^2} \qquad .$$

The traction matrix $[T]$ is calculated using the stress matrix, similar to that described in Eq. (B4) of section B.1. The one component of interest for $[T]$ is defined as

$$T_{zz} = [\,\sigma_{zx} \quad \sigma_{zy} \quad 0\,] \begin{bmatrix} n_x \\ n_y \\ 0 \end{bmatrix} = \sigma_{zx} n_x + \sigma_{zy} n_y \qquad . \tag{B9}$$

Using the shear modulus, μ, the stresses generated by an antiplane line load are

$$\sigma_{zx} = \mu\frac{\partial U_{zz}}{\partial x} = -\frac{ik}{4}\left[H_1^{(2)}(kR_1)\frac{\partial R_1}{\partial x} + H_1^{(2)}(kR_2)\frac{\partial R_2}{\partial x}\right] \quad , \tag{B10a}$$
$$\sigma_{zy} = \mu\frac{\partial U_{zz}}{\partial y} = -\frac{ik}{4}\left[H_1^{(2)}(kR_1)\frac{\partial R_1}{\partial y} + H_1^{(2)}(kR_2)\frac{\partial R_2}{\partial y}\right] \quad , \tag{B10b}$$

with

$$\frac{\partial R_1}{\partial x} = \frac{x-x_p}{R_1} \quad , \quad \frac{\partial R_2}{\partial x} = \frac{x-x_p}{R_2} \quad , \quad \frac{\partial R_1}{\partial y} = \frac{y-y_p}{R_1} \quad , \quad \frac{\partial R_2}{\partial y} = \frac{y+y_p}{R_2} \quad . \tag{B11}$$

B.3 Surface Green's Functions for a Semi-Infinite Medium

For the special case where the source and the observation points are both on the surface of the half-space, the semi-infinite space Green's function is simplified further as it is defined as

$$U_{zz} = -\frac{i}{2\mu}H_0^{(2)}(kR) \qquad , \tag{B12}$$

in which $R = |x - x_0|$. With the direction cosines of the outer normal defined by $n_x = 0$ and $n_y = 1$, the traction Green's Function $T_{zz} = \sigma_{zy}$ and it is 0 everywhere on the half-space surface. The representation theorem in Eq. (B2) is simplied to

$$\int_S U_{zz}(\vec{r}_p, \vec{r})\, t_z(\vec{r})\, dS = u_z(\vec{r}_p) \qquad , \tag{B13}$$

making the numerical solution much simpler.

Appendix C

Plane Strain Green's Function Matrices

To obtain the two-dimensional Green's function matrices $[U]$ and $[T]$ for application in the representation theorm, the solution for displacements and stresses caused by a line load must be considered. The first row of $[U]$, U_{11} and U_{12}, corresponds to the horizontal and vertical displacements induced by a horizontal line load while the second row of $[U]$, U_{21} and U_{22}, correspond to the horizontal and vertical displacements produced by a vertical line load, respectively.

The two rows of the matrix $[T]$ contain the tractions at the observation point generated by the respective line loads described above. They are calculated as the matrix product of the stress tensor generated by the line loads and the direction cosines of the outward normal vector at the surface.

C.1 Green's Functions for an Infinite Medium

For an infinite and homogeneous medium, the solution of a vertical line load can be used to produce the solution of a horizontal line load using an orthogonal transformation. In Section C.1.1, the solution for the vertical line load will be presented and the transformation necessary to obtain the results for the horizontal line load will be given in Section C.1.2.

C.1.1 Displacements and Stresses Generated by a Vertical Line Load

Shown in Fig. C1 is a concentrated line load Q_Y in the positive y-direction. The solution of the two-dimensional wave equation can be written in terms of two potential functions ϕ

and ψ as shown in Lamb's paper (1904) as

$$\phi = \frac{Q_Y}{4k^2\mu}\frac{\partial}{\partial y}D_0(hr) \qquad , \tag{C1}$$

$$\psi = \frac{Q_Y}{4k^2\mu}\frac{\partial}{\partial x}D_0(kr) \qquad , \tag{C2}$$

in which $r = \sqrt{x^2 + y^2}$, $x = x_o - x_s$ and $y = y_o - y_s$ are the relative position coordinates of the observation point with respect to the source point in the x- and y- directions, respectively. The function D_0, used by Lamb (1904) is related to the Hankel Function as, $D_0 = -iH_0^{(2)} = -Y_0 - iJ_0$.

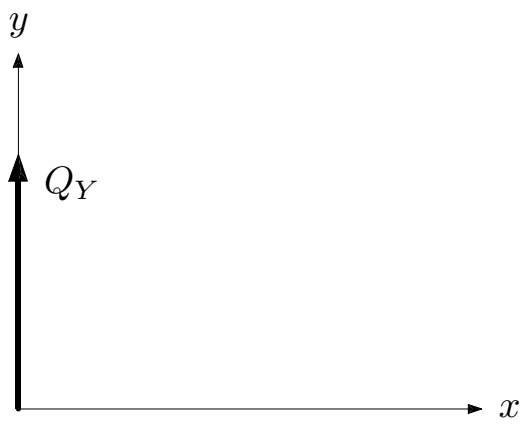

Figure C.1 – Vertical Q_Y Line Force Configuration.

The argument of ϕ, $hr = \omega r/\alpha$, is a dimensionless frequency normalized by the compressional wave velocity α, implying that ϕ is a potential for compressional waves. ψ, on the other hand, is the shear wave potential because $kr = \omega r/\beta$ is normalized by the shear wave velocity β. Note, the Hankel function of the second kind is used in this derivation because it represents an outgoing wave as $r \to \infty$ when associated with the harmonic time factor $e^{i\omega t}$.

For a unit load Q_Y in the vertical direction, let the amplitude $Q_Y = 1$, then

$$\phi = \frac{i}{4k^2\mu}\frac{\partial}{\partial y}H_0^{(2)}(hr) \qquad , \tag{C3}$$

and

$$\psi = \frac{-i}{4k^2\mu}\frac{\partial}{\partial x}H_0^{(2)}(kr) \qquad . \tag{C4}$$

C.1.1.1 – Displacements

Using the potentials ϕ and ψ, the displacements in the x- and y-directions, respectively, can be expressed as,

$$\begin{aligned} U_{21} &= \frac{\partial\phi}{\partial x} + \frac{\partial\psi}{\partial y} \\ &= \frac{i}{4k^2\mu}\left[\frac{\partial^2}{\partial x\partial y}H_0^{(2)}(hr) - \frac{\partial^2}{\partial y\partial x}H_0^{(2)}(kr)\right] \qquad , \end{aligned} \tag{C5}$$

and

$$\begin{aligned} U_{22} &= \frac{\partial\phi}{\partial y} - \frac{\partial\psi}{\partial x} \\ &= \frac{i}{4k^2\mu}\left[\frac{\partial^2}{\partial y^2}H_0^{(2)}(hr) + \frac{\partial^2}{\partial x^2}H_0^{(2)}(kr)\right] \qquad , \end{aligned} \tag{C6}$$

in which, the derivatives of the Hankel function are,

$$\frac{\partial^2}{\partial x^2}H_0^{(2)}(kr) = \frac{d^2}{dr^2}H_0^{(2)}(kr)\left[\frac{\partial r}{\partial x}\right]^2 + \frac{d}{dr}H_0^{(2)}(kr)\left[\frac{\partial^2 r}{\partial x^2}\right] \qquad , \tag{C7a}$$

$$\frac{\partial^2}{\partial y^2}H_0^{(2)}(kr) = \frac{d^2}{dr^2}H_0^{(2)}(kr)\left[\frac{\partial r}{\partial y}\right]^2 + \frac{d}{dr}H_0^{(2)}(kr)\left[\frac{\partial^2 r}{\partial y^2}\right] \qquad , \tag{C7b}$$

$$\frac{\partial^2}{\partial y\partial x}H_0^{(2)}(kr) = \frac{d^2}{dr^2}H_0^{(2)}(kr)\left[\frac{\partial r}{\partial x}\right]\left[\frac{\partial r}{\partial y}\right] + \frac{d}{dr}H_0^{(2)}(kr)\left[\frac{\partial^2 r}{\partial x\partial y}\right] \qquad , \tag{C7c}$$

and

$$\frac{d}{dr}H_0^{(2)}(kr) = -kH_1^{(2)}(kr) \qquad , \tag{C7d}$$

$$\frac{d^2}{dr^2}H_0^{(2)}(kr) = -k^2\left[H_0^{(2)}(kr) - \frac{1}{kr}H_1^{(2)}(kr)\right] \qquad . \tag{C7e}$$

In the above expressions, the derivatives of the distance r can be written as

$$\frac{\partial r}{\partial x} = \frac{x}{r} \quad , \tag{C8a}$$

$$\frac{\partial r}{\partial y} = \frac{y}{r} \quad , \tag{C8b}$$

$$\frac{\partial^2 r}{\partial x^2} = \frac{1}{r}\left(1 - \frac{x^2}{r^2}\right) \quad , \tag{C8c}$$

$$\frac{\partial^2 r}{\partial y^2} = \frac{1}{r}\left(1 - \frac{y^2}{r^2}\right) \quad , \tag{C8d}$$

and

$$\frac{\partial^2 r}{\partial x \partial y} = -\frac{xy}{r^3} \quad . \tag{C8e}$$

The expressions in Eq. (C7a) to Eq. (C7e) are the same for the function, $H_0^{(2)}(hr)$, except the wave number k is replaced by h.

C.1.1.2 – Stresses

The stress components, σ_{xx_Y}, σ_{xy_Y} and σ_{yy_Y} can be expressed in terms of the potential functions ϕ and ψ as

$$\begin{aligned} \frac{1}{\mu}\sigma_{xx_Y} &= -k^2\phi - 2\frac{\partial^2\phi}{\partial y^2} + 2\frac{\partial^2\psi}{\partial x \partial y} \qquad (C9) \\ &= \frac{i}{4k^2\mu}\left[-k^2\frac{\partial}{\partial y}H_0^{(2)}(hr) - 2\frac{\partial^3}{\partial y^3}H_0^{(2)}(hr) - 2\frac{\partial^3}{\partial x^2 \partial y}H_0^{(2)}(kr)\right] \quad , \\ \frac{1}{\mu}\sigma_{xy_Y} &= 2\frac{\partial^2\phi}{\partial x \partial y} - k^2\psi - 2\frac{\partial^2\psi}{\partial x^2} \qquad (C10) \\ &= \frac{i}{4k^2\mu}\left[2\frac{\partial^3}{\partial x \partial y^2}H_0^{(2)}(hr) + k^2\frac{\partial}{\partial x}H_0^{(2)}(kr) + 2\frac{\partial^3}{\partial x^3}H_0^{(2)}(kr)\right] \quad , \end{aligned}$$

and

$$\begin{aligned} \frac{1}{\mu}\sigma_{yy_v} &= -k^2\phi - 2\frac{\partial^2\phi}{\partial x^2} - 2\frac{\partial^2\psi}{\partial x \partial y} \qquad (C11) \\ &= \frac{i}{4k^2\mu}\left[-k^2\frac{\partial}{\partial y}H_0^{(2)}(hr) - 2\frac{\partial^3}{\partial x^2 \partial y}H_0^{(2)}(hr) + 2\frac{\partial^3}{\partial x^2 \partial y}H_0^{(2)}(kr)\right] \quad , \end{aligned}$$

in which,

$$\frac{\partial}{\partial x}H_0^{(2)}(kr) = \frac{d}{dr}H_0^{(2)}(kr)\left(\frac{\partial r}{\partial x}\right) \quad , \tag{C12a}$$

$$\frac{\partial}{\partial y}H_0^{(2)}(kr) = \frac{d}{dr}H_0^{(2)}(kr)\left(\frac{\partial r}{\partial y}\right) \quad , \tag{C12b}$$

$$\frac{\partial^3}{\partial x^3}H_0^{(2)}(kr) = \frac{d^3}{dr^3}H_0^{(2)}(kr)\left(\frac{\partial r}{\partial x}\right)^3 + 3\frac{d^2}{dr^2}H_0^{(2)}(kr)\left(\frac{\partial r}{\partial x}\right)\left(\frac{\partial^2 r}{\partial x^2}\right) + \frac{d}{dr}H_0^{(2)}(kr)\left(\frac{\partial^3 r}{\partial x^3}\right) \quad , \tag{C12c}$$

$$\frac{\partial^3}{\partial y^3}H_0^{(2)}(kr) = \frac{d^3}{dr^3}H_0^{(2)}(kr)\left(\frac{\partial r}{\partial y}\right)^3 + 3\frac{d^2}{dr^2}H_0^{(2)}(kr)\left(\frac{\partial r}{\partial y}\right)\left(\frac{\partial^2 r}{\partial y^2}\right) + \frac{d}{dr}H_0^{(2)}(kr)\left(\frac{\partial^3 r}{\partial y^3}\right) \quad , \tag{C12d}$$

$$\frac{\partial^3}{\partial x \partial y^2}H_0^{(2)}(kr) = \frac{d^3}{dr^3}H_0^{(2)}(kr)\left(\frac{\partial r}{\partial x}\right)\left(\frac{\partial r}{\partial y}\right)^2 + \frac{d}{dr}H_0^{(2)}(kr)\left(\frac{\partial^3 r}{\partial x \partial y^2}\right) + \frac{d^2}{dr^2}H_0^{(2)}(kr)\left[\frac{\partial^2 r}{\partial y^2}\frac{\partial r}{\partial x} + 2\frac{\partial r}{\partial y}\frac{\partial^2 r}{\partial x \partial y}\right] \quad , \tag{C12e}$$

$$\frac{\partial^3}{\partial x^2 \partial y}H_0^{(2)}(kr) = \frac{d^3}{dr^3}H_0^{(2)}(kr)\left(\frac{\partial r}{\partial x}\right)^2\left(\frac{\partial r}{\partial y}\right) + \frac{d}{dr}H_0^{(2)}(kr)\left(\frac{\partial^3 r}{\partial x^2 \partial y}\right) + \frac{d^2}{dr^2}H_0^{(2)}(kr)\left[\frac{\partial^2 r}{\partial x^2}\frac{\partial r}{\partial y} + 2\frac{\partial r}{\partial x}\frac{\partial^2 r}{\partial x \partial y}\right] \quad , \tag{C12f}$$

with

$$\frac{d^3}{dr^3}H_0^{(2)}(kr) = k^3\left\{H_1^{(2)}(kr)\left[1 - \frac{2}{(kr)^2}\right] + \frac{1}{kr}H_0^{(2)}(kr)\right\} \quad , \tag{C12g}$$

and the derivatives of the distance r expressed as

$$\frac{\partial^3 r}{\partial x^3} = \frac{3x}{r^3}\left(-1 + \frac{x^2}{r^2}\right) \quad , \tag{C13a}$$

$$\frac{\partial^3 r}{\partial y^3} = \frac{3y}{r^3}\left(-1 + \frac{y^2}{r^2}\right) \quad , \tag{C13b}$$

$$\frac{\partial^3 r}{\partial x^2 \partial y} = \frac{y}{r^3}\left(-1 + 3\frac{x^2}{r^2}\right) \quad , \tag{C13c}$$

$$\frac{\partial^3 r}{\partial x \partial y^2} = \frac{x}{r^3}\left(-1 + 3\frac{y^2}{r^2}\right) \quad . \tag{C13d}$$

The expressions in Eq. (C12a) to Eq. (C12e) are the same for the function, $H_0^{(2)}(hr)$, except the wave number k is replaced by h.

C.1.2 Displacements and Stresses Caused by a Horizontal Line Load

Since the infinite space is homogeneous and isotropic, the solution developed for a vertical line load Q_Y can be reused for a horizontal line load Q_X by doing a coordinate transformation.

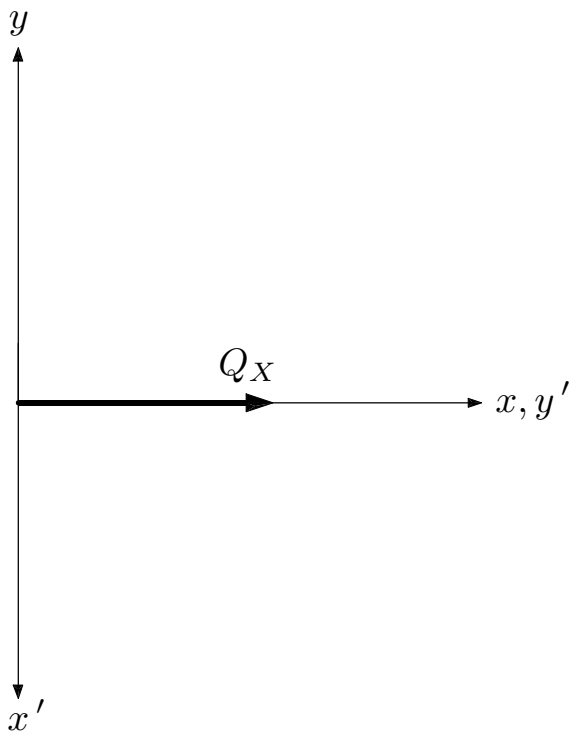

Figure C.2 – Horizontal Q_X Line Force Configuration.

Shown in Fig. C2 is an illustration of the horizontal line load in the x-direction using the (x, y) coordinate system. Also in the same figure is the (x', y') coordinate system.

The (x', y') system is rotated clockwise from the (x, y) system by $90°$. The orthogonal transformation between these systems can be expressed as

$$[Q(xy \longleftarrow x'y')] = \begin{bmatrix} 0 & 1 \\ -1 & 0 \end{bmatrix} \quad . \tag{C14}$$

To obtain the results for the horizontal point load Q_X, calculate the displacements and stresses in the (x', y') system using the expressions presented in Section C.1.1. This is done because Q_X is in the y'-direction, formerly the vertical direction. The values for the prime coordinates can be obtained from the position vector of the present configuration as

$$\begin{bmatrix} x' \\ y' \end{bmatrix} = [Q]^T \begin{bmatrix} x \\ y \end{bmatrix} = \begin{bmatrix} 0 & -1 \\ 0 & 1 \end{bmatrix} \begin{bmatrix} x \\ y \end{bmatrix} = \begin{bmatrix} -y \\ x \end{bmatrix} \quad . \tag{C15}$$

Use now the calculated displacements in the (x', y') system and transform them to the (x, y) system using

$$\begin{bmatrix} u_x \\ u_y \end{bmatrix} = [Q] \begin{bmatrix} u_{x'} \\ u_{y'} \end{bmatrix} = \begin{bmatrix} 0 & 1 \\ -1 & 0 \end{bmatrix} \begin{bmatrix} u_{x'} \\ u_{y'} \end{bmatrix} = \begin{bmatrix} u_{y'} \\ -u_{x'} \end{bmatrix} \quad . \tag{C16}$$

To transform the stress tensor, use the transformation of the form

$$[A(x, y)] = [Q][A(x', y')][Q]^T \quad , \tag{C17}$$

in which $[A]$ is any matrix, a tensor of second rank.

C.1.2.1 – Displacements

If the displacements in Section C.1 can be written in functional form as

$$\begin{bmatrix} U_{21}(x', y') \\ U_{22}(x', y') \end{bmatrix} \quad ,$$

then the displacements caused by a horizontal line load in the x-direction can be written as

$$\begin{bmatrix} U_{11}(x, y) \\ U_{12}(x, y) \end{bmatrix} = \begin{bmatrix} U_{22}(-y, x) \\ -U_{21}(-y, x) \end{bmatrix} \quad , \tag{C18}$$

in which the coordinates x, and y are the only parameters displayed because the material properties of the viscoelastic medium remain unchanged.

C.1.2.2 – Stresses

If the stress tensor in Section D.1 can be written in functional form as

$$\begin{bmatrix} \sigma_{xx_Y}(x',y') & \sigma_{xy_Y}(x',y') \\ \sigma_{yx_Y}(x',y') & \sigma_{yy_Y}(x',y') \end{bmatrix} \quad ,$$

then the stresses caused by a horizontal line load in the x-direction can be written as

$$\begin{bmatrix} \sigma_{xx_X}(x,y) & \sigma_{xy_X}(x,y) \\ \sigma_{yx_X}(x,y) & \sigma_{yy_X}(x,y) \end{bmatrix} = \begin{bmatrix} \sigma_{yy_Y}(-y,x) & -\sigma_{yx_Y}(-y,x) \\ -\sigma_{xy_Y}(-y,x) & \sigma_{xx_Y}(-y,x) \end{bmatrix} \quad . \qquad (C19)$$

C.1.3 Formation of [U] and [T]

Using the equations formulated in the two previous sections, the matrices $[U]$ and $[T]$ needed for the representation theorem can be formed as follows:

$$[U] = \begin{bmatrix} U_{11} & U_{12} \\ U_{21} & U_{22} \end{bmatrix} \quad , \qquad (C20)$$

$$[T] = \begin{bmatrix} T_{11} & T_{12} \\ T_{21} & T_{22} \end{bmatrix} \quad , \qquad (C21)$$

in which the matrix elements, T_{ij}, can be calculated as

$$\begin{bmatrix} T_{11} \\ T_{12} \end{bmatrix}^T = \begin{bmatrix} \sigma_{xx_X} & \sigma_{xy_X} \\ \sigma_{yx_X} & \sigma_{yy_X} \end{bmatrix} \begin{bmatrix} n_x \\ n_y \end{bmatrix} \quad , \qquad (C22)$$

and

$$\begin{bmatrix} T_{21} \\ T_{22} \end{bmatrix}^T = \begin{bmatrix} \sigma_{xx_Y} & \sigma_{xy_Y} \\ \sigma_{yx_Y} & \sigma_{yy_Y} \end{bmatrix} \begin{bmatrix} n_x \\ n_y \end{bmatrix} \quad . \qquad (C23)$$

In Eqn. (C22) and Eq. (C23), n_x and n_y are the direction cosines of the outer normal vector of the boundary surface.

C.2 Surface Green's Functions for a Semi-Infinite Medium

To obtain the two-dimensional Green's function matrices $[U]$ and $[T]$ for the surface of a semi-infinite medium, the solution for displacements and stresses caused by a line load must be considered. These solutions are available from the classical publication by Professor Horace Lamb (1903) in the Philosophical Transaction of the Royal Philosophical Society of London. In this section, the displacements and the line loads are all located at the surface of the semi-infinite space, simplifying the geometry of the problem.

The two rows of matrix $[T]$ contain the tractions at the observation point generated by the respective line loads described earlier. But since the stresses at the surface of the semi-infinite medium, by definition of the boundary conditions, are zero, the traction Green's function matrix $[T]$ is zero.

With the presence of the half-space surface, the mathematical formulation of the Green's functions become more tedious because of mode conversions between the P and SV waves. The advantage of a mirror image as exploited in Appendix B for SH-waves is no longer possible.

Using the notation adapted by Ewing et al (1957), and after a normalization with respect to $k_\beta = \omega/\beta$, the infinite integrals for the displacement Green's Functions can be expressed as:

$$U_{12} = \frac{i}{2\pi\mu}\int_{-\infty}^{\infty} \frac{k\left(2k^2 - 1 - 2\nu\nu'\right)}{F(k)}\, e^{-ia_0 kx}\, dk \qquad , \tag{C24}$$

$$U_{22} = -\frac{1}{2\pi\mu}\int_{-\infty}^{\infty} \frac{\nu}{F(k)}\, e^{-ia_0 kx}\, dk \qquad , \tag{C25}$$

$$U_{11} = -\frac{1}{2\pi\mu}\int_{-\infty}^{\infty} \frac{\nu'}{F(k)}\, e^{-ia_0 kx}\, dk \qquad , \tag{C26}$$

$$U_{21} = -\frac{i}{2\pi\mu}\int_{-\infty}^{\infty} \frac{k\left(2k^2 - 1 - 2\nu\nu'\right)}{F(k)}\, e^{-ia_0 kx}\, dk \qquad , \tag{C27}$$

in which $a_0 = \omega/\beta$, $\nu = \sqrt{k^2 - \gamma^2}$, $\nu' = \sqrt{k^2 - 1}$, $\gamma = \beta/\alpha$, and $F(k)$ is the well-known Rayleigh Determinant defined as $F(k) = (2k^2 - 1)^2 - 4k^2\nu\nu'$. The magnitude of the vertical and horizontal line sources were set at 1.

As it is given from Eq. (C24) to Eq. (C27), the infinite integrals are too complicated to be evaluated analytically. They are also not amenable to numerical methods because the Rayleigh Determinant has a root, known as the Rayleigh Pole, at $k = s$, within the interval of integration. For example, when $\gamma = \beta/\alpha = 1/2$, $s = 1.07236$. The location of the Rayleigh Poleon the k-axis is dependent on material properties, it represents physically the Rayleigh Surface Wave generated by the line sources.

Using a complex contour integration scheme as shown in detail in Chapter 2 of Ewing et al (1957), the infinite integral can be transformed into combination of finite integrals and residues that are relatively simple to evaluate numerically. They are shown below:

$$\begin{aligned}\pi\mu U_{11} = {} & i\pi \frac{\sqrt{s^2-1}}{\Delta_o'(s,\gamma)} e^{-ia_0 sx} - i\int_0^{\gamma} \frac{\sqrt{1-k^2}}{\Delta_1(k,\gamma)} e^{-ia_0 kx} dk \\ & - i\int_{\gamma}^{1} \frac{(2k^2-1)^2\sqrt{1-k^2}}{\Delta_2(k,\gamma)} e^{-ia_0 kx} dk + \int_0^{\infty} \frac{\sqrt{1+k^2}}{\Delta_3(k,\gamma)} e^{-a_0 kx} dk \quad ,\end{aligned} \tag{C28}$$

$$\begin{aligned}\pi\mu U_{21} = {} & -\pi \frac{s(2s^2-1) - 2s\sqrt{s^2-\gamma^2}\sqrt{s^2-1}}{\Delta_0'(s,\gamma)} e^{-ia_0 sx} \\ & + 2\int_{\gamma}^{1} \frac{k(2k^2-1)\sqrt{k^2-\gamma^2}\sqrt{1-k^2}}{\Delta_2(k,\gamma)} e^{-ia_0 kx}\, dk \quad ,\end{aligned} \tag{C29}$$

$$\pi\mu U_{12} = -\pi\mu U_{21} \quad , \tag{C30}$$

and

$$\pi\mu U_{22} = i\pi\frac{\sqrt{s^2-\gamma^2}}{\Delta_o'(s,\gamma)}e^{-ia_0sx} - i\int_0^{\gamma}\frac{\sqrt{\gamma^2-k^2}}{\Delta_1(k,\gamma)}e^{-ia_0kx}dk$$
$$- i\int_{\gamma}^{1}\frac{4k^2(k^2-\gamma^2)\sqrt{1-k^2}}{\Delta_2(k,\gamma)}e^{-ia_0kx}dk + \int_0^{\infty}\frac{\sqrt{k^2+\gamma^2}}{\Delta_3(k,\gamma)}e^{-a_0kx}dk \quad . \tag{C31}$$

In the above expressions, the important functions and parameters are

$$\Delta_0(k,\gamma) = (2k^2-1)^2 - 4k^2\upsilon\upsilon',$$
$$\Delta_1(k,\gamma) = (2k^2-1)^2 + 4k^2\sqrt{\gamma^2-k^2}\sqrt{1-k^2},$$
$$\Delta_2(k,\gamma) = (2k^2-1)^4 + 16k^4(k^2-\gamma^2)(1-k^2),$$
$$\Delta_3(k,\gamma) = (2k^2+1)^2 - 4k^2\sqrt{k^2+\gamma^2}\sqrt{k^2+1},$$
$$\Delta_0'(s,\gamma) = \frac{d}{dk}\Delta_0(k,\gamma)\bigg|_{k=s}$$
$$\Delta_0'(s,\gamma) = 8s\left[(2s^2-1) - \sqrt{s^2-\gamma^2}\sqrt{s^2-1}\right] - \frac{4s^3(2s^2-(1+\gamma^2))}{\sqrt{s^2-\gamma^2}\sqrt{s^2-1}}$$
$$\upsilon = \sqrt{k^2-\gamma^2},$$
$$\upsilon' = \sqrt{k^2-1},$$
$$a_0 = \omega b/\beta,$$

and

$$\gamma = \beta/\alpha.$$

The ratio of wave velocities, γ, can be expressed in terms of the Poisson Ratio, $\bar{\nu}$, as $\gamma = \sqrt{(1-2\bar{\nu})/(2(1-\bar{\nu}))}$.

The basic soil properties referenced, α, β and $\bar{\nu}$ are the compressional wave velocity, shear wave velocity and the Poisson's ratio for the semi-infinite medium, respectively. In elasticity, a combination of any two material constants is sufficient to uniquely determine a medium. The value of $s = c_R/\beta$, is the ratio of the Rayliegh Wave velocity c_R to the

shear wave velocity β. The value of s is the root of the equation $\Delta_0(s,\gamma) = 0$. Some frequently used values of s are 1.14412, 1.08766, 1.07236 and 1.04678 for γ^2 of $\frac{1}{2}$, $\frac{1}{3}$, $\frac{1}{4}$ and 0, repsectively.

The expressions in Eq. (C28) through Eq. (C31) contain many terms and each term has physical significance. The terms which contain $\Delta_0'(s,\gamma)$ as denominator are the Rayleigh surface wave terms and they are the residues from contour integration. The wave speed is a constant c_R controlled by the value of s in the complex exponential. The terms containing $\sqrt{1-k^2}$ are the contributions from S-waves; the radical expression is equivalent to a cosine function and the integral from 0 to 1 is a summation of all S-waves with a range of incident angles. Similarly, the integrals from 0 to γ which contains the radical $\sqrt{\gamma^2-k^2}$ represent the contributions from the P-waves. The range of admissible angles for P-waves is limited by a critical angle which is a function of the material properties. Additional waves beyond those described are not plane waves and they have complex amplitudes; their summation is acccomplished by the infinite integral.

The process to obtain the contour integration expressions is tedious, but the results can be coded simply in computer programs. Most integrals are finite and the four infinite integrals have exponentially decaying integrands. The computational effort is minimal. The difficulties which could arise numerically are either (1) the frequency ω is too high so that the integration of the harmonic functions is a challenge, or (2) the value of x is too small. For the latter case, the infinite integrals approach infinity as a logarithmic function. Therefore, the singular term of this set of Green's functions is the same as all other two-dimensional Grren's Functions discussed throughout this dissertation.

Appendix D

Wave Motion in a Semi-Infinite Medium

D.1 – Two-Dimensional Plane-Strain Problem

A general three-dimensional wave field can be represented by the superpostion of plane waves, therefore, it is a useful exercise to prepare an expression for several fundamental waves.

The displacements in elastic wave propagation can be expressed in terms of derivatives of two potential functions, ϕ and $\vec{\psi}$. The compressional wave potential, ϕ, is a scalar but the shear wave potential, $\vec{\psi}$, is a vector. For the two-dimensional plane strain wave problem under consideration, the z-component of the vector, ψ_z, is used and will be denoted as the scalar symbol ψ herein. The in-plane horizontal displacement, u, and the vertical displacement, v, can be written as (Ewing et al, 1957),

$$u = \frac{\partial \phi}{\partial x} + \frac{\partial \psi}{\partial y} \quad , \tag{D.1a}$$

and

$$v = \frac{\partial \phi}{\partial y} - \frac{\partial \psi}{\partial x} \quad , \tag{D.1b}$$

respectively. Defining the LaPlacian operator in two dimensions as

$$\nabla^2 = \frac{\partial^2}{\partial x^2} + \frac{\partial^2}{\partial y^2} \quad , \tag{D.2}$$

the two-dimensional stresses are then

$$\begin{aligned} \tau_{xx} &= \lambda \nabla^2 \phi + 2\mu \frac{\partial^2 \phi}{\partial x^2} + 2\mu \frac{\partial^2 \psi}{\partial x \partial y} \\ &= (\lambda + 2\mu)\nabla^2 \phi - 2\mu \frac{\partial^2 \phi}{\partial y^2} + 2\mu \frac{\partial^2 \psi}{\partial x \partial y} \quad , \end{aligned} \tag{D.3a}$$

$$\tau_{yy} = \lambda\nabla^2\phi + 2\mu\frac{\partial^2\phi}{\partial y^2} - 2\mu\frac{\partial^2\psi}{\partial x\partial y} \qquad (D.3b)$$
$$= (\lambda + 2\mu)\nabla^2\phi - 2\mu\frac{\partial^2\phi}{\partial x^2} - 2\mu\frac{\partial^2\psi}{\partial y\partial x} \quad ,$$

and

$$\tau_{xy} = \tau_{yx} = 2\mu\frac{\partial^2\phi}{\partial x\partial y} + \mu\frac{\partial^2\psi}{\partial y^2} - \mu\frac{\partial^2\psi}{\partial x^2} \quad . \qquad (D.3c)$$

D.2 – Incident P-Wave Solution

Let ϕ^i be the incident P-wave potential function, ϕ^r be the reflected P-wave potential function and ψ^rbe the reflected SV-wave potential function. An additional shear wave reflection, represented by ψ^r, is also necessary to satisfy both normal and shear stress boundary conditions at the free surface as shown in Fig. D.1.

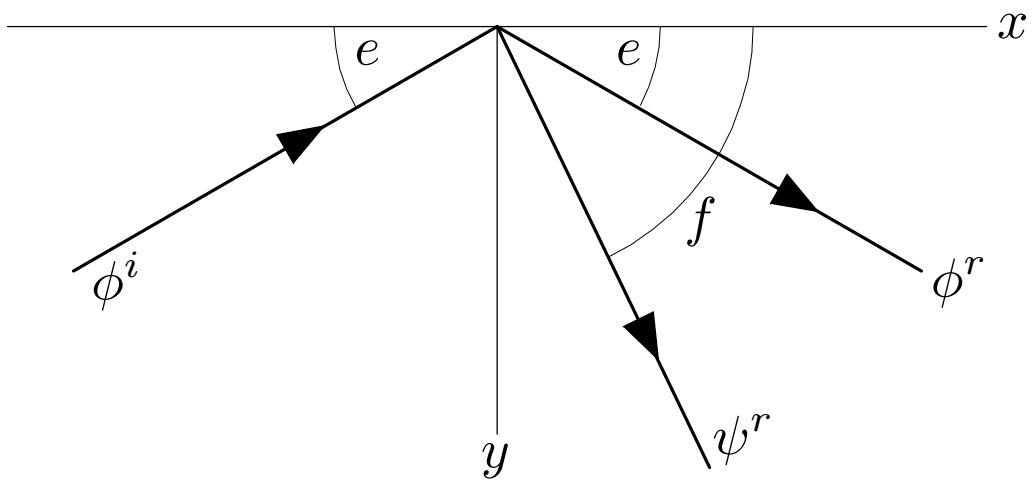

Figure D.1 – Incident and reflected P-wave.

Define the potentials as

$$\phi^i = Ae^{-ih(x\cos e - y\sin e)} \quad , \tag{D.4a}$$

$$\phi^r = Be^{-ih(x\cos e + y\sin e)} \quad , \tag{D.4b}$$

$$\psi^r = Ce^{-ik(x\cos f + y\sin f)} \quad , \tag{D.4c}$$

with $h = \omega/\alpha$ and $k = \omega/\beta$ defined as the wave numbers. The second partial derivatives of the potential functions can be written in the form

$$\frac{\partial^2\phi^i}{\partial x^2} = (-ih\cos e)^2\phi^i \quad , \tag{D.5a}$$

$$\frac{\partial^2\phi^r}{\partial x^2} = (-ih\cos e)^2\phi^r \quad , \tag{D.5b}$$

$$\frac{\partial^2\psi^r}{\partial x^2} = (-ik\cos f)^2\psi^r \quad , \tag{D.5c}$$

$$\frac{\partial^2\phi^i}{\partial y^2} = (ih\sin e)^2\phi^i \quad , \tag{D.5d}$$

$$\frac{\partial^2\phi^r}{\partial y^2} = (-ih\sin e)^2\phi^r \quad , \tag{D.5e}$$

$$\frac{\partial^2\psi^r}{\partial y^2} = (-ik\sin f)^2\psi^r \quad , \tag{D.5f}$$

$$\frac{\partial^2\phi^i}{\partial x\partial y} = (-ih\cos e)(ih\sin e)\phi^i \quad , \tag{D.5g}$$

$$\frac{\partial^2\phi^r}{\partial x\partial y} = (-ih\cos e)(-ih\sin e)\phi^r \quad , \tag{D.5h}$$

$$\frac{\partial^2\psi^r}{\partial x\partial y} = (-ik\cos f)(-ik\sin f)\psi^r \quad . \tag{D.5i}$$

Now apply the boundary conditions, $\tau_{yy}|_{y=0} = 0$ and $\tau_{yx}|_{y=0} = 0$. The first boundary condition yields,

$$\begin{aligned}\tau_{yy}|_{y=0} = \lambda(-h^2\cos^2 e)[A+B]e^{-ihx\cos e} + (\lambda+2\mu)(-h^2\sin^2 e)[A+B]e^{-ihx\cos e} \\ - 2\mu(-k^2\sin f\cos f)Ce^{-ikx\cos f} \quad ,\end{aligned} \tag{D.6}$$

and for the second boundary condition, $\tau_{yy}|_{y=0} = 0$, to be true over the entire range of x, the following requirement,

$$-ihx\cos e = -ikx\cos f \qquad , \tag{D.7}$$

is necessary. The above relationship defines the angle, f, based on the incident angle, e. The first boundary condition yields the following expression for the unknown coefficients,

$$\begin{aligned}[(\lambda+2\mu)(-h^2)+2\mu h^2\cos^2 e]A \\ +[(\lambda+2\mu)(-h^2)+2\mu h^2\cos^2 e]B+[2\mu k^2\sin f\cos f]C=0\ .\end{aligned} \tag{D.8}$$

The second boundary condition yields the relationship,

$$\begin{aligned}\tau_{yx}|_{y=0} = 2\mu(h^2\cos e\sin e)[A-B]e^{-ihx\cos e}+\mu(-k^2\sin^2 f)Ce^{-ikx\cos f} \\ -\mu(-k^2\cos^2 f)Ce^{-ikx\cos f} \qquad ,\end{aligned} \tag{D.9}$$

and with the relationship, $-ihx\cos e = -ikx\cos f$, the second simultaneous equation for the unknown coefficients is

$$\mu[2h^2\cos e\sin e]A-\mu[2h^2\cos e\sin e]B+\mu[k^2(\cos^2 f-\sin^2 f)]C=0\ . \tag{D.10}$$

The simultaneous equations for unknowns B/A and C/A can be written in matrix form as

$$\begin{aligned}\begin{bmatrix}(\lambda+2\mu)(-h^2)+2\mu h^2\cos^2 e & 2\mu k^2\sin f\cos f \\ 2\mu h^2\cos e\sin e & -\mu k^2(\cos^2 f-\sin^2 f)\end{bmatrix}\begin{Bmatrix}B/A\\ C/A\end{Bmatrix} \\ =\begin{Bmatrix}(\lambda+2\mu)h^2-2\mu h^2\cos^2 e\\ 2\mu h^2\cos e\sin e\end{Bmatrix}\end{aligned} \quad . \tag{D.11}$$

Define now the important material constant,

$$\gamma^2=\frac{h^2}{k^2}=\frac{\omega^2/\alpha^2}{\omega^2/\beta^2}=\frac{\beta^2}{\alpha^2}=\left(\frac{\beta}{\alpha}\right)^2 \qquad , \tag{D.12}$$

which can be related to the Lame constant as

$$\gamma^2 = \frac{\beta^2}{\alpha^2} = \frac{\mu/\rho}{(\lambda+2\mu)/\rho} = \frac{\mu}{\lambda+2\mu} \qquad . \tag{D.13}$$

With these new definitions, the matrix equation simplifies to

$$\begin{bmatrix} -\gamma^2 + 2\gamma^4 \cos^2 e & 2\gamma^2 \sin f \cos f \\ 2\gamma^2 \cos e \sin e & 1 - 2\cos^2 f \end{bmatrix} \begin{Bmatrix} B/A \\ C/A \end{Bmatrix} = \begin{Bmatrix} \gamma^2 - 2\gamma^4 \cos^2 e \\ 2\gamma^2 \cos e \sin e \end{Bmatrix} \quad . \tag{D.14}$$

The determinant of the matrix on the left side is

$$\begin{aligned} \Delta &= (-\gamma^2 + 2\gamma^4 \cos^2 e)(1 - 2\cos^2 f) - 4\gamma^4 \sin f \cos f \cos e \sin e \\ &= -\gamma^2(1 - 2\gamma^2 \cos^2 e)(1 - 2\cos^2 f) - 4\gamma^4 \sin f \cos f \cos e \sin e \end{aligned} \quad . \tag{D.15}$$

More simplification can be accomplished by recognizing that $h \cos e = k \cos f$, using the relationship,

$$\cos f = \frac{h}{k} \cos e = \gamma \cos e \qquad , \tag{D.16}$$

The determinant can be written in a better form:

$$\Delta = -\gamma^2(1 - 2\gamma^2 \cos^2 e)^2 - 4\gamma^4 \sin f \cos f \cos e \sin e \qquad . \tag{D.17}$$

Using Cramer's Rule for the matrix equation, the solution for the unknown coefficients is

$$\begin{aligned} \frac{B}{A} &= \frac{1}{\Delta} \begin{vmatrix} \gamma^2(1 - 2\gamma^2 \cos^2 e)^2 & 2\gamma^2 \sin f \cos f \\ 2\gamma^2 \cos e \sin e & 1 - 2\cos^2 f \end{vmatrix} \\ &= \frac{1}{\Delta} \left[\gamma^2(1 - 2\gamma^2 \cos^2 e)^2 - 4\gamma^4 \sin f \cos f \cos e \sin e\right] \end{aligned} \quad , \tag{D.18}$$

and

$$\begin{aligned} \frac{C}{A} &= \frac{1}{\Delta} \begin{vmatrix} -\gamma^2(1 - 2\gamma^2 \cos^2 e)^2 & \gamma^2(1 - 2\gamma^2 \cos^2 e)^2 \\ 2\gamma^2 \cos e \sin e 2\gamma^2 \cos e \sin e & \end{vmatrix} \\ &= \frac{1}{\Delta} \left[-4\gamma^4(1 - 2\gamma^2 \cos^2 e) \cos e \sin e\right] \end{aligned} \quad . \tag{D.19}$$

The above expressions are amenable to numerical computation, but a more symmetrical expression can be obtained using the expression $\cos f = \gamma \cos e$. Manipulation by trigonometric identities yields,

$$\sin^2 f = 1 - \cos^2 f = 1 - \gamma^2 \cos^2 e \quad , \tag{D.20}$$

$$\begin{aligned} \tan^2 f = \frac{\sin^2 f}{\cos^2 f} &= \frac{1 - \gamma^2 \cos^2 e}{\gamma^2 \cos^2 e} = \frac{\sin^2 e + \cos^2 e - \gamma^2 \cos^2 e}{\gamma^2 \cos^2 e} \\ &= \frac{1}{\gamma^2} \tan^2 e + \frac{(1 - \gamma^2)}{\gamma^2} \end{aligned} \quad , \tag{D.21}$$

and

$$\sin f \cos f = \tan f \cos^2 f = \gamma^2 \tan f \cos^2 e \quad . \tag{D.22}$$

With the angle e given as the input parameter, the first step is to determine $\tan f$ using Eq. (D.21) and then calculate the coefficients B/A and C/A using the expressions

$$\frac{B}{A} = \frac{-(1 - 2\gamma^2 \cos^2 e)^2 + 4\gamma^4 \tan f \sin e \cos^3 e}{(1 - 2\gamma^2 \cos^2 e)^2 + 4\gamma^4 \tan f \sin e \cos^3 e} \quad , \tag{D.23}$$

and

$$\frac{C}{A} = \frac{4\gamma^2 (1 - 2\gamma^2 \cos^2 e) \cos e \sin e}{(1 - 2\gamma^2 \cos^2 e)^2 + 4\gamma^4 \tan f \sin e \cos^3 e} \quad . \tag{D.24}$$

The value of A can be determined from the amplitude of the incident P-wave, $|P|$, of a compressional displacement pulse. The horizontal and vertical displacements of the incident pulse are

$$u^i = \frac{\partial \phi^i}{\partial x} = (-ih \cos e) \phi^i \quad , \tag{D.25a}$$

and

$$v^i = \frac{\partial \phi^i}{\partial y} = (ih \sin e) \phi^i \quad , \tag{D.25b}$$

respectively. Now compute the magnitude, $|P|$, from the displacements,

$$|P| = \sqrt{(u^i)^2 + (v^i)^2} = \sqrt{i^2 h^2 \cos^2 e \, A^2 + i^2 h^2 \sin^2 e \, A^2} = ihA \quad , \tag{D.26}$$

and in turn the coefficient A can be specified as

$$A = \frac{|P|}{ih} \qquad . \tag{D.27}$$

D.2.1 – Displacement Wavefields for Incident P-Waves

With the unknown coefficients determined, the horizontal displacement for all x and for $y \geq 0$, is

$$u = \frac{\partial \phi}{\partial x} + \frac{\partial \psi}{\partial y} = -ih \cos e \left(\phi^i + \phi^r\right) - ik \sin f \psi^r \qquad . \tag{D.28}$$

Using the relationships

$$k\gamma = \frac{\omega}{\beta}\frac{\beta}{\alpha} = \frac{\omega}{\alpha} = h \qquad , \tag{D.29}$$

and

$$k \sin f = k \tan f \cos f = \tan f \, k\gamma \cos e = h \tan f \cos e \qquad , \tag{D.30}$$

the horizontal displacement within the semi-infinite medium can be written as

$$u(x,y) = -ih \cos e \left[\phi^i(x,y) + \phi^r(x,y) + \tan f \psi^r(x,y)\right] \qquad . \tag{D.31}$$

and the horizontal displacement at the free surface is simply,

$$|u(x,0)| = P \cos e \left(1 + \frac{B}{A} + \frac{C}{A} \tan f\right) \qquad . \tag{D.32}$$

The vertical displacement for all x and $y \geq 0$ is,

$$v = \frac{\partial \phi}{\partial y} - \frac{\partial \psi}{\partial x} = ih \sin e \left(\phi^i - \phi^r\right) - (-ik \cos f)\psi^r \qquad . \tag{D.33}$$

Using the relationship between the angles,

$$k \cos f = k\gamma \cos e = \frac{\omega}{\beta}\frac{\beta}{\alpha} \cos e = h \cos e \qquad , \tag{D.34}$$

then

$$v(x,y) = ih\sin e\left[\phi^i(x,y) - \phi^r(x,y)\right] + ih\cos e\,\psi^r(x,y) \qquad . \qquad (D.35)$$

The vertical displacement at the free surface of the semi-infinite medium is

$$|v(x,0)| = P\left[\sin e\left(1 - \frac{B}{A}\right) + \frac{C}{A}\cos e\right] \qquad . \qquad (D.36)$$

Since the above expressions are strongly influenced by the ratio of shear to compressional wave speeds, γ, it is convenient to relate γ to the Poisson's Ratio, in this manner:

$$\gamma^2 = \frac{(1-2\nu)}{2(1-\nu)} \qquad . \qquad (D.37)$$

Using $\nu = 1/3$, $\gamma^2 = 1/4$, the normalized amplitudes for a unit, incident P-wave are

e	u^{ff}	v^{ff}
10°	0.8792	0.5283
20°	1.2745	0.8581
30°	1.3949	1.1168
40°	1.3507	1.3488
50°	1.1966	1.5597
60°	0.9633	1.7411
70°	0.6733	1.8812
80°	0.3460	1.9697
90°	0.0000	2.0000

D.2.2 – Stress Wavefields for Incident P-Waves

For the purpose of calculating tractions at the wave scatterer's surface, it is necessary to hae the expressions for the stresses. Using the known coefficients, A, B/A, C/A in terms

of P in eqns. (D.27), (D.23) and (D.24), respectively, the stresses can be expressed as

$$\tau_{xx} = \mu \left[(2h^2 \sin^2 e - k^2) \left(\phi^i(x,y) + \phi^r(x,y) \right) - 2k^2 \sin f \cos f \psi^r(x,y) \right] \quad , \tag{D.38}$$

$$\tau_{yy} = \mu \left[(2h^2 \cos^2 e - k^2) \left(\phi^i(x,y) + \phi^r(x,y) \right) + 2k^2 \sin f \cos f \psi^r(x,y) \right] \quad , \tag{D.39}$$

$$\tau_{xy} = \mu \left[2h^2 \sin e \cos e \left(\phi^i(x,y) - \phi^r(x,y) \right) + k^2 (\cos^2 f - \sin^2 f) \psi^r(x,y) \right] \quad , \tag{D.40}$$

in which the functions $\phi^i(x,y)$, $\phi^r(x,y)$ and $\psi^r(x,y)$ are given in eqns. (D.4a), (D.4b) and (D.4c), respectively.

D.3 – Incident SV-Wave Problem

Let ψ^i be the incident SV-wave potential function with a yet to be defined amplitude D, ψ^r be the reflected SV-wave potential function and ϕ^r be the reflected P-wave potential function written in the form,

$$\psi^i = D e^{-ik(x \cos f - y \sin f)} \quad , \tag{D.41a}$$

$$\psi^r = E e^{-ik(x \cos f + y \sin f)} \quad , \tag{D.41b}$$

and

$$\phi^r = F e^{-ih(x \cos e + y \sin e)} \quad , \tag{D.41c}$$

in which $h = \omega/\alpha$ and $k = \omega/\beta$ are the wave numbers. The unknown coefficients, E and F are to be determined later using the boundary conditions. Similar to the incident P-wave problem, ϕ^r is necessary to satisfy both boundary conditions at the free surface.

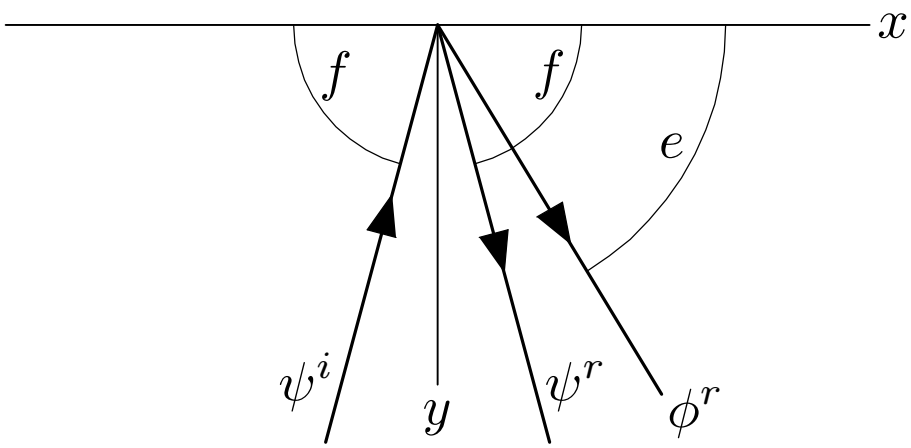

Figure D.2 – Incident and reflected SV-wave.

The second partial derivatives of the potential functions can be listed as

$$\frac{\partial^2\psi^i}{\partial x^2} = (-ik\cos f)^2\psi^i \quad , \tag{D.42a}$$

$$\frac{\partial^2\psi^r}{\partial x^2} = (-ik\cos f)^2\psi^r \quad , \tag{D.42b}$$

$$\frac{\partial^2\phi^r}{\partial x^2} = (-ih\cos e)^2\phi^r \quad , \tag{D.42c}$$

$$\frac{\partial^2\psi^i}{\partial y^2} = (ik\sin f)^2\psi^i \quad , \tag{D.42d}$$

$$\frac{\partial^2\psi^r}{\partial y^2} = (-ik\sin f)^2\psi^r \quad , \tag{D.42e}$$

$$\frac{\partial^2\phi^r}{\partial y^2} = (-ih\sin e)^2\phi^r \quad , \tag{D.42f}$$

$$\frac{\partial^2\psi^i}{\partial x\partial y} = (-ik\cos f)(ik\sin f)\psi^i \quad , \tag{D.42g}$$

$$\frac{\partial^2\psi^r}{\partial x\partial y} = (-ik\cos f)(-ik\sin f)\psi^r \quad , \tag{D.42h}$$

$$\frac{\partial^2\phi^r}{\partial x\partial y} = (-ih\cos e)(-ih\sin e)\phi^r \quad . \tag{D.42i}$$

Now apply the boundary conditions, $\tau_{yy}|_{y=0} = 0$ and $\tau_{yx}|_{y=0} = 0$. The first boundary condition yields,

$$\tau_{yy}|_{y=0} = \lambda(-h^2\cos^2 e)Fe^{-ihx\cos e} + (\lambda+2\mu)(-h^2\sin^2 e)Fe^{-ihx\cos e} \\ - 2\mu(-k^2\sin f\cos f\ D - k^2\sin f\cos f\ E)e^{-ikx\cos f} \qquad , \qquad (D.43)$$

For the second boundary condition, $\tau_{yy}|_{y=0} = 0$, to be true over the entire range of x, the following requirement,

$$-ihx\cos e = -ikx\cos f \qquad , \qquad (D.44)$$

is necessary. The above relationship defines e based on f, the incident angle. The first boundary condition also yields the following expression for the unknown coefficients,

$$-h^2(\lambda + 2\mu\sin^2 e)F - [2\mu k^2\sin f\cos f](D-E) = 0 \qquad . \qquad (D.45)$$

The second boundary condition yields the relationship,

$$\tau_{yx}|_{y=0} = 2\mu(-h^2\sin e\cos e)Fe^{-ihx\cos e} + \mu(-k^2\sin^2 f)[D+E]e^{-ikx\cos f} \\ - \mu(-k^2\cos^2 f)[D+E]e^{-ikx\cos f} \qquad , \qquad (D.46)$$

With the relationship, $-ihx\cos e = -ikx\cos f$, the second simultaneous equation for the unknown coefficients is

$$-2\mu h^2\sin e\cos e\ F + \mu k^2(\cos^2 f - \sin^2 f)[D+E] = 0 \qquad . \qquad (D.47)$$

The simultaneous equations for unknowns E/D and F/D can be written in matrix form as

$$\begin{bmatrix} 2\mu k^2\sin f\cos f & -h^2(\lambda+2\mu\sin^2 e) \\ \mu k^2(\sin^2 f - \cos^2 f) & 2\mu h^2\sin e\cos e \end{bmatrix} \begin{Bmatrix} E/D \\ F/D \end{Bmatrix} \\ = \begin{Bmatrix} 2\mu k^2\sin f\cos f \\ \mu k^2(\cos^2 f - \sin^2 f) \end{Bmatrix} \qquad . \qquad (D.48)$$

Now define the important material constant,

$$\gamma^2 = \frac{h^2}{k^2} = \frac{\omega^2/\alpha^2}{\omega^2/\beta^2} = \frac{\beta^2}{\alpha^2} = \left(\frac{\beta}{\alpha}\right)^2 \qquad , \tag{D.49}$$

which can be related to the Lame constant as

$$\gamma^2 = \frac{\beta^2}{\alpha^2} = \frac{\mu/\rho}{(\lambda+2\mu)/\rho} = \frac{\mu}{\lambda+2\mu} \qquad . \tag{D.50}$$

With the new definitions, the matrix equation simplifies to

$$\begin{bmatrix} 2\sin f\cos f & -1+2\gamma^2\cos^2 e \\ \sin^2 f - \cos^2 f & 2\gamma^2 \sin e\cos e \end{bmatrix} \begin{Bmatrix} E/D \\ F/D \end{Bmatrix} = \begin{Bmatrix} 2\sin f\cos f \\ (\cos^2 f - \sin^2 f) \end{Bmatrix} \qquad . \tag{D.51}$$

The determinant of the matrix on the left side of the equation is

$$\Delta = (1-2\gamma^2\cos^2 e)(1-2\cos^2 f) + 4\gamma^2 \sin f\cos f\sin e\cos e \qquad . \tag{D.52}$$

More simplification can be accomplished by recognizing that $h\cos e = k\cos f$, and using the relationship,

$$\cos f = \frac{h}{k}\cos e = \gamma\cos e \qquad , \tag{D.53}$$

the determinant can be written in a better form:

$$\Delta = (1-2\gamma^2\cos^2 e)^2 + 4\gamma^2 \sin f\cos f\sin e\cos e \qquad . \tag{D.54}$$

Using Cramer's Rule for the matrix equation, the solution for the unknown coefficients is,

$$\begin{aligned} \frac{E}{D} &= \frac{1}{\Delta}\begin{vmatrix} 2\sin f\cos f & -1+2\gamma^2\cos^2 e \\ (\cos^2 f - \sin^2 f) & 2\gamma^2\sin e\cos e \end{vmatrix} \\ &= \frac{-(1-2\gamma^2\cos^2 e)^2 + 4\gamma^2\sin f\cos f\sin e\cos e}{(1-2\gamma^2\cos^2 e)^2 + 4\gamma^2\sin f\cos f\sin e\cos e} \qquad , \end{aligned} \tag{D.55}$$

and

$$\begin{aligned} \frac{F}{D} &= \frac{1}{\Delta}\begin{vmatrix} 2\sin f\cos f & 2\sin f\cos f \\ \sin^2 f - \cos^2 f & (\cos^2 f - \sin^2 f) \end{vmatrix} \\ &= \frac{-4\sin f\cos f(1-2\gamma^2\cos^2 e)}{(1-2\gamma^2\cos^2 e)^2 + 4\gamma^2\sin f\cos f\sin e\cos e} \qquad . \end{aligned} \tag{D.56}$$

The value of D can be determined from the amplitude of the incident SV-wave, $|S|$, of a shear displacement pulse. The horizontal and vertical displacements of the incident pulse are

$$u^i = \frac{\partial \psi^i}{\partial y} = (ik \sin f)\psi^i \qquad , \qquad (D.57a)$$

and

$$v^i = -\frac{\partial \psi^i}{\partial x} = (ik \cos f)\psi^i \qquad , \qquad (D.57b)$$

respectively. Now compute the magnitude, $|S|$, from the displacements,

$$|S| = \sqrt{(u^i)^2 + (v^i)^2} = \sqrt{i^2 k^2 \sin^2 f \; D^2 + i^2 k^2 \cos^2 f \; D^2} = ikD \qquad , \qquad (D.58)$$

or

$$D = \frac{|S|}{ik} \qquad . \qquad (D.59)$$

D.3.1 – Displacement Wavefields for Incident SV-waves

With the unknown coefficients determined, the horizontal displacement for all x and for $y \geq 0$, is

$$u = \frac{\partial \phi}{\partial x} + \frac{\partial \psi}{\partial y} = -(ih \cos e)\phi^r + ik \sin f \left(\psi^i - \psi^r\right) \qquad . \qquad (D.60)$$

Using the relationship

$$k\gamma = \frac{\omega}{\beta}\frac{\beta}{\alpha} = \frac{\omega}{\alpha} = h \qquad , \qquad (D.61)$$

and

$$k \sin f = k \tan f \cos f = \tan f \, k\gamma \cos e = h \tan f \cos e \qquad , \qquad (D.62)$$

the horizontal displacement within the semi-infinite medium can be written as

$$u(x,y) = ik \left[(-\gamma \cos e)\phi^r(x,y) + \sin f \left(\psi^i(x,y) - \psi^r(x,y)\right)\right] \qquad , \qquad (D.63)$$

and the horizontal displacement at the free surface is simply,

$$|u(x,0)| = S\left[\left(1-\frac{E}{D}\right)\sin f - \frac{F}{D}(\gamma\cos e)\right] \qquad . \qquad (D.64)$$

The vertical displacement for all x and $y \geq 0$, is

$$v = \frac{\partial\phi}{\partial y} - \frac{\partial\psi}{\partial x} = -(ih\sin e)\phi^r + (ik\cos f)\left(\psi^i + \psi^r\right) \qquad . \qquad (D.65)$$

Using the relationship

$$k\gamma = h \qquad , \qquad (D.66)$$

then

$$v(x,y) = ik\left[(-\gamma\sin e)\phi^r(x,y) + \cos f\left(\psi^i(x,y) + \psi^r(x,y)\right)\right] \qquad . \qquad (D.67)$$

The vertical displacement at the free surface of the semi-infinite medium is

$$|v(x,0)| = S\left[\left(1+\frac{E}{D}\right)\cos f - \frac{F}{D}\gamma\sin e\right] \qquad . \qquad (D.68)$$

Using $\nu = 1/3$ or $\gamma^2 = 1/4$, the normalized amplitudes for a unit, incident SV-wave are

e	u^{ff}	v^{ff}
$60°$	3.4179	0.0000
$65°$	1.9877	0.6984
$70°$	1.9268	0.6275
$75°$	1.9438	0.4970
$80°$	1.9717	0.3417
$85°$	1.9925	0.1736
$90°$	2.0000	0.0000

D.3.2 – Stress Wavefields for Incident SV-Waves

Using the known coefficients, D, E/D, F/D in terms of S in eqns. (D.59), (D.55) and (D.56), respectively, the stresses can be expressed as

$$\tau_{xx} = \mu \left[(2h^2 \sin^2 e - k^2)\phi^r(x,y) + 2k^2 \sin f \cos f \left(\psi^i(x,y) - \psi^r(x,y) \right) \right] \quad , \tag{D.69}$$

$$\tau_{yy} = \mu \left[(2h^2 \cos^2 e - k^2)\phi^r(x,y) - 2k^2 \sin f \cos f \left(\psi^i(x,y) - \psi^r(x,y) \right) \right] \quad , \tag{D.70}$$

$$\tau_{xy} = \mu \left[-2h^2 \sin e \cos e \phi^r(x,y) + k^2 (\cos^2 f - \sin^2 f) \left(\psi^i(x,y) + \psi^r(x,y) \right) \right] \quad , \tag{D.71}$$

in which the functions $\psi^i(x,y)$, $\psi^r(x,y)$ and $\phi^r(x,y)$ are given in eqns. (D.41a), (D.41b) and (D.41c), respectively.

D.4 – Incident SH-Wave Solution

Unlike the plane strain wave problems, the SH, or anti-plane wave solution does not require potential functions, its solution satisfies the scalar wave equation and its harmonic wave solution satisfies the scalar Helmholtz equation,

$$\nabla^2 u_z + k^2 u_z = 0 \quad , \tag{D.72}$$

in which $k = \omega/\beta$ is the wave number for shear waves.

There is no mode conversion in this case, therefore, the compressional wave potential is absent. The incident SH-wave problem can be written easily by defining the incident wave,

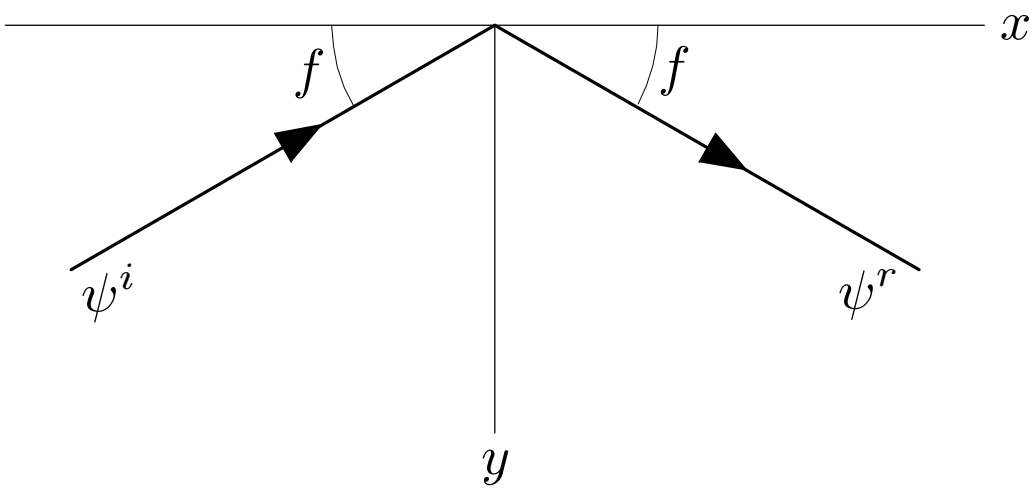

Figure D.3 – Incident and reflected SH-wave.

u_z^i, and the reflected wave, u_z^r, as

$$u_z^i = Se^{-ik(x\cos f - y\sin f)} \quad , \qquad (D.73a)$$

and

$$u_z^r = Se^{-ik(x\cos f + y\sin f)} \quad , \qquad (D.73b)$$

respectively. S is the amplitude of the incident wave pulse. It has been shown that a reflected wave with the same amplitude, S, would satisfy the shear stress boundary condition at the free surface as

$$\tau_{yz} = \mu \frac{\partial u_z}{\partial y}\bigg|_{y=0} = 0 \quad , \qquad (D.74)$$

in which $u_z = u_z^i + u_z^r$ is the total displacement in the semi-infinite medium.

D.4.1 – Displacement Wavefields for Incident SH-Waves

The anti-plane displacement, u_z, in the semi-infinite medium can be written as

$$u_z(x,y) = 2Se^{-ikx\cos f}\ \cos(ky\sin f) \qquad . \tag{D.75}$$

This is the summation of the incident and reflected waves as shown in Eq. (D.66). This shear wave only solution is not dependent on Poisson's Ratio, ν. The displacement amplitude at the free surface is a constant,

$$|u_z(x,0)| = 2S \qquad . \tag{D.76}$$

D.4.2 – Stress Wavefields for Incident SH-Waves

The shear stresses generated by incident SH-waves can be expressed simply as

$$\tau_{xz} = -2i\mu k\cos f\, e^{-ikx\cos f}\ \cos(ky\sin f) \qquad , \tag{D.77}$$

$$\tau_{yz} = -2\mu k\sin f\, e^{-ikx\cos f}\ \sin(ky\sin f) \qquad . \tag{D.78}$$

D.5 – Rayleigh Wave Solution

Unlike the body waves described in the previous sections, a semi-infinite medium is amenable to a surface wave and its larger amplitudes are confined near the free surface. If a harmonic wave function has the form

$$\phi = Ae^{-i\frac{\omega}{\alpha}(x\cos e - y\sin e)} \qquad , \tag{D.79}$$

it has an apparent velocity c on the free surface ($y = 0$). Consider the factor:

$$\frac{\omega}{\alpha}x\cos e = \frac{\omega x}{\alpha/\cos e} = \frac{\omega x}{c} \qquad , \tag{D.80}$$

the apparent velocity is defined as $c = \alpha/\cos e$ for this particular case. If $e \to 90°$, $c \to \infty$ because all particles on the surface appears to move in the same direction, therefore, it appears on the surface as if the wave is moving with an infinite speed.

Consider the case when $c < \beta < \alpha$ by defining the compressional potential and shear potential as

$$\phi = Ae^{-i\frac{\omega}{c}(x \pm \sqrt{\frac{c^2}{\alpha^2}-1}\, y)} \quad , \tag{$D.81a$}$$

$$\psi = Be^{-i\frac{\omega}{c}(x \pm \sqrt{\frac{c^2}{\beta^2}-1}\, y)} \quad , \tag{$D.81b$}$$

respectively. For the condition, $c < \beta < \alpha$: $\sqrt{\frac{c^2}{\beta^2}-1}$ is complex. The second partial derivatives of the potential functions can be listed as

$$\frac{\partial^2\phi}{\partial x^2} = (-i\frac{\omega}{c})^2\phi \quad , \tag{$D.82a$}$$

$$\frac{\partial^2\psi}{\partial x^2} = (-i\frac{\omega}{c})^2\psi \quad , \tag{$D.82b$}$$

$$\frac{\partial^2\phi}{\partial y^2} = \left(\mp i\frac{\omega}{c}\sqrt{\frac{c^2}{\alpha^2}-1}\right)^2\phi \quad , \tag{$D.82c$}$$

$$\frac{\partial^2\psi}{\partial y^2} = \left(\mp i\frac{\omega}{c}\sqrt{\frac{c^2}{\beta^2}-1}\right)^2\psi \quad , \tag{$D.82d$}$$

$$\frac{\partial^2\phi}{\partial x\partial y} = \left(-i\frac{\omega}{c}\right)\left(\mp i\frac{\omega}{c}\sqrt{\frac{c^2}{\alpha^2}-1}\right)\phi \quad , \tag{$D.82e$}$$

$$\frac{\partial^2\psi}{\partial x\partial y} = \left(-i\frac{\omega}{c}\right)\left(\mp i\frac{\omega}{c}\sqrt{\frac{c^2}{\beta^2}-1}\right)\psi \quad , \tag{$D.82f$}$$

The first boundary condition yields,

$$\begin{aligned}\tau_{yy}|_{y=0} &= (\lambda+2\mu)\nabla^2\phi - 2\mu\frac{\partial^2\phi}{\partial x^2} - 2\mu\frac{\partial^2\psi}{\partial y\partial x} \\ &= (\lambda+2\mu)\left[-\frac{\omega^2}{c^2} - \frac{\omega^2}{c^2}\left(\frac{c^2}{\alpha^2}-1\right)\right]Ae^{-i\omega x/c} \\ &+ 2\mu\frac{\omega^2}{c^2}Ae^{-i\omega x/c} - 2\mu\left[\mp\frac{\omega^2}{c^2}\sqrt{\frac{c^2}{\beta^2}-1}\right]Be^{-i\omega x/c} = 0\end{aligned} \tag{$D.83$}$$

Remove the harmonic time factor and divide the equation by $(\omega/c)^2$ and $(\lambda + 2\mu)$, the equation simplies to

$$\left(\frac{c^2}{\alpha^2} - 2\gamma^2\right) A \mp \left(2\gamma^2\sqrt{\frac{c^2}{\beta^2} - 1}\right) B = 0 \qquad (D.84)$$

Similarly, the second boundary condition,

$$\tau_{yx}|_{y=0} = 0 = 2\mu\frac{\partial^2\psi}{\partial y\partial x} + \mu\frac{\partial^2\psi}{\partial y^2} - \mu\frac{\partial^2\psi}{\partial x^2} \qquad (D.85)$$

can be simplified to

$$2\left(\pm\sqrt{\frac{c^2}{\alpha^2} - 1}\right) A + \left(\frac{c^2}{\beta^2} - 2\right) B = 0 \qquad (D.86)$$

Using the relationship

$$\frac{c^2}{\alpha^2}\frac{1}{\gamma^2} = \frac{c^2}{\alpha^2}\frac{\alpha^2}{\beta^2} = \frac{c^2}{\beta^2}$$

The first equation can be written as

$$\left(2 - \frac{c^2}{\beta^2}\right) A \pm 2\left(\sqrt{\frac{c^2}{\beta^2} - 1}\right) B = 0 \qquad (D.87)$$

The simultaneous equations can be written as a matrix equation as

$$\begin{bmatrix} \left(2 - \frac{c^2}{\beta^2}\right) & \pm 2\sqrt{\frac{c^2}{\beta^2} - 1} \\ \mp 2\sqrt{\frac{c^2}{\alpha^2} - 1} & \left(2 - \frac{c^2}{\beta^2}\right) \end{bmatrix} \begin{Bmatrix} A \\ B \end{Bmatrix} = \begin{Bmatrix} 0 \\ 0 \end{Bmatrix} \quad . \qquad (D.89)$$

The only nontrivial solution which exists is when the determinant of the above equation is zero, i.e.,

$$\left(2 - \frac{c^2}{\beta^2}\right)^2 + 4\left(\sqrt{\frac{c^2}{\alpha^2} - 1}\right)\left(\sqrt{\frac{c^2}{\beta^2} - 1}\right) = 0 \quad . \qquad (D.90)$$

A simpler transcendental equation can be obtained by defining a parameter, $q = c/\beta$ and using the fact that $c^2/\alpha^2 = \gamma^2 q^2$, that

$$q^6 - 8q^4 + (24 - 16\gamma^2)q^2 + 16(\gamma^2 - 1) = 0 \qquad . \qquad (D.91)$$

The table below shows the ratio, c/β, of the Rayleigh wave speed to the shear wave velocity as a function of the Poisson's Ratio $\bar{\nu}$. The ratio, $\gamma = \beta/\alpha$ is also shown. The relationship of γ and $\bar{\nu}$ can be expressed as $\gamma^2 = (1 - 2\bar{\nu})/(2(1 - \bar{\nu}))$. As shown, the Raleigh wave speed is from 13.6% to 4.5% slower than the shear wave velocity; it is always slower than the compressional wave velocity.

$\bar{\nu}$	c/β	$\lvert U_y/U_x \rvert$	γ^2	γ
0.00	0.874032	1.272020	0.5000	0.7071
0.05	0.883695	1.302284	0.4737	0.6509
0.10	0.893106	1.336414	0.4444	0.6667
0.15	0.902220	1.375033	0.4118	0.6417
0.20	0.910996	1.418579	0.3750	0.6124
0.25	0.919402	1.467894	0.3333	0.5774
0.30	0.927412	1.523749	0.2857	0.5345
1/3	0.932526	1.565199	0.2500	0.5000
0.35	0.935013	1.587326	0.2308	0.4804
0.40	0.942195	1.659775	0.1667	0.4082
0.45	0.948959	1.742982	0.0909	0.3015
0.50	0.955312	1.839271	0.0000	0.0000

D.5.1 – Displacement Wavefields for Incident Rayleigh-Waves

Using eq. (D.87) to relate the coefficient B to A, choose the second sign to ensure that the solution decays as y increases, i.e., a bounded solution. The horizontal and vertical displacements can be written as

$$u_x(x, y) = Re^{-ikx}\left[e^{-\nu_\alpha y} - \frac{1}{2}\left(2 - \frac{c^2}{\beta^2}\right)e^{-\nu_\beta y}\right] \qquad , \qquad (D.92)$$

$$u_y(x,y) = iRe^{-ikx}\left[-\sqrt{1-\frac{c^2}{\alpha^2}}e^{-\nu_\alpha y} + \frac{\left(2-\frac{c^2}{\beta^2}\right)}{2\sqrt{1-\frac{c^2}{\beta^2}}}e^{-\nu_\beta y}\right] \quad . \quad (D.93)$$

in which $k = \omega/c$, $R = -ikA$, and

$$\nu_\alpha = k\sqrt{1-\frac{c^2}{\alpha^2}} \quad ,$$

$$\nu_\beta = k\sqrt{1-\frac{c^2}{\beta^2}} \quad .$$

The ratio of the surface amplitudes of U_y and U_x are also shown in the above table as a function of $\bar{\nu}$. The u_y component has an imaginary exponent while the coefficient for u_x is real; this indicated those two components are out of phase by $\pi/2$ and they together produce a retrograde type of motion.

D.5.2 – Stress Wavefields for Incident Rayleigh-Waves

$$\tau_{xx}(x,y) = i\mu kRe^{-ikx}\left[-\left(\frac{c^2}{\beta^2}+2\left(1-\frac{c^2}{\alpha^2}\right)\right)e^{-\nu_\alpha y} + \left(2-\frac{c^2}{\beta^2}\right)e^{-\nu_\beta y}\right] \quad (D.94)$$

$$\tau_{yy}(x,y) = i\mu kRe^{-ikx}\left[\left(2-\frac{c^2}{\beta^2}\right)\left(e^{-\nu_\alpha y} - e^{-\nu_\beta y}\right)\right] \quad (D.95)$$

$$\tau_{xy}(x,y) = \mu kRe^{-ikx}\left[\frac{2\nu_\alpha}{k}\,e^{-\nu_\alpha y} - \frac{k\left(2-\frac{c^2}{\beta^2}\right)^2}{2\nu_\beta}\,e^{-\nu_\beta y}\right] \quad (D.96)$$

Appendix E

Accurate Calculation of Bessel's Functions

E.1 Functions with Small to Medium Arguments

The Bessel's Function of the First Kind and Zeroth Order can be determined as an infinite series in the form:

$$\begin{aligned} J_0(x) &= S_0 + S_1 + S_2 + S_3 + S_4 + \dots \\ &= 1 - \frac{(x/2)^2}{(1!)^2} + \frac{(x/2)^4}{(2!)^2} - \frac{(x/2)^6}{(3!)^2} + \frac{(x/2)^8}{(4!)^2} - \dots \end{aligned} \qquad (E1)$$

To calculate the terms, let $S_0 = 1$, then obtain the higher order terms in the series using the recurrence relationship

$$S_i = R_i^0 S_{i-1} \qquad ; \qquad i = 1, 2, 3, \dots \qquad (E2)$$

in which

$$R_i^0 = -\frac{x^2}{4i^2} \qquad . \qquad (E3)$$

To calculate the Bessel's Function of the Second Kind and Zeroth Order, the terms in the $J_0(x)$ can be reused as

$$Y_0(x) = \frac{2}{\pi}\left[\log\left(\frac{x}{2}\right) + \gamma\right] J_0(x) + \frac{2}{\pi}\left[S_1' + S_2' + S_3' + S_4' + \dots\right] \qquad . \qquad (E4)$$

The terms of the infinite series for $Y_0(x)$ can be determined from those of the J_0 series using the equation:

$$S_i' = -\alpha_i S_i \qquad ; \qquad i = 1, 2, 3, \dots \qquad (E5)$$

in which $\alpha_0 = 0$ and $\alpha_i = \alpha_{i-1} + 1/i$. The contant $\gamma = 0.57721566490153286$ is the Eluer's constant.

The Bessel's Function of the First Kind and First Order can be determined as an infinite series in the form:

$$\begin{aligned} J_1(x) &= T_1 + T_2 + T_3 + T_4 + \dots \\ &= \frac{x}{2} - \frac{(x/2)^3}{1!\,2!} + \frac{(x/2)^5}{2!\,3!} - \frac{(x/2)^7}{3!\,4!} + \dots \end{aligned} \qquad (E6)$$

To calculate the terms, let $T_1 = x/2$, then obtain the higher order terms in the series using the recurrence relationship

$$T_i = R_i^1 T_{i-1} \qquad ; \qquad i = 2, 3, 4, \dots \qquad (E7)$$

in which

$$R_i^1 = -\frac{x^2}{4i(i+1)} \qquad . \qquad (E8)$$

To calculate the Bessel's Function of the Second Kind and First Order, the terms in the $J_1(x)$ can be reused as

$$Y_1(x) = -\frac{2}{\pi z} + \frac{2}{\pi}\left[\log\left(\frac{x}{2}\right) + \gamma\right] J_1(x) - \frac{1}{\pi}\left[T_1' + T_2' + T_3' + T_4' + \dots\right] \quad . \qquad (E9)$$

The terms of the infinite series for $Y_0(x)$ can be determined from those of the $J_0(x)$ series using the equation:

$$T_i' = (\alpha_{i-1} + \alpha_i)\, T_i \qquad ; \qquad i = 1, 2, 3, \dots \qquad (E10)$$

in which α_i was defined earlier for $Y_0(x)$.

E.2 Functions with Large Arguments

For large aruments, the Hankel's Asymptotic Expansion is more efficient as it can yield accurate results with fewer terms. The expression for Bessel's Function of the First Kind and order n is

$$J_n(x) = \sqrt{\frac{2}{\pi x}}\left[\cos\left(x - \left(\tfrac{n}{2} + \tfrac{1}{4}\right)\pi\right) \cdot P_n(x) - \sin\left(x - \left(\tfrac{n}{2} + \tfrac{1}{4}\right)\pi\right) \cdot Q_n(x)\right] \quad . \qquad (E11)$$

The expression for Bessel's Function of the Second Kind and order n is similar,

$$Y_n(x) = \sqrt{\frac{2}{\pi x}} \left[\sin\left(x - \left(\tfrac{n}{2} + \tfrac{1}{4}\right)\pi\right) \cdot P_n(x) + \cos\left(x - \left(\tfrac{n}{2} + \tfrac{1}{4}\right)\pi\right) \cdot Q_n(x)\right] \quad . \tag{E12}$$

In the above expressions, P_n and Q_n are defined as

$$P_n(x) = \sum_{m=0}^{\infty} \frac{(-1)^m (n, 2m)}{(2x)^{2m}} \tag{E13a}$$

$$Q_n(x) = \sum_{m=0}^{\infty} \frac{(-1)^m (n, 2m+1)}{(2x)^{2m+1}} \tag{E13b}$$

in which the notation (n, m) is defined as

$$(n, m) = \frac{(4n^2 - 1^2)(4n^2 - 3^2) \ldots (4n^2 - (2m-1)^2)}{2^{2m}\, m!} \tag{E14}$$

For the special case of $J_0(x)$ and $Y_0(x)$, the Hankel Asymptotic Expansions are expressed as

$$J_0(x) = \sqrt{\frac{2}{\pi x}} \left[\cos\left(x - \tfrac{\pi}{4}\right) \cdot P_0(x) - \sin\left(x - \tfrac{\pi}{4}\right) \cdot Q_0(x)\right] \tag{E15a}$$

$$Y_0(x) = \sqrt{\frac{2}{\pi x}} \left[\sin\left(x - \tfrac{\pi}{4}\right) \cdot P_0(x) + \cos\left(x - \tfrac{\pi}{4}\right) \cdot Q_0(x)\right] \tag{E15b}$$

The series expansions for $P_0(x)$ and $Q_0(x)$ can be calculated as

$$P_0(x) = S_0 + S_2 + S_4 + S_6 + \ldots \tag{E16a}$$

$$Q_0(x) = T_1 + T_3 + T_5 + T_7 + \ldots \tag{E16b}$$

By recurrence, S_i and T_i can be calculated as

$$S_i = R_i S_{i-1} \quad , \quad i = 2, 4, 6, \ldots \tag{E17a}$$

$$T_i = R_i T_{i-1} \quad , \quad i = 3, 5, 7, \ldots \tag{E17b}$$

if R_i is defined as

$$R_i = -\frac{(2i-3)^2(2i-1)^2}{64i(i-1)x^2} \qquad , \tag{$E18$}$$

with the initial values set as $S_0 = 1$ and $T_1 = -1/(8x)$.

With the expansion as defined above, P_0 and Q_0 expanded to 8 terms have the coefficients defined as

$$\begin{aligned} P_0(x) =& 1 - \frac{9}{128\,x^2} + \frac{3675}{32768\,x^4} - \frac{2401245}{4194304\,x^6} + \frac{13043905875}{2147483648\,x^8} \\ & - \frac{30241281245175}{274877906944\,x^{10}} + \frac{213786613951685775}{70368744177664\,x^{12}} \\ & - \frac{1070401384414690453125}{9007199254740992\,x^{14}} + \dots \end{aligned} \tag{$E19$}$$

$$\begin{aligned} Q_0(x) =& -\frac{1}{8\,x} + \frac{75}{1024\,x^3} - \frac{59535}{262144\,x^5} + \frac{57972915}{33554432\,x^7} - \frac{418854310875}{17179869184\,x^9} \\ & + \frac{1212400457192925}{2199023255552\,x^{11}} - \frac{10278202593831046875}{562949953421312\,x^{13}} \\ & + \frac{60013837619516978071875}{72057594037927936\,x^{15}} - \dots \end{aligned} \tag{$E20$}$$

It is clear the coefficients would become larger and larger for the later terms. The denominator with the large powers of x would nevertheless make the series convergent when x is reasonably large.

The above formulas would have cancellation problems and the series can be made more accurate if they can be rewritten using two-angle formulas as

$$J_0(x) = \sqrt{\frac{2}{\pi x}}\,\beta_0(x)\cos\left(x - \tfrac{\pi}{4} - \alpha_0(x)\right) \qquad , \tag{$E21a$}$$

$$Y_0(x) = \sqrt{\frac{2}{\pi x}}\,\beta_0(x)\sin\left(x - \tfrac{\pi}{4} - \alpha_0(x)\right) \qquad , \tag{$E21b$}$$

in which

$$\beta_0^2(x) = P_0^2(x) + Q_0^2(x) \qquad , \tag{$E22$}$$

and

$$\alpha_0(x) = -\tan^{-1}\left(\frac{Q_0(x)}{P_0(x)}\right) \qquad . \tag{E23}$$

To obtain the expression for $\beta_0(x)$, assume it has the form

$$\beta_0(x) = a_0 + \frac{a_2}{x^2} + \frac{a_4}{x^4} + \frac{a_6}{x^6} + \frac{a_8}{x^8} + \ldots + \frac{a_{14}}{x^{14}} + \ldots \qquad , \tag{E24}$$

and substitute it in Eq. (E22) and match the coefficients according to the powers of x and that yields the formula to be

$$\begin{aligned}\beta_0(x) = 1 &- \frac{1}{16\,x^2} + \frac{53}{512\,x^4} - \frac{4447}{8192\,x^6} + \frac{3066403}{524288\,x^8} \\ &- \frac{896631415}{8388608\,x^{10}} + \frac{796754802993}{268435456\,x^{12}} - \frac{500528959023471}{4294967296\,x^{14}} + \ldots\end{aligned} \tag{E25}$$

To obtain α_0, first assume a series $r_0(x)$ as

$$r_0(x) = \frac{a_1}{x} + \frac{a_3}{x^3} + \frac{a_5}{x^5} + \frac{a_7}{x^7} + \ldots + \frac{a_{15}}{x^{15}} + \ldots \qquad , \tag{E26}$$

then obtain the unknown coefficients by comparing the polynomials of the two sides of the equation

$$r_0(x)P_0(x) = -Q_0(x) \qquad , \tag{E27}$$

then the resulting polynomial is equal to $-Q_0(x)/P_0(x)$. Apply now the series expansion for $\tan^{-1}$ as

$$\tan^{-1} r_0 = r_0 - \frac{r_0^3}{3} + \frac{r_0^5}{5} - \frac{r_0^7}{7} + \ldots \qquad , \tag{E28}$$

then $\alpha_0(x)$ can be expressed as

$$\begin{aligned}\alpha_0(x) = \frac{1}{8\,x} &- \frac{25}{384\,x^3} + \frac{1073}{5120\,x^5} - \frac{375733}{229376\,x^7} + \frac{55384775}{2359296\,x^9} \\ &- \frac{24713030909}{46137344\,x^{11}} + \frac{7780757249041}{436207616\,x^{13}} - \frac{5261793482424425}{6442450944\,x^{15}} + \ldots\end{aligned} \tag{E29}$$

With these detailed expressions, x can be as small as 15 to obtain 15 digits of accuracy (double precision) and as low as 10 to obtain 7 digits of accuracy (single precision).

For the special case of $J_1(x)$ and $Y_1(x)$, the Hankel Asymptotic Expansions are expressed as

$$J_1(x) = \sqrt{\frac{2}{\pi x}}\ \left[\cos\left(x - \tfrac{3}{4}\pi\right) \cdot P_1(x) - \sin\left(x - \tfrac{3}{4}\pi\right) \cdot Q_1(x)\right] \qquad (E30a)$$

$$Y_1(x) = \sqrt{\frac{2}{\pi x}}\ \left[\sin\left(x - \tfrac{3}{4}\pi\right) \cdot P_1(x) + \cos\left(x - \tfrac{3}{4}\pi\right) \cdot Q_1(x)\right] \qquad (E30b)$$

The series expansions for $P_1(x)$ and $Q_1(x)$ can be calculated as

$$P_1(x) = S_0 + S_2 + S_4 + S_6 + \ldots \qquad (E31a)$$

$$Q_1(x) = T_1 + T_3 + T_5 + T_7 + \ldots \qquad (E31b)$$

By recurrence, S_i and T_i can be calculated as

$$S_i = R_i S_{i-1} \quad , \quad i = 2, 4, 6, \ldots \qquad (E32a)$$

$$T_i = R_i T_{i-1} \quad , \quad i = 3, 5, 7, \ldots \qquad (E32b)$$

if R_i is defined as

$$R_i = -\frac{(4-(2i-3)^2)(4-(2i-1)^2)}{64i(i-1)x^2} \qquad (E33)$$

with the initial values set as $S_0 = 1$ and $T_1 = 3/(8x)$.

With the expansion as defined above, P_1 and Q_1 expanded to 8 terms have the coefficients defined as

$$\begin{aligned} P_1(x) =& 1 + \frac{15}{128\,x^2} - \frac{4725}{32768\,x^4} + \frac{2837835}{4194304\,x^6} - \frac{14783093325}{2147483648\,x^8} \\ &+ \frac{33424574007825}{274877906944\,x^{10}} - \frac{232376754295310625}{70368744177664\,x^{12}} \\ &+ \frac{1149690375852815671875}{9007199254740992\,x^{14}} - \ldots \end{aligned} \qquad (E34)$$

$$\begin{aligned} Q_1(x) =& \frac{3}{8\,x} - \frac{105}{1024\,x^3} + \frac{72765}{262144\,x^5} - \frac{66891825}{33554432\,x^7} + \frac{468131288625}{17179869184\,x^9} \\ &- \frac{1327867167401775}{2199023255552\,x^{11}} + \frac{111004588013375306 25}{562949953421312\,x^{13}} \\ &- \frac{641527229725871144906 25}{72057594037927936\,x^{15}} + \ldots \end{aligned} \qquad (E35)$$

As in the cases of the zeroth order functions, the coefficients become larger and larger for the later terms, however, the series converge when x is reasonably large.

To eliminate the cancellation problems, the series can be made more accurate if they are rewritten using two-angle formulas as

$$J_1(x) = \sqrt{\frac{2}{\pi x}}\,\beta_1(x)\cos\left(x - \tfrac{3}{4}\pi - \alpha_1(x)\right) \qquad , \qquad (E36a)$$

$$Y_1(x) = \sqrt{\frac{2}{\pi x}}\,\beta_1(x)\sin\left(x - \tfrac{3}{4}\pi - \alpha_1(x)\right) \qquad , \qquad (E36b)$$

in which

$$\beta_1^2(x) = P_1^2(x) + Q_1^2(x) \qquad , \qquad (E37)$$

and

$$\alpha_1(x) = -\tan^{-1}\left(\frac{Q_1(x)}{P_1(x)}\right) \qquad . \qquad (E38)$$

To obtain the expression for $\beta_1(x)$, assume it has the form

$$\beta_0(x) = a_0 + \frac{a_2}{x^2} + \frac{a_4}{x^4} + \frac{a_6}{x^6} + \frac{a_8}{x^8} + \ldots + \frac{a_{14}}{x^{14}} + \ldots \qquad , \qquad (E39)$$

and substitute it in Eq. (xx) and match the coefficients according to the powers of x and that yields the formula to be

$$\begin{aligned}\beta_1(x) = 1 + \frac{3}{16\,x^2} - \frac{99}{512\,x^4} + \frac{6597}{8192\,x^6} - \frac{4057965}{524288\,x^8} \\ + \frac{1113686901}{8388608\,x^{10}} - \frac{951148335159}{268435456\,x^{12}} + \frac{581513783771781}{4294967296\,x^{14}} - \ldots\end{aligned} \qquad (E40)$$

To obtain α_1, first assume a series $r_1(x)$ as

$$r_1(x) = \frac{a_1}{x} + \frac{a_3}{x^3} + \frac{a_5}{x^5} + \frac{a_7}{x^7} + \ldots + \frac{a_{15}}{x^{15}} + \ldots \qquad , \qquad (E41)$$

then obtain the unknown coefficients by comparing the polynomials of the two sides of the equation

$$r_1(x)P_1(x) = -Q_1(x) \qquad , \qquad (E42)$$

then the resulting polynomial is equal to $-Q_1(x)/P_1(x)$. Apply now the series expansion for $\tan^{-1}$ as

$$\tan^{-1} r_1 = r_1 - \frac{r_1^3}{3} + \frac{r_1^5}{5} - \frac{r_1^7}{7} + \dots \qquad , \tag{$E43$}$$

then $\alpha_1(x)$ can be expressed as

$$\begin{aligned}\alpha_1(x) = &-\frac{3}{8\,x} + \frac{21}{128\,x^3} - \frac{1899}{5120\,x^5} + \frac{543483}{229376\,x^7} - \frac{8027901}{262144\,x^9} \\ &+ \frac{30413055339}{46137344\,x^{11}} - \frac{9228545313147}{436207616\,x^{13}} + \frac{10139844510243441}{10737418240\,x^{15}} - \dots\end{aligned} \tag{$E44$}$$

With these expressions for J_1 and Y_1, x can be as small as 15 to obtain 15 digits of accuracy (double precision) and as low as 10 to obtain 7 digits of accuracy (single precision).

Appendix F

Three-Dimensional Green's Function Matrices Matrices for an Infinite Space

To obtain the three-dimensional Green's function matrices, $[U]$ and $[T]$, for application in the representation theorem, the solution for displacements and stresses generated by a point load must be considered. The first row of $[U]$, i.e., U_{11}, U_{12} and U_{13}, correspond to the displacements in the x, y and z-direction induced by a point load in the x-direction, respectively. The second row of $[U]$, i.e., U_{21}, U_{22} and U_{23}, correspond to the displacements in the x, y and z-direction induced by a point load in the y-direction, respectively. The third row of $[U]$, i.e., U_{31}, U_{32} and U_{33}, correspond to the displacements in the x, y and z-direction generated by a point load in the z-direction, respectively.

The respective rows of the 3×3 matrix, $[T]$, contain the tractions at the observation point generated by the point loads described above. They are calculated as the matrix product of the stresses generated by the point loads and the direction cosines of the outward normal vector at the surface.

F.1 Green's Functions for an Infinite Medium

For an infinite, homogeneous and isotropic medium, the solution of a vertical point load can be used to produce the solutions for point loads in the x and the y-direction using an orthogonal transformation.

F.1.1 Displacements and Stresses Generated by a Vertical Point Load

Shown in Fig. F.1 is a concentrated load Q in the positive z-direction. The solution of the three-dimensional wave equation can be written in terms of two potential functions ϕ

and χ as shown in Lamb's paper (1904) as

$$\phi = \frac{-Q}{4\pi k^2 \mu} \frac{\partial}{\partial z} \left(\frac{e^{-ihr}}{r} \right), \tag{F1}$$

$$\chi = \frac{Q}{4\pi k^2 \mu} \left(\frac{e^{-ikr}}{r} \right), \tag{F2}$$

in which $r = \sqrt{x^2 + y^2 + z^2}$, $x = x_o - x_s$, $y = y_o - y_s$ and $z = z_0 - z_s$ are the relative position of the observation point with respect to the source point in the x, y and z-directions, respectively.

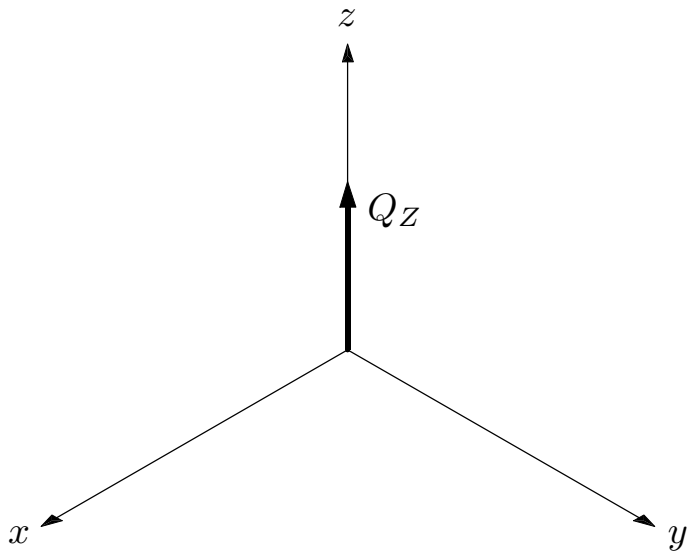

Figure F.1 – Vertical Q_Z Point Force Configuration.

The argument of ϕ, $hr = \omega r/\alpha$, is a dimensionless frequency normalized by the compressional wave velocity α, implying that ϕ is a potential for compressional waves. On the other hand, χ is the shear wave potential because $kr = \omega r/\beta$ is normalized by the shear wave velocity β. The exponential function with a negative argument is used in

this derivation because it represents an outgoing wave as $r \to \infty$ when associated with the harmonic time factor $e^{i\omega t}$.

For a unit applied load Q in the vertical (Z) direction, let the amplitude $Q = 1$. Also, define for convenience the parameters

$$\gamma_k = \left(\frac{1}{4\pi\mu k^2}\right), \tag{F3}$$

$$\varepsilon_h = \left(\frac{e^{-ihr}}{r}\right), \tag{F4}$$

and

$$\varepsilon_k = \left(\frac{e^{-ikr}}{r}\right), \tag{F5}$$

so that equations (F1) and (F2) can be written as

$$\phi = -\gamma_k \frac{\partial \varepsilon_h}{\partial z} \qquad \text{and} \qquad \chi = \gamma_k \varepsilon_k \qquad .$$

F.1.1.1 – Displacements

Using the potentials ϕ and χ, the displacements for a vertical load in the x, y, and z-directions, respectively, can be expressed as,

$$\begin{aligned} U_{31} &= \frac{\partial \phi}{\partial x} + \frac{\partial^2 \chi}{\partial x \partial z} \\ &= \gamma_k \left[\frac{\partial^2}{\partial x \partial z}\left(\varepsilon_k - \varepsilon_h\right)\right] \end{aligned} \tag{F6}$$

$$\begin{aligned} U_{32} &= \frac{\partial \phi}{\partial y} + \frac{\partial^2 \chi}{\partial y \partial z} \\ &= \gamma_k \left[\frac{\partial^2}{\partial y \partial z}\left(\varepsilon_k - \varepsilon_h\right)\right] \end{aligned} \tag{F7}$$

and

$$U_{33} = \frac{\partial \phi}{\partial z} + \frac{\partial^2 \chi}{\partial z^2} + k^2 \chi \qquad (F8)$$
$$= \gamma_k \left[\frac{\partial^2}{\partial z^2} \left(\varepsilon_k - \varepsilon_h \right) + k^2 \varepsilon_k \right]$$

in which, the derivatives of ε_k are represented by

$$\frac{\partial^2 \varepsilon_k}{\partial x \partial z} = \frac{xz}{r^3} \left[\frac{3}{r} \left(\frac{1}{r} + ik \right) - k^2 \right] e^{-ikr}, \qquad (F9a)$$

$$\frac{\partial^2 \varepsilon_k}{\partial y \partial z} = \frac{yz}{r^3} \left[\frac{3}{r} \left(\frac{1}{r} + ik \right) - k^2 \right] e^{-ikr}, \qquad (F9b)$$

and

$$\frac{\partial^2 \varepsilon_k}{\partial z^2} = \frac{1}{r^3} \left[\frac{(3z^2 - r^2)}{r} \left(\frac{1}{r} + ik \right) - k^2 z^2 \right] e^{-ikr}, \qquad (F9c)$$

The derivatives of ε_h are in the same form except the subscript and variable k should be replaced by h.

F.1.1.2 – Stresses

The stress components, σ_{xx_Z}, σ_{xy_Z}, σ_{xz_Z}, σ_{yy_Z}, σ_{yz_Z} and σ_{zz_Z} can be expressed in terms of the potential functions ϕ and χ as

$$\frac{1}{\mu} \sigma_{xx_Z} = -k^2 \phi - 2 \frac{\partial^2 \phi}{\partial y^2} - 2 \frac{\partial^2 \phi}{\partial z^2} + 2 \frac{\partial^3 \chi}{\partial x^2 \partial z} \qquad (F10)$$
$$= \gamma_k \left[k^2 \frac{\partial \varepsilon_h}{\partial z} + 2 \frac{\partial^3 \varepsilon_h}{\partial y^2 \partial z} + 2 \frac{\partial^3 \varepsilon_h}{\partial z^3} + 2 \frac{\partial^3 \varepsilon_k}{\partial x^2 \partial z} \right]$$

$$\frac{1}{\mu}\sigma_{xyz} = 2\frac{\partial^2\phi}{\partial x\partial y} + 2\frac{\partial^3\chi}{\partial x\partial y\partial z} \qquad (F11)$$
$$= 2\gamma_k\left[\frac{\partial^3}{\partial x\partial y\partial z}\left(\varepsilon_k - \varepsilon_h\right)\right]$$

$$\frac{1}{\mu}\sigma_{xzz} = 2\frac{\partial^2\phi}{\partial x\partial z} + 2\frac{\partial^3\chi}{\partial x\partial z^2} + k^2\frac{\partial\chi}{\partial x} \qquad (F12)$$
$$= \gamma_k\left[2\frac{\partial^3}{\partial x\partial z^2}\left(\varepsilon_k - \varepsilon_h\right) + k^2\frac{\partial\varepsilon_k}{\partial x}\right]$$

$$\frac{1}{\mu}\sigma_{yyz} = -k^2\phi - 2\frac{\partial^2\phi}{\partial x^2} - 2\frac{\partial^2\phi}{\partial z^2} + 2\frac{\partial^3\chi}{\partial y^2\partial z} \qquad (F13)$$
$$= \gamma_k\left[k^2\frac{\partial\varepsilon_h}{\partial z} + 2\frac{\partial^3\varepsilon_h}{\partial x^2\partial z} + 2\frac{\partial^3\varepsilon_h}{\partial z^3} + 2\frac{\partial^3\varepsilon_k}{\partial y^2\partial z}\right]$$

$$\frac{1}{\mu}\sigma_{yzz} = 2\frac{\partial^2\phi}{\partial y\partial z} + 2\frac{\partial^3\chi}{\partial y\partial z^2} + k^2\frac{\partial\chi}{\partial y} \qquad (F14)$$
$$= \gamma_k\left[2\frac{\partial^3}{\partial x\partial z^2}\left(\varepsilon_k - \varepsilon_h\right) + k^2\frac{\partial\varepsilon_k}{\partial y}\right]$$

and

$$\frac{1}{\mu}\sigma_{zzz} = -k^2\phi - 2\frac{\partial^2\phi}{\partial x^2} - 2\frac{\partial^2\phi}{\partial y^2} + 2\frac{\partial^3\chi}{\partial z^3} + 2k^2\frac{\partial\chi}{\partial z} \qquad (F15)$$
$$= \gamma_k\left[k^2\frac{\partial}{\partial z}\left(\varepsilon_h + 2\varepsilon_k\right) + 2\frac{\partial^3\varepsilon_h}{\partial x^2\partial z} + 2\frac{\partial^3\varepsilon_h}{\partial y^2\partial z} + 2\frac{\partial^3\varepsilon_k}{\partial z^3}\right]$$

in which,

$$\frac{\partial\varepsilon_k}{\partial x} = -\frac{x}{r^2}\left[ik + \frac{1}{r}\right]e^{-ikr}, \qquad (F16a)$$

$$\frac{\partial\varepsilon_k}{\partial y} = -\frac{y}{r^2}\left[ik + \frac{1}{r}\right]e^{-ikr}, \qquad (F16b)$$

$$\frac{\partial \varepsilon_k}{\partial z} = -\frac{z}{r^2}\left[ik + \frac{1}{r}\right]e^{-ikr}, \tag{F16c}$$

$$\frac{\partial^3 \varepsilon_k}{\partial x^2 \partial z} = \frac{e^{-ikr}}{r^3}\left\{-\frac{15xz}{r^3}\left(\frac{1}{r} + ikx\right) + \frac{3z}{r}\left(\frac{1}{r} + ik\right) + \frac{k^2x^2z}{r}\left(\frac{6}{r} + ik\right) - k^2z\right\} \tag{F16d}$$

$$\frac{\partial^3 \varepsilon_k}{\partial y^2 \partial z} = \frac{e^{-ikr}}{r^3}\left\{-\frac{15yz}{r^3}\left(\frac{1}{r} + iky\right) + \frac{3z}{r}\left(\frac{1}{r} + ik\right) + \frac{k^2y^2z}{r}\left(\frac{6}{r} + ik\right) - k^2z\right\} \tag{F16e}$$

$$\frac{\partial^3 \varepsilon_k}{\partial z^3} = \frac{e^{-ikr}}{r^3}\left\{-\frac{15z}{r^3}\left(\frac{1}{r} + ikz^2\right) + \frac{9z}{r}\left(\frac{1}{r} + ik\right) + \frac{k^2z^3}{r}\left(\frac{6}{r} + ik\right) - 3k^2z\right\} \tag{F16f}$$

$$\frac{\partial^3 \varepsilon_k}{\partial x \partial y \partial z} = \frac{xyz}{r^4}\left\{-\frac{15}{r^2}\left(\frac{1}{r} + ik\right) + k^2\left(\frac{6}{r} + ik\right)\right\}e^{-ikr} \tag{F16g}$$

$$\frac{\partial^3 \varepsilon_k}{\partial x \partial z^2} = \frac{x}{r^3}\left\{\frac{(3r^2 - 15z^2)}{r^3}\left(\frac{1}{r} + ik\right) + \frac{k^2z^2}{r}\left(\frac{6}{r} + ik\right) - k^2\right\}e^{-ikr} \tag{F16h}$$

and

$$\frac{\partial^3 \varepsilon_k}{\partial y \partial z^2} = \frac{y}{r^3}\left\{\frac{(3r^2 - 15z^2)}{r^3}\left(\frac{1}{r} + ik\right) + \frac{k^2z^2}{r}\left(\frac{6}{r} + ik\right) - k^2\right\}e^{-ikr} \tag{F16i}$$

The above expressions are quite lengthy to list mathematically, but since the infinite space is homogeneous and isotropic, the solution developed for a vertical point load Q_Z can be reused for horizontal point loads Q_X and Q_Y if proper transformations are performed. It

will be shown in the next two sections that it is quite simple to obtain the expression for the horizontal loads, only simple rearrangement of the spatial variables are required.

F.1.2 Displacements and Stresses Generated by a Point Load in the X-Direction

Shown in Fig. F.2 is an illustration of the horizontal point load in the x-direction using the (x, y, z) coordinate system. Also in the same figure is the (x', y', z') coordinate system. The (x', y', z') system is rotated from the (x, y, z) system by $90°$ about the y-axis. The orthogonal transformation between these systems can be expressed as

$$[Q(xyz \longleftarrow x'y'z')] = \begin{bmatrix} 0 & 0 & 1 \\ 1 & 0 & 0 \\ 0 & 1 & 0 \end{bmatrix} \quad .$$

To obtain the results for the horizontal point load Q_X, two steps are required:

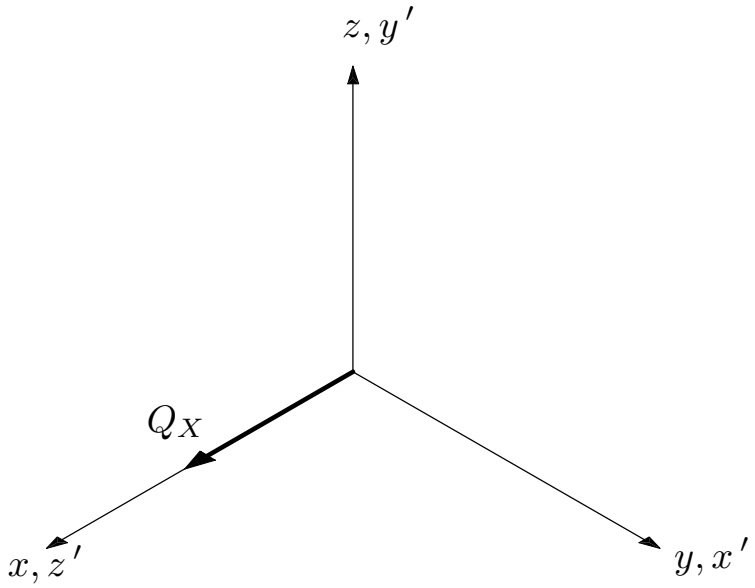

Figure F.2 – Horizontal Q_X Point Force Configuration.

(1) Calculate the displacements and stresses in the (x', y', z') system using the expressions presented in Section F.1. This is done because Q_X is in the z'-direction, formerly the vertical direction. The values for the prime coordinates can be obtained from the position vector of the present configuration as

$$\begin{bmatrix} x' \\ y' \\ z' \end{bmatrix} = [Q]^T \begin{bmatrix} x \\ y \\ z \end{bmatrix} = \begin{bmatrix} 0 & 1 & 0 \\ 0 & 0 & 1 \\ 1 & 0 & 0 \end{bmatrix} \begin{bmatrix} x \\ y \\ z \end{bmatrix} = \begin{bmatrix} y \\ z \\ x \end{bmatrix} \quad .$$

(2) Use the calculated displacements in the (x', y', z') system and transform them to the (x, y, z) system using

$$\begin{bmatrix} u_x \\ u_y \\ u_z \end{bmatrix} = [Q] \begin{bmatrix} u_{x'} \\ u_{y'} \\ u_{z'} \end{bmatrix} = \begin{bmatrix} 0 & 0 & 1 \\ 1 & 0 & 0 \\ 0 & 1 & 0 \end{bmatrix} \begin{bmatrix} u_{x'} \\ u_{y'} \\ u_{z'} \end{bmatrix} = \begin{bmatrix} u_{z'} \\ u_{x'} \\ u_{y'} \end{bmatrix} \quad .$$

To transform the stress tensor, use the transformation of the form

$$[A(x, y, z)] = [Q][A(x', y', z')][Q]^T \quad ,$$

in which $[A]$ is any matrix, a tensor of second rank.

F.1.2.1 – Displacements

If the displacements in Section F.1 can be written in functional form as

$$\begin{bmatrix} U_{31}(x', y', z') \\ U_{32}(x', y', z') \\ U_{33}(x', y', z') \end{bmatrix}$$

then the displacements caused by a horizontal point load in the x-direction can be written as

$$\begin{bmatrix} U_{11}(x, y, z) \\ U_{12}(x, y, z) \\ U_{13}(x, y, z) \end{bmatrix} = \begin{bmatrix} U_{33}(y, z, x) \\ U_{31}(y, z, x) \\ U_{32}(y, z, x) \end{bmatrix} \qquad (F17)$$

in which the coordinates x, y and z are the only parameters displayed because the material properties of the viscoelastic medium remain unchanged.

F.1.2.2 – Stresses

If the stress tensor in Section F.1 can be written in functional form as

$$\begin{bmatrix} \sigma_{xx_Z}(x',y',z') & \sigma_{xy_Z}(x',y',z') & \sigma_{xz_Z}(x',y',z') \\ \sigma_{yx_Z}(x',y',z') & \sigma_{yy_Z}(x',y',z') & \sigma_{yz_Z}(x',y',z') \\ \sigma_{zx_Z}(x',y',z') & \sigma_{zy_Z}(x',y',z') & \sigma_{zz_Z}(x',y',z') \end{bmatrix}$$

then the stresses caused by a horizontal point load in the x-direction can be written as

$$\begin{bmatrix} \sigma_{xx_X}(x,y,z) & \sigma_{xy_X}(x,y,z) & \sigma_{xz_X}(x,y,z) \\ \sigma_{yx_X}(x,y,z) & \sigma_{yy_X}(x,y,z) & \sigma_{yz_X}(x,y,z) \\ \sigma_{zx_X}(x,y,z) & \sigma_{zy_X}(x,y,z) & \sigma_{zz_X}(x,y,z) \end{bmatrix} \qquad (F18)$$
$$= \begin{bmatrix} \sigma_{zz_Z}(y,z,x) & \sigma_{zx_Z}(y,z,x) & \sigma_{zy_Z}(y,z,x) \\ \sigma_{xz_Z}(y,z,x) & \sigma_{xx_Z}(y,z,x) & \sigma_{xy_Z}(y,z,x) \\ \sigma_{yz_Z}(y,z,x) & \sigma_{yx_Z}(y,z,x) & \sigma_{yy_Z}(y,z,x) \end{bmatrix}$$

F.1.3 Displacements and Stresses Generated by a Point Load in the Y-Direction

Shown in Fig. F.3 is an illustration of the horizontal point load in the y-direction using the (x,y,z) coordinate system. Also in the same figure is the (x',y',z') coordinate system. The (x',y',z') system is rotated from the (x,y,z) system by 90° about the x-axis. The orthogonal transformation between these systems can be expressed as

$$[Q(xyz \longleftarrow x'y'z')] = \begin{bmatrix} 0 & 1 & 0 \\ 0 & 0 & 1 \\ 1 & 0 & 0 \end{bmatrix} \qquad .$$

To obtain the results for the horizontal point load Q_Y, the same type of procedures as those used in Section F.2 can be applied. First calculate the displacements and stresses in the (x',y',z') system using the expressions presented in Section F.1. This is done because Q_Y is in the z'-direction, formerly the vertical direction. The values for the prime coordinates can be obtained from the position vector of the present configuration as

$$\begin{bmatrix} x' \\ y' \\ z' \end{bmatrix} = [Q]^T \begin{bmatrix} x \\ y \\ z \end{bmatrix} = \begin{bmatrix} 0 & 0 & 1 \\ 1 & 0 & 0 \\ 0 & 1 & 0 \end{bmatrix} \begin{bmatrix} x \\ y \\ z \end{bmatrix} = \begin{bmatrix} z \\ x \\ y \end{bmatrix} \qquad .$$

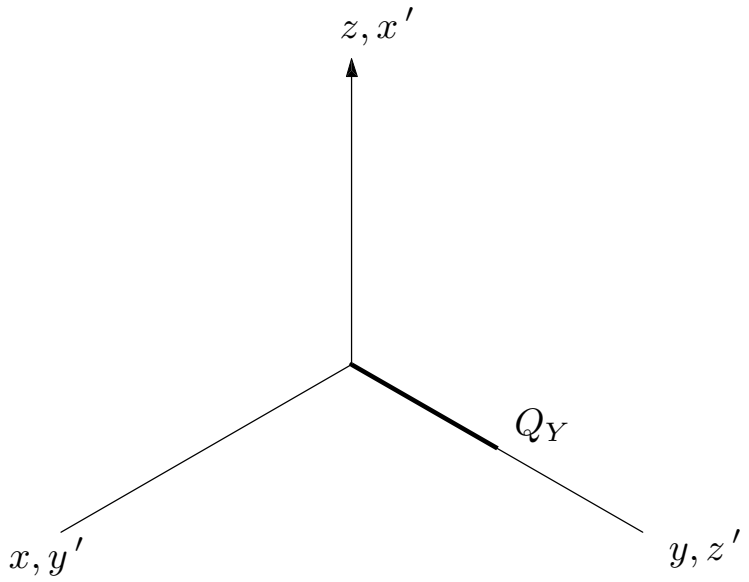

Figure F.3 – Horizontal Q_Y Point Force Configuration.

Next use the calculated displacements in the (x', y', z') system and transform them to the (x, y, z) system using

$$\begin{bmatrix} u_x \\ u_y \\ u_z \end{bmatrix} = [Q] \begin{bmatrix} u_{x'} \\ u_{y'} \\ u_{z'} \end{bmatrix} = \begin{bmatrix} 0 & 1 & 0 \\ 0 & 0 & 1 \\ 1 & 0 & 0 \end{bmatrix} \begin{bmatrix} u_{x'} \\ u_{y'} \\ u_{z'} \end{bmatrix} = \begin{bmatrix} u_{y'} \\ u_{z'} \\ u_{x'} \end{bmatrix} \qquad .$$

To transform the stress tensor, use the transformation of the form

$$[A(x, y, z)] = [Q][A(x', y', z')][Q]^T \qquad ,$$

in which $[A]$ is any matrix, a tensor of second rank.

F.1.3.1 – Displacements

In terms of the displacements in Section F.1.1, the displacements caused by a horizontal point load in the y-direction can be written as

$$\begin{bmatrix} U_{21}(x, y, z) \\ U_{22}(x, y, z) \\ U_{23}(x, y, z) \end{bmatrix} = \begin{bmatrix} U_{32}(z, x, y) \\ U_{33}(z, x, y) \\ U_{31}(z, x, y) \end{bmatrix} \qquad (F19)$$

F.1.3.2 – Stresses

In terms of the stress tensor presented in Section F.1, the stresses caused by a horizontal point load in the y-direction can be written as

$$\begin{bmatrix} \sigma_{xx_Y}(x,y,z) & \sigma_{xy_Y}(x,y,z) & \sigma_{xz_Y}(x,y,z) \\ \sigma_{yx_Y}(x,y,z) & \sigma_{yy_Y}(x,y,z) & \sigma_{yz_Y}(x,y,z) \\ \sigma_{zx_Y}(x,y,z) & \sigma_{zy_Y}(x,y,z) & \sigma_{zz_Y}(x,y,z) \end{bmatrix} = \begin{bmatrix} \sigma_{yy_Z}(z,x,y) & \sigma_{yz_Z}(z,x,y) & \sigma_{yx_Z}(z,x,y) \\ \sigma_{zy_Z}(z,x,y) & \sigma_{zz_Z}(z,x,y) & \sigma_{zx_Z}(z,x,y) \\ \sigma_{xy_Z}(z,x,y) & \sigma_{xz_Z}(z,x,y) & \sigma_{xx_Z}(z,x,y) \end{bmatrix} \quad (F20)$$

F.1.4 Formation of matrices $[U]$ and $[T]$

Using the expressions derived in Sections F.1.1, F.1.2 and F.1.3, the Green's function matrices $[U]$ and $[T]$ for the boundary integral equation can be formed as

$$[U] = \begin{bmatrix} U_{11} & U_{12} & U_{13} \\ U_{21} & U_{22} & U_{23} \\ U_{31} & U_{32} & U_{33} \end{bmatrix} \quad (F21)$$

and

$$[T] = \begin{bmatrix} T_{11} & T_{12} & T_{13} \\ T_{21} & T_{22} & T_{23} \\ T_{31} & T_{32} & T_{33} \end{bmatrix} \quad (F22)$$

in which the elements of $[T]$ can be calculated by the matrix products

$$\begin{bmatrix} T_{11} \\ T_{12} \\ T_{13} \end{bmatrix}^T = \begin{bmatrix} \sigma_{xx_X} & \sigma_{xy_X} & \sigma_{xz_X} \\ \sigma_{yx_X} & \sigma_{yy_X} & \sigma_{yz_X} \\ \sigma_{zx_X} & \sigma_{zy_X} & \sigma_{zz_X} \end{bmatrix} \begin{bmatrix} n_x \\ n_y \\ n_z \end{bmatrix} \quad (F23)$$

$$\begin{bmatrix} T_{21} \\ T_{22} \\ T_{23} \end{bmatrix}^T = \begin{bmatrix} \sigma_{xx_Y} & \sigma_{xy_Y} & \sigma_{xz_Y} \\ \sigma_{yx_Y} & \sigma_{yy_Y} & \sigma_{yz_Y} \\ \sigma_{zx_Y} & \sigma_{zy_Y} & \sigma_{zz_Y} \end{bmatrix} \begin{bmatrix} n_x \\ n_y \\ n_z \end{bmatrix} \quad (F24)$$

and

$$\begin{bmatrix} T_{31} \\ T_{32} \\ T_{33} \end{bmatrix}^T = \begin{bmatrix} \sigma_{xx_Z} & \sigma_{xy_Z} & \sigma_{xz_Z} \\ \sigma_{yx_Z} & \sigma_{yy_Z} & \sigma_{yz_Z} \\ \sigma_{zx_Z} & \sigma_{zy_Z} & \sigma_{zz_Z} \end{bmatrix} \begin{bmatrix} n_x \\ n_y \\ n_z \end{bmatrix} \quad (F25)$$

In the above equations, the vector elements n_x, n_y and n_z are the direction cosines of the outer normal vector at the boundary surface.

F.2 Surface Green's Functions for a Semi-Infinite Medium

To obtain the three-dimensional Green's function matrices $[U]$ and $[T]$ for the surface of a semi-infinite medium, the solution for displacements and stresses caused by 3 orthogonal point forces must be considered. These solutions are available from the classical publications by Lamb (1903) and Nakano (1908). Because of the axisymmetric properties of a point force, the cylindrical coordinates system was utilized for its solution and the results are expressed in Hankel Transforms. In this section, the displacements and the point forces are all located on the surface of the semi-infinite space, simplifying the geometry of the problem.

The three rows of matrix $[T]$ contain the tractions at the surface S generated by the respective point forces at the observation point as described earlier. But since the tractions at the surface of the semi-infinite medium, as defined by the boundary conditions, are zero, the traction Green's function matrix $[T]$ is zero.

F.2.1 Surface Displacements Generated by Point Forces

With the presence of the half-space surface, the mathematical formulation of the Green's functions become more tedious than the infinite space formulation because of the mode conversions between the compressional and shear waves. The advantage of a mirror image as exploited in Appendix B for SH-waves is not possible for the present scenario. The normal practice for a half spce formulation is to use a mirror image source to eliminate one

of the surface stresses and to use the Hankel Transform to remove the other component. The Hankel Transforms leave the solutions in the form of an infinite integral as shown below:

Case One: A vertical Point Source

$$u_{zz} = \frac{f_{zz}}{\mu r} P_z = -\frac{P_z}{2\pi\mu}\left(\frac{a_o}{r}\right)\int_0^\infty \frac{k\nu}{(2k^2-1)^2 - 4k^2\nu\nu'}\, J_0(a_0 k)\, dk \quad , \quad (F26)$$

$$u_{rz} = \frac{f_{rz}}{\mu r} P_z = \frac{P_z}{2\pi\mu}\left(\frac{a_o}{r}\right)\int_0^\infty \frac{k^2[(2k^2-1) - 2\nu\nu']}{(2k^2-1)^2 - 4k^2\nu\nu'}\, J_1(a_0 k)\, dk \quad , \quad (F27)$$

$$u_{\psi z} = \frac{f_{\psi z}}{\mu r} P_z = 0 \quad . \quad (F28)$$

Case Two: A Horizontal Point Source

$$\begin{aligned} u_{rr} &= \frac{f_{rr}}{\mu r} P_r \cos\psi \\ &= \frac{P_r}{2\pi\mu}\left(\frac{a_o}{r}\right)\cos\psi \left[\int_0^\infty \frac{k\nu'\,(J_2(a_0k) - J_0(a_0k))\; dk}{(2k^2-1)^2 - 4k^2\nu\nu'} \right. \\ &\qquad \left. + \int_0^\infty \frac{k}{\nu'}\,(J_2(a_0k) + J_0(a_0k))\;\; dk \right] \quad , \end{aligned} \quad (F29)$$

$$\begin{aligned} u_{zr} &= \frac{f_{zr}}{\mu r} P_r \cos\psi \\ &= -\frac{P_r}{2\pi\mu}\left(\frac{a_o}{r}\right)\cos\psi \int_0^\infty \frac{k^2[(2k^2-1) - 2\nu\nu']}{(2k^2-1)^2 - 4k^2\nu\nu'}\, J_1(a_0 k)\, dk \quad , \end{aligned} \quad (F30)$$

$$\begin{aligned} u_{\psi r} &= \frac{f_{\psi r}}{\mu r} P_r \sin\psi \\ &= \frac{P_r}{2\pi\mu}\left(\frac{a_o}{r}\right)\sin\psi \left[\int_0^\infty \frac{k\nu'\,(J_2(a_0k) + J_0(a_0k))\; dk}{(2k^2-1)^2 - 4k^2\nu\nu'} \right. \\ &\qquad \left. + \int_0^\infty \frac{k}{\nu'}\,(J_2(a_0k) - J_0(a_0k))\;\; dk \right] \quad . \end{aligned} \quad (F31)$$

in which $a_0 = \omega r/\beta$, $\nu = \sqrt{k^2 - \gamma^2}$, $\nu' = \sqrt{k^2 - 1}$ and $\gamma = \beta/\alpha$.

Eq. (F29) and Eq. (F31) have integrals which do not contain the Rayleigh Determinant, $F(k) = (2k^2-1)^2 - 4k^2\nu\nu'$, but rather a denominator of the form $\nu' = \sqrt{k^2-1}$. These

terms are motion caused by pure shear waves without interaction with the compressional waves. These integrals are absent in the motion generated by a vertical point force.

To simplify the numerical implmentation, contour integration can be used to evaluate the infinite integrals as were the cases in Appendix C.

F.2.2 Formation of $[U]$ and $[T]$

Since the Green's Functions given in Section F.2.1 were derived using a cylindrical coordinate system, some re-organization is necessary to put the results into a form for the applications in this dissertation. The displacements for the vertical point force can be uaed quite readily by transforming u_r and u_ψ into u_x and u_y using simple triginometric functions; the vertical displacement is already in the z-direction. The displacement for the horizontal force must be converted and applied to two different horizontal directions in the $x-$ and $y-$ directions by shifting the azimuthal properties of the results.

Consider now the coordinate system illustrated in Fig. F.4. Note that the polar coordinate system is defined with the z-axis pointing downward, which is the typical convention for classical geophysical problems. The origin of the polar coordinate system is defined at the source point, $\vec{r}_p$, therefore, the observation point, $\vec{r}$, is located at the coordinates, (r, ψ, z), in which

$$r = |\vec{r} - \vec{r}_p| = \sqrt{(x - x_p)^2 + (y - y_p)^2} \qquad (F32)$$

and

$$\psi = \arg(\vec{r} - \vec{r}_p) = \tan^{-1}\left(\frac{y - y_p}{x - x_p}\right) \qquad . \qquad (F33)$$

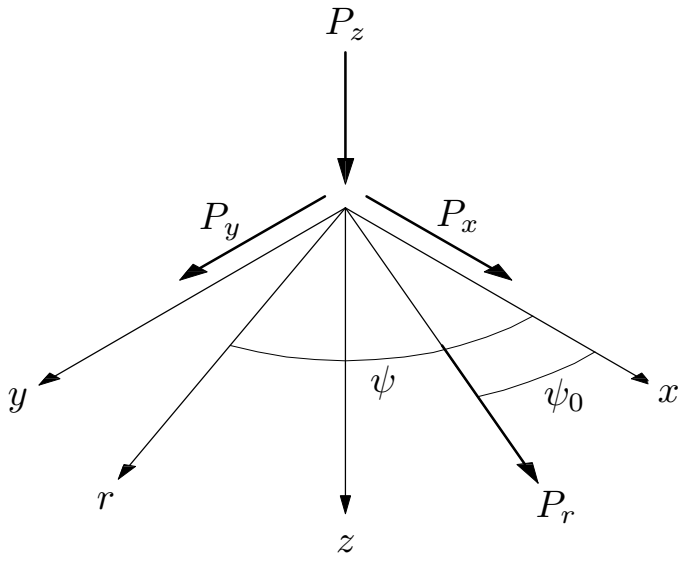

Figure F.4 – The Definition of the Cylindrical Coordinate System.

The z-dependency of the Green's Functions is included in the functions f.

Using the polar coordinate system, all horizontal point forces can be represented by $P_r(\psi_0)$ because the reference angle can be varied to match any orientation. Therefore, the general displacement-force relationship can be written in a form of a 3×2 matrix as

$$\left\{ \begin{array}{c} u_r(r,\psi) \\ u_\psi(r,\psi) \\ u_z(r,\psi) \end{array} \right\} = \frac{1}{\mu r} \left[\begin{array}{cc} f_{rr}\cos(\psi-\psi_0) & f_{rz} \\ f_{\psi r}\sin(\psi-\psi_0) & 0 \\ f_{zr}\cos(\psi-\psi_0) & f_{zz} \end{array} \right] \left\{ \begin{array}{c} P_r(\psi_0) \\ P_z \end{array} \right\} \quad . \qquad (F34)$$

To obtain a displacement-force relationship in the Cartesian coordinate system, the following mapping of the forces and the displacements may be used:

$$\left\{ \begin{array}{c} P_x(\vec{r}_p) \\ P_y(\vec{r}_p) \\ P_z(\vec{r}_p) \end{array} \right\} = \left\{ \begin{array}{c} P_r(0) \\ P_r(\pi/2) \\ P_z \end{array} \right\} \quad , \qquad (F35)$$

and

$$\left\{ \begin{array}{c} u_x(\vec{r}) \\ u_y(\vec{r}) \\ u_z(\vec{r}) \end{array} \right\} = \left[\begin{array}{ccc} \cos\psi & -\sin\psi & 0 \\ \sin\psi & \cos\psi & 0 \\ 0 & 0 & 1 \end{array} \right] \left\{ \begin{array}{c} u_r(r,\psi) \\ u_\psi(r,\psi) \\ u_z(r,\psi) \end{array} \right\} \quad . \qquad (F36)$$

The first, Eq. (F34), can be used with Eq. (F35) to relate the displacements in polar coordinates to the forces in Cartesian Coordinates as

$$\left\{ \begin{array}{c} u_r(r,\psi) \\ u_\psi(r,\psi) \\ u_z(r,\psi) \end{array} \right\} = \frac{1}{\mu r} \left[\begin{array}{ccc} f_{rr}\cos\psi & f_{rr}\sin\psi & f_{rz} \\ f_{\psi r}\sin\psi & -f_{\psi r}\cos\psi & 0 \\ f_{zr}\cos\psi & f_{zr}\sin\psi & f_{zz} \end{array} \right] \left\{ \begin{array}{c} P_x(\vec{r}_p) \\ P_y(\vec{r}_p) \\ P_z(\vec{r}_p) \end{array} \right\} \quad , \qquad (F37)$$

Now apply the transformation (F36) to both sides of Eq. (F37). The result is a displacement-force relationship in Cartesian coordinates written as

$$\left\{ \begin{array}{c} u_x(\vec{r}) \\ u_y(\vec{r}) \\ u_z(\vec{r}) \end{array} \right\} = \frac{1}{\mu r} \big[G\big] \left\{ \begin{array}{c} P_x(\vec{r}_p) \\ P_y(\vec{r}_p) \\ P_z(\vec{r}_p) \end{array} \right\} \quad , \qquad (F38)$$

in which

$$\big[G\big] = \left[\begin{array}{ccc} f_{rr}\cos^2\psi - f_{\psi r}\sin^2\psi & (f_{rr}+f_{\psi r})\sin\psi\cos\psi & f_{rz}\cos\psi \\ (f_{rr}+f_{\psi r})\sin\psi\cos\psi & f_{rr}\sin^2\psi - f_{\psi r}\cos^2\psi & f_{rz}\sin\psi \\ f_{zr}\cos\psi & -f_{zr}\sin\psi & f_{zz} \end{array} \right] \quad . \qquad (F39)$$

Using Cartesian coordinates, the factors, $\sin\psi$ and $\cos\psi$, can be evaluated simply as

$$\sin\psi = \frac{y - y_p}{r} \quad , \qquad (F40)$$

and

$$cos\psi = \frac{x - x_p}{r} \quad . \qquad (F41)$$

If the elements of matrix $[G]$ are defined with subscripts as

$$\big[G\big] = \left[\begin{array}{ccc} G_{xx} & G_{xy} & G_{xz} \\ G_{yx} & G_{yy} & G_{yz} \\ G_{zx} & G_{zy} & G_{zz} \end{array} \right] \quad , \qquad (F42)$$

then the matrix $[U(\vec{r}_p|\vec{r})]$ can be formed as

$$\big[U(\vec{r}_p|\vec{r})\big] = \frac{1}{\mu r} \left[\begin{array}{ccc} G_{xx} & G_{yx} & G_{zx} \\ G_{xy} & G_{yy} & G_{zy} \\ G_{xz} & G_{yz} & G_{zz} \end{array} \right] \quad . \qquad (F43)$$

A column in $[G]$ represents the displacements caused by a point load in a particular direction, following the order x, y, z, respectively. In the matrix $[U(\vec{r}_p|\vec{r})]$, however, the same displacement components are stored as a row. The reason for this transposition can be observed by the definition of $[U]$ in Appendix A.